Development of Time-Resolved XAFS Spectroscopy Techniques

Applications in Homogeneous Catalysis

Moniek Tromp

Development of Time-Resolved XAFS Spectroscopy Techniques

Applications in Homogeneous Catalysis

Ontwikkeling van Tijdsopgeloste XAFS Spectroscopie Technieken

Toepassingen in Homogene Katalyse

(met een samenvatting in het Nederlands)

Proefschrift

ter verkrijging van de graad van doctor aan de Universiteit Utrecht
op gezag van de Rector Magnificus, Prof. Dr. W. H. Gispen
ingevolge het besluit van het College voor Promoties in het openbaar te verdedigen op
maandag 19 april 2004 des middags te 2:30 uur

door

Moniek Tromp

geboren op 7 september 1977, te Apeldoorn.

Promotores: Prof. Dr. Ir. D. C. Koningsberger,
               Debye Institute, Utrecht University, Utrecht, The Netherlands

               Prof. Dr. G. van Koten,
               Debye Institute, Utrecht University, Utrecht, The Netherlands

Co-promotores: Dr. J. A. van Bokhoven,
               Institute for Chemical- and Bioengineering, Swiss Federal Institute of
               Technology (ETH), Zurich, Switzerland

               Dr. G. P. F. van Strijdonck,
               Van 't Hoff Institute for Molecular Sciences, University of Amsterdam,
               Amsterdam, The Netherlands

Ma vie n'est pas derrière moi
Ni avant
Ni maintenant
Elle est dedans

Jacques Prévert

Contents

Chapter 1

General Introduction
and
Outline Thesis

Introduction

Catalysis

In the last decades, enormous emphasis is placed on the world's responsibility to take care of the environment. For the chemical industry, this means that there is a growing demand for the production of compounds in a responsible and sustainable manner. New processes have to be developed which require a minimum amount of energy and resources and produce the least possible waste.

One of the main methods to obtain products in a selective and sustainable manner is catalysis. A catalyst increases the rate of a chemical reaction, without being consumed itself. Moreover, since a catalyst can also direct the product selectivity of a reaction, many compounds cannot be produced without a catalyst. In catalysis, three fields can be distinguished: homogeneous catalysis in which both the reactants and catalysts have the same aggregation phase, heterogeneous catalysis in which the reactants and catalyst possess a different phase, and biocatalysis which uses enzymes as a catalyst.[1]

In the petrochemical industry and during large-scale production of base chemicals mainly heterogeneous catalysts are used, because of their easy separation from products and reactants. Moreover, they are thermally stable. Homogeneous catalysts, however, are in general more active and selective. The electronic and steric properties of homogeneous transition metal catalysts can be fine-tuned in a controlled manner by changing the ligands around the metal center. In this way their activity and selectivity can be directed and the stability can be increased. Several drawbacks of these catalysts exist. The development costs are high and the difficult separation and fast degradation of the catalyst prevents an easy recycling. Consequently, homogeneous catalysts are mainly used in small batch reaction processes that have high demands for pure and selective products, which occurs e.g. in the pharmaceutical industry.

Revealing Reaction Mechanisms in Homogeneous Catalysis

To improve the performance of catalytic processes, detailed knowledge about the catalytic system is crucial. Therefore, characterization techniques are required that provide detailed structural information about the working catalytic system. Ideally, the structure of the catalytically active site is determined during the catalytic reaction, *in situ* and in a time-resolved mode. Establishing structure – performance relationships leads to fundamental understanding of the catalytic processes.

In general, homogeneous catalysts have a well-defined structure in contrast to heterogeneous systems. Better insights in and understanding of the catalytic complex and catalytic cycle are therefore obtained in homogeneous catalysis. Crystal structures give detailed structural information about the catalytic complex and extensive kinetic studies lead to information about the reaction mechanisms. Sometimes, reaction intermediates or resting states are isolated and crystallized. In many studies presented in the literature however, a catalytic cycle is proposed using indirect evidence, without detailed structural information about the reaction intermediates themselves.

The arsenal of generally applied characterization techniques does not enable such detailed structural determination. Nuclear Magnetic Resonance (NMR) yields the local coordination of atoms. It can identify structural units from their characteristic chemical shifts and detects atom connectivities and distances in structures through coupling patterns. The application of this technique however is limited to accessible nuclei and *in situ* experiments are often difficult. Techniques like Infra Red and UV-Vis spectroscopy can generally be performed *in situ* and time-resolved, but are only able to identify a limited number of functional groups within molecules, local symmetry and bond angles or specific electronic transitions respectively.

An experimental technique that fills the gap in structural analysis and that can be applied *in situ* and in a time-resolved mode is X-ray absorption fine structure (XAFS) spectroscopy.[2] XAFS is a very powerful technique to determine the local structure in materials (type and number of neighboring atoms, distances, electronic properties of absorber atom). Since the technique does not require long-range ordering of the material, amorphous materials and solutions can be studied. The technique is today broadly applied in heterogeneous catalysis. Only a few good examples in homogeneous catalysis are known, although the properties of XAFS spectroscopy suggest that it can be applied successfully. Detailed electronic and structural information about the homogeneous catalysts in their chemical active environment can be obtained and structure – performance relationships derived. The limited amount of applications in homogeneous catalysis may be due to the complicated data-analysis, which will be illustrated in **Chapter 3** of this thesis.

As any technique, XAFS spectroscopy has limitations. It is a bulk technique, so an average of all different compounds in the reaction mixture is obtained which severely complicates the data-analysis and interpretation. Moreover, the concentration of the species under investigation should be high enough to be able to measure them with a good signal to noise ratio in order to characterize them accurately. A specific compound in a mixture can only be distinguished if it is present in amounts higher than 10 to 20 %. Experiments should therefore be chosen carefully.

It is clear that XAFS spectroscopy is complementary to other techniques. A combination of different spectroscopic techniques is required to unravel the complete catalytic system under investigation.

XAFS Spectroscopy

In this thesis the application of XAFS spectroscopy in homogeneous catalysis is explored. Developments of theory and data-analysis procedures, and instrumentation to monitor homogeneous catalytic reactions *in situ* and in a time-resolved mode are described. Therefore, an introduction into the technique will be presented here. The different set-ups and instrumentation to perform XAFS experiments, including the novel time-resolved *in situ* XAFS set-up, are described in **Chapter 2**.

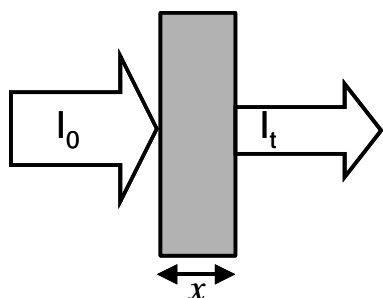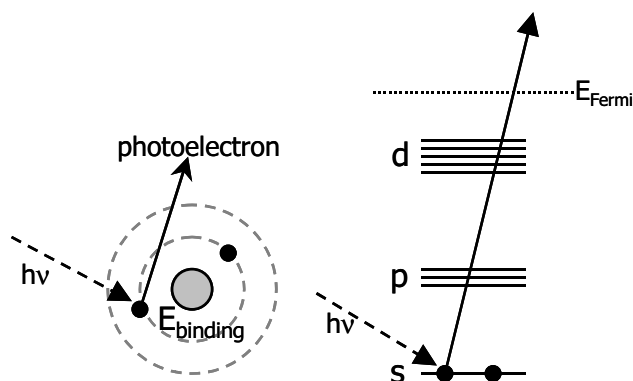**Figure 1.** Attenuation of an X-ray beam by an absorbing sample; Lambert's Law.

Figure 2. The photoelectric effect: Excitation of a core electron to an empty state or the continuum.

XAFS Theory

In an X-ray absorption experiment a sample is exposed to high-energy X-rays that are produced by a synchrotron. The sample absorbs part of the photons, dependent on its absorption characteristics. The incoming X-ray beam with intensity I_0 is attenuated by the sample according to Lambert's Law (Figure 1):

$$I_t = I_0 e^{-\mu(E)x}, \tag{1}$$

where I_t is the intensity of the transmitted photons, $\mu(E)$ the linear absorption coefficient and x the absorption path length which is the thickness of the sample. If the energy of the X-ray photons is high enough to excite a core electron to an empty state or the continuum (Figure 2) a strong increase in absorption is observed. This is called the photo-electronic effect as drawn in Figure 2. In a plot that shows the absorption as a function of energy, a step is visible, the so-called absorption edge (Figure 3).[2] Since the absorption edge is correlated to the binding energy E_0 of an electron, the absorption edge is element specific.

At energies of the incident X-ray beam I_0 larger than E_0, the photoelectron obtains a kinetic energy E_{kin} defined by:

$$E_{kin} = h\nu - E_0. \tag{2}$$

The outgoing photoelectron can be regarded as a spherical wave with wavelength $\lambda = 2\pi/k$ and is defined as:

$$k = \sqrt{\left[\left(\frac{8\pi^2 m}{h^2}\right)(h\nu - E_0)\right]}, \tag{3}$$

with m the electron mass and h Planck's constant.

The absorption coefficient, $\mu(E)$, of the sample is proportional to the probability of the photoelectric effect. Within the dipole approximation, which is only valid for photon wavelengths longer than atomic dimensions,[3] the transition probability is a function of the initial state ψ_i and final state ψ_f wave functions according to Fermi's Golden Rule:[4]

$$\mu(E) \propto \left|\left\langle \psi_f \left| \hat{\mathbf{e}} \bullet \mathbf{r} \right| \psi_i \right\rangle\right|^2 \delta(E_f - E_i - h\nu). \tag{4}$$

In this formula, **ê** is the electric field polarization vector of the photon and **r** the coordinate vector of the electron. The delta function describes the conservation of energy.

The outgoing electron scatters against the electron clouds of neighboring atoms, creating a backscattered wave that interferes with the outgoing wave. The final state wave function is thus a superposition of the outgoing and backscattered waves. The interference between these waves is a function of the energy and depends on the local structure of the absorber atom. In an X-ray absorption spectrum (Figure 3), this interference appears as oscillations in the absorption spectrum, which is called fine structure. The absorption coefficient above the absorption edge is defined as:

$$\mu_{tot} = \mu_0\left(1 + \chi(k)\right) \tag{5}$$

with μ_0 the atomic background and χ the oscillatory EXAFS part of the spectrum as a function of k.

Figure 3 displays the absorption spectrum of Cu foil. It can be divided in three parts. The first part, A, is the so-called pre-edge part giving information about the oxidation state and the geometry. The features in the second part B, the X-ray absorption near-edge spectroscopy (XANES) part, provide information about the coordination geometry and oxidation state. Finally, part C is the extended x-ray absorption fine structure (EXAFS) from which detailed geometrical data can be derived.
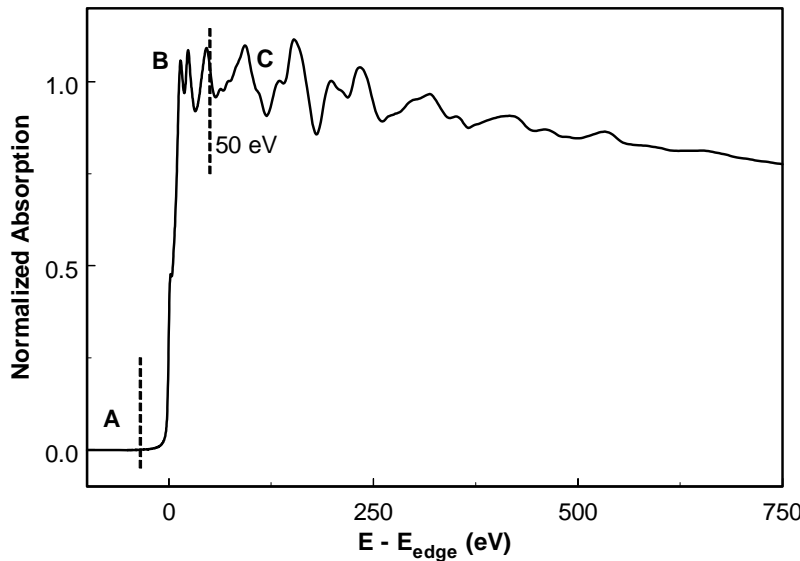

Figure 3. Typical x-ray absorption spectrum, showing (1) the pre-edge, (2) the X-ray absorption near edge region (XANES) including absorption edge and (3) the extended x-ray absorption fine structure (EXAFS) region.

Geometrical Information from EXAFS

As mentioned above, EXAFS, which is the fine structure observed in Figure 3(C), originates from scattering of the outgoing electron against the electron clouds of neighboring atoms, creating a backscattered wave that interferes with the outgoing photoelectron.[2] The interference pattern is not only determined by the type of atoms but also by the positions of these atoms. In a single scattering approximation the photoelectron scatters only once before it returns to the absorber atom (see Figure 3). This simplification is sufficient to describe and analyze the EXAFS signals in most experimental data. The EXAFS function can be described as a summation over all interference patterns scattered off of all neighboring atoms:

$$\chi(k) = \sum_j A_j(k) \sin\left(2kR_j + \varphi_j(k)\right) \qquad (6)$$

with j referring to the jth coordination shell, R_j the distance of the absorber atom to this coordination shell, $A_j(k)$ the backscattering amplitude, and $\varphi_j(k)$ the phase shift experienced by the photoelectron.

The backscattering amplitude $A_j(k)$ is a function of k:

$$A_j(k) = \frac{S_0^2 e^{-2R_j/\lambda}}{kR_j^2} N_j F_j(k) e^{-2\sigma_j^2 k^2} . \qquad (7)$$

It contains the coordination number, N_j, and the magnitude of the backscattering amplitude $F_j(k)$ which is element specific. In addition damping of the amplitude occurs. S_0^2 is an amplitude reduction factor and approximates the loss in photon intensity caused by many-body effects like shake-up and shake-off due to relaxation processes after electron excitation.[2] The exponential term containing the mean free path of the photoelectron λ accounts for the finite lifetime of the excited state. The thermal motion and structural disorder in the distance R_j is described by the Debye-Waller factor σ.

Fourier transformation of the EXAFS data results in a radial atomic distribution function.[5] Analysis of the EXAFS data will thus yield the type and number of neighbors, their distance to the scatterer and their disorder.[6] A careful data-analysis procedure[6] is required to obtain reliable geometric information. This procedure will be explained in detail in **Chapter 3**.

AXAFS

The outgoing electron can also scatter against the electron cloud of the absorber atom itself. This is called Atomic XAFS.[7,8,9] This scattering results in a peak in the Fourier Transform at approximately the atomic radius and contains information on the interatomic potential, i.e. the electronic structure as determined by the absorber atom and its neighbors. Controversy exists in the literature about the existence of Atomic XAFS and the assignments of the low *R*-peaks in the Fourier transform of the oscillatory part of the XAFS data.[10] Careful background subtraction and EXAFS data-analysis procedures are required to properly isolate the AXAFS contribution from the total XAFS data.[9] This will be discussed in **Chapter 5** and evidence for the existence of AXAFS will be provided.

XANES

The XANES part of the absorption spectrum (Figure 3(B)) is determined by the empty density of states (DOS). The empty DOS is probed by multiple scattering of the outgoing electron.[2] At energies just above the absorption edge, the excited photoelectron possesses a low kinetic energy. Few processes exist that are able to absorb this low amount of energy, resulting in a long mean free path. The long mean free path allows the photoelectron to scatter more than once (Figure 4), and even against rather distant atoms (up to 30Å). This multiple scattering thus can give information about relative positions of these neighboring atoms. Stereochemical information like coordination and bond angles can be obtained from this part of the absorption spectrum. An extensive XANES study is described in **Chapter 4**, revealing important information on the DOS of and charge distribution within the samples under investigation.

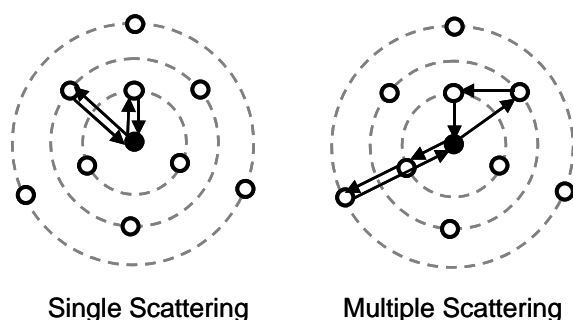

Single Scattering   Multiple Scattering

Figure 4. After excitation of an electron of the absorber atom (solid black circle) to the continuum, the photoelectron scatters against neighboring atoms (empty black circles). Examples of single scattering and multiple scatterings paths are indicated.

Outline Thesis

In the standard scanning data acquisition mode of XAFS data (described in **Chapter 2**), collection times of EXAFS spectra vary from minutes to hours. As there is interest in obtaining structural information on dynamic systems, an alternative data acquisition method, i.e. energy dispersive (ED) mode, has been developed allowing short collection times.[11] The time-resolution achievable at the moment is in the millisecond to second range. The ED-XAFS technique (**Chapter 2**) is further developed and applied to homogeneous catalytic systems in order to determine catalytic reaction intermediates and to gain insights into selected homogeneous catalytic reaction mechanisms. Moreover, since a combination of spectroscopic techniques gives complementary information about the system under investigation, a new set-up is developed to allow simultaneous time-resolved UV-Vis and ED-XAFS measurements. This set-up and its instrumentation are described in detail in **Chapter 2**.

The structures of the homogeneous catalysts, catalytic precursors and resting states in the catalytically active phase, i.e. solution, are determined with 'normal' scanning XAFS. The EXAFS data-analysis for organometallic complexes is very difficult. Thus a procedure that accurately analyzes EXAFS data of organometallic systems was required. A new refined data-analysis procedure is developed which is described in **Chapter 3.** Although the crystal structures of many of these catalytic compounds are well known, the structures in reaction medium are often unclear. Measuring the catalysts in reaction medium can give essential information regarding their catalytic activity and selectivity as shown in **Chapters 3, and 6a**.

X-ray absorption near edge spectroscopy (XANES) and Atomic XAFS (AXAFS) studies are performed, in combination with theoretical FEFF8.0 and DFT (ADF) calculations, to learn more about the electronic and geometrical properties of different organometallic complexes. The Pd K-edge of series of organometallic (PP)Pd(XX) complexes is studied extensively in **Chapter 4**. Detailed information about the positions of molecular orbitals and charge distribution within these complexes is obtained. In **Chapter 5** clear evidence for the existence and correctness of the recently developed AXAFS technique is presented. It will be shown that AXAFS provides direct information about electron density changes of the metal under investigation. Moreover, it is demonstrated that AXAFS can be used to probe the electronic properties of principally every atom. This is especially interesting for systems that, e.g., are not amenable to NMR.

Different homogeneous systems are studied in detail using the newly developed time-resolved spectroscopic techniques. Homogeneous palladium catalysts are found to be very active and selective in various organic synthesis reactions. However, their stability is often too low for large-scale industrial processes. Bidentate diphosphine ligands are used to influence the properties of the catalyst and thereby the performance of the catalyst and its stability towards deactivation. In **Chapter 6b**, the size and nature of the different inactive Pd-clusters formed during the allylic substitution reaction as a function of ligand and solvent are studied in detail using a combination of ED-XAFS and time-resolved UV-Vis experiments. Important insights in the deactivation mechanism of this system are obtained.

The novel combined set-up, allowing simultaneous acquisition of ED-XAFS and time-resolved UV-Vis, was used to study copper(II) catalyzed arylation reactions in **Chapter 7**. Clear changes in both the UV-Vis spectra and the ED-XANES spectra are observed, giving insights in changing oxidation states and geometry of the copper catalysts. Moreover, the combination with additional techniques like NMR, XRD, EPR and IR made it possible to propose a new reaction mechanism.

References

1. R. A. van Santen, P. W. N. M. van Leeuwen, J. A. Moulijn, B. A. Averill (Editors), *Catalysis: An Integrated Approach, Second, Revised and Enlarged Edition*, Elsevier, Amsterdam, **1999**.
2. For example, *X-ray Absorption, principles, applications, techniques of EXAFS, SEXAFS and XANES*, eds. D. C. Koningsberger and R. Prins, Wiley Interscience, New York, **1988**.
3. B. L. Henke, W. M. Gullikson, J. C. Davis, *At. Data and Nucl. Data Tables* **1993**, *53*, 181.
4. J. A. Muller, J. W. Wilkins, *Phys. Rev. B* **1984**, *29*, 4331.
5. D. E. Sayers, E. A. Stern, F. W. Lyttle, *Phys. Res. Lett.* **1971**, *27*, 1204.
6. D. C. Koningsberger, B. L. Mojet, G. E. van Dorssen, D. E. Ramaker, *Top. Catal.* **2000**, *10*, 143.
7. B. W. Holland, J. B. Pendry, R. F. Pettifer, J. Bordas, *J. Phys. C: Solid State Phys.* **1978**, *11*, 633.
8. J. J. Rehr, C. H. Booth, F. Bridges, S. I. Zabinsky, *Phys. Rev. B* **1994**, *49*, 12347.
9. G. E. van Dorssen, D. C. Koningsberger, D. E. Ramaker, *J. Phys.: Condens. Matter* **2002**, *14*, 13529.
10. A. Filliponi, A. Di Cicco, *Phys. Rev. B* **1996**, *53*, 9466.
11. For example M. A. Newton, A. J. Dent, J. Evans, *Chem. Soc. Rev.* **2002**, *31*, 83.

Chapter 2

XAFS Data Acquisition

Methods and Set-ups

&

Novel Combined Time-Resolved

ED-XAFS / UV-Vis Set-up

Introduction

The traditional and most used XAFS data acquisition mode is the 'normal' scanning mode, allowing data-acquisition times in the range from minutes to hours. Exact data-acquisition times depend on the element and concentration. As there is interest in obtaining structural information on dynamic systems such as chemical reactions, which occur on faster time scales, alternative methods of data acquisition have been developed. Nice overviews on time-resolved XAFS have appeared in literature.[1,2,3] In this chapter the different data acquisition methods and corresponding set-ups will be described. The strengths and limitations are discussed. Some emphasis is placed on the energy dispersive data acquisition mode. Moreover, the development of a new set-up that enables the *simultaneous* acquisition of time-resolved UV-Vis and ED-XAFS data on homogeneous systems is presented in detail. The basic principles of XAFS spectroscopy have been discussed in **Chapter 1**. [4,5]

XAFS Data Acquisition

I. Scanning XAFS

In the standard data acquisition mode, the photon energy is scanned in a step-by-step mode, i.e. monochromatic light is used to measure the absorption as a function of energy, yielding spectra of very high quality.[5] A schematic representation of the set-up is shown in Figure 1. The entrance and exit slits (items I and III in Figure 1) define the size of the X-ray beam spot. The double crystal monochromator (item II in Figure 1) isolates a specific energy from the synchrotron beam according to the Bragg relation:

$$n\lambda = 2d \sin\theta_i, \tag{1}$$

with the order of reflection n, the wavelength λ, the lattice spacing d, and the angle of incident beam θ_i. The double crystal is used to maintain the horizontal direction of the reflected beam.

Detection of the x-rays can be performed by ionization chambers (IV, VI and VIII) and is based on ionization of noble gasses by photons. Different gas mixtures are required for different energy ranges to obtain a linear ionization with the amount and energy of the photons. The sample (V) is placed between the first and second ionization chamber. A reference sample (VII) (e.g. foil) can be measured simultaneously between the second and

third ionization chamber. This results in measuring I_0 in the first, I_t in the second and I_r in the third ionization chamber.

Alternative detection methods, such as fluorescence and electron yield are also possible.[5] These detection methods are required when the absorption of the sample is very high and the EXAFS signal is only a small fraction of the total absorption. In these cases, it is desirable to enhance the signal of interest by using the proper detector to discriminate the XAFS signal from the background. The fluorescence technique, for example, gives in general better data than transmission when the absorption of the element of interest is less than a few percent of the total absorption of the sample. This is the case for low energy edge or element present in low concentrations. Electron yield detection is a method for example used to enhance the surface sensitivity of the XAFS technique. Only transmission-type experiments are described in this thesis.

Figure 1. Schematic representation of a normal scanning XAFS set-up with (I) entrance slits, (II) double crystal monochromator, (III) exit slits, (IV) ionization chamber I_0, (V) sample, (VI) ionization chamber I_t, (VII) reference, (VIII) ionization chamber I_{ref}.
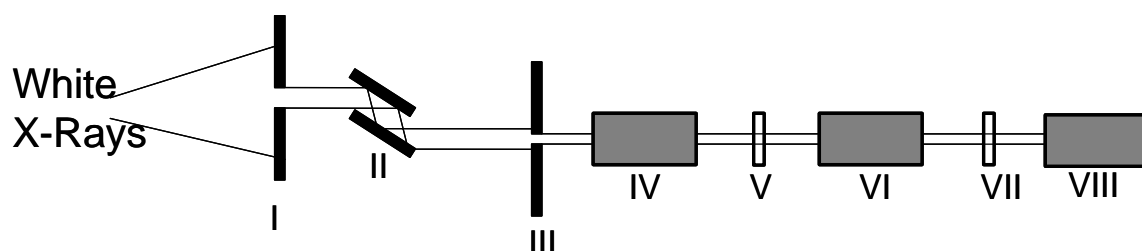
II. Quick-EXAFS

The experimental set-up used for QEXAFS experiments is similar to that of the 'normal' scanning XAFS. Again, the energies are measured energy-by-energy using stepper motors, but now the monochromator is continuously driven through the required energy range with a simultaneous detector read-out.[6] The absorption of the sample can be measured in both the forward and reverse direction. The data acquisition time of QEXAFS is therefore determined by (i) the achievable velocity of the movement of the monochromator, (ii) the integration time required per point in energy to achieve acceptable statistics and (iii) the reproducibility of the monochromator movements. Collection times vary from tens of a second to a few minutes, depending on the energy scan range. Channel-cut monochromators adjusted by piezo crystals, can further reduce the measuring time by a factor of ~100.[7]

Utilization of this set-up allows the simultaneous acquisition of a reference compound, which is especially important to correct for possible beam instabilities. Since no real changes in data acquisition method in comparison to the 'normal' scanning mode exist, the QEXAFS technique allows all detection methods. This enables the application of QEXAFS to e.g. dilute systems with fluorescence detection.[8]

Caution has to be taken for the homogeneity of the sample and its stability during the scan. Since the absorption spectrum is measured set-by-step, small changes in the beam position on the sample will occur as for the 'normal' scanning mode. Moreover, to observe any intermediate in fast dynamic systems, it must be generated in high proportion and identified prior to their decay.

Figure 2. Schematic representation of a curved crystal.
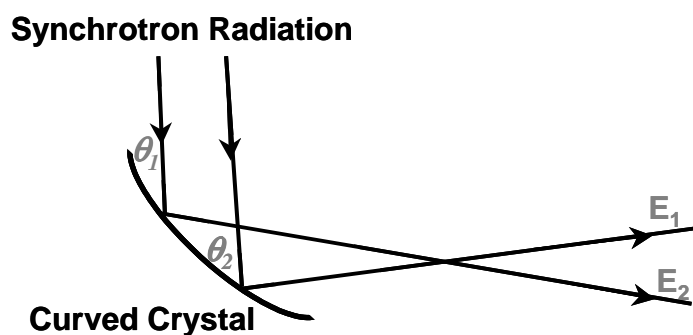
III. Energy Dispersive XAFS

The energy dispersive approach to obtain time-resolved EXAFS data is based upon a completely different solution to the need for fast data-acquisition (in comparison to QEXAFS). The set-up is based on dispersive optics, i.e. a bent perfect crystal, which reflects a polychromatic beam out of a white source.[2] A schematic representation is given in Figure 2. Again the Bragg relation (1) is valid here. Since the crystal is curved, the incident angle of all X-rays is different causing the X-rays to reflect with different energies in different directions. The crystal focuses all X-rays with different energies in one point. The sample is placed at this point. A position-sensitive detector able to work under high-flux conditions then collects the photons. In Figure 3 the complete ED-XAFS set-up is drawn. The energy-direction correlation given by the curved crystal is transformed into an energy-position correlation at the detector position. A mirror is placed behind the monochromator to reject

the higher harmonic contributions. Since all data of a spectrum are acquired simultaneously, the time resolution achievable is in the sub-second range.

The energy-dispersive data acquisition has a number of advantages over the scanning method.[2,9,16,10,11] First of all, since a broad range of energies is measured at once, different edges can be measured simultaneously. Due to the lack of mechanical movements, the energy scale is very stable once the optics is tuned for a given energy range because instabilities and time delays associated with changing the energy are absent. This enables extreme sensitivity and detection of any small change in absorption induced by chemical changes. The required sample size is very small since the dispersed beam passes through a focus at the sample position. Since the whole spectrum is measured simultaneously, fluctuations in the incident X-ray beam intensity do not disadvantageously affect the quality of the recorded spectrum.

Figure 3. Schematic representation of the combined ED-XAFS / UV-Vis set-up.
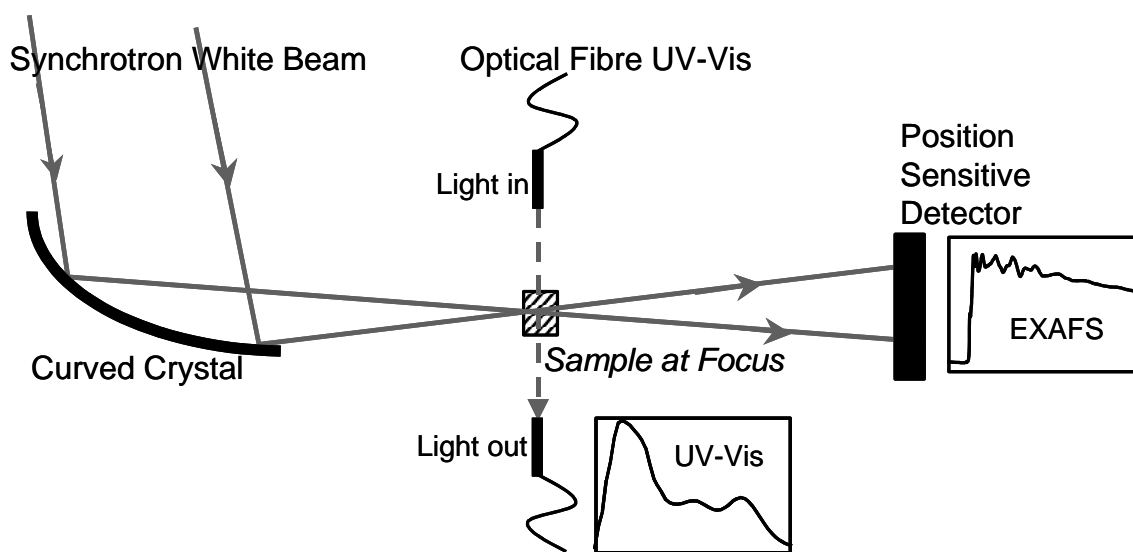
However, the reduction of the source size and the lengthening of beamline have also introduced new problems related to the much higher sensitivity to beam instabilities. [2,11,16,12] The higher sensitivity arises mainly because the spectra are obtained as 1D images and they suffer from distortions due to phase contrast phenomena associated to imperfections in the optics and to small-angle scattering from the sample. This strongly affects the quality of the data particularly on powder samples. The presence of such spatial intensity modulations on

the image clearly amplifies the effect of beam instabilities. Because the intensity before (I_0) and after the sample (I_t) cannot be measured simultaneously, the dispersive set-up is intrinsically more sensitive to instabilities with respect to the conventional scanning mode. Additionally, this leads to normalization problems.

EXAFS data that are collected the energy dispersive data acquisition mode are always detected in transmission mode. Therefore, highly concentrated samples are needed which limits the application range of this type of XAFS experiments. Additionally, since the sample is exposed to all X-ray energies at once, the intensity of the beam on the sample is very high and caution has to be taken for beam-induced changes like sample degradation and heating of the sample. Altogether, it is clear that experiments for ED-XAFS have to be carefully prepared.

Crystals

In ED-XAFS the curved crystal monochromator can be in either Bragg (reflection) or Laue (transmission) geometry[13,14,15,16] (Figure 4a). To satisfy the best energy resolution requirements without limiting the energy bandwidth, the energy range which is reflected or transmitted at once, too much, Si(111) crystals are used in Bragg geometry when working at energies from 5 to 12 keV and in Laue geometry from 12 to 25 keV.[2,13,14,15]

These types of horizontally diffracting monochromators originally used a triangular crystal, because of simple engineering. However, the focal spot is not uniform, but it has a cusp form because of imperfect clamping and heating effects, and because the ideal surface is an ellipse. These problems can be avoided by using a rectangular crystal. [2,13-17,18,19] A picture of the Laue crystal, mounted in its bender at ID24 is given in Figure 4b.

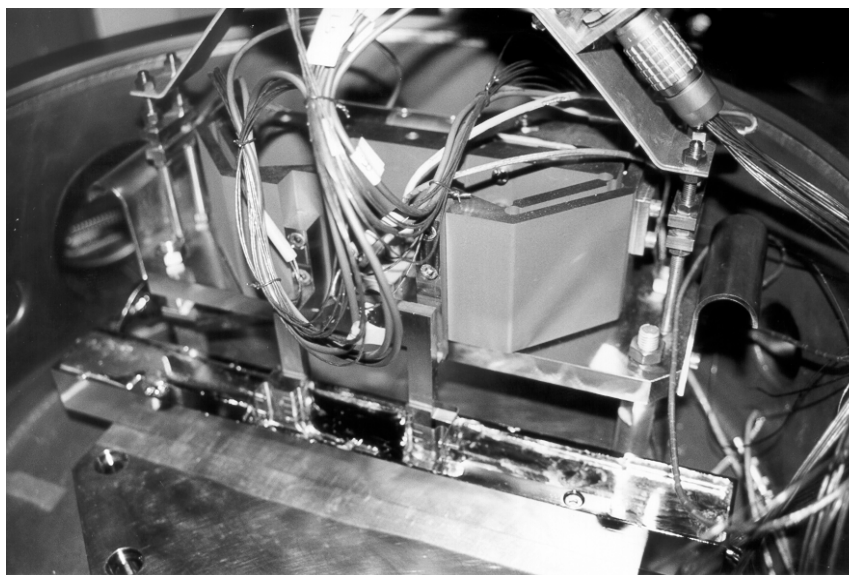**Figure 4a.** The different curved crystals (a) Bragg and (b) Laue.
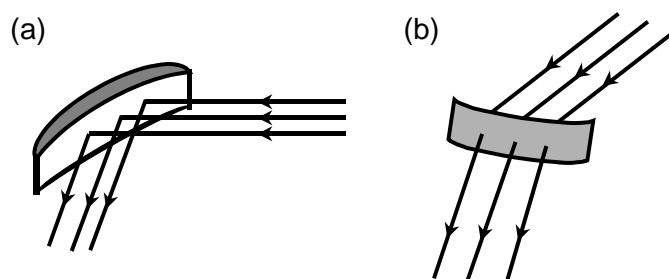
Figure 4b. Picture of the Laue crystal in its bender (ID24, ESRF, Grenoble, France).

Position Sensitive Detector

A photodiode array or CCD screen is typically used as a position sensitive detector. The X-ray flux is determined at each pixel. The saturation time of the pixels is depending on the sample and determines the acquisition time of a full XAFS spectrum. By averaging a number of spectra, the signal to noise ratio is improved. The time resolution depends on the acquisition time per spectrum, the amount of spectra needed to acquire an acceptable signal to noise ratio and the detector read-out time. Recent reports in the literature show spectra with a time resolution in the sub-second range.[17,20,21,22]

At beamline ID24 (ESRF, Grenoble, France),[18,23,24] where the ED-XAFS experiments that are described in this thesis have been performed, an X-ray camera acting as a position sensitive detector was developed. This camera is based on a Peltier-cooled CCD camera of 1242 x 1152 pixels, of which 1242 x 64 pixels are exposed. The rest of the camera is physically masked. Instead of exposing the CCD camera directly to an X-ray beam, a scintillating screen (phosphorus screen) is coupled to the active part of the CCD via a lens system. By changing the scintillating screen, the camera can be easily adapted to the experimental needs, e.g. energy, time-resolution. A schematic drawing of the X-ray camera is shown in Figure 5a and a picture in Figure 5b.

The use of a scintillating screen in an X-ray camera avoids radiation damage by the indirect exposure. It allows working at higher photon energies, because the absorption of the photons is performed by the rare-earth phosphor film and not in the Si photodiode

itself. By using the masked part of the CCD-chip as a fast analogue buffer, 18 spectra can be taken with exposure times in the sub ms-range, and negligible dead time.

The conversion from spatial position on the detector to energy scale can be calculated from the Bragg angle equation (1), which defines the energy of the photons. The relationship between position and energy is almost linear in the energy range of interest. However, since the relationship is not completely linear, it is practically easier and principally better to avoid non-accurate geometrical measurements, to scale the spectra by using the energies of two edges or a reference EXAFS spectrum (e.g. a metal foil).[2,25]

Figure 5. The position sensitive detector at the ERSF (a) schematic drawing, (b) picture.
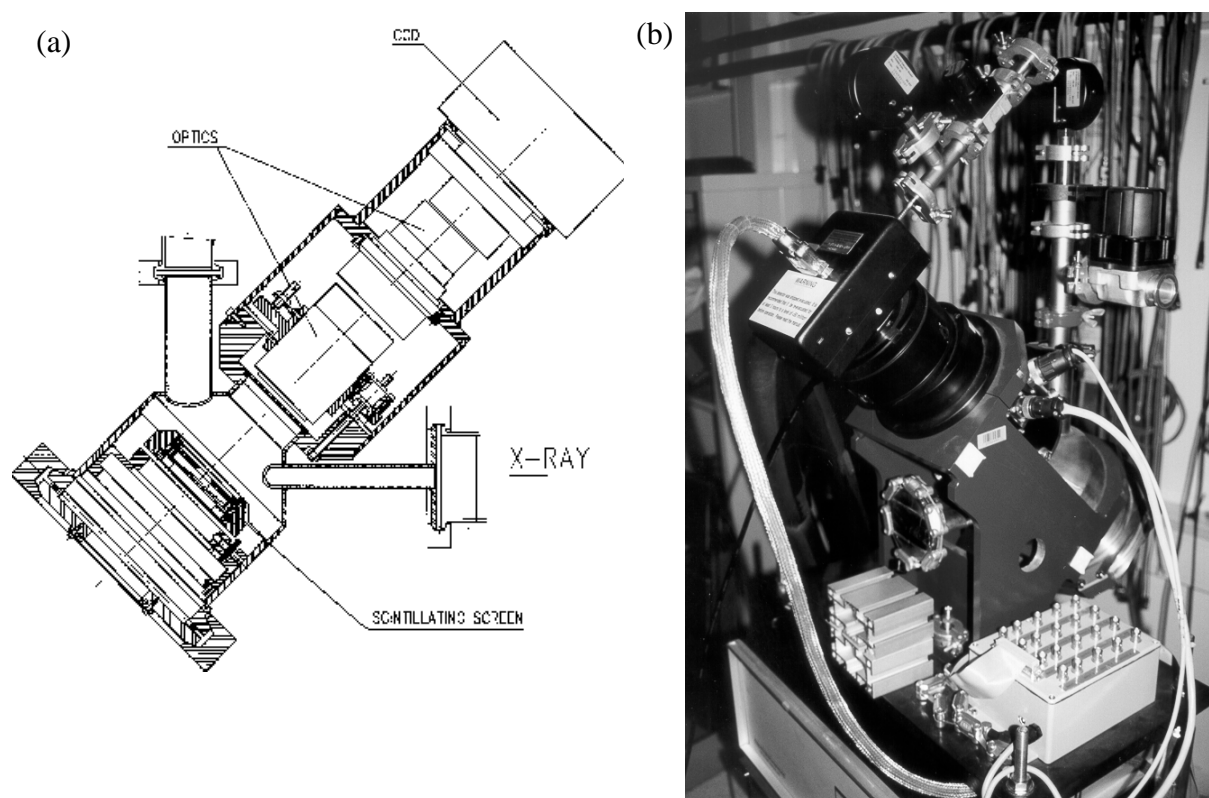
IV. Turbo-XAFS

An experimental set-up where the I_0 and I_t are simultaneously recorded is intrinsically less sensitive to beam instabilities. Therefore, an experimental set-up, the so-called Turbo-XAFS, has been developed which is incorporated in the energy dispersive mode.[26,27] In Turbo-XAFS (Figure 6), absorption spectra are recorded using two ionization chambers, positioned before and after the focus point, and thus the sample, respectively. A monochromatic beam is generated by scanning a narrow slit immediately after the curved crystal through the energy band produced by this crystal. This results in a scanning data acquisition mode (as in QEXAFS), however, without the corresponding instrumentation movements. Moreover, since the energies are measured step-by-step, simultaneous measurements of sample and reference and application of other detection techniques becomes possible. The Turbo-XAFS data acquisition method thus combines the high stability of the energy dispersive set-up with simultaneous normalization of the obtained data and allows a broader range of systems to be investigated due to the increased range of detection methods. A good time resolution of a few seconds is maintained.
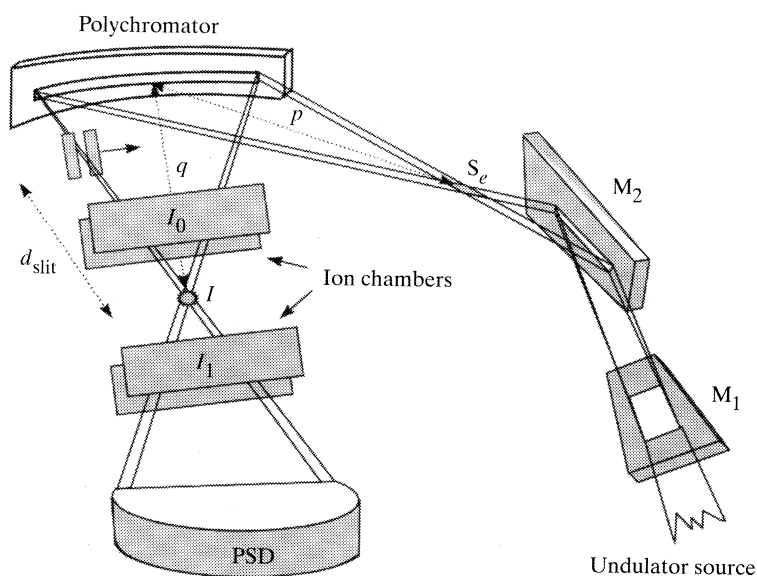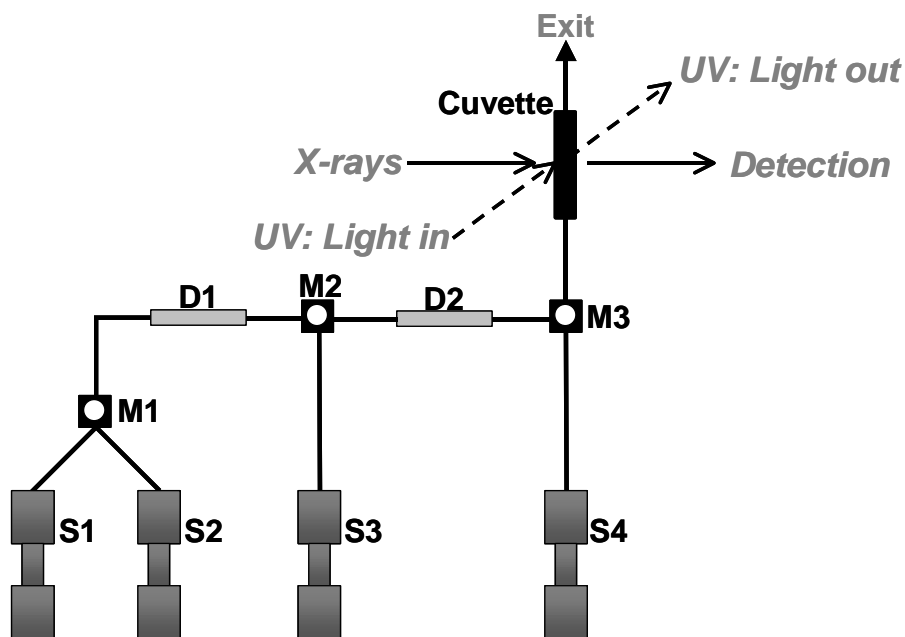

Figure 6. Schematic representation of the Turbo-XAFS set-up.

Novel Combined Time-Resolved ED-XAFS / UV-Vis Set-up

For the research carried out in this thesis, a new set-up has been developed to study homogeneous catalytic system and which combines ED-XAFS with time-resolved UV-Vis spectroscopy. The two spectroscopic techniques can be applied simultaneously. The set-up is schematically drawn in Figure 3. The ED-XAFS data-acquisition set-up as described above is used. Time-resolved UV-Vis spectra are collected in a direction perpendicular to the x-ray beam of the EDXAFS.

To be able to perform homogeneous reactions, a stopped-flow module (Biologic SFM-400) is used as schematically drawn in Figure 7. Four syringes (S1-S4) can be filled with 10 ml of reaction solution or solvent. The system is computer controlled and allows injection of precise volumes with controlled injection rates (and thus injection times). The solutions are injected using stepper motors via the delay lines (D1-D2) and the mixers (M1-M3) into the cuvette and finally, after measurement, through the cuvette into a waste flask. A total volume of 180 µl is injected each time to refresh all delay lines, mixers and the total cuvette content. The stopped-flow system has a dead time of ~3 ms, the time for the solutions to mix and reach the cuvette.

Figure 7. Schematic representation of the Stopped Flow Module with four syringes (S1-S4), three mixers (M1-M3) and two delay lines (D1-D2).

Side View A   **Side View B**

Liquid out

X-rays in   X-rays out

Light in   Light out
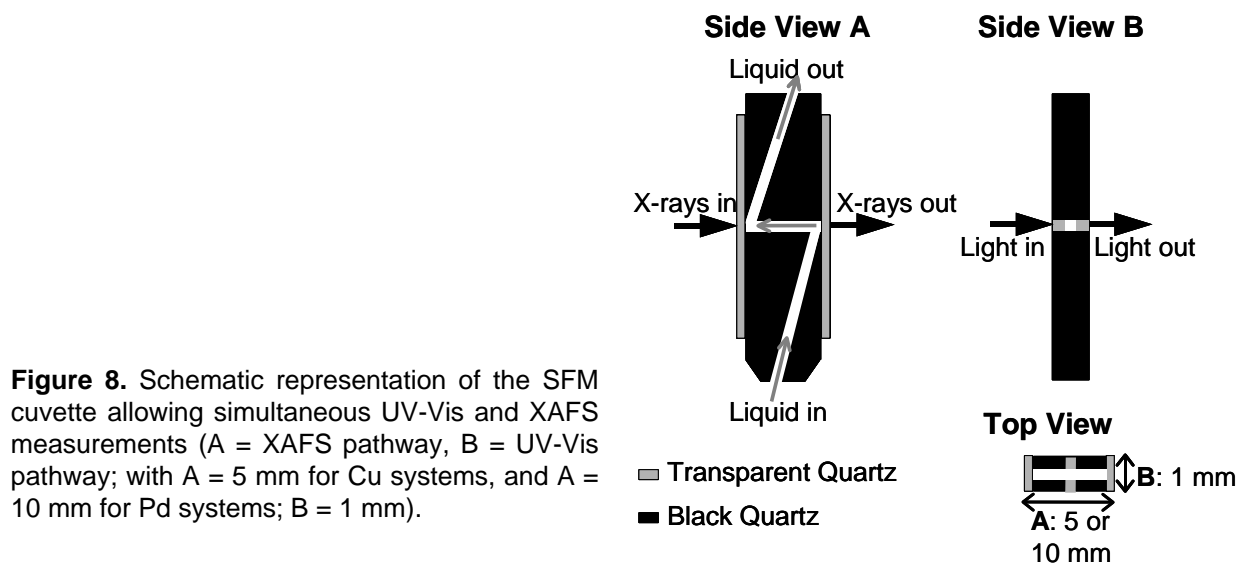
Figure 8. Schematic representation of the SFM cuvette allowing simultaneous UV-Vis and XAFS measurements (A = XAFS pathway, B = UV-Vis pathway; with A = 5 mm for Cu systems, and A = 10 mm for Pd systems; B = 1 mm).

Liquid in

▭ Transparent Quartz
▬ Black Quartz

Top View

B: 1 mm

A: 5 or 10 mm

Special quartz cuvettes have been designed (Figure 8), in which the X-rays and UV-Vis light traverse perpendicular to each other (Figures 7 and 8). Cuts in different directions through the capillary are shown. Due to the different sensitivity of the two techniques for different (metal) systems, different path lengths are required (A = XAFS pathway, B = UV-Vis pathway) to allow simultaneous measurements on the same reaction mixture. For the Cu and Pd systems described in this thesis, B is 1mm and A is 5 and 10 mm, respectively. Moreover, due to the lower energy of the Cu K-edge, leading to a higher absorption of the x-rays in quartz, the quartz windows are polished from the standard 300 μm thickness (as used for Pd) down to 100 μm. A picture of the observation head of the stopped-flow module with cuvette and optical fibers is given in Figure 9.

Figure 9. Picture of the cuvette in the observation head of the stopped-flow module with optical fibers connected.

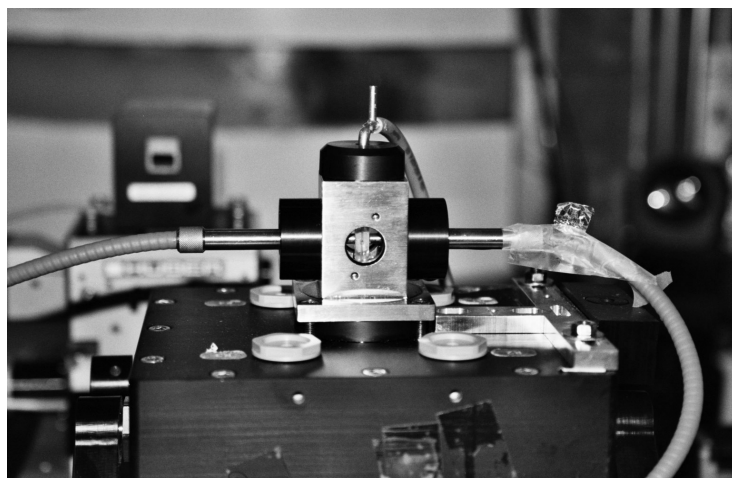As already mentioned before, due to the high photon flux at the sample position, sample degradation or heating can occur. Therefore, a shutter consisting of a small lead plate is placed between the incoming X-ray beam and the cuvette. In this way the beam can be taken away from the sample during for example the detector read-out, without moving the set-up or closing the complete beamline shutter. This method allows long time-resolved experiments with the shortest possible time of beam exposure on the sample. Moreover, simultaneously the shutter avoids saturation of the detector. An overview picture of the complete set-up is given in Figure 10. In the left upper part (the 'back' part) of the picture the detector can be seen. In the middle of the picture, the UV-Vis apparatus (white box) is observed. The optical fibers are connected to the observation head on the stopped-flow module. A waste tube on top of the observation head leads the chemicals out of the cuvette into a waste flask. The four syringes are recessed in the upper black box of the stopped-flow module, with the stepper motors in the lower one. The drive syringes are filled through the orifices on top of the syringe block (visible as white ring in picture 10).

Figure 10. Picture of the ED-XAFS/UV-Vis set-up at the Beamline (ID24, ESRF, Grenoble, France).
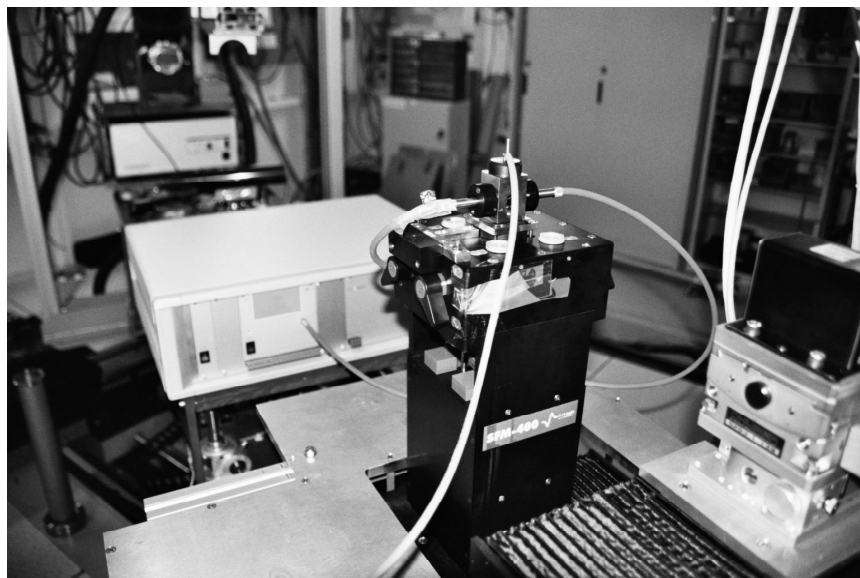
The ED-XAFS experiments are performed as described above. An optical fiber UV-Vis apparatus (MMS-UV1/500-1 High speed Diode Array Spectrometer with fiber optics) allowed the simultaneous acquisition of time-resolved UV-Vis data. To be able to synchronize the injections of the reactants, the ED-XAFS and UV-Vis data acquisition, and the opening and closing of the shutter, digital pulse generators are applied to individually delay the activation signals to the for different apparatus. The use of oscilloscopes allows the visualization and alignments of all pulses. The system is set up such that at the end of the injection of the reactants the ED-XAFS and UV-Vis measurements start. Since each instrument has its typical response time, different delay times have to be used in the measurement program. The time-resolutions achieved for the acquisition of time-resolved UV-Vis and ED-XAFS spectra for the systems described in this thesis are respectively in the sub-second and sub-second to second range.

References

1. M. A. Newton, A. J. Dent, J. Evans, *Chem. Soc. Rev.* **2002**, *31*, 83.
2. A. Fontaine, E. Dartyge, J. P. Itie, A. Jucha, A. Polain, H. Tolentine, G. Tourillon, *Topics in Current Chem.* **1989**, *151*, 179.
3. A. J. Dent, *Top. Catal.* **2002**, *18*(1-2), 27.
4. D. C. Koningsberger, B. L. Mojet, G. E. van Dorssen, D. E. Ramaker, *Top. Catal.,* **2000**, *10*, 143.
5. For example, *X-ray Absorption, principles, applications, techniques of EXAFS, SEXAFS and XANES*, eds. D. C. Koningsberger and R. Prins, Wiley Interscience, New York, **1988**.
6. R. Frahm, *Nucl. Instr. And Meth. In Phys. Res. A* **1988**, *270*, 578.
7. M. Richwin, R. Zaeper, D. Lutzenkirchen-Hecht, R. Frahm, *Rev. Sci. Instrum.* **2002**, *73*, 1668.
8. L. M. Murphy, B. R. Dobson, M. Neu, C. A. Ramsdale, R. W. Strange, S. S. Hasnain, *J. Sychrotron Rad.* **1995**, *2*, 64.
9. R. P. Phizackerly, Z. U. Rek, G. B. Stephenson, S. D. Conradson, K. O. Hodgson, T. Matsushita, H. Oyanagi, *J. Appl. Cryst.* **1983**, *16*, 220.
10. T. Matsushita, R. P. Phizackerley, *Jpn. J. of Appl. Phys.* **1986**, *20*(11), 2223.
11. S. Pascarelli, T. Neisius, S. De Panfilis, M. Bonfirm, S. Pizzini, K. Mackay, S. David, A. Fontaine, A. San Miguel, J. P. Itie, M. Gauthier, A. Polian, *J. Synchrotron Rad.* **1999**, *6*, 146.
12. S. Pascarelli, T. Neisius, S. De Panfilis, *J. Synchrotron Rad.* **1999**, *6*, 1044.
13. J. Pellicer-Porres, A. San Miguel, A. Fontaine, *J. Synchrotron Rad.* **1998**, *5*(5), 1250.
14. A. San Miguel, M. Hagelstein, J. Borrel, G. Marot, M. Renier, *J. Synchrotron Rad.* **1998**, *5*(6), 1396.
15. M. Hagelstein, C. Ferrero, M. Sanchez del Rio, U. Hatje, T. Ressler, W. Metz, *Physica B* **1995**, *208&209*(1-4), 223.
16. J. Evans, *Chem. Soc. Rev.* **1997**, 11.
17. A. Dent, J. Evans, M. Newton, J. Corker, A. Russell, M. B. Abdul Rahman, S. Fiddy, R. Mathew, R. Farrow, G. Salvini, P. Atkinson, *J. Synchrotron Rad.* **1999**, *6*(3), 381.
18. M. Hagelstein, A. San Miguel, A. Fontaine, J. Goulon, *J. Phys. IV France* **1997**, *7*(C2), 879.
19. M. Hagelstein, C. Ferrero, U. Hatje, T. Ressler, W. Metz, *J. Synchrotron Rad.* **1995**, *2*, 174.
20. R. Frahm, *Nucl. Instr. And Meth. In Phys. Res. A* **1998**, *270*, 578.
21. M. Kovalenko, V. Mironov, V. Shaliapin, S. Tiutiunnikov, *J. Alloys Compd.* **1999**, *286*, 26.
22. G. Salvini, D. Bogg, A. J. Dent, G. E. Derbyshire, R. C. Farrow, A. Felton, C. A. Ramsdale, *Physica B* **1995**, *208&209*, 229.
23. M. Hagelstein, A. Fontaine, J. Goulon, *Jpn. J. Appl. Phys.* **1993**, *32*, 240.
24. J. L. Hodeau, J. Vacinova, Y. garreau, A. Fontaine, M. Hagelstein, E. Elkaim, J. P. Lauriat, A. Prat, P. Wolfers, *Rev. Sci. Instrum.* **1995**, *66*, 1499.
25. A. M. Flank, A. Fontaine, A. Jucha, M. Lemonnier, D. Raoux, C. Williams, *Nucl. Instr. and Meth.* **1983**, *208*, 651.
26. S. Pascarelli, T. Neisius, S. De Panfilis, *J. Synchrotron Rad.* **1999**, *6*, 1044.
27. S. Pascarelli, S. De Panfilis, T. Neisius, *Phys. Rev. B* 2000, **62**, 3717.

Chapter 3

Cu K-edge EXAFS Characterization of Copper(I) Arenethiolate Complexes in both Solid and Liquid State: Detection of Cu-Cu Coordinations

Abstract

This paper describes a structural characterization with EXAFS of the structure of copper(I) arenethiolate complexes in both solid and liquid state. Previously observed difficulties in the detection of the Cu-Cu interaction were attributed to anti phase behavior of different Cu–Cu-neighbor contributions. A data analysis procedure solely based on EXAFS parameters is presented which resolves these problems.

A careful analysis of the individual coordination shells and the use of different k-weightings during the data analysis are shown to be an absolute necessity to obtain reliable analysis results. During R-space fitting, the difference file technique is used to separate, examine and compare the individual contributions. Using this technique their statistical significance and correctness can be determined. Anti phase behavior can be detected and accounted for in this way. An additional mixed organocopper aggregate $[Cu_4(SAr)_2(Mes)_2]$ with different Cu-sites is analyzed and proves the value of the above described analysis procedure. Moreover, this newly developed EXAFS data analysis procedure is applicable to any other EXAFS spectrum obtained.

The structural analysis of these organocopper complexes with EXAFS provides information about their actual structure and dynamic behavior in solution. Moreover, the technique can now be used to obtain insights in the reactivity of these complexes and their way to form catalytic reaction intermediates.

Chapter 3

Introduction

An important reaction in organic synthesis is the (selective) carbon-carbon bond formation for which organocuprates $[R_2CuLi]$[1-3], $[R_2Cu(CN)Li]$[4,5], $[R_2Cu(CN)Li_2]$[6] are most widely applied.[7-12] In our ongoing studies in the field of organo-copper and cuprate chemistry, we have synthesized well defined heterocuprates derived from the aminoarenecopper species $(CuSC_6H_4CH(Me)NMe_2-2)_3$[13-15] (**1**) which contain an *S,N*-bidentate coordinated arenethiolate. This complex and related chiral copper arenethiolates promote selective group transfer of Grignard reagents (RMgX) to various organic substrates [16-24], *e.g.* chemo- and enantio-selective 1,4-addition to acyclic enones.[17] Specifically, the latter is the first reported case in which a copper complex, *i.e.* enantiopure **1** (*R, R, R* or *S, S, S*), has been used in catalytic amounts to achieve enantioselective C-C bond formation.[17,18,20,22,23]

The nature of the active cuprate species in these and related reactions is still largely unknown. Extended X-ray Absorption Fine Structure (EXAFS) spectroscopy provides local structural information about a specific element in a compound. In contrast to X-Ray Diffraction (XRD), EXAFS spectroscopy does not require long-range ordering of the material. Therefore, EXAFS can be applied in structural studies of molecules in any state of aggregation. EXAFS has been used for the elucidation of the co-ordination sphere of metal centers in enzymes[25,26] and for the determination of the structure of compounds in solid state and liquid state.[27] EXAFS is unique in unraveling the structure of species under non-ambient conditions, as it can be applied *in situ*, under high pressure, temperature, and in the presence of gasses. In organometallic chemistry the technique is complementary to Infra-Red spectroscopy (IR), Nuclear Magnetic Resonance spectroscopy (NMR) and XRD. Studies of $^{63,65}Cu$ NMR on organo-copper complexes, that could provide direct detailed information about the coordination sphere of the copper site(s) in organocuprates, is hampered by the large nuclear quadrupole moment of the copper nucleus.

EXAFS spectroscopy of organo-copper and -cuprate mixtures is not straightforward.[25,26,28-32] In the recent literature, several examples exist where Cu-Cu coordinations were not detected or very difficult to detect by EXAFS, although in some cases XRD and/or other chemical information strongly suggested that Cu neighbors around the photon-absorbing Cu ion were present.[28,30-35] Sometimes Cu-Cu contributions were not detected at all or unexpected Cu-Cu contributions were found (wrong distances), in combination with incorrect Cu-C or Cu-N contributions. These problems are often encountered for Cu complexes in which Cu···C distances are in the same range as the

Cu···Cu distances.[33] Examples are: (i) organocopper reagents (CuCN + BuLi and CuCN·2LiCl)[28,30-32], (ii) phenoxo-bridged dicopper(I) compounds[34] and (iii) copper(I)-thiolate clusters in the native protein [Cu-(αEC)$_n$G].[35]

Figure 1. Schematic structures of Cu(I) arenethiolate complexes **1** and **2** as determined in solid state by XRD, see references 13, 14 and 15 for full structural details.

1   **2**
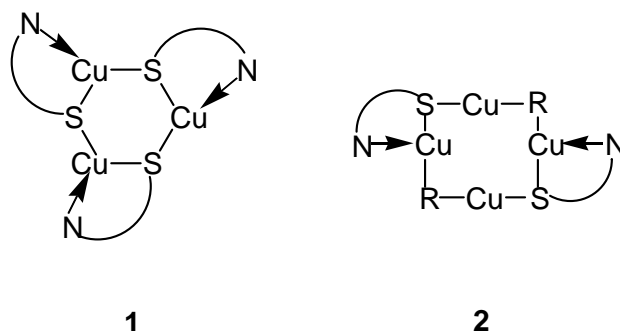
In a quest to improve and understand the mechanistic aspects of the copper-based catalytic systems for enantioselective synthesis, we have applied EXAFS spectroscopy to identify the catalytic site(s) of the key intermediates in our system. In this study a systematic method for the analysis of Cu K-edge EXAFS spectra is presented that allows the proper detection of Cu-Cu contributions. The analysis method will be established by means of Cu K-edge EXAFS spectroscopy on the copper(I) arenethiolate species (CuSC$_6$H$_4$CH(Me)NMe$_2$-2)$_3$ (further abbreviated as [Cu$_3$(SAr*)$_3$]; **1**) (Figure 1). The structure of this Cu arenethiolate complex is well known by single crystal XRD.[13-15] The detectability of the Cu-Cu coordination is investigated using the structural information obtained from single crystal XRD as a starting basis for the EXAFS analysis. The analysis strategy will be demonstrated on the solid state [Cu$_3$(SAr*)$_3$] EXAFS spectra measured at room temperature. Subsequently, the analysis procedure will be applied to the EXAFS data of [Cu$_3$(SAr*)$_3$] dissolved in toluene measured at room temperature. The structure of a related mixed organo(arenethiolate)copper(I) aggregate [Cu$_4$(SAr)$_2$(Mes)$_2$] (**2**) (Figure 1), that contains distinctly different Cu sites[21] has been determined with EXAFS using the newly developed analysis procedure to confirm and demonstrate the validity of the developed analysis procedure.

The results of the EXAFS analysis provide essential information about the structure and dynamics of the complexes and of the vibrating Cu$_3$S$_3$ ring of the trimeric CuSAr-aggregate. This information will be important for an understanding of the formation of the kinetic intermediates between the organo-copper catalyst precursor of the Grignard reagent and the substrate from which ultimately the C-C coupled product is generated.

EXAFS Data-Analysis Methods

Reference Compounds

Theoretical references were used for the analysis of the Cu-S, Cu-N, Cu-Cu and Cu-C coordinations. The theoretical references were generated using the code FEFF8.[36] EXAFS data from reference compounds were used to calibrate the theoretical references: Cu foil (7 μm) for Cu-Cu, ZnS for Cu-S[37] and copper phthalocyanine for both Cu-N[37] and Cu-C since N and C are neighboring atoms in the periodic table. The XDAP program[38] was used for the reference data fitting. The theoretical references were optimized as described in ref. 39. Table 1a gives the FEFF8 input parameters. For all atom pairs a partially non-local potential was used.[36] V_i is estimated to be 3 eV. S_0^2, the Debye-Waller factor and V_r were varied until the generated references optimally fit in R-space the first coordination shell of the experimental EXAFS spectra of the above mentioned reference compounds (see Table 1b). The reference spectra were measured at room temperature, so the references are optimized for the room temperature situation. These calibrated references can then be used to fit the EXAFS data of the samples down to very low values of k ($k \geq 2.5$ Å^{-1}).[39]

Table 1a: FEFF8 input parameters used for the calculations of phase shifts and backscattering amplitudes. For all atom pairs a partially non-local potential is used.[36]

Atom Pair	σ^2 [Å^2]	S_0^2	V_r [eV]	V_i [eV]
Cu-Cu	0.009	0.92	4.0	3.0
Cu-S	0.005	0.88	2.5	3.0
Cu-C	0.000	0.92	1.0	3.0
Cu-N	0.002	0.84	-3.1	3.0

Table 1b: Best fit results for the experimental data using the theoretical references, including fitting parameters. Fits were performed in R-space, k^3-weighted.

Shell	N_{XRD}	R_{XRD} [Å]	N	R [Å]	$\Delta\sigma^2$ [Å^2]	E_0 [eV]	Δk [Å^{-1}]	ΔR [Å]
Cu-Cu	12	2.56	11.9	2.54	0.000	-0.2	2.9-12.5	1.5-2.7
Cu-S	4	2.35	4.0	2.35	0.001	0.4	2.9-12.5	1.0-2.4
Cu-C	4	1.95	4.0	1.96	0.001	-1.2	3.5-12.5	1.0-2.0
Cu-N	4	1.93	4.0	1.94	-0.001	-2.3	3.5-12.5	0.0-2.1

R-space fit

The EXAFS data were analyzed using the commercially available program XDAP.[38] This program allows multiple-shell fitting in *R*-space by minimizing the residuals between both the magnitude and imaginary part of the Fourier transforms of the data and the fit. *R*-space fitting has important advantages compared to the usually applied fitting in *k*-space, as is extensively discussed in ref. 39. *R*-space fitting makes Fourier filtering unnecessary, which is of great advantage if overlapping shells are present. Moreover, by choosing the proper window in *R*-space the background subtraction errors and the presence of further higher shells can be avoided. Another important advantage is that the amount of information (number of independent data points, *vide infra*) is not decreased by a shortening of the range of reliable data in *k*-space due to Fourier filtering errors.

Variance and Number of Independent Data Points

The errors in the structural parameters were calculated from the covariance matrix taking into account the statistical noise of the EXAFS data and the correlations between the different coordination parameters. The standard deviation per data point was estimated by averaging 3 data scans. The number of independent data points (N_{indp}) was determined as outlined in the "Reports on Standard and Criteria in XAFS Spectroscopy"[40]:

$$N_{indp} = \frac{2 * \Delta k * \Delta R}{\pi} + 2 \ .$$

(1)

A large number of independent data points is especially important if several contributions are present and overlapping, to reliably fit the data and account for possible anti phase behavior of different contributions as shown in this study.

The variances of the magnitude and imaginary part of the Fourier transforms of fit and data were calculated according:

$$k^n \ \text{variance} = \frac{\int \left[k^n \left(\text{FT}_{\text{model}}(R) - \text{FT}_{\text{exp}}(R) \right) \right]^2 \mathrm{d}R}{\int \left[k^n \text{FT}_{\text{exp}}(R) \right]^2 \mathrm{d}R} \times 100 \ .$$

(2)

Chapter 3

Difference File Technique

The difference file technique was applied together with phase-corrected Fourier transforms to resolve the different contributions in the EXAFS data.[39,41] The difference file technique allows the observation of each individual contribution with respect to the other contributions present in the EXAFS spectrum. The experimental $\chi_{EXP}(k)$ in the range R_{min} to R_{max} can be described by summation of different model EXAFS contributions $\chi_{MOD,j}(k)$, describing each coordination shell:

$$\chi_{EXP}(k) = \sum_{j=1}^{Shells} \chi_{MOD,j}(k) . \tag{3}$$

For each individual fitted contribution m the following equation should then logically be valid:

$$\chi_m = \chi_{EXP} - \sum_{i=1 \text{ and } i \neq m}^{j} \chi_{MOD,i} . \tag{4}$$

The right side of this equation is further denoted as the difference file of shell m. A sensitive and practical method to check whether a contribution is statistically significant consists of a comparison of the amplitude of χ_m with the noise level present in the difference file (the noise in the difference file is essentially the same as the noise in the experimental data). The total variances between total fit and data determine the correctness of the total analysis of the obtained EXAFS data. Moreover, the use of the difference file technique enables one to observe and examine the individual contributions and their position, intensity and influence on each other during the analysis procedure.

Weight Factor k^n

The phase shift and backscattering amplitude of each neighboring atom are in principle element specific and have a characteristic dependency of the wave factor k. Normally, a combination of a k^0- and k^3-weighting during the EXAFS data-analysis is used in order to separate each individual contribution.[39] Moreover, in this study the use of both k^0- and k^3-weighting was crucial in order to unravel interference effects of higher co-ordination shells. Principally, different k-weightings should yield identical results and a good fit in one weighting should be good in all other weightings applied.[39] As discussed to be of vital importance in this study, a fit in k^n-weighting is only considered correct if other k^n-weightings show minima in variances too. In a system with many contributions such as in this case, a single k^n-weighting may well show several minima in variances obscuring the true minimum.

Results

Single Crystal X-ray Diffraction on [Cu₃(SAr*)₃]

Single Crystal X-ray Diffraction on [Cu$_3$(SAr*)$_3$]

The crystal structure of the copper(I) arenethiolate [Cu$_3$(SAr*)$_3$] (**1**) is known from obtained Single Crystal X-ray Diffraction data.[13-15] The molecular structure of **1** shows a triangular trimeric aggregate which comprises three identical (crystallographic related) CuSAr units that are held together by bridging of the thiolate sulfur atom between adjacent copper atoms. This structure is shown in Figure 2 in which only one of the three chelating arms is displayed completely. The position of the other two arms is indicated by showing only the nitrogen atom.

Figure 2. [Cu$_3$(SAr*)$_3$] (**1**) showing only one of the three chelating arms. The position of the other two arms is only indicated by the nitrogen atom. The C-atoms having about the same Cu···C distance have identical color.
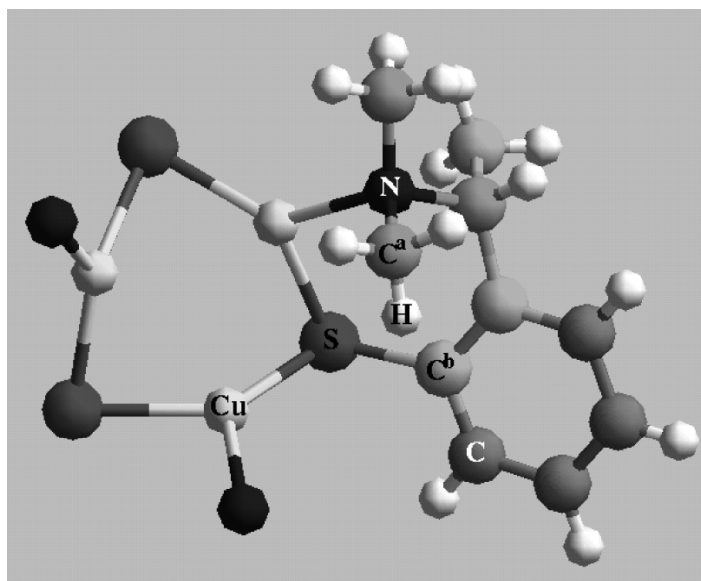
The crystallographic Cu-neighbor distances are given in Table 2.[13-15] Three carbon neighboring atoms (further denoted as C^a) are located at a distance of 2.96 Å; three other carbon atoms (further denoted as C^b), also relevant for the EXAFS analysis, can be distinguished at a distance of 3.31 Å (see also Figure 2). The values for the coordination distances for the Cu-S, Cu-Cu, Cu-C^a and Cu-C^b pairs are average values and the maximum deviation in the distance is given in between brackets in Table 2.

Table 2: Single Crystal X-ray Diffraction on [Cu$_3$(SAr)$_3$] at 110K.

Ab-Sc Pair[a]	N	R [Å][b]
Cu-N	1	2.08
Cu-S	2	2.21 (± 0.02)
Cu···Cu	2	2.83 (± 0.00)
Cu···C^a	3	2.96 (± 0.02)
Cu···C^b	3	3.31 (± 0.14)

[a] Abbreviations: Ab = absorber; Sc = scatterer.
[b] In between brackets the maximum deviation in distances is given.

EXAFS Data of [Cu$_3$(SAr)$_3$] in the Solid State and Solution (at Room Temperature)*

Figure 3 displays the Cu K-edge EXAFS data of [Cu$_3$(SAr*)$_3$] obtained in the solid state (solid line) and solution (dotted line). The signal to noise ratio is very good, the data can be analyzed up to k = 12.5 Å^{-1}. The corresponding k^0- and k^3-weighted Fourier transforms (for 2.9 < k < 12.5 Å^{-1}) are given in respectively Figure 4a and 4b. It can be observed that the intensity in the Fourier Transforms for the sample in solution is in both k-weightings slightly higher. Moreover, for R > ~2 Å some small but significant changes in the imaginary parts can be observed. A very important observation and crucial for the EXAFS data-analysis to be applied in this study is the fact that for the k^3-weighted Fourier transforms almost no intensity is observed for R > 2.2 Å, whereas in the k^0-weighted Fourier transforms there is.

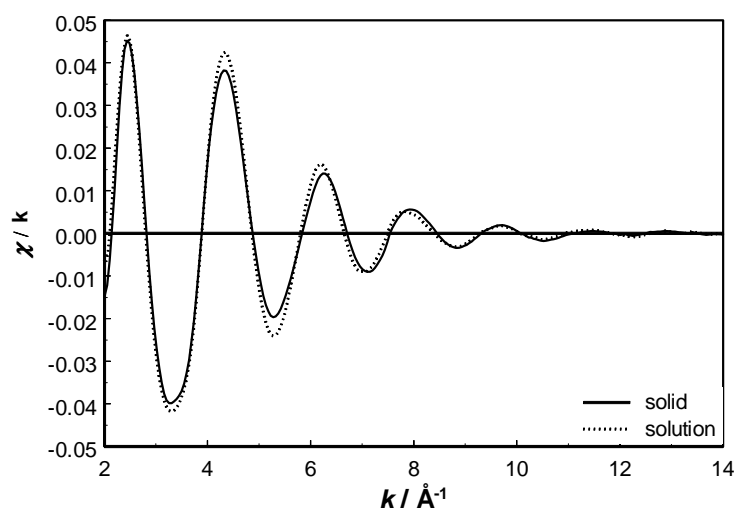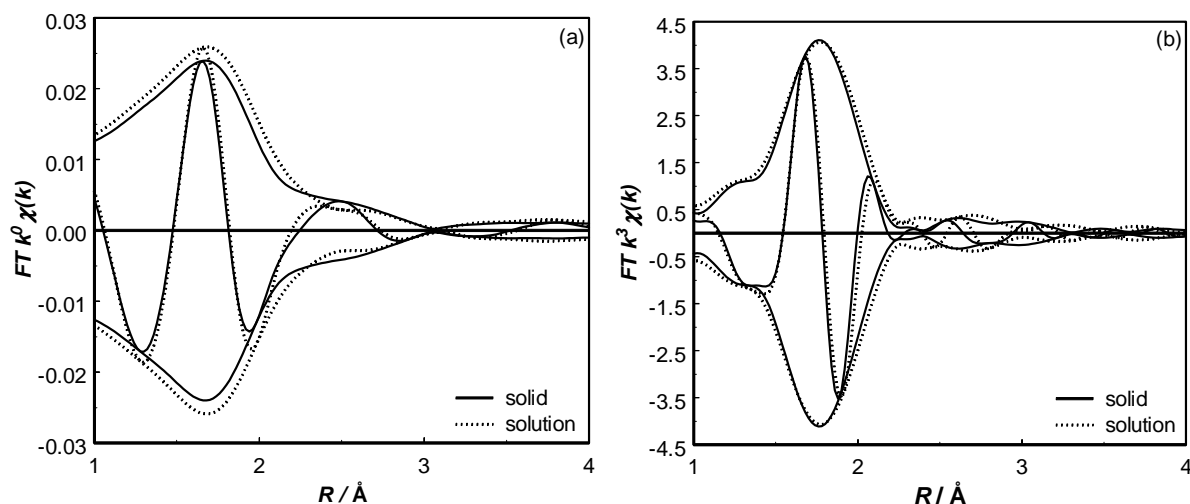**Figure 3.** Raw EXAFS data of [Cu$_3$(SAr*)$_3$] in solid state (solid line) and in solution (dotted line).

Figure 4. Fourier transforms of the EXAFS data of [Cu$_3$(SAr*)$_3$] in solid state (solid line) and in solution (dotted line) for 2.9 < k < 12.5 Å^{-1} (a) k^0-weighted and (b) k^3-weighted.

First the [Cu$_3$(SAr*)$_3$] sample in solid state is analyzed since the crystal structure of this sample is known from single crystal XRD. For the initial analysis in R-space of the [Cu$_3$(SAr*)$_3$] EXAFS data a k^0-weighted factor was used. In the next step the correctness of the fit was checked by using a higher k-weighting (k^1, k^2, k^3). Additionally, the influence of an increasing number of coordination shells is observed carefully. The crystallographically known values for the coordination numbers (N) and distances (R) (Table 2) were used as starting input parameters. The data were analyzed by using an R-space fit with k-range of 2.9 < k < 12.5 Å^{-1} and R-range of 1.0 < R < 4.0 Å. Both the absolute and the imaginary part of the Fourier transform were optimized. Each shell was fitted by iteratively allowing the parameters (R, N, $\Delta\sigma^2$ and ΔE_0) of that shell to be free. An increasing number of coordination shells were used to fit the data. A two-shell fit (Cu-N, Cu-S), a three-shell fit (Cu-N, Cu-S, Cu-Cu), a four-shell fit (Cu-N, Cu-S, Cu-Cu, Cu-C^a) and a five-shell fit (Cu-N, Cu-S, Cu-Cu, Cu-C^a, Cu-C^b) were used to observe the influence of an increasing number of coordination shells (Table 3).

Table 3: EXAFS analysis of [$Cu_3(SAr)_3$] (solid, RT), k^0-weighted fit, 2 – 5 shells.[a]

| Ab-Sc Pair[b]	N	R [Å]	$\Delta\sigma^2$ [Å²]	ΔE_0 [eV]		Var. Im.[b]	Var. Abs.[b]
2-shell fit							
Cu-N	2.1	2.20	0.040	7.8	k^0:	2.0	0.96
Cu-S	2.0	2.21	0.000	2.4	k^3:	4.3	2.0
3-shell fit							
Cu-N	1.1	2.04	0.008	9.3	k^0:	0.17	0.083
Cu-S	2.0	2.22	0.002	-0.2	k^3:	1.4	0.64
Cu···Cu	6.9	2.96	0.040	-6.9			
4-shell fit							
Cu-N	1.0	2.08	0.005	1.0	k^0:	0.037	0.063
Cu-S	2.0	2.21	0.003	0.4	k^3:	0.44	0.21
Cu···Cu	2.8	3.00	0.014	-3.7			
Cu···C^a	3.1	3.15	0.007	5.9			
5-shell fit							
Cu-N	1.0	2.05	0.001	0.6	k^0:	0.017	0.012
Cu-S	1.9	2.23	0.003	-1.4	k^3:	0.20	0.10
Cu···Cu	1.7	2.84	0.016	1.7			
Cu···C^a	3.3	2.99	0.010	7.9			
Cu···C^b	2.8	3.45	0.013	-1.3			

[a] N_{indp} = 20. Fit: *R*-space, 2.89 < *k* <12.50; 1.0 < *R* <4.0, all parameters iteratively refined.
[b] Abbreviations: Ab = absorber; Sc = scatterer. Var. Im. and Var. Abs. are the variances of the fit of the Imaginary and Absolute part, respectively.

The final five-shell total fit for $[Cu_3(SAr^*)_3]$ at RT (k^0-weighted) is given in Figure 5a. To show that the obtained fit is correct also the fit in an other k-weighting, i.e. k^3, is shown in Figure 5b, with the fit variances given in Table 3. As the difference file technique was used for the analysis of the EXAFS spectra, the individual contributions can be analyzed separately and should also fit correctly to be able to conclude a good analysis. In Figure 6 the Fourier transforms of the individual difference files are given, including the fits for the individual shells. The Cu-N contribution, displayed in Figure 6a is fitted very well in the analysis range applied ($1.0 < R < 4.0$ Å). The Cu-S single-shell is the largest contribution in the analysis and fits perfectly as can been seen in Figure 6b. In Figure 6c the Cu-Cu contribution is shown. The Cu-C^a contribution given in Figure 6d fits very well and the Cu-C^b contribution, which is displayed in Figure 6e, shows a little noise on the measured data. It can be observed that both Cu-C contributions are larger than the Cu-Cu contribution. Only little noise can be seen in the Fourier Transforms of the difference files of the smallest contributions (Cu-Cu, Cu-C^a, Cu-C^b). From these Figures it is clear that these individual contributions are well above the noise, and thus are significant, and that they are fitted very well. The final EXAFS co-ordination parameters are summarized in Table 3.

Figure 5. Fourier Transforms of raw data (solid line) and *R*-space fit (dotted line) ($2.9 < k < 12.5$ Å^{-1} and $1.0 < R < 4.0$ Å) with 5 coordination shells of $[Cu_3(SAr^*)_3]$ in solid state (a) k^0-weighted, (b) k^3-weighted.
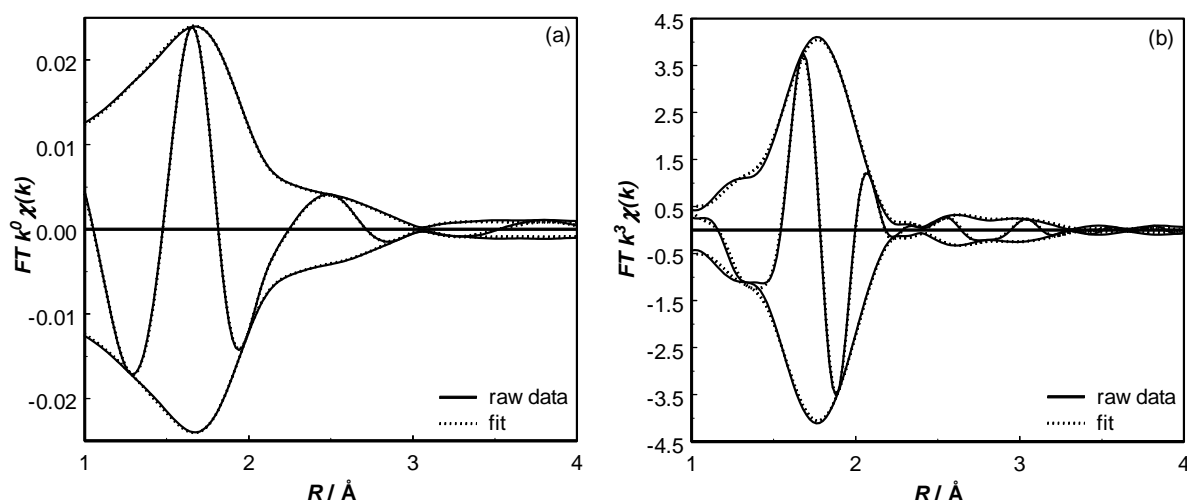
Figure 6. Fitted single shell contributions (dotted line) and difference files (solid line) of 5 shell *R*-space fit (k^0, $2.9 < k < 12.5$, $1.0 < R < 4.0$) of $[Cu_3(SAr^*)_3]$ in solid state measured at RT. (a) Cu-N, (b) Cu-S, (c) Cu-Cu, (d) Cu-C[a] and (e) Cu-C[b].
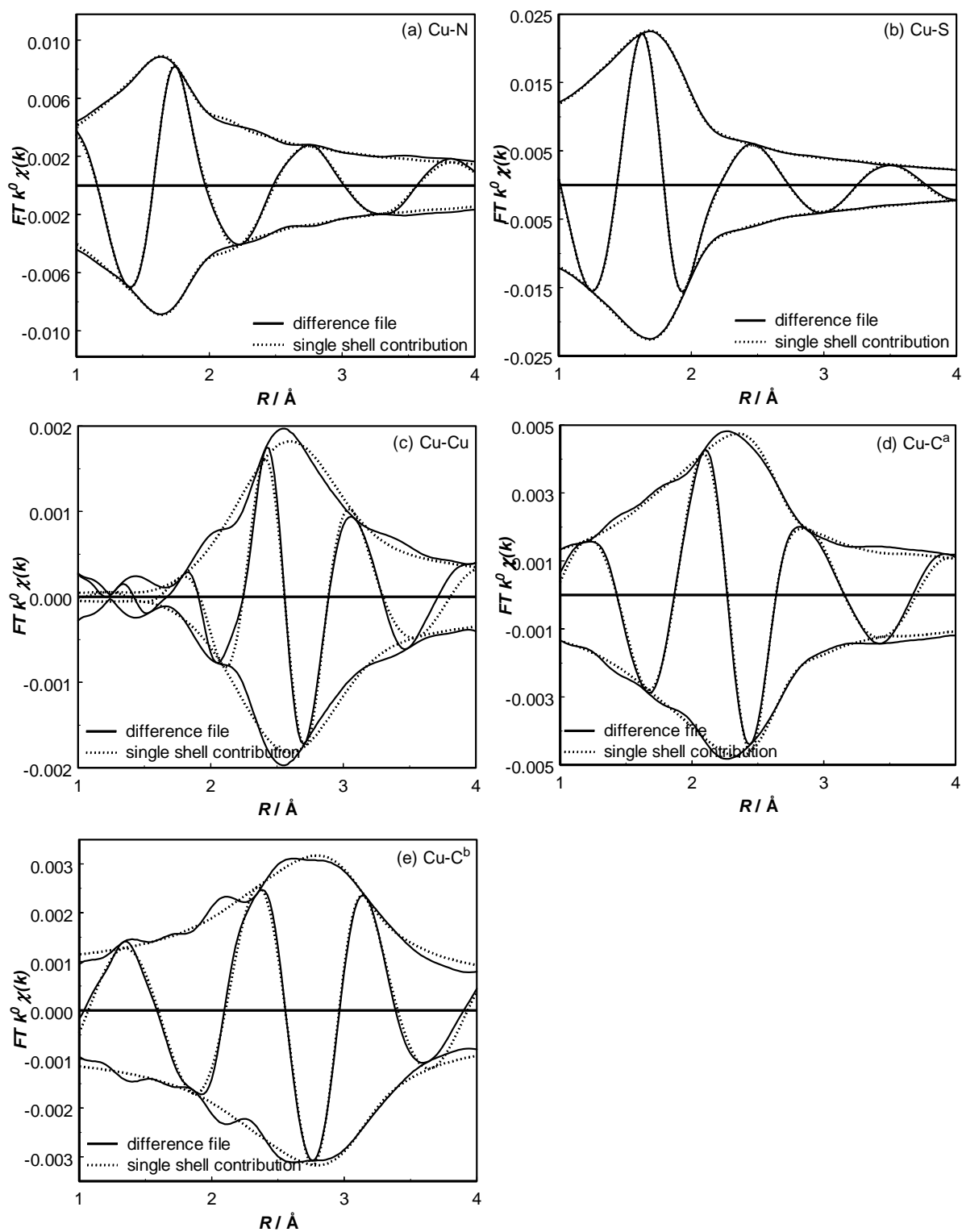
The [Cu$_3$(SAr*)$_3$] was also measured in solution, i.e. in toluene. In Figure 7a the Fourier transforms (2.9 < k < 12.5 Å^{-1}) of both the k^0- and k^3-weighted spectrum are given. In the k^3-weighted spectrum a very low intensity of the signal is observed between 2 and 2.5 Å, whereas in the k^0-weighted spectrum a clear signal remains present (note the differences in axis). A five-shell analysis has been performed using a k^0-weighting. The crystallographic results are used as starting input parameters and the shells are iterative refined leaving step by step (shell by shell) all parameters free. The k^0-weighted R-space fit is shown in Figure 7b and the results are given in Table 4. The correctness of the fit is also shown in Figure 7c for the k^3-weighted fit using the obtained parameters, with the calculation variances given in Table 4.

Figure 7. (a) Fourier transform (2.9 < k < 12.5 Å^{-1}) of raw EXAFS data of [Cu$_3$(SAr)$_3$] in solution k^0-weighted (solid line), k^3-weighted (dotted line). (b) k^0-weighted and (c) k^3-weighted R-space fit (2.9 < k < 12.5 Å^{-1} and 1.0 < R < 4.0 Å) with 5 co-ordination shells of [Cu$_3$(SAr*)$_3$] in solution (RT).
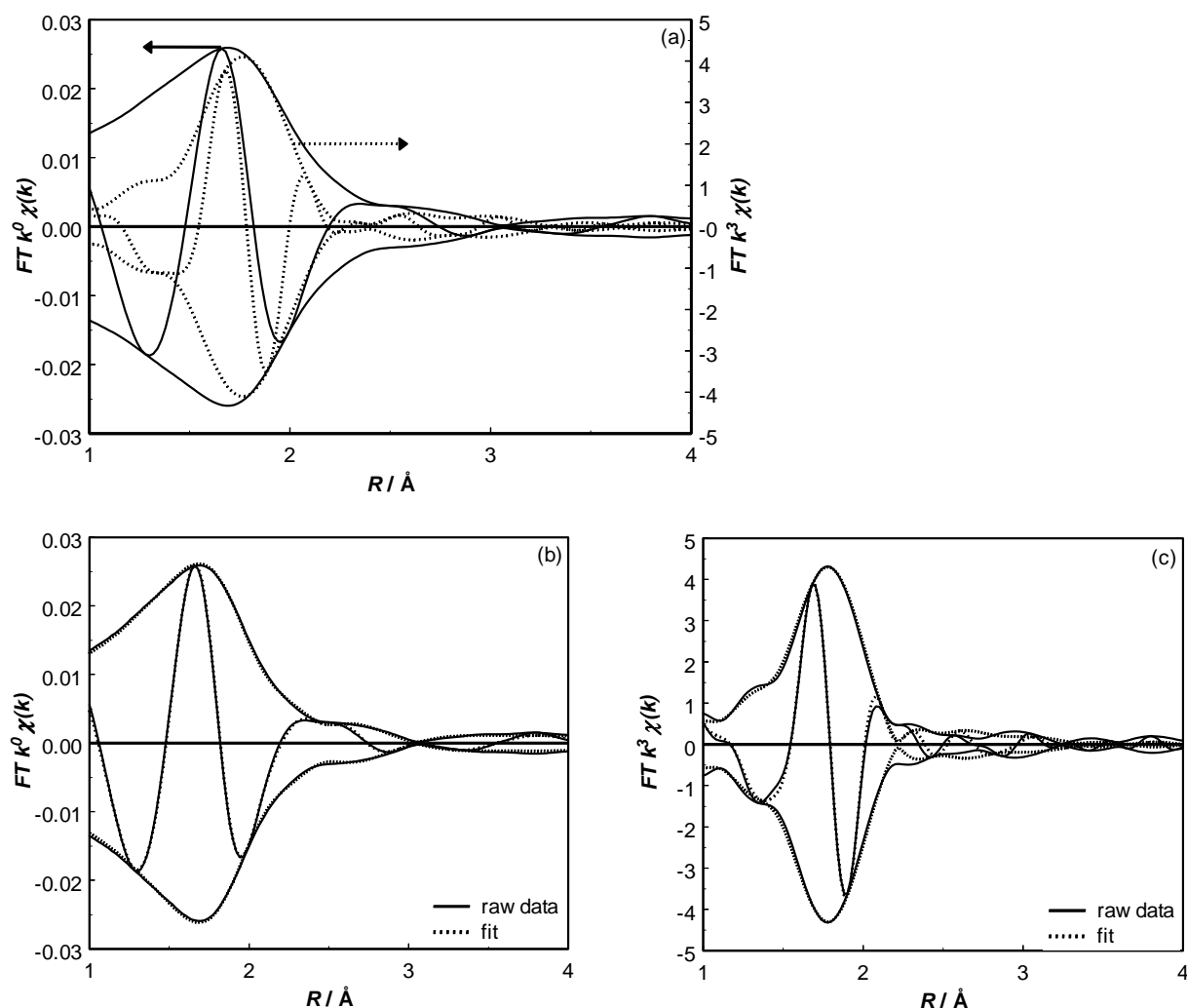
Table 4. EXAFS analysis results of [Cu$_3$(SAr)$_3$] (solution, RT), k^0-weighted 5-shell fit.[a]

Ab-Sc Pair[b]	N	R [Å]	Δσ² [Å²]	ΔE₀ [eV]		Var. Im.[b]	Var. Abs.[b]
Cu-N	1.1	2.01	0.003	1.0	k^0:	0.07	0.04
Cu-S	1.9	2.25	0.004	-2.0	k^3:	0.32	0.16
Cu···Cu	2.1	2.83	0.018	-5.7			
Cu···Cᵃ	2.8	2.95	0.012	11.0			
Cu···Cᵇ	2.6	3.50	0.015	-0.9			

[a] N_{indp} = 20. <u>Fit</u>: *R*-space, 2.89 < k < 12.50; 1.0 < *R* < 4.0, all parameters iteratively refined.
[b] Abbreviations: Ab = absorber; Sc = scatterer. Var. Im. and Var. Abs. are the variances of the fit of the Imaginary and Absolute part, respectively.

Table 5. EXAFS analysis of Cu$_4$(SAr)$_2$(Mes)$_2$.[a]

Ab-Sc Pair[b]	N	R [Å]	Δσ² [Å²]	ΔE₀ [eV]		Var. Im.[b]	Var. Abs.[b]	N_{lit}	R_{lit} [Å]
Cu-Cᵃ	1.0	1.91	0.008	6.4	k^3:	0.04	0.02	1	2.02
Cu-N	0.5	2.27	-0.006	-7.3	k^0:	0.24	0.05	0.5	2.14
Cu-S	1.0	2.21	-0.003	-7.3				1	2.22
Cu···Cuᵃ	1.0	2.44	0.002	-0.7				1	2.40
Cu···Cuᵇ	1.5	2.74	0.017	5.7				1.5	2.74
Cu···Cᵇ	3.0	2.96	0.001	13.2				3	2.93

[a] N_{indp} = 14. <u>Fit</u>: *R*-space, 2.89 < *k* < 12.50; k^0- weighted 1 < *R* < 1.7 & 2.2 < *R* < 3 and k^3-weighted 1 < *R* < 2.5. *N* fixed, all other parameters iteratively refined.
[b] Abbreviations: Ab = absorber; Sc = scatterer. Var. Im. and Var. Abs. are the variances of the fit of the Imaginary and Absolute part, respectively.

Analysis of Cu$_4$(SAr)$_2$(Mes)$_2$

The structure of the tetranuclear aggregate Cu$_4$(SAr)$_2$(Mes)$_2$ (**2**) has two non-equivalent Cu atoms and comprises the binding of two different anions, i.e. the arenethiolate anion and the mesityl anion.[21] The Cu-neighbor coordination numbers (N_{xrd}) and distances (R_{xrd}) of this aggregate as obtained with single crystal XRD are given in Table 5.[21] Both the k^0- and the k^3-weighted Fourier transforms of the measured EXAFS data (2.89 < k < 12.5 Å^{-1}) are given in Figure 8a. It can be seen that using different weightings for the Fourier transforms leads to a loss in intensity in several (different) *R*-ranges. So in different *R*-ranges, a different *k*-weighting will result in a most reliable fit. The fitting procedure is done using a k^0-weighting for 1.0 < R < 1.7 Å and 2.2 < R < 3.0 Å, and a k^3-weighting for 1.0 < R < 2.5 Å.

During the fitting procedure the coordination numbers were fixed, all other parameters were iteratively refined. The final fit is shown in Figure 8b and Figure 8c for the R-space fit with k^0 and k^3 weightings, respectively. The obtained parameters are given in Table 5. In both k-weightings an excellent total fit is obtained, showing the correctness of the analysis procedure.

Figure 8. (a) Fourier transforms (2.9 < k < 12.5 Å^{-1}) of raw EXAFS data of [Cu$_4$(SAr)$_2$(Mes)$_2$] in solid state measured at RT, k^0-weighted (solid line) and k^3-weighted (dotted line). (b) k^0-weighted and (c) k^3-weighted R-space fit (2.9 < k < 12.5 Å^{-1} and 1.0 < R < 3.0 Å) with 6 coordination shells of [Cu$_4$(SAr)$_2$(Mes)$_2$] measured at RT.
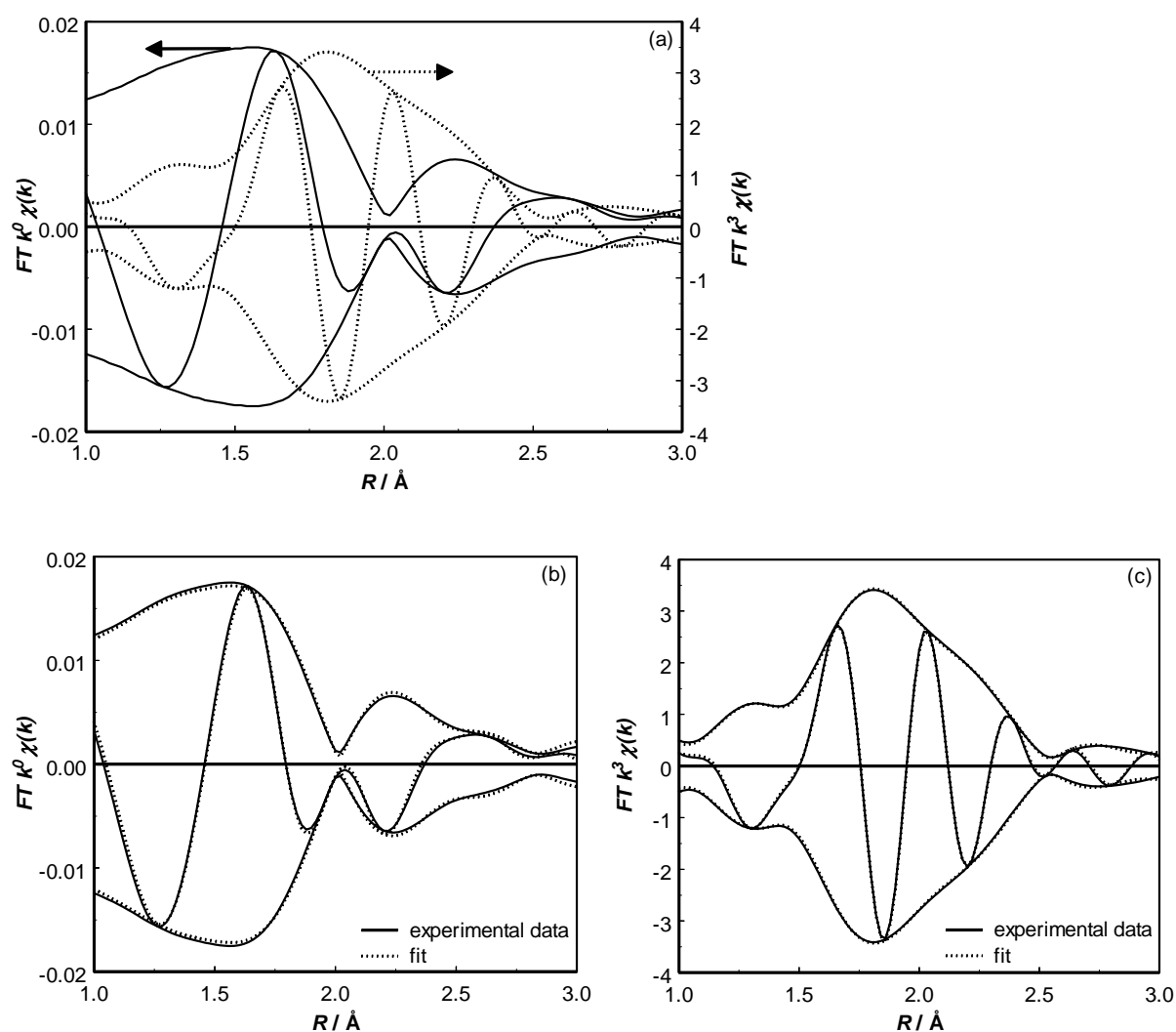
Discussion

Determination of the Weight Factor(s) used for the EXAFS Data-Analysis
Detection of Anti-Phase Behavior

Fitting a spectrum of a compound with a well-known structure provides information about the reliability of the EXAFS data-analysis procedure. The influence of different k-weightings and inclusion of an increasing number of shells on the fit variances can then be studied. The difference file technique can separate the single shells and compare the different shells to each other. The goodness of the fit can be observed and the statistical significance of the individual contributions can be evaluated. Fitting in R-space is essential to prevent truncation errors. Using a Fourier transform of the EXAFS data and applying different weightings can immediately reveal the presence of anti-phase behavior of the EXAFS oscillations of the different coordination shells. Moreover, in literature, regularly the peaks observed in the total Fourier Transform of the EXAFS data are simply assigned to the separate contributions in a spectrum. However, overlap of different shells (and especially in case of anti-phase behavior) can significantly change the shape and intensity of the total Fourier Transform peak(s) or shift the position of the total peak,[39] as also demonstrated in this study. In this way the amount and position of contributions can be underestimated and interpreted wrongly.

For the $[Cu_3(SAr^*)_3]$ sample in the solid and liquid state measured at RT a R-space fit of a k^0-weighted EXAFS including 5 coordination shells leads to a good agreement with the results of single crystal XRD (Tables 3, 4). Both a k^0- and a k^3-weighting have to be used for the analysis of $Cu_4(SAr)_4(Mes)_2$ (Table 5). When the data analysis procedure has been performed using the best k-weighting as a starting point, an important check has to be performed. Only if the fitting parameters obtained also result in a good agreement in (all) other k-weightings, a correct EXAFS data analysis is concluded. This study makes clear that criteria solely based on analysis of EXAFS data can be established, which can be applied to straightforwardly determine the structure of unknown compounds.

EXAFS Data-Analysis of [Cu$_3$(SAr)$_3$] (**1**) in Solid state and Solution*
Statistical Significance and Analysis of Anti-Phase Behavior

As shown in Figure 4, a k^3-weighted Fourier transform of the EXAFS data leads to a very small amplitude of the higher shells peaks. Freeing all parameters iteratively resulted in a good fit with coordination parameters, which are in good agreement with the results of single crystal XRD when using k^0-weighting for the analysis of the RT data. These results can be understood by a more detailed examination of the single-shell EXAFS contributions of the optimized fit.

Figure 9a displays the calculated Cu-Cu, Cu-C^a and Cu-C^b EXAFS functions determined for the analysis of the solid state EXAFS data. All EXAFS oscillations are well above the noise band of ± 0.00025. A maximum noise level of 0.0005 is determined in the raw EXAFS data at k = 14 Å^{-1}. Not only from the Fourier transforms of the difference files as plotted in Figure 6 but also from Figure 9 it can therefore be concluded that these higher shell contributions are statistically significant. Moreover, it can be seen also that the Cu-Cu and the Cu-C^b EXAFS functions are opposite in phase with the Cu-C^a EXAFS function in the range of 4.0 < k < 9.0 Å^{-1}. This results in a strong damping of the total higher shell EXAFS contributions (Cu-Cu + Cu-C^a + Cu-C^b) at these high k-values, which is shown in Figure 9b. A high k-weighting will therefore make the fits insensitive to these higher shells.

Figure 9. (a) Fitted single shell Cu-Cu, Cu-C^a and Cu-C^b EXAFS contributions of 5 shell fit of [Cu$_3$(SAr*)$_3$] in solid state (b) Total higher shell contributions (Cu-Cu + Cu-C^a + Cu-C^b) of 5 shell fit of [Cu$_3$(SAr*)$_3$].
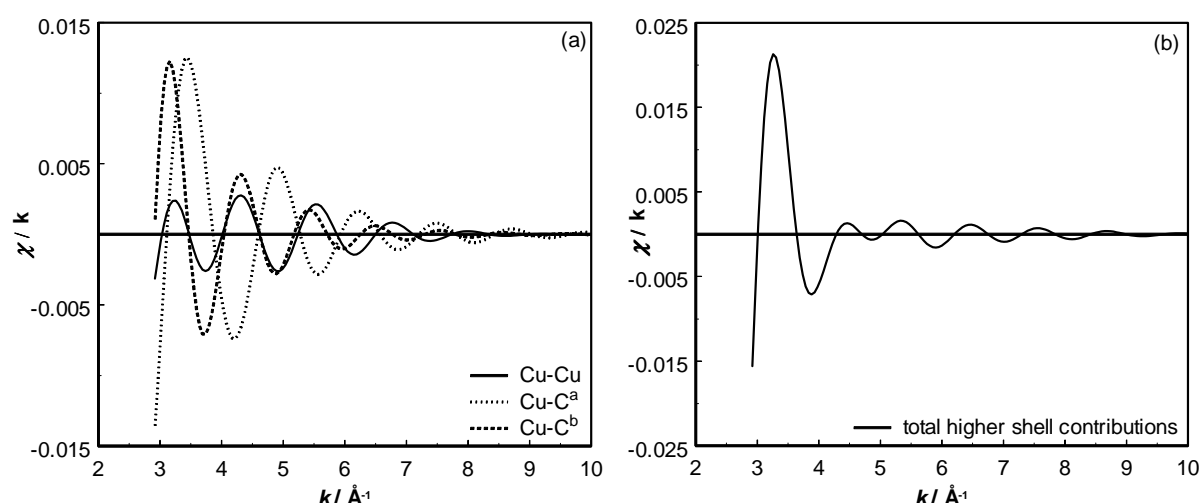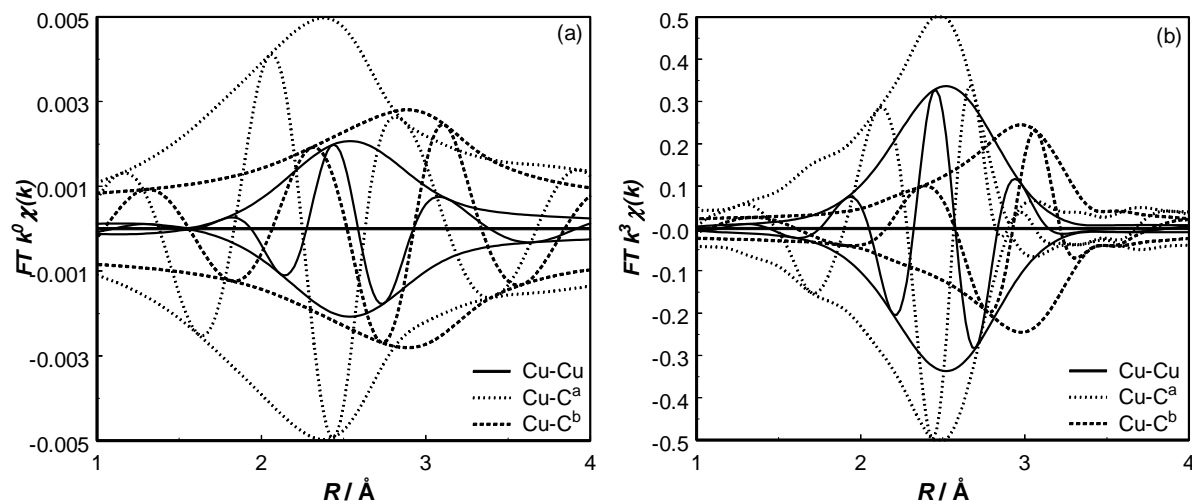
Figure 10. Fourier transform (k^0, 2.9 < k < 12.5 Å^{-1}) of fitted single shell Cu-Cu (solid line), Cu-C^a (dotted line) and Cu-C^b (dashed line) contributions of five shell fit of [Cu$_3$(SAr*)$_3$] solid state (a) k^0-weighted, (b) k^3-weighted.

The interference effects have a strong influence on the analysis of the Cu-Cu contributions. As can be observed in Table 3 only after inclusion of the fifth shell (Cu-C^b), the EXAFS analysis leads to a proper Cu⋅⋅Cu distance and structural parameters, which correspond to the single crystal XRD results. In case of a four shell fit, the Cu-Cu difference file is compensating the lack of an additionally Cu-C shell, explaining why a wrong Cu⋅⋅Cu distance is found in this case. Moreover, when the Fourier transforms of the Cu-Cu and Cu-C^a single shell contributions, displayed here for the [Cu$_3$(SAr*)$_3$] (solid) in Figure 10, are examined more carefully, the Cu-C^a contribution peaks at an even lower distance than the Cu-Cu coordination although its distance is larger. This is due to the fact that the position of the peak in the Fourier transform is determined by the argument (Φ) of the EXAFS function and not solely by R:

$$\Phi = 2kR + \varphi, \qquad (5)$$

with φ the phase function of the absorber-backscatterer pair. Although the Cu-Cu co-ordination distance is smaller than for Cu-C^a, the phase function (φ) of the Cu-C^a is more negative than that of the Cu-Cu EXAFS, leading to a Cu-C^a peak in the non-phase corrected Fourier transform at lower values of R. This has important consequences in examining the Fourier transforms of the difference files for the analysis of the EXAFS data of these classes of Cu complexes.

In case of a two-shell fit, all parameters obtained for the Cu-N contribution are wrong. The coordination number is twice as high as expected, the distance is 0.1 Å too large and the Debye-Waller factor is unrealistically high. Normally, the first shell in an EXAFS data analysis procedure can be determined with the highest accuracy. However, in this case, the inclusion of higher contributions is required to obtain the correct parameters. Additionally, the Cu-S shell can be determined accurately and correctly in all fitting procedures and is not dependent on additional contributions. The explanation for these phenomena consists of two parts: the Cu-S shell is the biggest contribution to the total EXAFS spectrum, it has the highest amplitude as can be seen in the Fourier Transforms of the difference files given in Figures 6a-e. Therefore, the Cu-S contribution can be determined with the highest accuracy. Since the Cu-S shell is overlapping especially with the Cu-N contribution due to their comparable distances, the analysis of this Cu-N is more complicated. Moreover, the Cu-Cu and Cu-C contributions also have a significant amplitude at lower k- and lower R-range, causing overlap with the Cu-N contribution. A reliable Cu-N analysis can thus only be done after inclusion of these higher shells.

To be able to conclude a correct EXAFS analysis the obtained parameters have to fit also correctly using other k-weightings. The parameters obtained in the k^0-weighted fit of the $[Cu_3(SAr^*)_3]$ (RT) have been imported in a k^3-weighted analysis (as fixed parameters), resulting also in a good fit as can be seen in Figure 5b and concluded from the low fit variances as given in Table 3. Moreover, the single shell contributions are also fitted significantly using an other k-weighting. Therefore, solely based on EXAFS parameters it can be concluded that the data are analyzed correctly.

The same observation can be made for the complex in solution, resulting in a good fit in different weightings as can be observed in Figure 7b and 7c and Table 4. It can be concluded that the resulting parameters give an identical structure to the solid state, but with a higher disorder for all contributions.

Using a k^3-weighted data analysis as normally used in literature a good fit but without a Cu-Cu contribution is obtained as can be observed in Table 6. The obtained fit displays reasonably small variances in both the absolute and the imaginary part of the Fourier transforms in both weightings. Moreover, the difference files of all contributions are fitted well in this k^3-weighted Fourier transform. However, if the obtained parameters are imported in a k^0-weighted fit (as fixed parameters), it can be observed that the higher shell contributions (Cu-C^a and Cu-C^b) do not fit well in this weighting. In Figure 11a the total fit of the k^0-weighted Fourier transform is displayed, in which for R > 2.2 Å significant differences in absolute and imaginary part can be observed. These differences can be observed more closely by looking at the fits of the difference files of these higher shells Cu-C^a and Cu-C^b given in Figure 11b and 11c. Clear differences between difference files and singles shell contributions are visible over the whole fitting range, indicating a poor fit for these contributions. Apparently, during fitting, using a single k^n-weighted analysis, a local minimum can be found which results in a seemingly good analysis without the Cu-Cu contribution. This demonstrates the importance of fitting while carefully observing all difference files and totals fits in all k-weightings.

Anti-phase behavior can be detected and accounted for by performing a multiple shell analysis. In order to fit multiple shells the data must be of sufficient quality to allow the required number of data points (N_{ind}). Dependent on which contributions are in anti-phase, first or higher shells, the number of independent data points and consequently the quality of the data needed is respectively lower or higher.

Table 6. EXAFS analysis results of [Cu$_3$(SAr)$_3$], k^3-weighted 4-shell fit (without Cu···Cu contribution).[a]

Ab-Sc Pair[b]	N	R [Å]	$\Delta\sigma^2$ [Å^2]	ΔE_0 [eV]		Var. Im.[b]	Var. Abs.[b]
Cu-N	1.2	2.08	0.002	0.8	k^0:	0.42	0.08
Cu-S	2.0	2.21	0.003	0.2	k^3:	0.36	0.17
Cu···C^a	2.9	2.98	0.017	8.0			
Cu···C^b	3.2	3.39	0.011	1.4			

[a] N_{indp} = 20. <u>Fit</u>: *R*-space, 2.89 < k < 12.50; 1.0 < R < 4.0, all parameters iteratively refined.
[b] Abbreviations: Ab = absorber; Sc = scatterer; Var. Im. and Var. Abs. are the variances of the fit of the Imaginary and Absolute part, respectively.

Figure 11. Fourier Transforms of the EXAFS data of [Cu$_3$(SAr*)$_3$] in solid state for a single k^3-weighted fitting procedure (2.9 < k < 12.5, 1.0 < R < 4.0) without a Cu-Cu contribution, implemented in a k^0-weighted analysis. (a) Total Fourier Transforms raw data and fit, (b) Fitted single shell contribution Cu-C^a, (c) Fitted single shell contribution Cu-C^b.
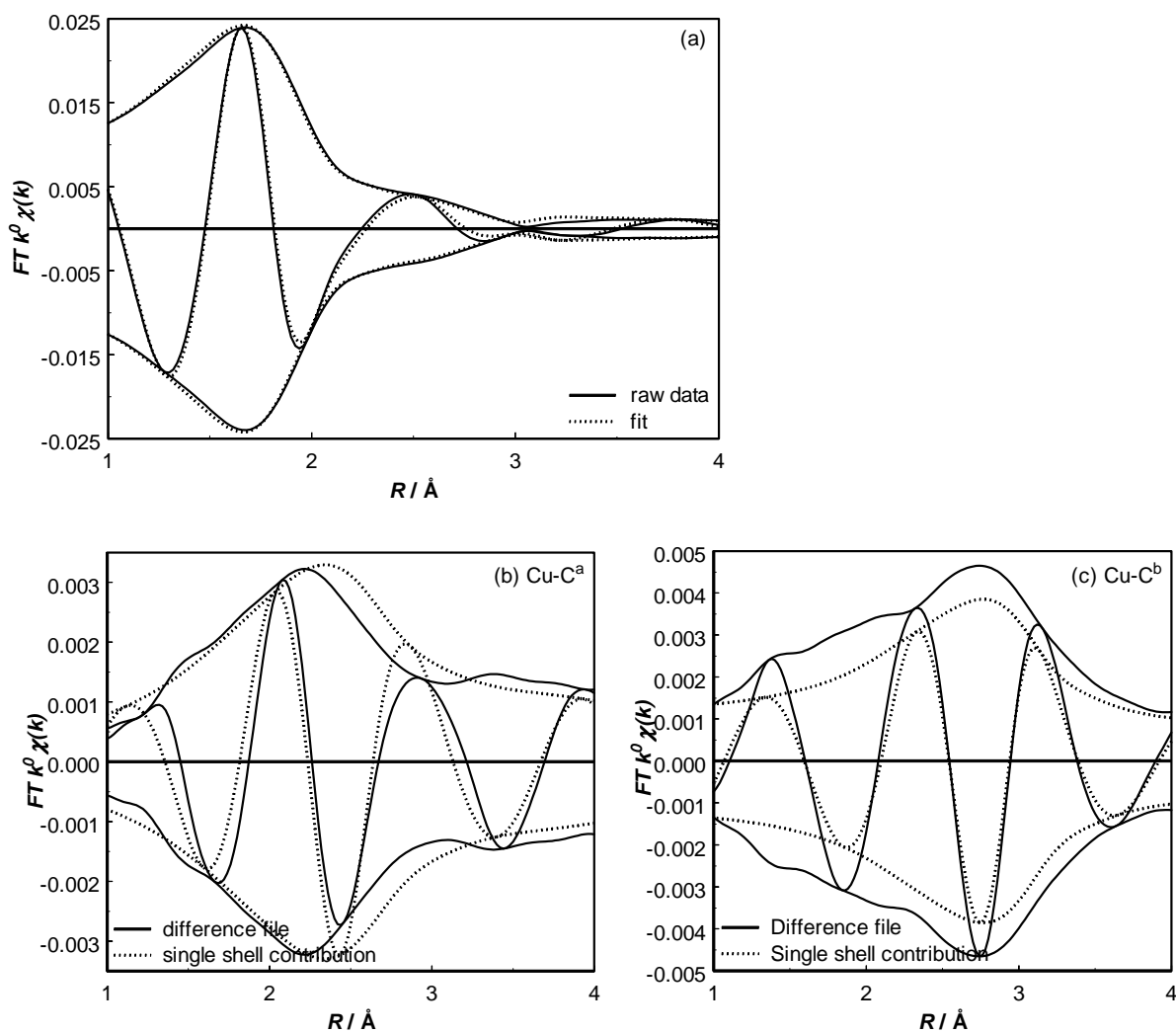
EXAFS Data-Analysis of Cu$_4$(SAr)$_2$(Mes)$_2$ (2) (Solid, RT)

The Cu$_4$(SAr)$_2$(Mes)$_2$ (**2**) compound is a mixed organo(arenethiolate)copper(I) aggregate, which contains distinctly different Cu sites. Different Cu··Cu distances are present, making the EXAFS data analysis extra complicated. Figure 8a displays the Fourier transforms of the EXAFS data using different k-weightings. Depending on the k-weighting a lack of intensity is observed in different R-ranges of the Fourier transforms. This also strongly indicates the presence of anti-phase behavior of the different EXAFS coordination shells.

Figure 12. (a) Single shell Cu-Cu^b and Cu-C^b contributions for [Cu$_4$(SAr)$_2$(Mes)$_2$] (2.9 < k < 12.5, 1.0 < R < 3.0). (b) Fitted single shell Cu-Cu^a and Cu-C^b contributions for [Cu$_4$(SAr)$_2$(Mes)$_2$] (2.9 < k < 12.5, 1.0 < R < 3.0).
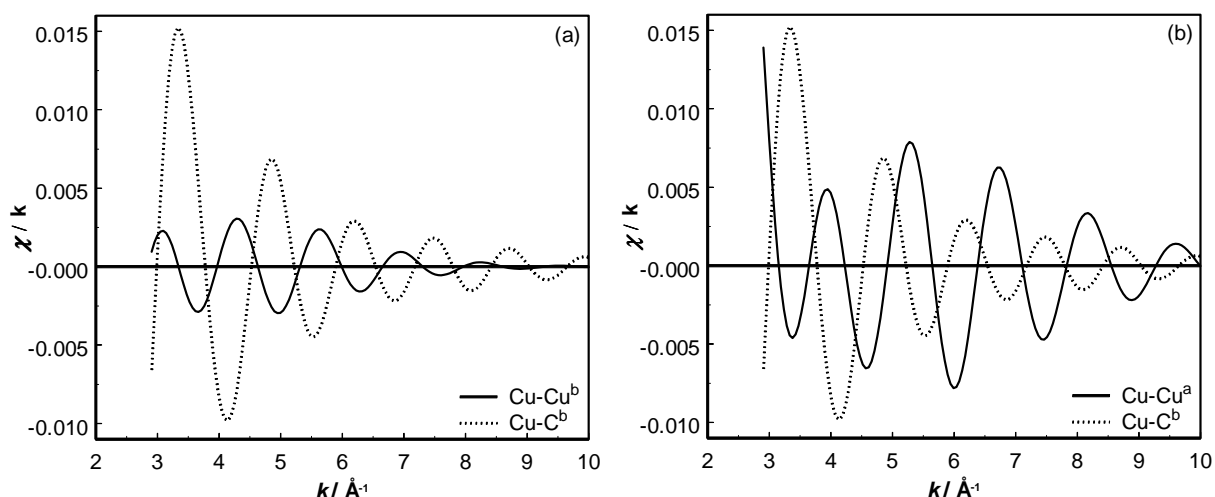
The single-shell contributions as fitted using the difference file technique show anti-phase behavior between different shells in different parts of the spectrum. Two clear examples are given in Figure 12a and 12b. Figure 12a shows for the Cu-Cu^b contribution an opposite phase as for the Cu-C^b contribution in the range of 4.0 < k < 8.0 Å^{-1}. The anti-phase behavior found for low values of k results in a low intensity in a k^0-weighted Fourier transform and consequently in a less reliable fit using only a k^0-weighted analysis. In Figure 12b the anti-phase behavior of the Cu-Cu^a and the Cu-C^b contributions is displayed. Due to the anti-phase behavior found at higher values of k a small intensity was observed in a k^3-weighted Fourier transform resulting in a less reliable fit for the k^3-weighted analysis in this

range. A reliable analysis of the data can be performed by dividing the Fourier transform in several regions and fit these regions with a proper k-weighting. The separate difference files with the single-shell fits and the resulting total fit have to be examined in all k-weightings in order to detect anti-phase behavior and to determine the most reliable analysis.

EXAFS Data-Analysis of Copper Carbon Complexes: Detection of Cu-Cu Contributions

As described in the introduction it can be inferred from the literature[25,26,28-35] and confirmed in this study that detection with EXAFS of a Cu-Cu contribution in copper-carbon complexes is very difficult. Although a Cu-Cu contribution is expected based on other characterization techniques as XRD, some authors have been able to analyze their data and to find a good fit without the inclusion of a Cu-Cu contribution.[28,30-32,34,35]

Many authors are using a k^3-weighted fit in k-space by default, since this type of weighting normally makes the fit sensitive to the presence of high Z scatterers. If the fit is not checked in a different (low) k-weighting a wrong fit without a Cu-Cu contribution can be obtained with low fit variances. Cu has a maximum in its backscattering amplitude around $k = 8$ Å^{-1}, whereas C or N have an amplitude function which is rapidly decaying with k. However, a high dynamical or structural disorder of the Cu-Cu contribution in a Cu-compound will have a detrimental effect on its EXAFS amplitude at high values of k. The detection of Cu-Cu contributions was in literature already recognized to be extra complicated if additional Cu-C shells are present in the same distance range as the Cu-Cu contribution.[33] This can be explained by the fact that Cu-Cu and Cu-C shells can have an opposite phase. When anti-phase behavior is observed especially at higher k-weightings, a single k^3-weighted analysis will not be sensitive for these higher shells. Only, if anti-phase behavior is observed at low k-ranges or if no anti-phase behavior is observed at all, a single k^3-weighted fit results in a reliable analysis of the EXAFS data. In addition to the application of the appropriate weighting(s), it is demonstrated in this paper that R-space fitting while using the difference file technique enables a careful examination of the different contributions, both individually and relative to each other. This can lead to the unraveling of anti-phase behavior and therefore to a reliable analysis of the EXAFS data.

The Structure as a Function of the State of Aggregation

The structure of [$Cu_3(SAr^*)_3$] contains a Cu_3S_3 six-membered ring in a chairlike conformation with alternating copper and sulfur atoms. The $C_6H_3((R)$-CH(Me)NMe_2)-2 group is bonded on each sulfur atom equatorially with respect to this ring. The bonding behavior of the Cu-S-Cu bridge in the Cu_3S_3 ring is discussed extensively in different references.[14,21] It is clear that the complex is still present as a trimer in solution and that the structure is in fact identical to that in the solid state. The dynamics of the vibrating ring is adding an additional contribution to the Debye-Waller factor, which is comparable for all interactions. This indicates that dissolving the complex only influences its vibrational behavior and no preferable vibrations or vibration direction of the ring can be observed.

The results discussed above make clear that only after understanding how Cu K-edge EXAFS in organo copper samples should be analyzed, structural information about these complexes in both solid and solution can be obtained. It has been shown that different states of aggregation give additional information about the dynamics of the Cu arenethiolate complexes. The technique has proven its strengths and possibilities and can now be used for the determination of reaction intermediates in the mentioned C-C bond formation reactions.

Conclusions

With a systematic analysis of the Cu K-edge EXAFS data, XAFS spectroscopy is a very good tool for the investigation of Cu complexes, both in the solid phase and in solution. The obtained EXAFS data have to be analyzed very carefully, especially by looking at the influence of different k-weightings as using a single k-weighting may lead to false minima in variances. When during R-space fitting the difference file technique is applied, the different individual contributions to the total EXAFS spectrum can be examined in detail, which helps to detect and unravel anti-phase behavior of different contributions. When all contributions are statistically relevant (i.e. well above the noise level) and the total fit as well as all individual contributions fit the obtained EXAFS data very well in all different k-weightings, a good and reliable analysis can be concluded. This analysis procedure is solely based on EXAFS parameters making it applicable to every (non-Cu) EXAFS spectrum obtained.

In this study is shown that Cu K-edge EXAFS spectroscopy can provide detailed information about the homogeneous catalysts in reaction medium and can now be used to give insights in the reactivity of homogeneous complexes and their way to form catalytic intermediates in the presence of the Grignard reagents and the substrates.

Chapter 3

Experimental Section

All experiments were carried out using standard Schlenk techniques under an inert oxygen-free nitrogen atmosphere using flame-dried glassware. The samples were sealed in the EXAFS probe in a Faircrest glove-box equipped with O_2 and H_2O indicators, operating on 3 inch nitrogen over-pressure. Boron nitride (99%) and anhydrous toluene (99+%) were purchased from Aldrich Chemical Co., UK. [Cu_3{SC_6H_4((R)-CH(Me)NMe$_2$)-2}$_3$] (**1**)[14], [$Cu_4(SAr)_2(Mes)_2$] (**2**)[21] were prepared according to literature methods.

EXAFS Data Collection

Copper K-edge (8979.0 eV) EXAFS spectra were measured at the Synchrotron Radiation Source (SRS) in Daresbury, United Kingdom, Station 8.1, using a Si(220) double crystal monochromator and at the European Synchrotron Radiation Facility (ESRF) in Grenoble, France, Beamline 29, using a Si(111) double crystal monochromator. The monochromator was detuned to 50% intensity to avoid effects of higher harmonics present in the X-ray beam. The measurements were done in the transmission mode using optimized ion chambers as detectors. To decrease noise, three scans were collected for each sample and averaged.

Sample Preparation in the Solid State. Solid material and a known amount of boron nitride were thoroughly mixed and pressed into a self-supporting wafer (calculated to have a maximum total absorbance of 2.5 with a preferable step-size of 1) and placed in an air- and water-tight EXAFS cell provided with X-ray transparent beryllium windows.[42]

Sample Details:

[$Cu_3(SAr^*)_3$] (1), Solid. A self-supporting wafer was pressed from 35.5 mg **1** and boron nitride (50 mg).

[$Cu_3(SAr^*)_3$] (1) in Solution. [$Cu_3(SAr^*)_3$] (33.4 mg, 0.0457 mmol) was dissolved in toluene (1.1 mL) and this solution was transferred into the EXAFS liquid cell making sure that the cell was completely filled.

[$Cu_4(SAr)_2(Mes)_2$] (2), Solid. A wafer was pressed from 9 mg **2** and boron nitride (63 mg).

Acknowledgements

References

1. H. Hope, M. M. Olmstead, P. P. Power, J. Sandell, X. Xu, *J. Am. Chem. Soc.* **1985**, *107*, 4337.
2. P. Leoni, M. Pasquali, C. A. Ghilardi, *J. Chem. Soc., Chem. Commun.* **1983**, 240.
3. G. van Koten, J. G. Noltes, *J. Am. Chem. Soc.* **1979**, *101*, 6593.
4. G. Boche, F. Bosold, H. Marsch, K. Harms, *Angew. Chem.* **1998**, *110*, 1779; *Angew. Chem. Int. Ed.* **1998**, *37*, 1684.
5. C-S. Hwang, P. P. Power, *J. Am. Chem. Soc.* **1998**, *120*, 6409.
6. C. M. P. Kronenburg, J. T. B. H. Jastrzebski, A. L. Spek, G. van Koten, *J. Am. Chem. Soc.* **1998**, *120*, 9688
7. B. H. Lipshutz, R. S. Wilhelm, *J. Am. Chem. Soc.* **1981**, *103*, 7672.
8. G. H. Posner, *An introduction to Synthesis Using Organocopper Reagents,* John Wiley & Sons, New York, **1980**.
9. B. H. Lipshutz, S. Sengupta, *Org. React.* **1992**, *41*, 139.
10. B. H. Lipshutz, R. S. Wilhelm, J. A. Kozlowski, *Tetrahedron* **1984**, *40*, 5005.
11. S. H. Bertz, E. H. Fairchild, *Encyclopedia of Reagents for Organic Synthesis*, Wiley, New York, 1995; pp1312-1315, 1341-1343, 1346-1349.
12. N. Krause, A. Gerold, *Angew. Chem.* **1997**, *109*, 194; *Angew. Chem. Int. Ed. Engl.* **1997**, *36*, 186.
13. D. M. Knotter, G. van Koten, H. L. van Maanen, D. M. Grove, A. L. Spek, *Angew. Chem.* **1989**, *101*, 341.
14. D. M. Knotter, H. L. van Maanen, D. M. Grove, A. L. Spek, G. van Koten, *Inorg. Chem.* **1991**, *30*, 3309.
15. M. D. Janssen, D. M. Grove, G. van Koten, *Progr. Inorg. Chem.* **1997**, *46*, 97.
16. M. van Klaveren, F. Lambert, D. J. F. M. Eijkelkamp, D. M. Grove, G. van Koten, *Tetrahedron Lett.* **1994**, *35*, 6135.
17. A. Haubrich, M. van Klaveren, G. van Koten, G. Handke, N. Krause, *J. Org. Chem.* **1993**, *58*, 5849.

18. M. van Klaveren, E. S. M. Persson, D. M. Grove, J. E. Bäckvall, G. van Koten, *Tetrahedron Lett.* **1994**, *35*, 5931.

19. G. van Koten, *J. Organomet. Chem.* **1990**, *400*, 283.

20. F. Lambert, D. M. Knotter, M. D. Janssen, M. van Klaveren, J. Boersma, G. van Koten, *Tetrahedron Asymm.* **1991**, *2*, 1097.

21. D. M. Knotter, D. M. Grove, W. J. J. Smeets, A. L. Spek, G. van Koten, *J. Am. Chem. Soc.* **1992**, *114*, 3400.

22. G. van Koten, *J. Organometal. Chem.* **1990**, *400*, 483.

23. G. van Koten, *Pure and Appl. Chem.* **1994**, *66(7)*, 1455.

24. Q. Zhou, A. Pfaltz, *Tetrahedron Lett.* **1993**, *34*, 7725.

25. G. Henkel, A. Müller, S. Weissgräber, G. Buse, T. Soulimane, G. C. M. Steffens, H-F. Nolting, *Angew. Chem.* **1995**, *107*, 847; *Angew. Chem. Int. Ed.* **1995**, *34*, 1488.

26. H. Bertagnolli, W. Kaim, *Angew. Chem.* **1995**, *107*, 847; *Angew. Chem.* **1995**, *34*, 771.

27. D. C. Koningsberger, R. Prins, *X-ray Absorption: Principles, Applications, Techniques of EXAFS, SEXAFS and XANES,* John Wiley & Sons, New York, **1988**.

28. H. Huang, C. H. Liang, J. E. Penner-Hahn, *Angew. Chem.* **1998**, 110, 1628; *Angew. Chem. Int. Ed.* **1998**, *37*, 1564.

29. J. H. Bitter, B. L. Mojet, M. D. Janssen, D. M. Grove, G. van Koten, D. C. Koningsberger, D. C. *J. Synchrotron Rad.* **1999**, *6*, 423.

30. T. M. Barnhart, J. E. Penner-Hahn, *Physica B* **1995**, *208&209*, 709.

31. T. Stemmler, J. E. Penner-Hahn, P. Knochel, *J. Am. Chem. Soc.* **1993**, *115*, 348.

32. T. Stemmler, T. M. Barnhart, J. E. Penner-Hahn, C. E. Tucker, P. Knochel, H. Böhme, G. Frenking, *J. Am. Chem. Soc.* **1995**, *117*, 12489.

33. R. A. Scott, M. K. Eidsness, *Comments Inorg. Chem.* **1988**, *7(5)*, 235, and references therein.

34. N. J. Blackburn, R. W. Strange, R. W. Cruse, K. D. Karlin, *J. Am. Chem. Soc.* **1987**, *109*, 1235.

35. I. Persson, J. E. Penner-Hahn, K. O. Hodgson, *Inorg. Chem.* **1993**, *32*, 2497.

36. A. L. Ankudinov, B. Ravle, J. J. Rehr, S. D. Conradson, *Phys. Rev. B.* **1998**, 7565.

37. A. Lommen, K. I. Pandya, D. C. Koningsberger, G. W. Canters, *Biochim. Biophys. Acta* **1991**, *1076*, 439.

38. M. Vaarkamp, J. C. Linders, D. C. Koningsberger, *Physica B.* **1995**, *208&209*, 159.

39. D. C. Koningsberger, B. L. Mojet, G. E. van Dorssen, D. E. Ramaker, *Top. Catal.* **2000**, *10*, 143.

40. D. C. Koningsberger, *Jpn. J. Appl. Phys.* **1993**, *32 suppl. 32-2*, 877.

41. J. B. A. D. van Zon, D. C. Koningsberger, H. F. J. van Blik, D. E. Sayers, *J. Chem. Phys.* **1985**, *82*, 5742.

42. F. W. H. Kampers, T. M. J. Maas, J. van Grondelle, P. Brinkgreve, D. C. Koningsberger, *Rev. Sci. Instrum.* **1989**, *60*, 2635.

Chapter 4

Probing the Molecular Orbitals and Charge Redistribution in Organometallic (PP)Pd(XX) Complexes. A Pd K-edge XANES study

Abstract

Pd K-edge X-ray absorption near-edge spectroscopy (XANES) is used to probe the unoccupied molecular orbitals and thereby obtain information on the mechanisms of charge redistribution in bidentate diphosphine Pd complexes. Complexes containing a series of bidentate diphosphine ligands (PP) are measured to study the effect of the ligand bite angle on the charge redistribution in these complexes. Different coordinating moieties (XX) have been used to induce a range of Pd oxidation states. XANES spectroscopy directly probes unoccupied molecular orbitals. A full interpretation of the Pd K-edge XANES data is presented. Taking the negative second derivative of these XANES data provides direct information on the energy and electronic distribution of the different molecular orbitals probed. The obtained data thus gives essential information on the electronic properties of the sample under investigation. The charge redistributions within the complexes, as reflected in the effective Pd oxidation state, are indicated by both the intensity of the first edge feature, the 'Pd d peak', and the energy of the second edge feature, the 'Pd p peak', which are observed in the negative second derivative of the normalized X-ray absorption data. Additionally, the changing covalent interaction between the Pd and coordinated moieties via the Pd p orbitals is reflected directly in the energy splitting of the 'Pd p' peak. Investigation of the molecular orbitals of these (PP)Pd(XX) complexes, some used as catalysts in organic synthesis, with XANES spectroscopy leads to essential information on their electronic properties. The Pd K-edge XANES spectroscopy study, as described in this paper, can be applied to investigate the molecular orbitals of and charge redistributions within any kind of sample.

Introduction

Palladium is one of the most widely used metals in transition-metal-catalyzed organic synthesis, as it is capable of catalyzing a wide variety of commercially important reactions.[1] Various ligands, most often phosphine ligands, are employed to tune the performance and increase the stability of the Pd catalysts. Changing the ligands enables fine-tuning of the steric and electronic properties of the catalyst and thereby the activity and selectivity of the catalyst.[2]

Bidentate diphosphine ligands are widely applied and their utility in homogeneous catalysts and metal complexes has been the subject of research for many years. An important ligand parameter to describe the bidentate diphosphine ligand (PP) complexes is the so-called bite angle β, i.e. the P-M-P angle.[3,4] The natural preferred bite angle, β_n, of a bidentate diphosphine ligand can be calculated using molecular mechanics.[5] In this way, ligand bite angle trends can be deduced without the requirement of crystal structures. The P-Pd-P bite angles reported in this study (Table 1), however, are obtained from crystal structure analyses.

Several studies[2,3,4,6,7] discussed the ligand bite angle effect observed for different catalytic systems. The steric and electronic changes after ligand modification are investigated and different effects are suggested to be important for different reactions. For example, large differences in regioselectivity with bite angle were observed in the allylic alkylation reaction using (PP)Pd catalysts. Therefore, the [(PP)Pd(allyl)]$^+$ reaction intermediates have been isolated and characterized in detail to gain more insight into the observed activity and selectivity of these catalysts.[7] The [(PP)Pd(allyl)]$^+$ complexes have been studied by molecular modeling, X-ray crystallography, (solution-) NMR and EXAFS techniques in order to obtain information on their steric and electronic properties.[7,8] Additionally, a series of theoretical papers modeling these complexes have appeared proposing orbital interaction diagrams and discussing the influence of ligand modification and consequent catalytic properties.[9]

To gain more detailed electronic information on different (PP)Pd complexes, we have applied X-ray absorption fine structure (XAFS) spectroscopy. XAFS spectroscopy is capable of providing structural and electronic information about a specific element in a compound in any state of aggregation.[10] In this manuscript we will focus on the electronic properties of the (PP)Pd complexes by performing a detailed X-ray absorption near edge spectroscopy (XANES) study.

Detailed XANES studies have been described in the literature previously for transition metal complexes showing that the X-ray absorption edges are very sensitive to the chemical

environment.[11] Moreover, the pre-edge is indicative of different oxidation states and geometry of the samples under investigation.[11] For metals like palladium and rhodium, the K edge is observed at high energies (the Pd K edge at 24350 eV), showing a very broad and seemingly nondescript edge. Perhaps for this reason, no detailed studies on these edges have been reported, at least to our knowledge.

Here, series of (PP)Pd(XX) complexes are characterized with Pd K-edge XANES spectroscopy, in which the 1s to 5p orbital transition is primarily probed. This provides information about empty molecular orbitals that consist of, or overlap with, the metal Pd 5p orbital. We will show that this technique is very suitable for probing the molecular orbitals of the Pd organometallic complexes and gives detailed information about the covalent binding and charge redistribution within these systems. Additional ab-initio full multiple scattering calculations with the FEFF8 code have been performed to validate the electronic structure of these Pd complexes. This study demonstrates that XANES spectroscopy is a very powerful tool in unraveling the electronic properties of these organometallic complexes and leads therefore to a better understanding of their properties such as catalytic activity and selectivity.
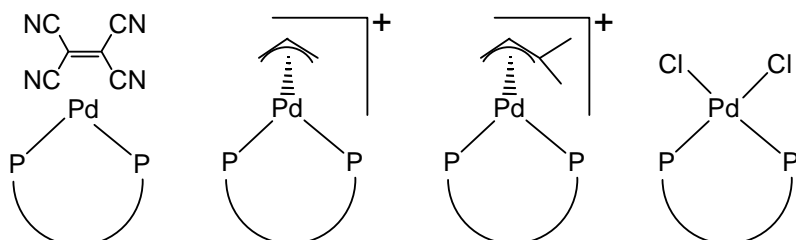
A series of bidentate diphosphine ligand (PP)Pd(XX) complexes are studied with XANES spectroscopy. Different coordination moieties (XX) are used to determine oxidation state trends and different (PP) ligands with different bite angles are used to determine bite angle trends. Scheme 1 provides an overview of the different complexes under investigation.

The coordinating moieties (XX) are tetracyanoethylene (TCNE), allyl $[(C_3H_5)]^-$, 1,1-dimethyl-allyl $[(1,1-(CH_3)_2-C_3H_3)]^-$ and chloride (2 Cl$^-$), respectively. The oxidation state of Pd in these complexes is increasing for these moieties from a formal Pd oxidation state of 0 for the neutral (PP)Pd(TCNE) complexes to a formal Pd oxidation state of 2+ for the neutral (PP)Pd(II) complexes with two ionicly bonded Cl$^-$ ions. The (PP)Pd(allyl/dimethyl-allyl) complexes are cationic (PP)Pd(II) complexes with a (mainly) covalently bonded allyl anion moieties. The effective Pd oxidation state will consequently go down from the formally 2+ towards 1+.[12] In this study, the 'formal' oxidation state of both the [(PP)Pd(allyl)]$^+$ and [(PP)Pd(1,1-dimethylallyl)]$^+$ complexes will be taken as 1+ to clearly distinguish between the different series. The Pd oxidation states, determined with XANES spectroscopy will be further addressed as the effective Pd oxidation state. No quantification of the oxidation states will be done and only the trends are considered.
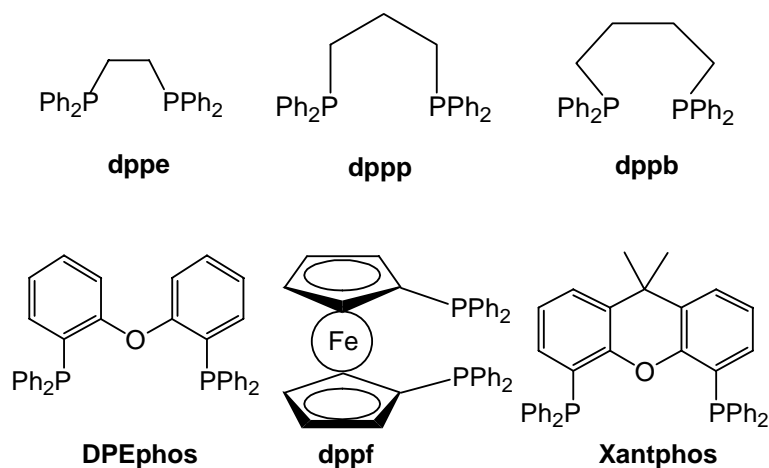
Scheme 1. Overview of the (PP)Pd(XX) complexes used in this study.

Pd complexes:

Ligands with increasing P-Pd-P bite angle:

dppe   dppp   dppb

DPEphos   dppf   Xantphos

A series of bidentate diphosphine ligands are used which induce increasing P-Pd-P bite angles (Scheme 1), i.e. dppe 1,2-bis(diphenylphosphino)ethane, dppp 1,2-bis(diphenylphosphino)propane, dppb 1,2-bis(diphenylphosphino)butane, dppf 1,2-bis(diphenylphosphino)ferrocene, DPEphos 2,2-bis(diphenylphosphino(diphenylether) and Xantphos. The corresponding bite angles as determined from crystal structure analyses are summarized in Table 1.4.[7a,13,14]

Table 1. Bite angles for series of (PP)Pd(XX) complexes.

Complex	β (º)	Complex	β (º)
(dppe)Pd(TCNE)	82.55(3.65)[a]	[(dppe)Pd(C$_3$H$_5$)]$^+$	85.77[d]
(dppf)Pd(TCNE)	98.74(3.42)[a]	[(dppp)Pd(C$_3$H$_5$)]$^+$	95[d]
(DPEphos)Pd(TCNE)	101.46(3)[b]	[(DPEphos)Pd(C$_3$H$_5$)]$^+$	99[d]
(Xantphos)Pd(TCNE)	101.64(5)[b]	[(Xantphos)Pd(C$_3$H$_5$)]$^+$	108.11(7)[e]
		[(dppe)Pd(C$_5$H$_9$)]$^+$	85.77[e]
		[(dppp)Pd(C$_5$H$_9$)]$^+$	95[e]
(dppe)PdCl$_2$	85.8[c]	[(dppb)Pd(C$_5$H$_9$)]$^+$	99[e]
(dppf)PdCl$_2$	99.07[c]	[(dppf)Pd(C$_5$H$_9$)]$^+$	101.2(3)[e]
(DPEphos)PdCl$_2$	101.46[a]	[(DPEphos) Pd(C$_5$H$_9$)]$^+$	103.93(6)[e]
(Xantphos)PdCl$_2$	101.64[a]	[(Xantphos) Pd(C$_5$H$_9$)]$^+$	108.11(7)[e]

[a] Estimated based on Reference 4.
[b] Reference 13.
[c] Reference 14.
[d] Taken as C$_5$H$_9$.
[e] Reference 7a.

Chapter 4

Methods

Experimental

Synthesis of (PP)Pd(XX) Complexes

The (PP)Pd(TCNE),[13] [(PP)Pd(allyl)]$^+$ complexes7[b,15,16] with counter ion [OTf] or [BF$_4$-] and (PP)PdCl$_2$ complexes14,[17,18] were synthesized as described in literature.

EXAFS Data Collection

Palladium K-edge (24350.0 eV) EXAFS spectra were measured at the European Synchrotron Radiation Facility (ESRF) in Grenoble, France, Beamline 29, and at the Hamburger Synchrotronstrahlungslabor (Hasylab), Germany, Beamline X1. At both beamlines a Si(311) double crystal monochromator was used. The monochromators were detuned to 50% intensity to avoid effects of higher harmonics present in the X-ray beam. The measurements were performed in the transmission mode using optimized ion chambers as detectors. To decrease noise, three scans were averaged for each sample. A Pd foil is simultaneously measured with each sample. The spectra are energy calibrated by aligning the 1st peak of the 1st derivative of the Pd foil to 24350.0 eV.

Negative 2nd Derivatives XANES Data

To highlight different features present in the Pd K-edge more clearly, the negative 2nd derivative of the normalized absorption data is taken by using the Savitsky-Golay smoothing and differentiation procedure. The first[11d,e] and negative second derivative procedure[11a,b,f] has been used previously by Hodgson *et al.* and others.[11] In this work, the negative second derivative is calculated on an energy grid of 250 points separated by 0.5 eV, using a smoothing order of 7, which is the number of surrounding points to be used in computing the smoothed second derivative. This results in a 2nd derivative energy window of 3.5 eV.

Theory

Two quite different, but complementary, theoretical calculations are performed on the organometallic complexes to interpret the XANES data and understand and validate the results obtained. Density functional theory calculations (DFT), using the Amsterdam Density Functional (ADF) package[19], are utilized to calculate the density of states of the allyl and 1,1-dimethyl-allyl anion moieties. Slater type orbitals are used to represent the atomic orbitals, with basis sets consisting of triple-ζ quality, extended with two polarization functions. These calculations represent the bonding orbitals of the system very well. The complete complexes are difficult to calculate and interpret using this method due to the large amount of atoms present and are not discussed here.

These density functional calculations do not approximate the anti-bonding and continuum orbitals 10-50 eV above the Fermi level adequately, which is necessary to interpret the XANES data. Therefore, real-space full multiple scattering calculations utilizing a muffin-tin potential are performed on the full Pd complexes. These calculations approximate effectively the continuum orbitals, and because of the full multiple scattering, also approximate the strong anti-bonding resonances present in this energy region.

The FEFF8 code was used to perform ab-initio self-consistent field, real-space, full multiple scattering calculations.[20] FEFF8 implements self-consistent field potentials for the determination of the Fermi-level and the charge transfer. The calculations were performed using the Hedin-Lundquist exchange correlation potential. A core-hole is included on the absorber atom in order to mimic the final state of the photon absorption process. The absorption XANES data and the density of states (DOS) are calculated for a relatively narrow bite angle complex $[(dppe)Pd(1,1-(CH_3)_2-C_3H_3)]^+$ ($\beta = 86°$) and two wider bite angle complexes $[(dppf)Pd(1,1-(CH_3)_2-C_3H_3)]^+$ ($\beta = 101°$) and $[(DPEphos)Pd(1,1-(CH_3)_2-C_3H_3)]^+$ ($\beta = 104°$). Neither E_0 nor experimental resolution corrections have been applied.

Results

Pd K-edge XANES data are recorded for the different types of (PP)Pd(XX) complexes and a number of selected Pd reference complexes, viz. Pd foil, $PdCl_2$ and $PdBr_2$. Figure 1a shows normalized raw XANES data for the Pd references. The Pd K-edge exhibits a very broad edge containing no distinct pre-edge features, but some small features and shoulders can be observed which vary for the different samples.

Figure 1. Pd K-edge X-ray absorption data of Pd references (a) Normalized XANES spectra, (b) Negative 2nd derivative of the normalized XANES data.
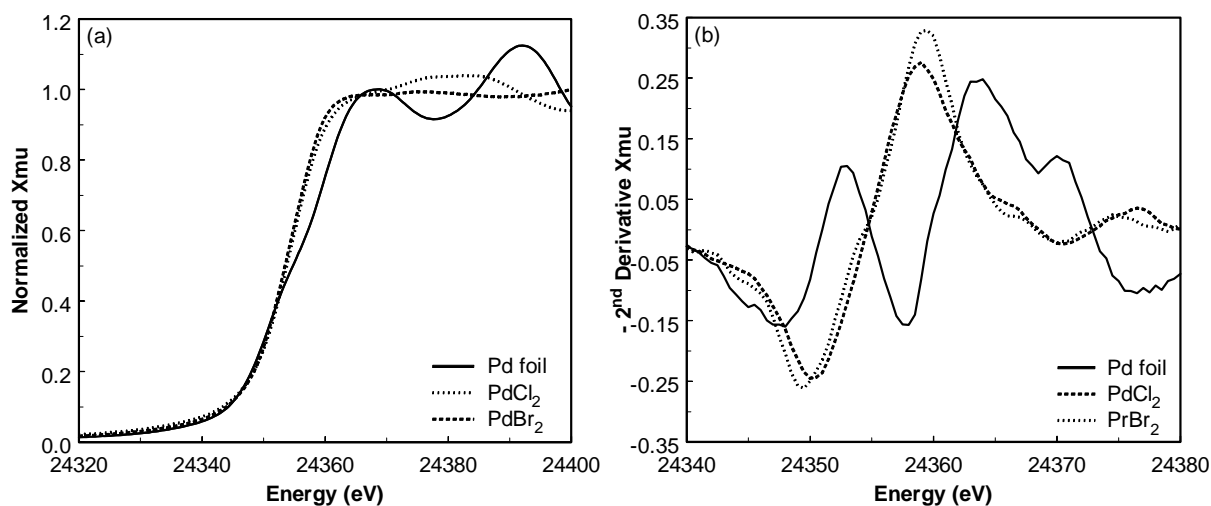

To highlight these differences in the Pd K-edge, the negative 2nd derivative of the normalized absorption spectra data, $-d^2\mu/dE^2$, are given in Figure 1b. Clearly, two different peaks can be observed in the spectrum of Pd foil. Moreover, the second feature is split up into two peaks. The spectra of $PdCl_2$ and $PdBr_2$ are dominated by one major peak.

The normalized XANES data and the corresponding negative 2nd derivatives for the four different series of palladium complexes: (PP)Pd(TCNE), $[(PP)Pd(C_3H_5)]^+$, $[(PP)Pd(1,1-(CH_3)_2-C_3H_3)]^+$ and (PP)$PdCl_2$ are given in Figures 2-5(a) and Figures 2-5(b), respectively. The negative 2nd derivative accentuates the noise level, and clearly the noise level in the data for the (PP)Pd(TCNE) complexes is somewhat higher than those in the other three series,

especially for the (dppf)Pd(TCNE) complex (Figure 2b). With increasing bite angle, some small changes in intensity of the first peak are observed, and the second feature clearly broadens and splits from one peak into two peaks. For the series of $[(PP)Pd(C_3H_5)]^+$ complexes (Figure 3), larger differences in the intensity of the first peak are observed. Again, the second feature displays a significant broadening and simultaneous splitting upon increasing the bite angle of the ligand. For a larger series of $[(PP)Pd(1,1-(CH_3)_2-C_3H_3)]^+$ complexes (Figure 4), large deviations in the intensity of the first peak are observed, although no clear trend with bite angle can be easily determined. The second feature again broadens and splits with increasing bite angle. For the $(PP)PdCl_2$ series (Figure 5), only small changes in the first peak and a small shift in the second feature of the negative 2nd derivative are observed when changing the ligand.

Figure 2. Pd K-edge absorption spectroscopy data of bidentate diphosphine ligand palladium tetracyanethylene complexes (PP)Pd(TCNE), with a series of bite angles. (a) Normalized XANES spectra, (b) Negative 2nd derivative of XANES data.
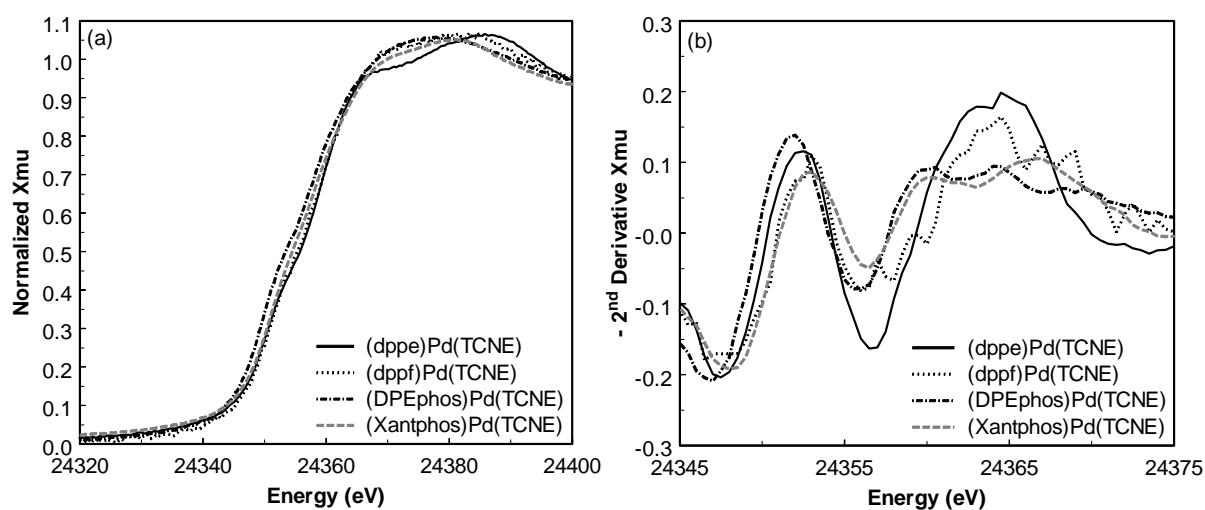
Figure 3. Pd K-edge absorption spectroscopy data of bidentate diphosphine ligand palladium allyl complexes [(PP)Pd(C_3H_5)]$^+$, with a series of bite angles. (a) Normalized XANES spectra, (b) Negative 2nd derivative of XANES data.
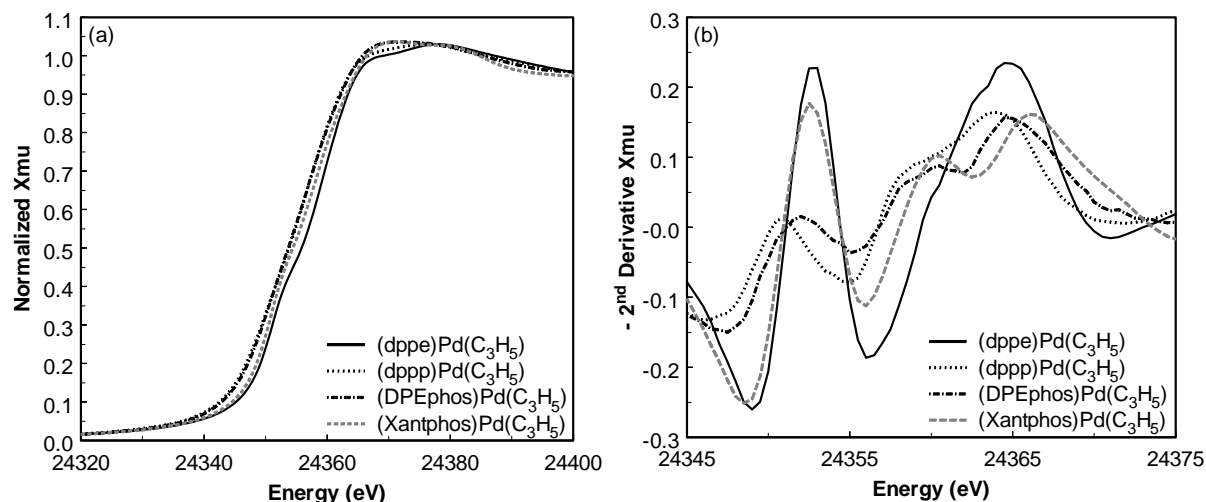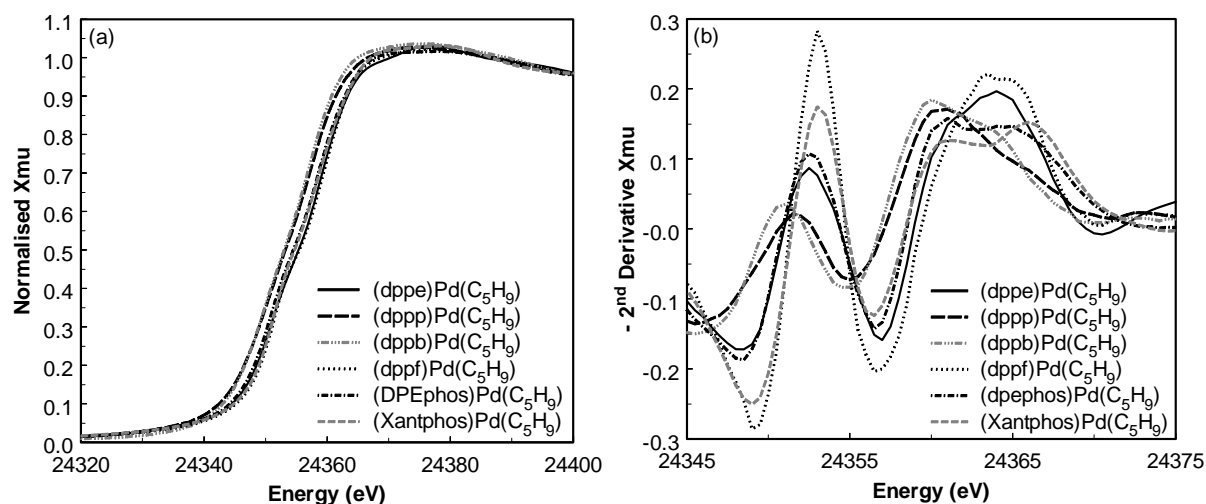

Figure 4. Pd K-edge absorption spectroscopy data of bidentate diphosphine ligand palladium 1,1-dimethylallyl complexes [(PP)Pd(1,1-(CH_3)$_2$-C_3H_3)]$^+$, with a series of bite angles. (a) Normalized XANES spectra, (b) Negative 2nd derivative of XANES data.

Figure 5. Pd K-edge absorption spectroscopy data of bidentate diphosphine ligand palladium chlorides (PP)PdCl$_2$, with a series of bite angles. (a) Normalized XANES spectra, (b) Negative 2nd derivative of XANES data.
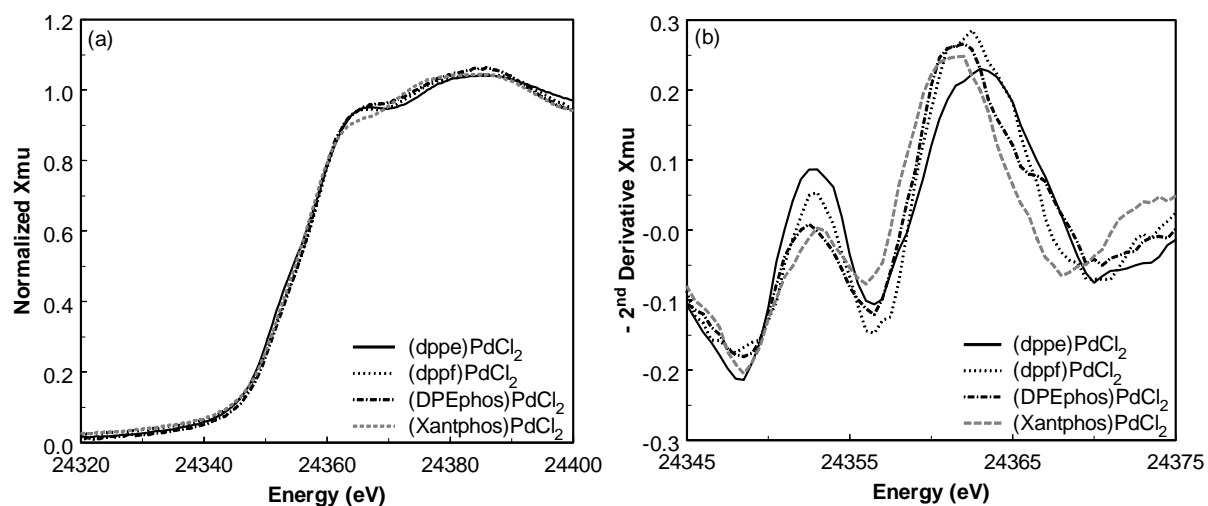
Discussion

Dependence of XANES on Pd Symmetry

The negative 2nd derivative spectrum of a palladium foil exhibits two clear features, whereas in those of the $PdCl_2$ and $PdBr_2$ references only one peak is observed (Figure 1b). The crystal structure of Pd foil is face-centered cubic (fcc) with each Pd having 12 nearest neighbors. In this symmetry, the Pd p orbitals hybridize with the Pd d and s orbitals. The Pd K-edge probes the 1s to 5p orbital transition. The 1s to 4d transition is formally dipole forbidden, though a small intensity may originate from the quadruple transition.[11] Hybridization of Pd p with the Pd d orbitals enables the dipolar transition to occur at the energy of the quadrupolar transition, i.e. the first peak in the negative 2nd derivative. Because of the dominant Pd d character, we will call this the Pd d peak. The second peak originates from the allowed 1s to 5p orbital transition and is further denoted as the Pd p peak. We consider this peak the absorption edge. Due to the symmetry of the Pd metal the Pd p density of states (DOS) is split as shown by the second feature in this Pd p peak.

Figure 6. Orbital interaction diagram for complexes with square planar D_{4h} geometry.
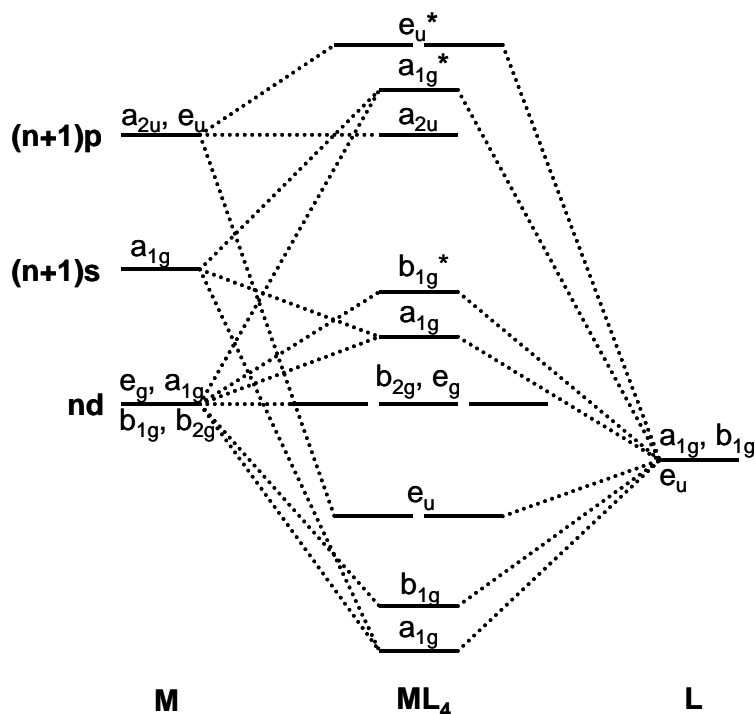
The $PdCl_2$ and $PdBr_2$ solids have square planar D_{4h} symmetry with each Pd surrounded by 4 Cl^- or Br^- ions. The orbital diagram for D_{4h} symmetry is shown in Figure 6. The symmetries of the Pd d orbitals compared to the Pd p orbitals are different in square planar geometry, therefore mixing of these orbitals is not allowed and only one peak, the Pd p peak, is observed in the negative 2nd derivative of the XANES data. Thus, the presence of a Pd d peak indicates a lowering of the square planar geometry.

Dependence of XANES on the Formal Pd Oxidation State

The position of the Pd p peak in the negative 2nd derivative of the XANES data of the $PdCl_2$ and $PdBr_2$ is shifted downward in energy by almost 5 eV relative to Pd foil. This shift reflects the increasing effective oxidation state of the complexes; going from a formal oxidation state of 0 for Pd foil to a formal valence state of 2+ for $PdCl_2$ and $PdBr_2$.

The energy *hv* of the metal X-ray absorption edge is determined by the difference between the energy of the initial state, i.e. the core level at energy E_C from which the electron is ejected, and the final state, i.e. the valence level at energy $E_V + U_{CV}$ that accepts the electron in the final state. Here, U_{CV} is the core-hole electron attraction energy, which the final valence electron experiences due to the presence of the core hole.

Figure 7. Energy of the metal K-edge X-ray absorption edge as a function of metal oxidation state. The energy *hv* is determined by the energy of the initial state (E_C = core level energy) and final state (E_V = valence level energy). (L) Final state mainly located on the ligand, (M) Final state mainly localized on the metal (absorber).
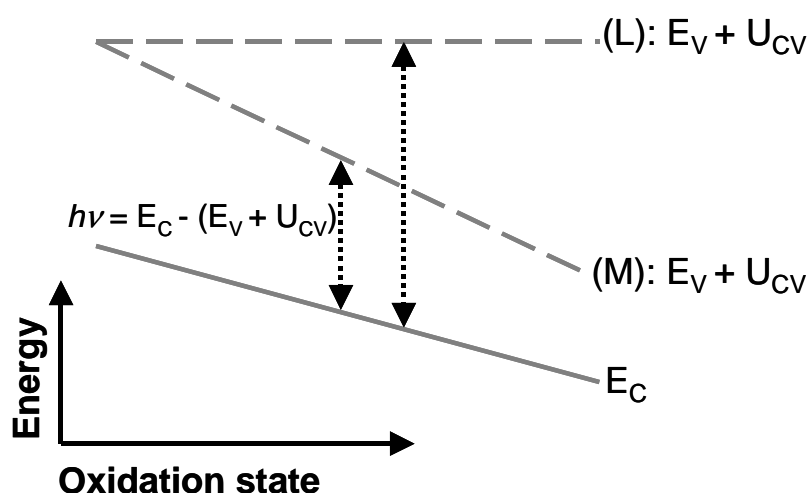
With increasing oxidation state of the metal atom, the orbitals generally contract thereby lowering the energy of the initial state (solid line in Figure 7). This is the usual shift observed in similar core-level X-ray photoelectron spectroscopy (XPS) data.[21] The final state can respond in different ways depending on the nature and localization of the valence state. The increased Coulomb charge with increasing metal oxidation state is mainly felt by electrons on the metal. Consequently, the energy of the metal valence orbitals is large and the energy of the final state will shift similar to the energy of the core level E_C (dashed line (M) in Figure 7). Because the U_{CV} also increases with oxidation state, the shift of E_v+U_{cv} may be even larger than that for E_C. As a result, the energy difference between the initial and final state is decreasing as observed in the energy of the absorption edge. This is what we observe for the Pd complexes, since the energy of the absorption edge decreases with increasing the Pd oxidation state (Figure 1). More often, the K-edge increases with metal oxidation state.[11] This occurs when the final state is localized on the ligand. In such a case, the final state does not experience the full increased Coulomb potential from the core-hole on the metal atom, thus the final state remains relatively un-shifted (dashed line (L)) as shown in Figure 7. The decreasing photon energy with oxidation level in the Pd complexes reported here indicates that the charge density in the final Pd p state is mainly localized at the metal absorber atom.

In the organometallic Pd complexes the formal Pd oxidation state is increasing for the series (PP)Pd(TCNE), [(PP)Pd(C_3H_5)]$^+$, [(PP)Pd(1,1-(CH_3)$_2$-C_3H_3)]$^+$ and (PP)PdCl$_2$. The position of the absorption edge (Pd p peak) can be determined by calculating the centroid of this peak or, in case of splitting, the centroid of the two overlapping peaks. The energy position of the centroid is plotted in Figure 8 as a function of the 'formal' oxidation state of the Pd atom. The 'formal' Pd oxidation states of the [(PP)Pd(allyl)]$^+$ and [(PP)Pd(1,1-dimethyl-allyl)]$^+$ are taken as 1+ in this figure to be able to clearly distinguish between the different series. It is observed in this figure that for a certain (PP) ligand the energy of the centroid is decreasing with increasing oxidation state of the Pd, as expected. Figure 8 also shows that within a series of coordinating moiety (XX), the effective oxidation state also depends on the bite angle, which will be further discussed below.

Figure 8. The position of the Pd p peak in the 2nd derivative of the XANES data, determined by the centroid of the total peak, as a function of "formal" Pd oxidation state i.e. coordinating moiety for series of bidentate diphosphine palladium complexes (PP)Pd(XX).
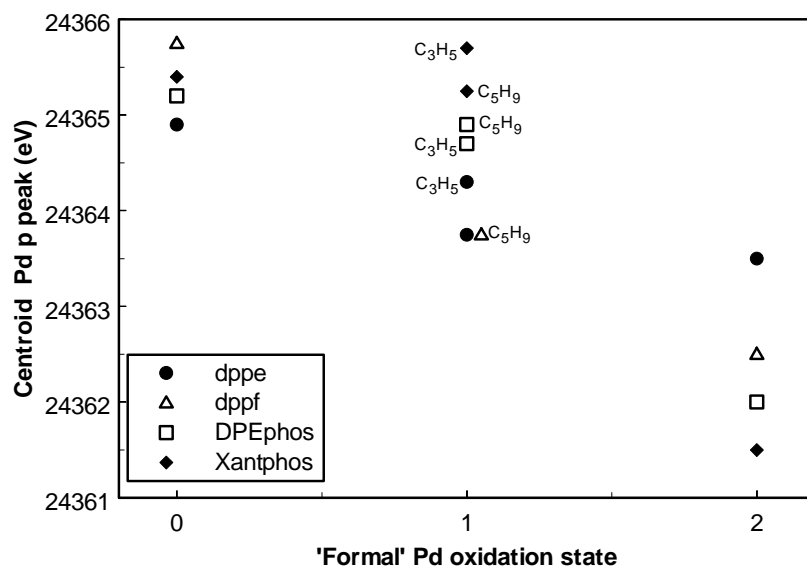
Dependence of the MO Structure on Bite Angle

By changing the backbone of a bidentate diphosphine ligand, the P-Pd-P bite angle can be changed systematically (Table 1). This change in geometry will have a steric influence on the metal complex but it will also induce an electronic effect.[12] The effect of the bite angles on the energy of the molecular orbitals and the charge redistribution in the (PP)Pd complexes can be understood by investigating the ligand-metal (LL)M orbital interaction diagram, the so-called Walsh diagram[4,22,23] given in Figure 9.

Figure 9. Walsh diagram for Pd(PP) complexes.
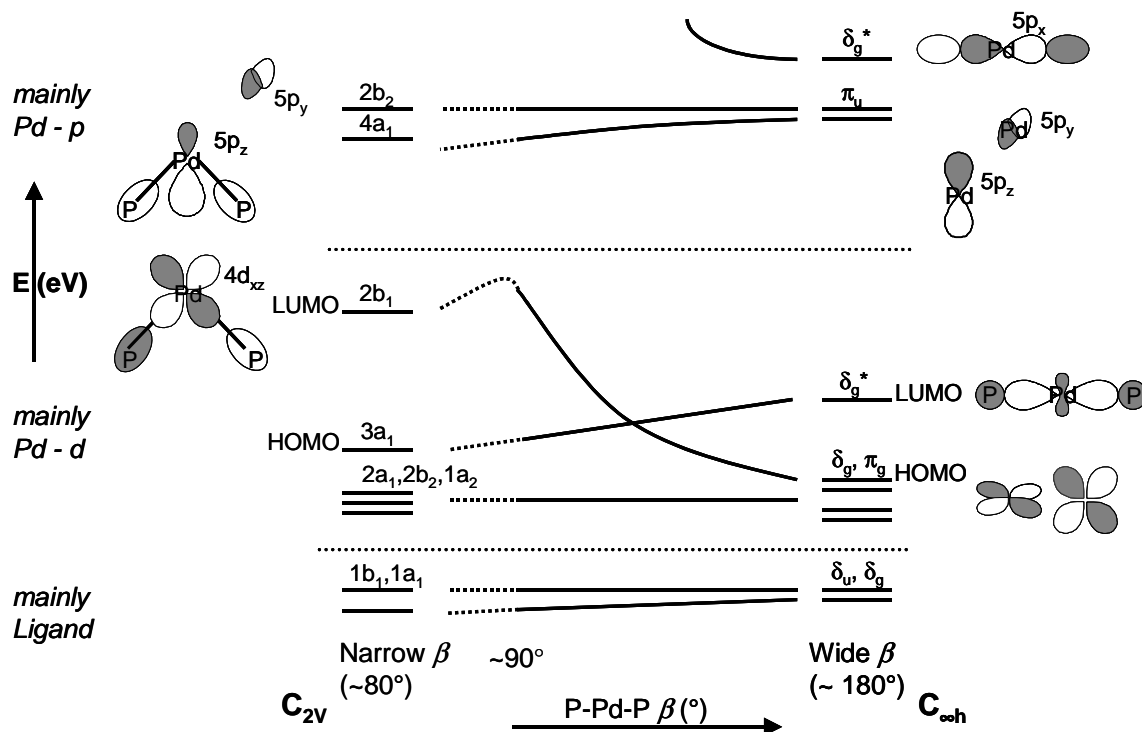
The Walsh diagram is calculated for d^{10}-metal complexes and a bite angle range of 90° to 180° (solid lines in Figure 9). Only the relevant ligand metal interactions (metal 4d and 5p orbitals) are shown here. The lower two orbitals originate primarily from the ligand, in our case the P donor atoms. At higher energy, the five Pd 4d and the three Pd 5p orbitals are shown. The diagram is based on the extended Hückel MO method, assuming C_{2v} symmetry for the L-M-L complex (Table 2a) and only σ-type orbitals for the ligands are considered.[22,23] The anti-bonding $\delta_g{}^*$ or $3a_1$ orbital is constructed from an out-of-phase combination of mainly Pd $4d_{z^2}$ and L 3s atomic orbitals, and stabilizes with decreasing bite

angle. As the L-M-L bite angle decreases (bending in the xz plane), the L 3s orbitals start to mix in with the $5p_x$ and $4d_{xz}$ of the metal, resulting in the formation of the hybridized orbital $2b_1$. With decreasing bite angle, the $5p_x$ component of this orbital decreases, while the $4d_{xz}$ character increases.

The $[(PP)Pd]^{2+}$ fragment of the complexes in this work are considered to have a d^8 metal electron configuration regardless of oxidation state, although we will see below that the molecular orbitals involving the Pd orbitals can be delocalized over the coordinating moieties (XX) and ligands (PP). For these $[(PP)Pd]^{2+}$ fragments, the first four Pd 4d orbitals are occupied (Figure 9). For a complex with a relatively narrow bite angle of 90°, the $2b_1$ molecular orbital is the lowest unoccupied molecular orbital (LUMO), whereas for linear complexes with a P-Pd-P angle of 180°, the δ_g^* orbital is the LUMO. The character of the HOMO and LUMO orbitals thus switch with the bite angle increasing from 90° to 180°. Since Pd complexes in the bite angle range 80° to 110° are studied in this work, the Walsh diagram is extrapolated to bite angles smaller than 90° (dotted lines in Figure 9). This extrapolation is based on the experimental results and theoretical considerations presented here (*vide infra*). In summary, the Walsh diagram shows that changing the bite angle of the complex results in large changes in both the position and symmetry of the Pd 4d and Pd 5p orbitals.

Table 2. Group symmetry matrices:
(a) C_{2v} symmetry.

C_{2v}	E	C_2	$\sigma_v(xz)$	$\sigma_v'(yz)$		
A_1	1	1	1	1	z	x^2, y^2, z^2
A_2	1	1	-1	-1	R_z	xy
B_1	1	-1	1	-1	x, R_y	xz
B_2	1	-1	-1	1	y, R_x	yz

(b) C_s symmetry.

C_S	E	σ_h		
A'	1	1	z, y	x^2, y^2, z^2, yz
A''	1	-1	x	xy, xz

*Dependence of the MO Structure on Allyl Interaction*

The Walsh diagram (Figure 9) ignores the interaction of the $[(PP)Pd]^{2+}$ fragment with the coordinating moiety (XX). For a more complete description of the (PP)Pd(XX) complexes these interactions must also be included, especially in cases where this interaction is covalent in nature. In the $(PP)PdCl_2$ complexes, the Pd has a formal oxidation state of 2+. The electronegative chloride ion forms an almost pure ionic bond with palladium. The Cl^- atomic orbitals therefore have large binding energies and undergo little interaction with the Pd atom orbitals. Consequently, the orbital interaction diagram for this series of complexes is similar to the Walsh diagram shown in Figure 9.

On the other hand, the allyl moieties interact mainly covalently to the $[(PP)Pd]^{2+}$ ligand fragment. The orbital interaction diagram between $[(PP)Pd]^{2+}$ and a $(C_3H_5)^-$ moiety has already been described and discussed in the literature.[9] The $[(PP)Pd(C_3H_5)]^+$ complex has a lower symmetry C_S relative to the $[(PP)Pd]^{2+}$ fragment (Table 2b). Since the complexes studied in this work have bite angles of 80° to 110°, the levels calculated for narrow bite angles (Figure 9) are used to construct the orbital interaction diagram between the $[(PP)Pd]^{2+}$ fragment and the coordinating allyl moiety.

Two π orbitals (bonding and anti-bonding) and one non-bonding π orbital (n_π) are present within the allylic fragment. The density of states (DOS), calculated using density functional theory as incorporated into the ADF code, and consequent orbital pictures are shown in Figure 10a and agree with literature results.[9,12] In Figure 10a, the relative sizes of the p orbitals on each C atom indicate their relative contributions obtained from the ADF calculations. Coordination of the allyl moiety to the $[(PP)Pd]^{2+}$ fragment causes the $2b_1$ (LUMO) (PP)Pd $4d_{xz}$ orbital (taken from the Walsh diagram Figure 9) to interact with the n_π orbital forming orbitals 1a" (filled) and 2a" (non-filled) as shown in Figure 11a. Since after coordination of the allyl to the $[(PP)Pd]^{2+}$ fragment, the symmetry of the complex is lowered from C_{2v} to C_S, the orbital $2b_1$ should now be denoted as a" (see Figure 11a and Table 2). The bonding π and anti-bonding π^* orbitals of the allylic fragment interact with the (PP)Pd-$5p_z$ $4a_1$ or a' orbital, as can be expected from the symmetry of the three orbitals (Figures 9, 10a and 11a). These form one filled and two non-filled MO's, 1a', 2a' and 3a'. The (PP)Pd-$5p_y$ $2b_2$ orbital is close in energy too, but this orbital is not able to interact with the allyl moiety as it lies perpendicular to the plane of the complex (see Figures 9 and 10a). In Figure 11a this $2b_2$ orbital ends up in the orbital interaction diagram as a non-bonding orbital. The Pd $5p_x$ orbital is able to mix with the $4d_{xz}$ orbital as both are of b_1 symmetry in the C_S point group, but the extent of this mixing depends strongly on the symmetry and bite angle of the complex.

Figure 10. Calculated density of states and corresponding (quantitative) orbital pictures of (a) plain allyl C_3H_5 and (b) 1,1-disubstituted allyl C_5H_9 anions.
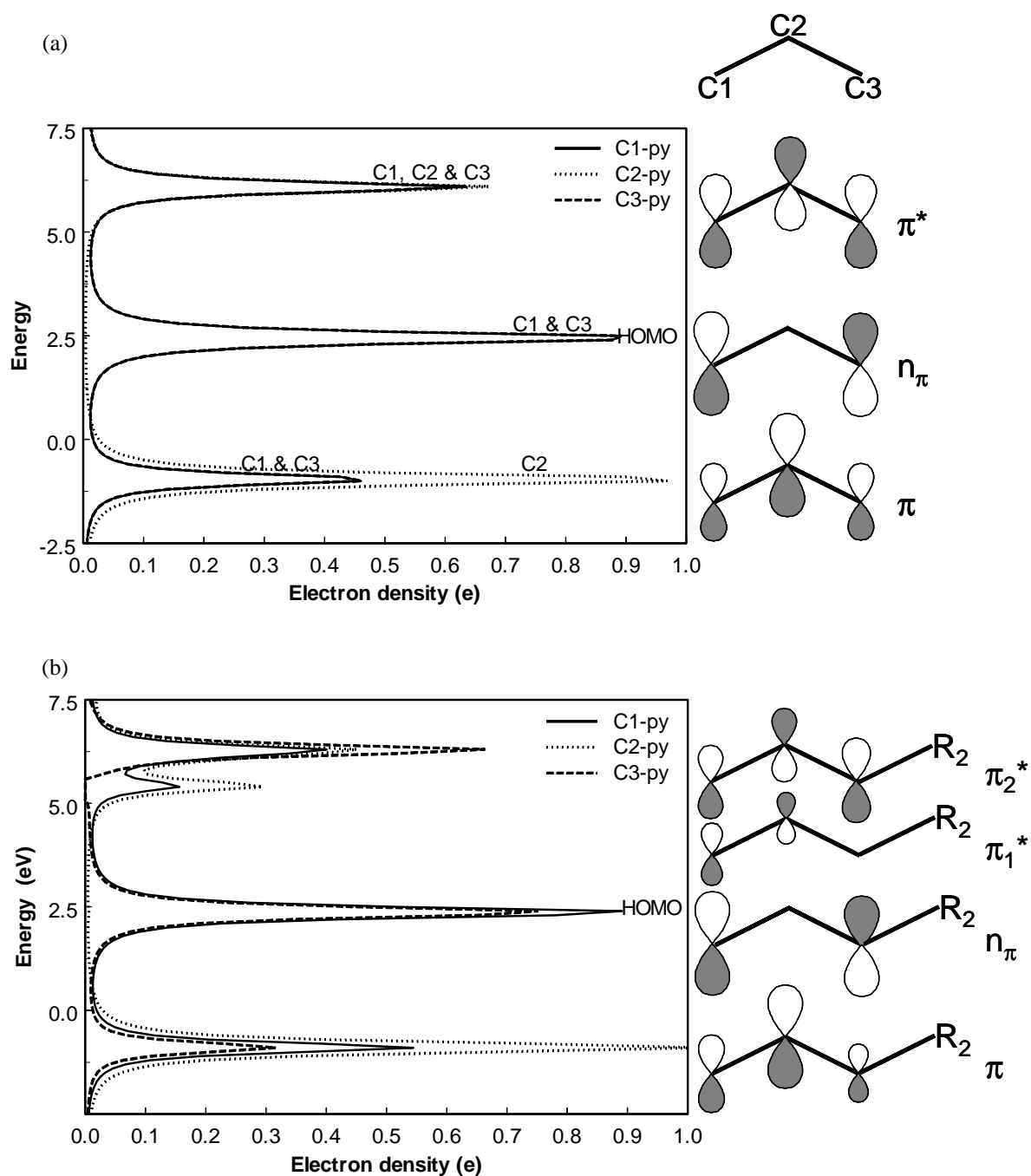
The assignment of either 2a' or 2a" as the LUMO has been discussed in the literature.[9] It was suggested that for π-acceptor ligands like phosphine, the Pd d orbitals (a") are destabilized due to back donation of charge from the metal to the ligand, thereby decreasing the splitting of the 1a" and 2a" orbitals. As a result the 2a" orbital will be the LUMO. This is exactly what we observe in our XAS data. The 2a" orbital is mainly Pd d in character whereas the 2a' consists of mainly Pd p DOS. The Pd d peak stemming form the 2a" orbital is always the lowest energy (first) peak for the complexes studied here and is the LUMO in these complexes. The Pd d peak is visible in the XANES, which reflects p DOS, because of some hybridization of the Pd $4d_{xz}$ with the Pd $5p_x$ orbital in these low symmetry complexes. Note that it was not observed in the square-planar reference samples as discussed above. Although the Pd d orbital energy is sensitive to changes in the bite angle as indicated in Figure 9, the 2a" (Pd $4d_{xz}$) orbital remains the first peak regardless of bite angle ($< 110°$ for the complexes studied). The presence of a Pd d peak for all the complexes studied indicates that the LUMO is indeed the $2b_1$ orbital throughout the $80°$ to $110°$ bite angle range, since the $3a_1/\delta_g*$ orbital cannot overlap with the non-bonding allylic orbital n_π due to its b_2 symmetry (Figure 9 and 11a). Thus the left part of the Walsh diagram shown in Figure 9 is valid for the [(PP)Pd(allyl)]$^+$ complexes discussed in this work. The LUMO/HOMO orbital switch is believed to occur at bite angles larger than $110°$.

The orbital interaction diagram in Figure 11a also explains the splitting of the Pd p peak in the negative 2nd derivative of the XAS data. Overlap of the empty (PP)Pd-$5p_z$ orbital with the allyl moiety $\pi*$ orbital, results in a bonding (2a') and anti-bonding (3a') molecular orbital combination. Additionally, the non-bonding Pd-$5p_y$ ($2b_2$) peak, na", is present in between 2a' and 3a'. The Pd K-edge XANES probes the lower energy 2a' and na" molecular orbitals. The 3a" molecular orbital is not detected since it is probably too high in energy and consequently severely broadened with the continuum orbitals.

The 1,1-dimethyl-substituted allyl [(PP)Pd(1,1-$(CH_3)_2$-C_3H_3)]$^+$ complexes possess a similar orbital interaction diagram as the un-substituted allyl (Figure 11a), but the symmetry of the allyl orbitals is different. The density of states of the (1,1-$(CH_3)_2$-C_3H_3) anion calculated with ADF is presented in Figure 10b. The shapes and sizes of the molecular orbitals indicate that the allylic orbitals of (1,1-$(CH_3)_2$-C_3H_3)$^-$ are slightly asymmetric, with the un-substituted carbon atom (C_1) more pronounced in the bonding π molecular orbital and the substituted carbon atom (C_3) more pronounced in the anti-bonding π_2* molecular orbital. An additional anti-bonding π_1* molecular orbital is formed, its size however is very small and its symmetry does not allow overlap with the [Pd(PP)]$^{2+}$ fragment. From modeling and single-crystal X-ray analysis studies, it is known that with increasing bite angle,

steric hindrance causes the allyl coordination to shift from an η_3-allyl to a more η_1-η_2-like coordination.[7a-b,12,24]

Figure 11. Orbital interaction diagram for (a) (η_3-allyl)Pd(P-P) and (b) (TCNE)Pd(PP) complexes.
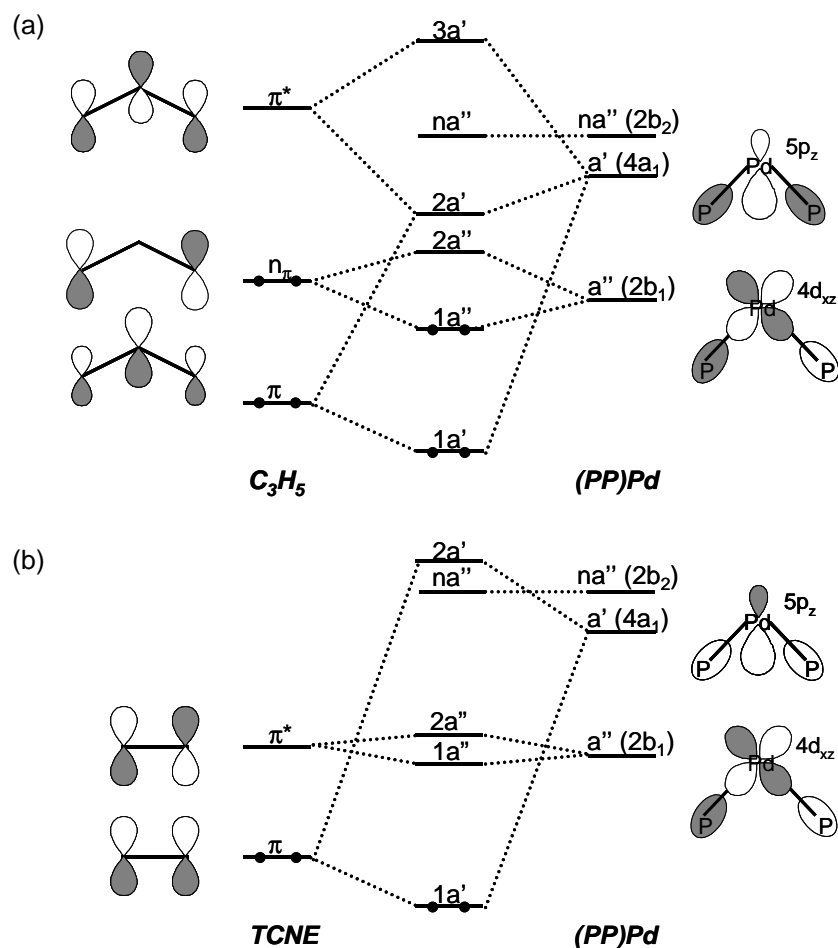
The coordination of the TCNE molecule to the [(PP)Pd]$^{2+}$ fragment is, like the allyl moieties, covalent in character. Due to the simpler alkene molecular orbital structure, pure π bonding and π^* anti-bonding overlap occurs with the Pd. The orbital interaction diagram simplifies to that shown in Figure 11b. The π orbital interacts with the Pd p orbital and the Pd d orbital interacts with the allyl π^* orbital. The Pd d bonding and anti-bonding molecular orbitals (1a" and 2a") are now probably both present in the feature appearing near the threshold in the XANES data, and may account for the broadening of this feature compared to the Pd d peaks in the other complexes. The broadening and splitting of the

Chapter 4

higher energy Pd p feature is slightly different compared to the allyl complexes; it now arises from the separation between the non-bonding (na") and anti-bonding (2a') orbital, the latter now lower in energy.

Changes in the XANES with Bite Angle

The negative 2nd derivatives of the XANES data (Figures 2b-5b) show multiple differences with varying the bite angle of the complexes. The reason for these changes are explained in terms of the orbital interaction diagrams discussed above.

We first consider the changes in the Pd p peak since these are more pronounced than those for the Pd d peak. Except for the (PP)PdCl$_2$ series, a splitting of the Pd p peak is observed with increasing bite angle. Moreover, the position of the Pd p peak shifts with both bite angle and as expected with oxidation state (Figure 8). To study these changes in more detail, three different plots are constructed as a function of the bite angle within the different series (Figures 12-14). The energy centroid of the Pd p peak is plotted in Figure 12 and the splitting of the Pd p peak defined as the energy difference between the two component features is plotted in Figure 13. The intensity of the Pd d peak versus bite angle is plotted in Figure 14. Each of these figures is discussed in separate sections below.

Figure 12. The position of the Pd p peak in the negative 2nd derivative of the XANES data, determined as the centroid of the total feature, as a function of bite angle for all series of bidentate diphosphine palladium complexes (PP)Pd(XX).
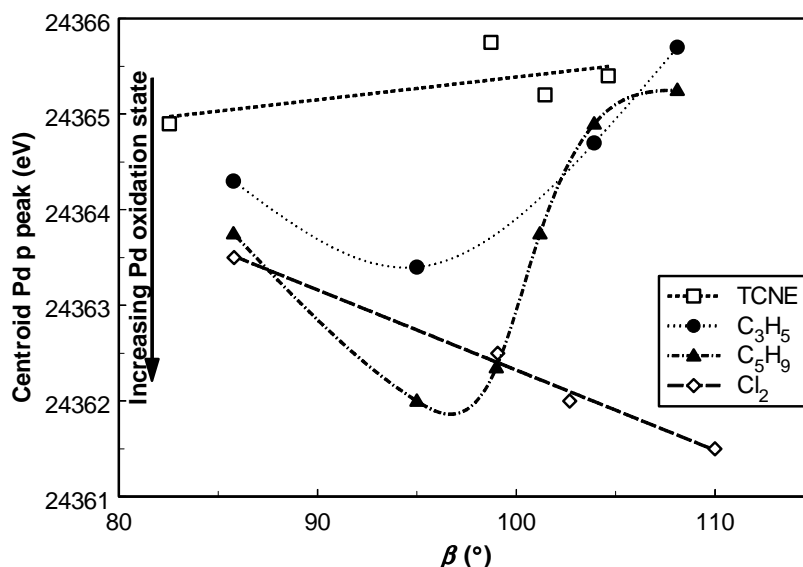
Pd p Centroid Energy: An Indicator of the Oxidation State of Pd

The Pd oxidation states, determined with XANES spectroscopy are clearly changing with coordinating moiety (XX) and bite angle ((PP) ligand). This measured Pd oxidation state will be further addressed as the effective Pd oxidation state. No quantification of the oxidation state will be done and only the trends are considered here.

Figure 8 showed that the energy of the Pd p peak decreases with increasing the formal oxidation state from 0 in Pd foil to 2+ in $PdCl_2$ and $PdBr_2$. Therefore, this shift can serve as an indicator of the Pd oxidation state. The position of the Pd p peak as a function of the bite angle is displayed in Figure 12 for the different (PP)Pd(XX) series. Linear correlations are found for the $(PP)PdCl_2$ and (PP)Pd(TCNE) series. The slopes of these correlations, however, differ significantly in size and sign. The (PP)Pd(TCNE) series shows a small decrease in effective oxidation state with increasing bite angle, whereas the $(PP)PdCl_2$ complexes show a larger increase in effective oxidation state with bite angle. The allyl series, both $[(PP)Pd(C_3H_5)]^+$ and $[(PP)Pd(1,1-(CH_3)_2-C_3H_3)]^+$ complexes, show a maximum in effective oxidation state and thus a minimum in energy position at intermediate bite angles. The effective oxidation state of the $[(PP)Pd(C_3H_5)]^+$ complexes is always lower than for the analogous $[(PP)Pd(1,1-(1,1-(CH_3)_2-C_3H_3)]^+$ complexes.

The change in effective Pd oxidation state of the $(PP)PdCl_2$ complexes with bite angle are dominated by a charge redistribution within the metal-ligand system, since the metal – Cl bond is mainly ionic and is thus not expected to be dependent on the bite angle. The (PP) ligand 3s overlaps with the Pd 5p orbital forming the $4a_1$ molecular orbital. This overlap decreases with increasing P-Pd-P bite angle, as shown schematically in Figure 15a. This results in a more ionic Pd – (PP) bond. As a consequence, the (PP) ligand cannot effectively donate electron density to the Pd center resulting in an increased oxidation state of the Pd atom with increasing bite angle. It has to be emphasized here that this reduced electron density donation of the PP ligands in the $4a_1$ (or a') molecular orbital with increasing bite angle occurs in all the (PP)Pd(XX) complex series regardless of the (XX) moiety.

The TCNE complexes also display a linear behavior of oxidation state with bite angle, with the opposite trend as the dichloride complexes. In contrast to the Pd – Cl bonds, the coordinating TCNE moiety is (mainly) covalently bonded to the Pd atom, i.e. the Pd p and Pd d orbitals are covalently overlapping with the coordinating TCNE orbitals to form the a'' and a' molecular orbitals. As shown in Figure 11b, only the 1a' molecular orbital is occupied and can donate electron density. Figure 15b illustrates how the Pd – (PP) ligand overlap decreases, while the Pd – TCNE overlap increases for complexes with wider bite angles. It is this change in the 1a' molecular orbital which results in donation of electron density from

the TCNE moiety to the Pd thereby decreasing the effective Pd oxidation level, i.e. charge back donation is dominating here. This increasing Pd – TCNE covalent interaction with increasing bite angle will be discussed later.

For the two series of allyl and 1,1-disubstituted allyl (PP)Pd complexes, a maximum in the effective Pd oxidation state is observed at a bite angle of around 95° to 100°. The variation in oxidation state is larger than that of the (PP)PdCl$_2$ or (PP)Pd(TCNE) complexes. This strongly suggests that additional charge redistribution involving the Pd d orbitals is occurring in these systems. Figure 15c illustrates why this occurs. The Walsh diagram in Figure 9 shows that the 2b$_1$ LUMO decreases sharply in energy as the bite angle increases above 90°. From Figure 15c it is clear that this originates from anti-bonding overlap with orbitals from the PP ligands, with a maximum at a bite angle ~90°. This change in anti-bonding character changes the energy of the Pd 4d$_{xz}$ orbital. Due to the shape of the Pd 4d$_{xz}$ orbital, the strongest Pd (PP) ligand anti-bonding overlap will occur at ~90°, where it has a maximum in energy. The energy shift of the Pd 4d$_{xz}$ orbital strongly alters the localization or interaction with the allyl n$_\pi$ orbital as illustrated. The 1a" molecular orbital is localized mainly on the allyl for the complex with a bite angle around 90° and shifts to the Pd as the bite angle decreases or increases from 90°. Thus the charge redistribution for the allylic complexes is dominated by the Pd d orbital, and the maximum Pd oxidation state occurs around 90°.

Although the Pd-allyl charge redistribution is dominated by the Pd d orbitals, charge rearrangement via the a' molecular orbital, involving the Pd p orbitals, is also occurring as was illustrated in Figure 15b. The energy of the Pd 5p$_z$ orbital increases with bite angle and this affects the localization of the 1a', 2a' and 3a' orbitals. At narrow bite angle the occupied 1a' molecular orbital is mainly allyl π in character, and with increasing bite angle the overlap with the Pd 5p$_z$ orbital increases. This facilitates charge redistribution from the coordination moiety to Pd with increasing bite angle. The increasing covalent interaction with bite angle is similar for both Pd 5p$_z$ with π and Pd 5p$_z$ with π*, and thus also influences the Pd p peak splitting (*vide infra*).

Although the formal Pd oxidation state for the [(PP)Pd(C$_3$H$_5$)]$^+$ and [(PP)Pd(1,1-(CH$_3$)$_2$-C$_3$H$_3$)]$^+$ complexes is the same, the effective oxidation state of Pd is always lower for the 1,1-di-substituted allyl complexes than for the corresponding un-substituted allyl complexes. As observed in Figure 9b, the DOS of the n$_\pi$ orbital on the C$_1$ and C$_3$, indicated by the size of the 2p orbital on each carbon atom, is identical in both fragments. This indicates that the charge redistribution via the Pd 4d$_{xz}$ orbital, which is overlapping with the n$_\pi$ orbital, is approximately the same for both series of complexes. For (1,1-(CH$_3$)$_2$-C$_3$H$_3$)$^-$, however, the π and π* molecular orbitals show a significant asymmetry between the un-

substituted C_1 and substituted C_3 carbon atoms: i.e., larger on the C_1 atom in the π orbital, larger on the C_3 atom in the π^* orbital. This asymmetry makes the electron density redistribution less effective because the Pd $5p_z$ orbital is oriented to maximize the covalent overlap with the π^* orbital. The π^* orbital is closer in energy and therefore the orbital mixing with the occupied π orbital, which is the only orbital through which the charge redistribution is possible, decreases. A net higher effective Pd oxidation state is found for the $[(PP)Pd(1,1-(CH_3)_2-C_3H_3)]^+$ complexes since the allyl π Pd $5p_z$ charge redistribution (via 1 a') is less effective in this case. At wider bite angles, the Pd oxidation states for the $[(PP)Pd(1,1-(CH_3)_2-C_3H_3)]^+$ complexes may also level off compared to the un-substituted allyl case due to the distortion of the $(1,1-(CH_3)_2-C_3H_3)^-$ moiety caused by steric hindrance. This is confirmed by the crystal structure showing an increase in Pd-C_{allyl} distances, and asymmetric bond lengths (Pd-C_1>Pd-C_3). [24]

The effects of the three different charge rearrangements as described above, are shown qualitatively in Figure 16. Depending on the type of overlap between the $[(PP)Pd]^{2+}$ fragment and the coordinating moiety, and the occupation of the molecular orbitals for the complete (PP)Pd(XX) complex, one, two or all three charge rearrangements can take place in the complex, as denoted in Table 3.

The change in effective Pd oxidation for the allylic (PP)Pd complexes is large, varying in magnitude from as small as that in the (PP)Pd(TCNE) complexes to as large as that in the (PP)PdCl$_2$ complexes. This shows the dramatic effect of the bite angle on the oxidation level in these complexes. It should thus not be surprising that this very large change in the oxidation state of the Pd can have enormous effects on the activity and selectivity of these Pd catalytic complexes.[4,7]
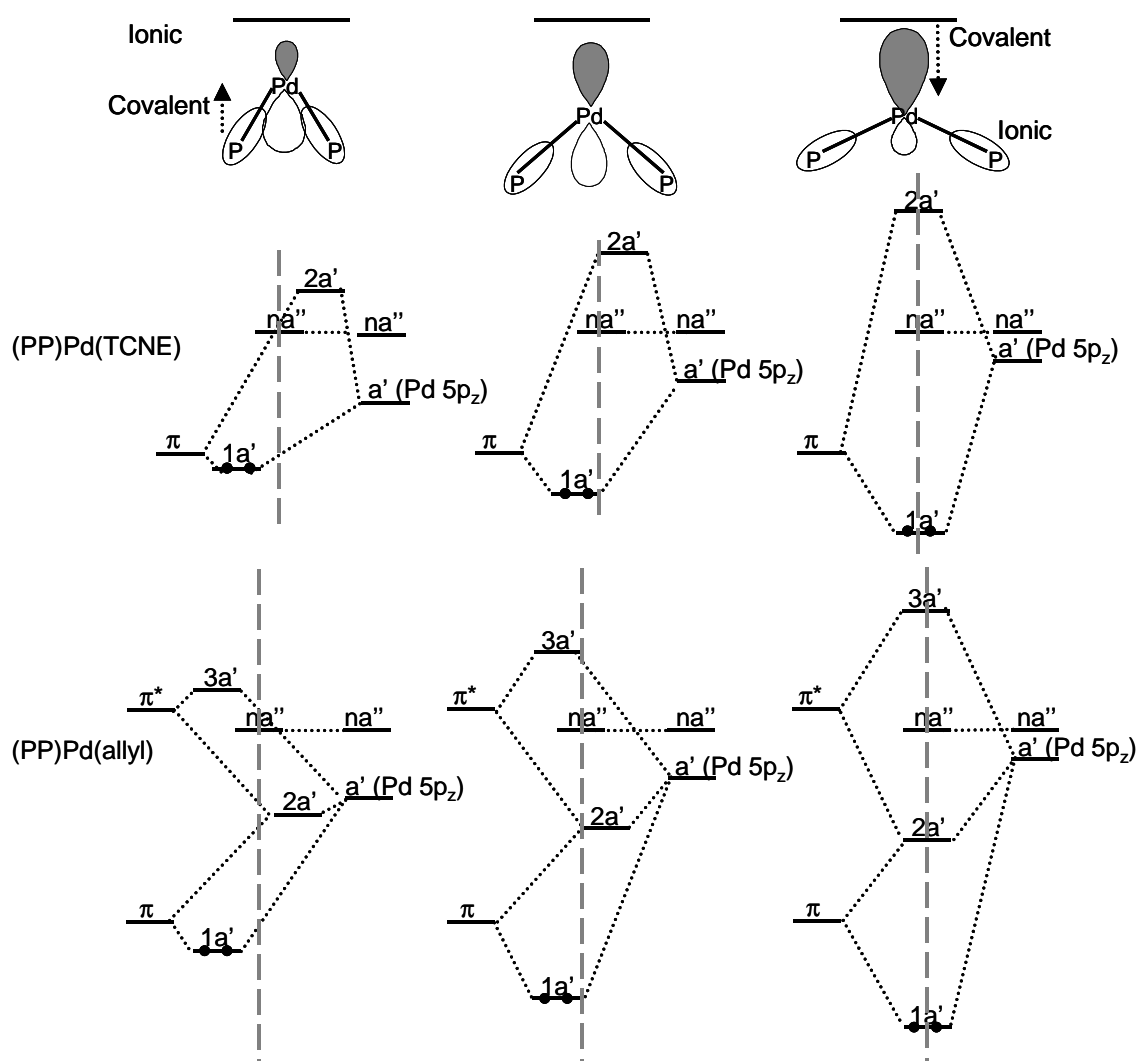
Figure 15. Orbitals in (PP)Pd(XX) complexes and charge redistribution with increasing bite angle. The placement of MO orbital lines, about vertical center lines (grey striped lines), reflect relative atomic charge distribution in MO, but the relative positions are exaggerated for clarity.

(a) Charge redistribution within (PP)Pd fragment.
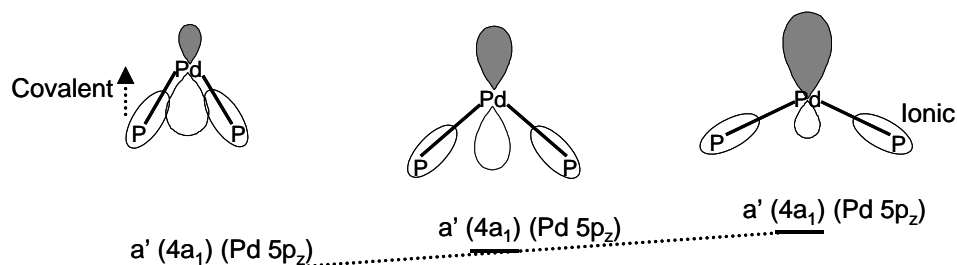
(b) Charge redistribution with coordinating moiety via Pd $5p_z$ orbitals for complexes with covalent bonded moieties for (PP)Pd(TCNE) and [(PP)Pd(allyl)]$^+$ complexes respectively.

(c) Charge redistribution with coordinating moiety via Pd $4d_{xz}$ orbitals for allyl complexes.
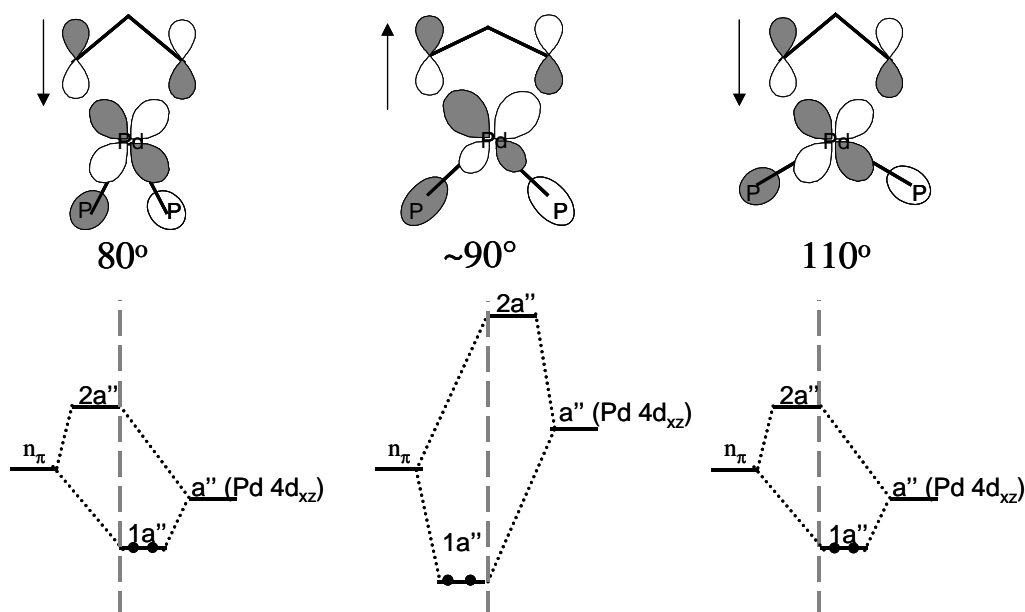
Table 3. The charge redistribution effects occurring within the different complexes.

	(PP)Pd(TCNE)	(PP)Pd(C$_3$H$_5$)	(PP)Pd(1,1-(CH$_3$)$_2$-C$_3$H$_3$)	(PP)PdCl$_2$
(PP)Pd	YES	YES	YES	YES
Pd 5p	YES	YES	YES	NO
Pd 4d	NO	YES	YES	NO

Figure 16. The qualitative effects of the three different charge distribution mechanisms on the effective Pd oxidation state as a function of bite angle.
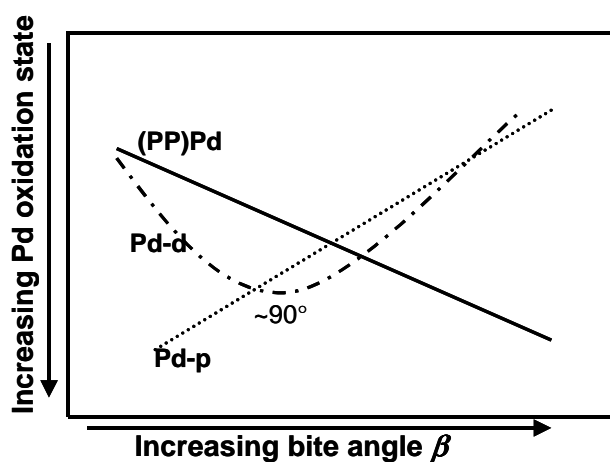
*Pd p Energy Splitting: An Indicator of the Pd p and Allyl Covalent Interaction*

For a large number of the (PP)Pd(XX) complexes, a splitting of the Pd p peak is observed. The magnitude of this splitting is plotted in Figure 13 as a function of the bite angle of the (PP) ligand. The (PP)PdCl₂ complexes display only one Pd p peak for the complete bite angle range, i.e. no splitting is observed for these complexes and thus no results for the (PP)PdCl₂ are displayed in Figure 13.

The presence of only one peak for the (PP)PdCl₂ complexes is expected based on the orbital interaction diagram (Figure 9), since the $4a_1$ and $2b_2$ molecular orbitals are sufficiently close in energy to appear as one Pd p peak. The $4a_1$ and $2b_2$ molecular orbitals are nearly degenerate when no bonding occurs with the coordinating moiety, which is visible by the small difference in the Walsh diagram in Figure 9. The presence of a splitting for the other complexes confirms that it originates from a covalent interaction of Pd with the allyl and TCNE moieties.
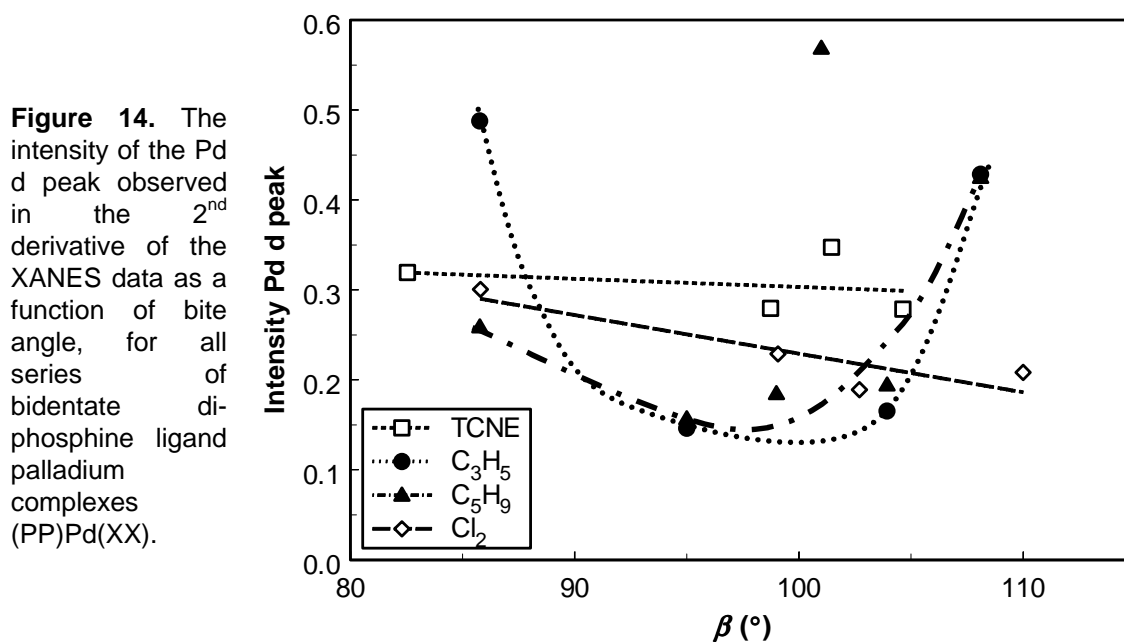
Figure 13. The splitting of the Pd p peak in the 2nd derivative of the XANES data as a function of bite angle, for series of bidentate diphosphine ligand palladium complexes (PP)Pd(XX).
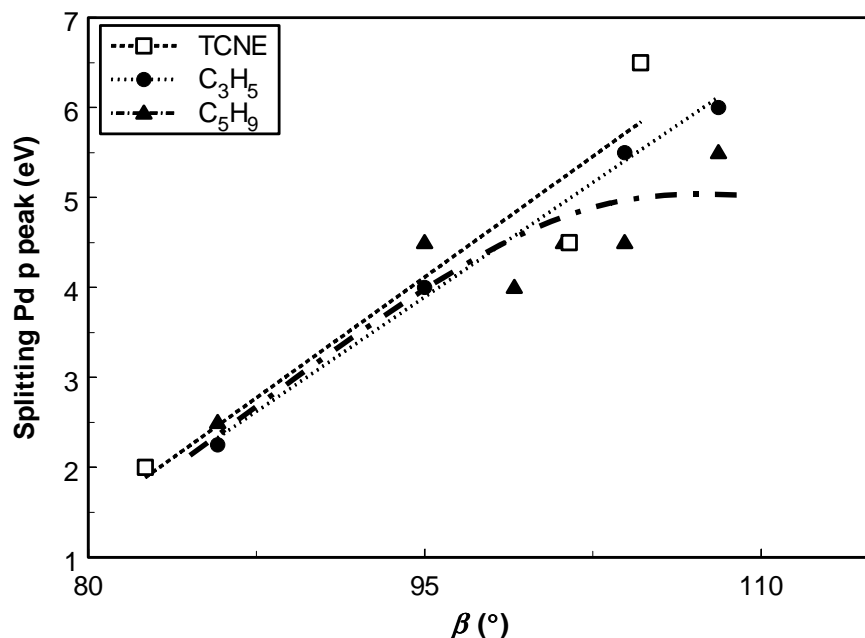
The allyl and TCNE bearing Pd complexes display an increased splitting with increasing bite angle, as shown in Figure 13. The splitting could be determined for only three of the (PP)Pd(TCNE) complexes. Due to the low signal to noise ratio of the (dppf)Pd(TCNE) data, a point for this sample could not be determined, thus the correlation of the linear fit with the points is rather low. A good linear correlation is found between the energy of the splitting and bite angle ($R^2 = 0.99$) for the $[(PP)Pd(C_3H_5)]^+$ complexes. In contrast, the $[(PP)Pd(1,1-(CH_3)_2-C_3H_3)]^+$ complexes show a linear correlation up to a bite angle of about 95° to 100° after which the curve levels off.

Somewhat surprisingly, the $[(PP)Pd(C_3H_5)]^+$ and $[(PP)Pd(1,1-(CH_3)_2-C_3H_3)]^+$ series display a similar Pd p peak splitting at low bite angles, even though the charge redistribution is less effective for the $(1,1-(CH_3)_2-C_3H_3)$ complexes. Apparently, the Pd p - π^* covalent interaction is similar for both moieties, regardless of the asymmetry in the $(1,1-(CH_3)_2-C_3H_3)$ complexes, as suggested above, and it is only the interaction with the π orbital that severely suffers in the $(1,1-(CH_3)_2-C_3H_3)$ case. At wider bite angles, however, the splitting for the $(1,1-(CH_3)_2-C_3H_3)$ complexes levels off, whereas the splitting for the un-substituted allyl (C_3H_5) complexes continues to increase. For large bite angle complexes, the covalent interaction with the $(1,1-(CH_3)_2-C_3H_3)^-$ is diminished due to steric hindrance. With increasing bite angle, the symmetry of the $(1,1-(CH_3)_2-C_3H_3)$ moiety transforms from a η_3 coordination, identical to C_3H_5, to a distorted n η_1-η_2 like coordination.[7a-b,12,24]

Figure 14. The intensity of the Pd d peak observed in the 2nd derivative of the XANES data as a function of bite angle, for all series of bidentate di-phosphine ligand palladium complexes (PP)Pd(XX).

The (PP)Pd(TCNE) series shows the largest covalent interaction consistent with the larger radial extent of the Pd d orbitals in a Pd complex with a formal oxidation state of zero. Its increased slope at larger bite angle is also consistent with this.

Pd d Intensity: An Indicator of Charge Redistribution Involving the Pd d Orbitals

The first peak in the negative 2nd derivative of the normalized XAS data, the Pd d peak, shows clear changes in intensity for the different complexes. The intensity of this peak, determined by taking the difference in magnitude between the maximum and (left) minimum of this first peak in the negative 2nd derivative, is plotted as a function of bite angle for all complexes (Figure 14). The trends with bite angle show at first glance a striking similarity with the bite angle trends shown in Figure 12 for the Pd p energy centroid. This similarity strongly suggests that the Pd d band intensity is somehow reflecting the Pd oxidation level, at least its change with bite angle. However, the Pd d band intensity is going in the opposite direction from what one initially might expect based on oxidation level, i.e. with increasing oxidation one would expect some of the charge removed from the Pd d levels (and this is even seen in the Figures 12 and 14 already discussed above). Thus its intensity is not tracking with the magnitude of the empty Pd d_{xz} DOS in the $2b_1$ molecular orbital but in the opposite direction.

The reason for this reverse correlation can be understood from Figure 15b and the knowledge that the intensity of the Pd d peak does not correlate with Pd d peak intensity in the $2b_1$ molecular orbital, but with the amount of mixing in of the Pd $5p_x$ orbital dictated by the dipole approximation for a 1s to p transition. The Pd $5p_x$ orbital cannot directly mix with the Pd $4d_{xz}$ orbital, because they have different symmetry. They appear together in the $2b_1$ molecular orbital because of a covalent mixing in of either ligand or moiety (XX) orbitals. We already noted in the Walsh diagram of Figure 9, that the (bite angle dependent) mixing of these two components in the $2b_1$ molecular orbital is due to hybridization with the ligand 3s orbital. However, for the small bite angle range of 25° investigated, the change in 3s mixing is expected to be small and in any event monotonic with bite angle, so such mixing involving the ligand cannot explain the observed minima in the Pd d intensity. However, the mixing in of the allylic n_π orbital enables Pd $5p_x$ to mix in as well. Thus, the intensity of the Pd d peak mainly correlates with the amount of n_π character in the 2a" molecular orbital, and this tracks in the reverse direction with the Pd d_{xz} orbital component as illustrated in Figure 15b. Therefore, the intensity of the Pd d peak in the XANES is a measure for the magnitude of the allyl to Pd $4d_{xz}$ orbital charge distribution.

The TCNE and dichloride moieties do not experience any charge redistribution involving the Pd $4d_{xz}$ orbital as indicated above. Even though the Pd $4d_{xz}$ orbitals mix with the TCNE π^* orbital, both the bonding and anti-bonding 1a" and 2a" molecular orbitals are empty, so the Pd d peak is unaffected by this mixing. Nevertheless the Pd d peak intensity still appears to reflect the Pd oxidation level; thus it must depend partly on the charge redistribution involving the Pd $5p_z$ orbital. Apparently the mixing of the Pd $5p_x$ and $4d_{xz}$ orbitals is sensitive to the radial extent of the $5p_x$ orbital; as the oxidation state increases, the contraction of the $5p_x$ orbital decreases this mixing. Thus through a smaller "second order" effect, the intensity of the Pd d peak also reflects the oxidation level brought about by charge redistribution facilitated by the Pd p orbitals. For the allylic complexes, the Pd $4d_{xz}$ orbital charge redistribution overrules this "second order" effect due to the Pd p orbital screening.

One remark has to be made here. As can be seen for the $(1,1-(CH_3)_2-C_3H_3)$ series in Figure 14, the $[(dppf)Pd(1,1-(CH_3)_2-C_3H_3)]^+$ complex ($\beta = 101°$) has a very high Pd d peak intensity, not consistent with the bite angle trend derived. It is believed that this results from the presence of the Fe atom in the (dppf) ligand. Although the distance of the Fe atom to the Pd atom is ~4 Å, its radial extent is sufficiently large that it overlaps with the Pd d orbitals and consequently increase the Pd d peak intensity.[25] This is validated with theoretical FEFF8 calculations below (*vide infra*).

Although the intensity of the Pd d peak appears to mirror the oxidation level with bite angle just like the energy of the Pd p peak does, a more detailed comparison of Figures 12 and 14 reveals significant differences. Further significant differences occur between the (C_3H_5) and $(1,1-(CH_3)_2-C_3H_3)$ allyl moieties. These differences include the following:

a)   Whereas Figure 12 shows the oxidation level to be larger for the $[(PP)Pd(1,1-(CH_3)_2-C_3H_3)]^+$ complexes, Figure 14 shows the Pd d intensity at the minima to be quite similar. This occurs because the Pd d charge redistribution via the n_π orbital within the Pd-ligand complex is similar in both cases, but the Pd p distribution is much smaller in the $(1,1-(CH_3)_2-C_3H_3)$ case because of the asymmetry in the π and π^* orbitals as discussed above.

b)   Whereas Figure 12 shows that the oxidation level reaches a maximum (energy a minimum), around a bite angle of 95° (C_3H_5) to 98° $(1,1-(CH_3)_2-C_3H_3)$, the minimum in Pd d peak intensity in Figure 14 occurs around 100° (C_3H_5) to 95° $(1,1-(CH_3)_2-C_3H_3)$. Apparently the Pd d orbital charge redistribution is maximal around 95-100°, and the Pd p orbital charge redistribution is maximal at larger bite angle. When the two effects are added together for the allyl complexes (Figure 12), the maximum oxidation state moves down from 100° to ~95°. This is confirmed by comparison of the shift in the minima of the two allyl moieties as observed in Figure 14. In the $(1,1-(CH_3)_2-C_3H_3)$ case, the Pd p orbital

charge redistribution is much less efficient and therefore the two minima, the effective Pd oxidation state and the Pd d peak intensity, occur at approximately the same angle.

c)   The difference in Pd d peak intensity between (PP)Pd(TCNE) and (PP)PdCl$_2$ complexes is small in Figure 14 compared to the much larger difference in Pd P peak position in Figure 12. The former small difference reflects the small "second order" effect of the Pd d orbital mixing on the Pd d peak intensity.

Validation with Theoretical Calculations

Pd K-edge XANES spectroscopy directly probes different unoccupied molecular orbitals in the Pd complexes. Density functional calculations do not approximate the unoccupied molecular orbitals, necessary to properly interpret the XANES data adequately. Therefore, theoretical FEFF8 calculations have been performed, which give an estimate of the absorption spectrum and the DOS for three different $[(PP)Pd(1,1\text{-}(CH_3)_2\text{-}C_3H_3)]^+$ complexes.

Figure 17. Negative 2nd derivative of theoretical XANES data for $[(dppe)Pd(C_5H_9)]^+$, $[(dppf)Pd(C_5H_9)]^+$ and $[(DPEphos)Pd(C_5H_9)]^+$ complexes, calculated using FEFF8.0.
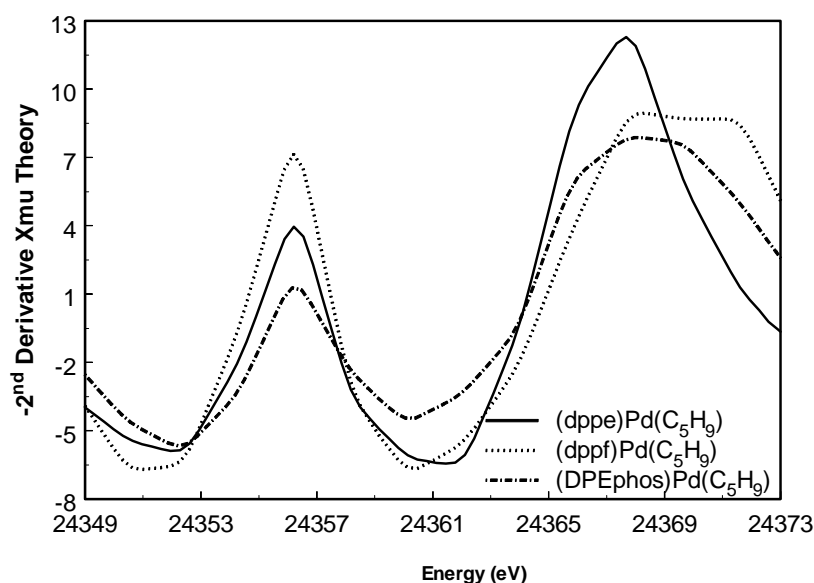
The absorption XANES data and the DOS are calculated for a relatively narrow bite angle complex $[(dppe)Pd(1,1\text{-}(CH_3)_2\text{-}C_3H_3)]^+$ (86°) and two complexes with wider bite angles $[(dppf)Pd(1,1\text{-}(CH_3)_2\text{-}C_3H_3)]^+$ (101°) and $[(DPEphos)Pd(1,1\text{-}(CH_3)_2\text{-}C_3H_3)]^+$ (104°). The negative second derivative is taken for these data as was done with the experimental data and these are shown in Figure 17. The shape of the theoretical negative 2nd derivatives is similar to the experimental data (Figure 4b). A large and small increase in the Pd d peak intensity is observed for the (dppf) ($\beta = 101°$) and the (DPEphos) complexes ($\beta = 104°$)

respectively in comparison to the (dppe) complex ($\beta = 86°$), similar to the experimental data (Figures 17 and 4b). The Pd p peak broadens with increasing bite angle with a simultaneous splitting pattern into two peaks as observed in the experiment data.

The Pd d, Pd p, P p and C_{allyl} p density of states (DOS) for the small bite angle complex [(dppe)Pd(1,1-$(CH_3)_2$-C_3H_3)]$^+$ are given in Figure 18. FEFF8 calculated a Fermi level (E_F), which is given as a solid line at –8.551 eV. Below this Fermi level, two occupied molecular orbitals are visible which are mainly Pd d and Pd p in character and are assigned as 1a'' and 1a', respectively. The energy positions of these two molecular orbitals are reversed to the order as was expected based on the orbital interaction diagram (Figure 11a). The empty DOS above this E_F line are probed with Pd K-edge XAS. The first peak in the negative second derivative of the XANES data was assigned as the Pd d peak. This is confirmed by the FEFF8 calculation, showing just above the HOMO, a sharp Pd d peak (orbital 2a'') with a Pd p mixing in allowing the Pd p peak to be monitored with Pd K-edge XAS. Additionally, a small shoulder of the C_{alllyl} p DOS lines up with this feature, confirming the Pd 4d n_π orbital interaction in this 2a'' MO (Figure 11a). At ~4eV the Pd p peak can be observed, i.e. a sharp maximum in the Pd p orbital. This peak (orbital 2a') is overlapping with the C_{allyl} p DOS as expected based on the orbital interaction diagram (Figure 11a). A third Pd p maximum is observed at ~6 eV, corresponding to the non-bonding na'' orbital. No alignment with P or C_{allyl} orbitals is observed in this region, consistent with the fact that no overlap with metal or ligand orbitals takes place for this non-bonding Pd p_y orbital.
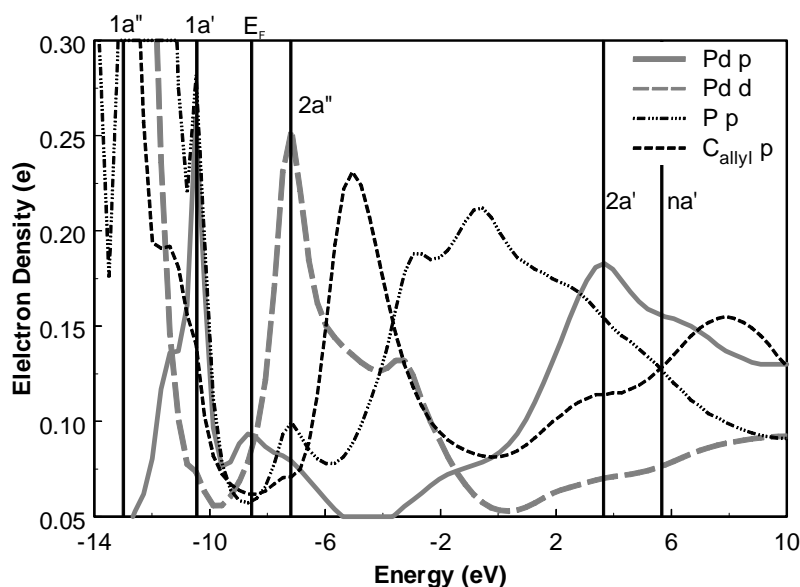

Figure 18. Density of states of the [(dppe)Pd(C_5H_9)]$^+$ complex ($\beta = 86°$), calculated using FEFF8.0. The vertical lines (solid black lines) indicate the position of the molecular orbitals.

The DOS for the $[(dppf)Pd(1,1-(CH_3)_2-C_3H_3)]^+$ complexes is shown in Figure 19. The calculated Fermi level is given at –8.788 eV. Again the order of the two occupied molecular orbitals 1a'' and 1a' are in contrast to the orbital interaction diagram (Figure 11a). The three XANES absorption peaks are predicted as indicated by the vertical lines. Just above the HOMO level, a Pd d peak with clear amount of Pd p DOS mixing in is evident. Moreover, an enormous Fe d DOS overlapping with the Pd d peak is observed (the electron density is going off scale for the Fe d DOS here). This confirms, as suggested above,[25] that the anomalous high Pd d peak intensity is caused by the presence of the Fe atom. Although the Fe atom is located at a distance of ~4 Å to the Pd absorber atom, the radial extend of the Fe d orbital is large enough to mix in with the Pd d. In the range of ~6 to 6 eV a relatively broad Pd p peak can be observed. This Pd p peak is lining up with the C_{allyl} p at ~3 eV confirming this as the 2a' molecular orbital. The maximum at ~5.5 eV is assigned to the na'' molecular orbital.

Figure 19. Density of states of the $[(dppf)Pd(C_5H_9)]^+$ complex ($\beta = 101°$), calculated using FEFF8.0. The vertical lines (solid black lines) indicate the position of the molecular orbitals.
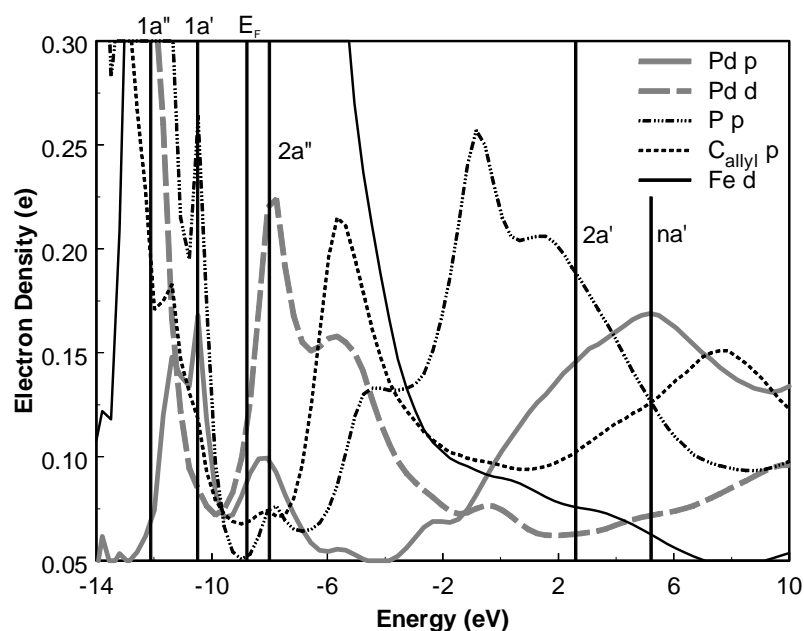
In Figure 20 the DOS of the $[(DPEphos)Pd(1,1-(CH_3)_2-C_3H_3)]^+$ is displayed. The Fermi level is calculated at -8.910 eV, which is exactly at the occupied 1a" molecular orbital. The occupied 1a' molecular orbital, which is mainly Pp p in character is now found at lower energy than he HOMO 1a", consistent with the orbital interaction diagram. The three absorption peaks are predicted. A large overlap from the Pd d peak with C_{allyl} p is indicated, as expected for these large bite angle complexes (Figure 15). From ~3 until ~ 7 eV a broad Pd p peak is indicated, which is at ~3.5 eV lining up with the C_{allyl} p indicating this is the 2a' orbital and at the maximum around ~6eV from the na" orbital.

In conclusion, although the experimental and modeled XAFS results are not identical, the general trends found for the $[(PP)Pd(allyl)]^+$ complexes are similar. The self consistent field muffin-tin approximation made in FEFF8 is known not to be fully adequate for charge-transfer complexes such as those studied here. Moreover, as FEFF8 is developed to calculate the unoccupied molecular orbitals, it may predict the bonding orbitals wrongly. It is therefore not surprising that FEFF8 does not predict all the different charge redistribution effects (including the occupied molecular orbitals 1a' and 1a" for these complexes) perfectly well. However, it should be emphasized that FEFF8 does predict the proper general trends and helps us interpret and assign the different molecular orbitals observed in the experimental data.

Figure 20. Density of states of the $[(DPEphos)Pd(C_5H_9)]^+$ complex ($\beta = 104°$), calculated using FEFF8.0. The vertical lines (solid black lines) indicate the position of the molecular orbitals.
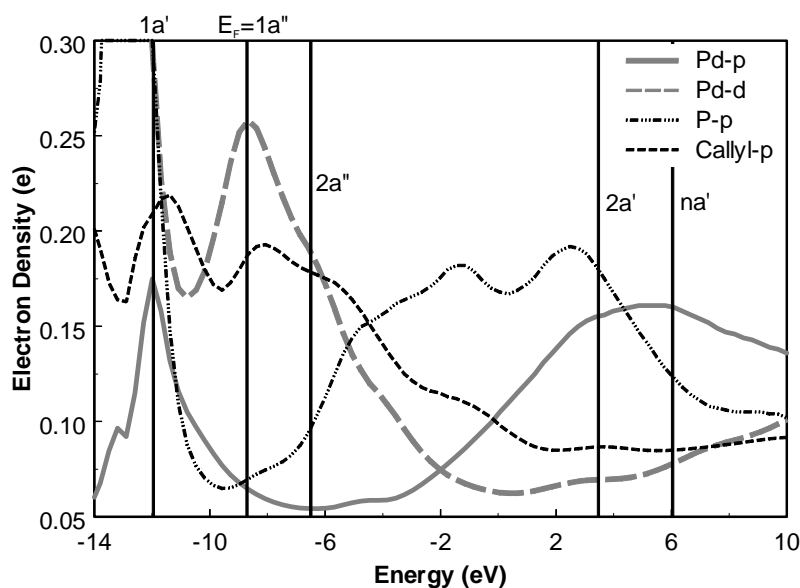
Summary and Conclusions

Pd K-edge XANES spectroscopy probes different molecular orbitals and consequently the charge distribution in a series of (PP)Pd(XX) complexes. The charge redistribution as reflected in the Pd oxidation level is indicated by both the intensity of the Pd d band and the energy of the Pd p band. Further, the increasing covalent interaction between the Pd and coordinated moieties via the Pd p orbitals is directly reflected in the energy splitting seen in the Pd p band.

Figure 15 gives an overview of the different charge distributions possible within (PP)Pd(XX) complexes as a function of the bite angle. The effects of the different charge redistribution mechanisms on the Pd oxidation state are qualitatively shown and summarized in Figure 16 and Table 2. Both the Pd d and Pd p orbitals facilitate the (PP) ligand to Pd and moiety (XX) to Pd charge redistribution, the magnitude strongly depending on the bite angle. Depending on the nature of the coordinating moiety, which determines the interaction with the $[Pd(PP)]^{2+}$ fragment (the latter determined by the bite angle), different amounts of charge redistribution can occur.

For coordinating moieties (XX) with a small covalent interaction within the $[Pd(PP)]^{2+}$ fragment, the charge distribution involves only the metal-ligand system. As shown in Figure 15a, at narrow bite angles, the Pd p and (PP) ligand covalent interaction is large, shifting charge to the Pd. As the bite angle increases this charge is donated back to the (PP) ligands, making it more ionic in character. Increasing the bite angle further decreases the Pd-(PP) covalent interaction, thereby increasing the effective Pd oxidation state (Figure 16).

For coordinating moieties with a more covalent interaction with the Pd(PP) fragment, the empty Pd $4d_{xz}$ and Pd $5p_z$ orbitals mix with the coordinating moiety and form molecular orbitals. Thus, charge distribution from the (XX) moiety to the Pd can also take place. Depending on the coordinating moiety (XX), the (XX) moiety to Pd charge redistribution can be facilitated by only the Pd p orbital, or by both the Pd p and Pd d orbitals.

In cases where only the molecular orbital consisting of Pd p is occupied (e.g., TCNE), both (PP) ligand to Pd and (XX) moiety to Pd p charge redistribution occur. As shown in Figures 15a, 15b and 16, the former dominates at narrow bite angle and the latter at wide bite angle. If both the Pd p and Pd d molecular orbitals are filled, the charge redistribution is almost completely dominated by the Pd d charge redistribution. The anti-bonding interaction between the Pd $4d_{xz}$ and ligand is largest near ~90°, causing the Pd d orbital to have an maximum in energy at this bite angle as shown in Figures 9 and 15c. The resulting overlap with the coordinating moiety causes the molecular orbital to be mainly located on

the allyl, whereas for bite angles narrower and wider than 90° the molecular orbital is mainly located on the Pd. The moiety (XX) to Pd charge redistribution facilitated by the Pd d produces a maximum in the Pd oxidation state around 90° (Figures 15c and 16).

The total charge rearrangement for $(1,1-(CH_3)_2-C_3H_3)$ moiety complexes is less than for (C_3H_5) because of asymmetry in the π orbitals. This asymmetry makes the moiety to Pd redistribution less efficient via the Pd p orbitals. Steric effects may inhibit the covalent interaction at very large bite angles in the $(1,1-(CH_3)_2-C_3H_3)$ case.

The allyl complexes, frequently used as catalysts in organic synthesis, show electron density movements from the allyl moiety to the $[(PP)Pd]^{2+}$ fragment with increasing bite angle above 90°. This electron density movement away from the allyl anion activates the allyl moieties for nucleophilic attack. Figures 12 and 14 suggest that the maximum charge on the allyl moieties is present in complexes with the largest bite angles; however, the optimal activity (and selectivity for the $(1,1-(CH_3)_2-C_3H_3)$ case) occurs at angles smaller than 110°. This strongly suggests that steric effects, which become larger at increasing bite angles,[12] result in less reactive complexes at large bite angles even though the negative charge on the allyl moiety is still decreasing (enhancing nucleophilic attack). Thus the optimal bite angle is determined both by electronic and steric effects consistent with previous suggestions in the literature.[7]

The XANES spectroscopy techniques described in this paper can be applied to investigate in principle the molecular orbitals of and charge distributions within every kind of sample. XANES spectroscopy directly probes molecular orbitals. Taking the negative second derivative of these XANES data provides direct information on the energy and charge distribution within the different molecular orbitals probed. The obtained data thus gives essential information about the electronic properties of the sample under investigation.

References

1. (a) L. Hegedus, *Transition Metals in the Synthesis of Organic Molecules*; University Science Books, 1994. (b) B. M. Trost, D. V. van Franken, *Chem. Rev.* **1996**, *96*, 395.

2. C. A. Tolman, *Chem. Rev.* **1977**, *77*, 31.

3. P. W. N. M. van Leeuwen, P. C. J. Kamer, J. N. H. Reek, P. Dierkes, *Chem. Rev.* **2000**, *100*, 2741.

4. P. Dierkes, P. W. N. M. van Leeuwen, *J. Chem. Soc., Dalton Trans.* **1999**, 1519.

5. C. P. Casey, G. T. Whiteker, *Isr. J. Chem.* **1990**, *30*, 299.

6. Z. Freixa, P. W. N. M. van Leeuwen, *Dalton Trans.* **2003**, 1890.

7. (a) R. J. van Haaren, K. Goubitz, J. Fraanje, G. P. F. van Strijdonck, H. Oevering, B. Coussens, J. N. H. Reek, P. C. J. Kamer, P. W. N. M. van Leeuwen, *Inorg. Chem.* **2001**, *40*, 3363; (b) R. J. van Haaren, H. Oevering, B. Coussens, G. P. F. van Strijdonck, J. N. H. Reek, P. C. J. Kamer, P. W. N. M. van Leeuwen, *Eur. J. Inorg. Chem.* **1999**, 1237; (c) M. P. T. Sjorgen, S. Hansson, B. Åkermark, A. Vitagliano, *Organometallics* **1994**, *13*, 1963; (d) R. J. van Haaren, C. J. M. Druijven, G. P. F. van Strijdonck, H. Oevering, J. N. H. Reek, P. J. C. Kamer, P. W. N. M. van Leeuwen, *J. Chem. Soc. Dalton Trans.* **2000**, *10*, 1549.

8. M. Tromp, J. A. van Bokhoven, R. J. van Haaren, G. P. F. van Strijdonck, A. M. J. van der Eerden, P. W. N. M. van Leeuwen, D. C. Koningsberger, *J. Am. Chem. Soc.* **2002**, *124*(50), 14814.

9. e.g. (a) K. J. Szabó, *Organometallics* **1996**, *15*, 1128, and references therein. (b) A. Aranyos, K. J. Szabó, A. M. Castaño, J.-E. Bäckvall, *Organometallics* **1997**, *16*, 1058. (c) F. Delbecq, C. Lapouge, C., *Organometallics* **2000**, *19*, 2716.

10. D. C. Koningsberger, B. L. Mojet, G. E. van Dorssen, D. E. Ramaker, *Topics Catal.* **2000**, *10*, 143-155.

11. e.g. *Cu XANES*: (a) S. DeBeer, D. W. Randall, A. M. Nersissian, J. Selverstone Valentine, B. Hedman, K. O. Hodgson, E. I. Solomon, *J. Phys. Chem. B* **2000**, *104*(46), 10814. (b) J. L. DuBois, P. Mukherjee, T. D. P. Stack, B. Hedmann, E. I. Solomon, K. O. Hodgson, *J. Am. Chem. Soc.* **2000**, *122*, 5775. (c) L.-S. Kau, J. Spira-Solomon, J. E. Penner-Hahn, K. O. Hodgson, E. I. Solomon, *J. Am. Chem. Soc.* **1987**, *109*, 6433. *V XANES*: (d) P. Frank, K. O. Hodgson, *Inorg. Chem.* **2000**, *39*, 6018. (e) J. Wong, F. W. Lytle, R. P. Messmer, D. H. Maylotte, *Phys. Rev. B.* **1984**, *3*, 5596. *Fe XANES* (f) W. E. Westre, P. Kennepohl, J. G. DeWitt, B. Hedman, K. O. Hodgson, E. I. Solomon, *J. Am. Chem. Soc.* **1997**, *119*, 6297.

12. R. J. van Haaren, thesis **2002**.

13. M. Kranenburg, J. G. P. Delis, P. C. J. Kamer, P. W. N. M. van Leeuwen, K. Vrieze, N. Veldman, A. L. Spek, K. Goubitz, J. Fraanje, *J. Chem. Soc., Dalton Trans.* **1997**, 1839.

14. T. Hayashi, M. Konishi, Y. Kobori, M. Kumada, T. Higuchi, K. Hirotsu, *J. Am. Chem. Soc.* **1984**, *106*, 158.

15.   W. D. Dent, R. Long, A. J. Wilkinson, *J. Am. Chem. Soc.* **1964**, 1585.

16.   (a) P. E. Blöchl, A. Togni, *Organometallics*, **1996**, *15*, 4125-4132, and references therein. (b) R. Pretot, A. Pfaltz, *Angew. Chem. Int. Ed.* **1998**, *37*, 323. (c) S. Vyskocil, M. Smrcina, V. Hanus, M. Polasek, P. Kocovsky, *J. Org. Chem.* **1998**, *63*, 7738.

17.   W. L. Steffen, G. Palenik, *J. Inorg. Chem.* **1976**, *15*, 2432.

18.   M. Kranenburg, P. C. J. Kamer, P. W. N. M. van Leeuwen, *Eur. J. Inorg. Chem.* **1998**, 155.

19.   Amsterdam Density Functional Package ADF 2000.02, Department of Theoretical Chemistry, Vrije Universiteit, Amsterdam. http://www.scm.com.

20.   A. L. Ankudinov, B. Ravel, J. J. Rehr, S. D. Conradson, *Phys. Rev. B.* **1998**, *58*, 7565.

21.   *'Handbook of X-ray Photoelectron Spectroscopy'*, J. F. Moulder, W. F. Stickle, P. E. Sobol, K. D. Bomben, Eds., Physical Electronics, Inc. **1995**.

22.   T. Yoshida, K. Tatsumi, S. Otsuka, *Pure & Appl. Chem.* **1980**, *52*, 713.

23.   S. Otsuka, *J. Organomet. Chem.* **1980**, *200*, 191.

24.   (a) B. Åkermark, K. Zetterberg, S. Hansson, B. Krakenberger, A. Vitagliano, *J. Organomet. Chem.* **1987**, *335*, 133.

25.   M. A. Zuideveld, B. H. G. Swennenhuis, M. D. K. Boele, Y. Guari, G. P. F. van Strijdonck, J. N. H. Reek, P. C. J. Kamer, K. Goubitz, J. Fraanje, M. Lutz, A. L. Spek, P. W. N. M. van Leeuwen, *J. Chem. Soc., Dalton Trans.* **2002**, 2308.

Chapter 5

Atomic XAFS as a Probe of Charge Redistribution within Organometallic Complexes

Abstract

The Atomic XAFS contributions in the Pt $L_{2,3}$ X-ray absorption fine structure spectra (XAFS) of [PtCl(NCN)-Z] pincer complexes are shown to be a sensitive probe of changes in the electron density on the Pt atom induced by changes in a *para*-substituent on the neighboring benzene ring. Such electron density information is similar yet complementary to NMR data. These complexes provide a unique system for examining inductive effects on the AXAFS data, since the geometry around the Pt atom remains unchanged. The results presented here validate the AXAFS technique and the AXAFS theoretical interpretation in particular. The isolation of the AXAFS data from the oscillatory part of the XAFS spectrum is extensively described. The different effects on the AXAFS shape and intensity are shown and discussed in detail.

Introduction

Transition metal complexes with NCN-pincer ligands (NCN = [2,6-(Me$_2$NCH$_2$)$_2$C$_6$H$_3$]$^-$) have been prepared for numerous applications in the fields of catalysis, catalyst immobilization, supramolecular assembly, and sensor materials.[1] The introduction of substituents at the *para*-position of the pincer ligand benzene ring allows one to tune the metal center electronically. This functionalization has been most successful with pincer complexes from the nickel triad (Ni, Pd, Pt), due to their exceptional stability. The electronic tuning of pincer complexes has shown to be a very powerful tool for tuning the reactivity of the catalytically active pincers, e.g. NCN-pincer nickel complexes used for the Karasch addition. Para-substituents which donate electrons decrease the oxidation potential of the Ni(II)/Ni(III) couple, resulting in more active atom transfer catalysts.[2]

Recently we have been able to synthesize a library of *para*-substituted NCN-pincer platinum complexes [PtCl(NCN-Z)] (Scheme 1) to study the influence of the substituent on the electronic properties of the metal centre.[3] It would be very useful to be able to determine the electron density of the pincers directly. In the case of [PtCl(NCN-Z)] pincer complexes, this has been shown to be possible using ^{195}Pt NMR.[3b] However, NMR can only be applied to a limited amount of atoms and thus other techniques need to be explored. Recently, we have developed a new technique, which directly provides information about the electronic structure of the metal under investigation, so-called Atomic X-ray Absorption Fine Structure Spectroscopy (AXAFS). So far, AXAFS has been demonstrated for mainly electrochemical systems and heterogeneous catalysts[4,5] in which both geometric and electronic effects simultaneously influence the AXAFS signal. This complicates the analysis and interpretation.

In this study the above described [PtCl(NCN-Z)] pincer complexes are used as model complexes to validate the AXAFS technique and to verify the AXAFS theoretical interpretation. The electronic properties of the Pt pincer complexes can be tuned selectively via the *para*-substituent. The geometry of the coordination environment of the platinum nucleus stays nearly unchanged upon *para*-substitution; consequently, changes in the electron density of the Pt pincer complexes arising from factors other than the *para*-substitution can be neglected. This makes the Pt pincer system perfect for extensively demonstrating and proving the AXAFS theory. Moreover, the strength of the AXAFS technique for the direct electron density determination is shown.

Experimental

Synthesis [PtCl(NCN-Z)] pincers

The [PtCl(NCN-Z)] pincers were synthesized as described in the literature with a series of different *para*-substituents, i.e. from substituents with electron withdrawing (Z = COOH) to electron donating properties (Z = NH_2) and a neutral substituent H.[3]

Pt L_2 and L_3 edge XAFS

Pt L_2- and L_3-edge (respectively 11564 and 13272 eV) EXAFS spectra were measured at the Hamburger Synchrotronstrahlungslabor (Hasylab), Germany, on Beamline X1, using a Si(311) double crystal monochromator. The monochromator was detuned to 50% intensity to avoid effects of higher harmonics. The measurements were done in the transmission mode using optimized ion chambers as detectors. To decrease noise, three scans were collected for each sample and averaged.

Both Pt L_2 and L_3 edge XAFS data were collected on the solid samples at liquid nitrogen temperature. Solid material and a known amount of boron nitride were thoroughly mixed and pressed into a self-supporting wafer (calculated to have a maximum total absorbance of 2.5 with a preferable step-size of 1) and placed in an air- and water-tight EXAFS cell provided with X-ray transparent beryllium windows.[6]

Theory and Background Subtraction

AXAFS

X-ray absorption fine structure (XAFS) spectroscopy is a technique based on the photoelectric effect. After absorption of an X-ray photon, a core electron is ejected to the continuum. This photoelectron can be described by a spherical wave, which travels outward and interacts with its surroundings. For extended XAFS (EXAFS) the outgoing electron scatters against the potential (electron clouds) of neighboring atoms (Figure 1), creating a backscattered wave that interferes with the outgoing photoelectron wave. The resultant EXAFS data give information about the geometry around the absorber atom.

The total X-ray absorption $\mu(k)$ is normally defined as $\mu(k) = \mu_0(k)(1+\chi_{EX})$, with χ_{EX} the EXAFS function and $\mu_0(k)$ the atomic X-ray absorption coefficient, or atomic background. Conventionally, this atomic background was assumed to be smooth and non-oscillatory. However, several authors[7,8,9] have shown in the past few years that this does not have to be true since the atomic X-ray absorption coefficient can have structure due to scattering of the photoelectron against the potential determined by the electron cloud of the atom from which the photoelectron is excited. Therefore this structure is called atomic XAFS (AXAFS). The atomic absorption coefficient can thus be written as $\mu_0(k) = \mu_{FREE}(1+\chi_{AX})$, with χ_{AX} the AXAFS fine structure and μ_{FREE} the free atomic background.[7,10]

Figure 1. Physical origin of EXAFS and AXAFS in a schematic potential model, with A = Absorber, B = Scatterer, E_v = vacuum level, R = distance.
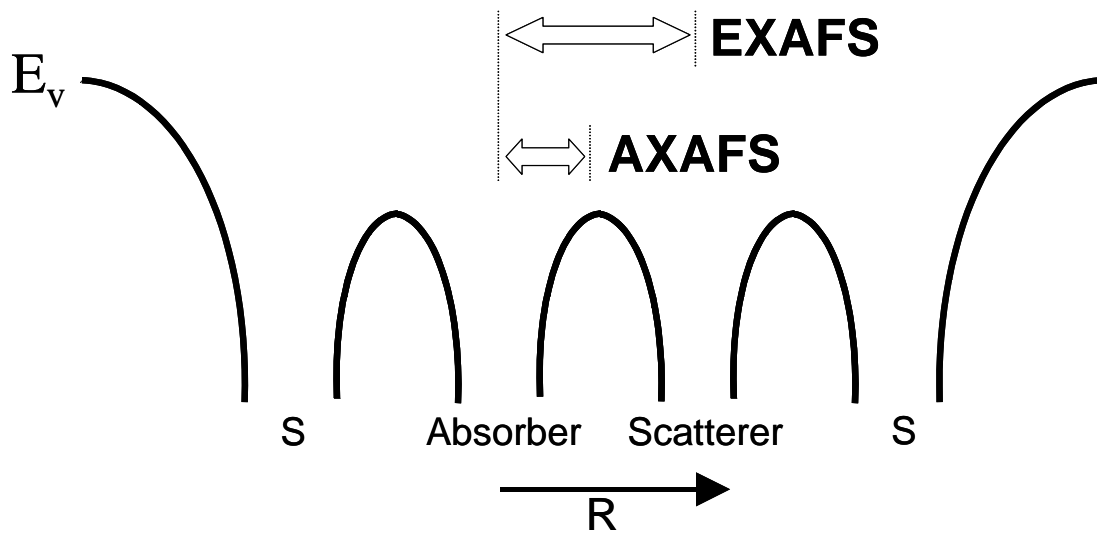
AXAFS represents the change in scattering by the embedded absorber atom relative to the free absorber atom (Figure 1). This change is due to bonding of the absorbing atom with its environment and thus gives information about the electronic structure of the absorber atom. Consequently, any change in the environment altering the electronic structure of the absorbing atom, should be reflected in the AXAFS.

In Figure 2, AXAFS is schematically described using the well-known muffin-tin approximation,[9,11] which is a good method to approximate the embedded atom potential. The interstitial potential V_{int} determines the zero energy of the system.[10] The free atom potential U_{free} reflects the electron distribution in the free atom, whereas the embedded potential U_{emb} reflects the electron distribution after embedding the free atom into its chemical environment and allowing interaction with neighbors (note potentials which are functions of R are denoted with U, constants with V). The AXAFS is best reflected in the Fourier Transform (FT) of the χ_{AX} producing the first peak at approximately ½ the first shell bond length. The FT of AXAFS is then shown to be directly proportional to $U_{emb}(R)$-$U_{free}(R)$ and therefore its shape and intensity directly reflect electronic and chemical bonding information.[10]

Scheme 1. *Para*-substituted NCN-pincer platinum complexes, Z creates an inductive effect on (a) benzene ring (b) Pt atom.
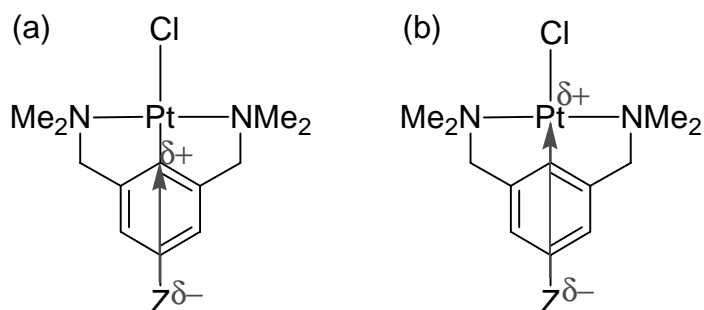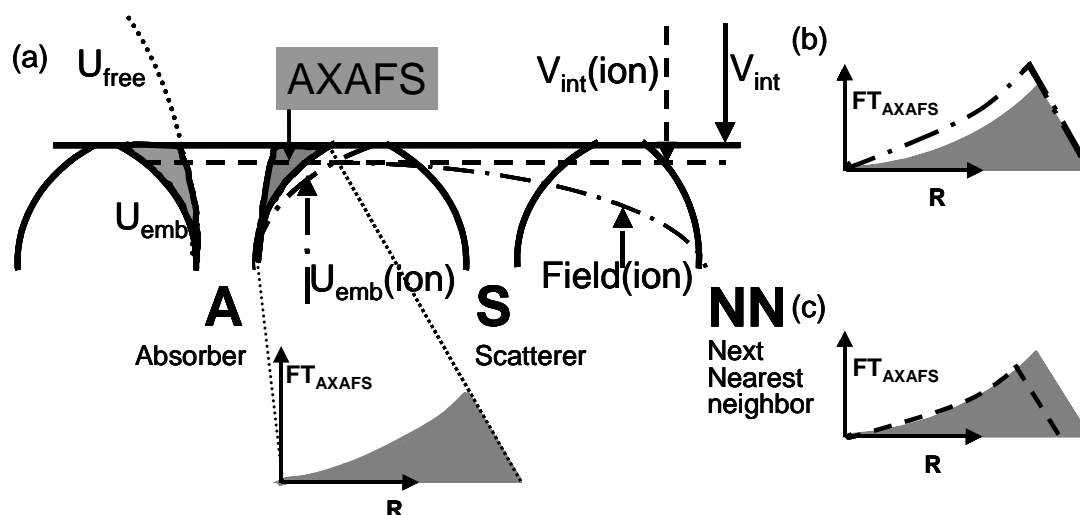
Figure 2. Schematic physical potential model, based on the Muffin Tin Approximation, defining AXAFS as the dark grey area (a) Changing AXAFS intensity and shape (striped and stripe-dotted lines) due to exclusively (b) Coulomb field effect (stripe-dotted lines) or (c) bond inductive effect (striped lines) from change in the NN (i.e., in this work change in para substituent).

Two effects distinguished with AXAFS

Due to polarization of the absorbing atom by its neighbors, two important effects on the electronic properties can be distinguished with AXAFS: (a) the Coulomb field effect, i.e. the effect induced by a Coulomb field, correlated to different charges on neighboring substituents (thereby altering the "roll over" of the interatomic potential, stripe-dotted lines in Figure 2a and 2b) and (b) the bond inductive effect, induced by a difference in electronegativity of the substituent (thereby altering the value of V_{int}, striped lines in Figure 2a and 2c). For an isolated Coulomb field effect as shown in Figure 2a (stripe-dotted lines), the AXAFS intensity increases and a simultaneous shift to lower radius is observed (Figure 2b). For the isolated bond inductive effect as shown in Figure 2a (striped), the intensity goes down with a simultaneous shift to lower distance (Figure 2c). Moreover, the difference in AXAFS shape change illustrated is typical for the two different effects ('lower R part' increased by field effect vs. 'higher R part' decreased by inductive effect).

From a more chemical viewpoint, and specifically applied to the Pt-pincers described in this study, the two effects can be described as follows. The placement of a more electronegative element Z (Scheme 1) creates an inductive effect on the benzene ring. In Scheme 1a the inductive effect stops at the benzene ring, leaving positive charges at the carbon atoms near Pt. This creates a Coulomb field change on the Pt, which shifts the valence orbitals to higher binding energy, thereby increasing the AXAFS (Figure 2b). In

contrast, if the inductive effect proceeds all the way to the Pt (Scheme 1b), the reduced electron density near the Fermi level or HOMO decreases the AXAFS (Figure 2c). Therefore, the relative change in the AXAFS directly reflects the response of the absorber atom to the placement of that substituent in the molecule.

Resonance effects can also play a role in these [PtCl(NCN-Z)] pincer complexes, especially for complexes with substituents with a lone pair of electrons. AXAFS however will not be able to distinguish between inductive and resonance effects since both result in a similar electron density change on the Pt atom. Moreover, the resonance effects in the Pt complexes described in this study are not expected to play a big role, since the Pt-C and Pt-Cl distances are the same for all complexes (*vide infra*). Here, we will thus only distinguish between Coulomb and inductive effects.

Background subtraction

Isolation of the AXAFS contribution from the XAS data requires a very careful background subtraction procedure. First the pre-edge background, which is approximated by a modified Victoreen curve,[12] is subtracted after which the edge position is chosen.[13] The post-edge background is approximated by a normal cubic-spline function.[13,14] The background subtraction procedure is extensively described in the literature.[9] Detailed criteria are given how to optimize both the AXAFS χ_{AX} and EXAFS χ_{EX} contributions in the resulting XAFS data, and how to separate double electron excitations (DEE) and the Ramsauer - Townsend resonances (RTR) that are present in the free atom contribution from the oscillatory part of the spectrum. In order to perform a careful DEE/AXAFS/EXAFS separation, it is important to have the ability to use a continuous adjustable smooth parameter. The importance of this capability will be shown in this study.

The criteria for background removal were defined previously as follows:[9,10]

a) In the FT diminish the contribution at R < 0.5 Å, i.e. the DEE and RTR, as much as possible. Check whether the DEE and RTR fully remain in the background by examining the background.

b) Make sure the EXAFS intensity is unchanged (unreduced).

c) Check both k^1- and k^3-weigthed spectra, for different k-ranges, including low k-values.

These criteria can be applied generally. However, they were constructed for XAFS data of samples in which the AXAFS and the EXAFS peaks in the Fourier transform of the XAFS data have less or no overlap. For these cases, applying the criteria is easy and straightforward. For the [PtCl(NCN-Z)] pincer complexes studied in this paper, we will see

that the criteria are much more difficult to apply due to tailing of the EXAFS first shell contribution down to 0 Å and consequently severely overlapping with the AXAFS (*vide infra*).

EXAFS data analysis

For the EXAFS data-analysis the commercially available program XDAP[15] was used. Theoretical data for phase shifts and backscattering amplitudes were generated using the FEFF8 code.[16] EXAFS data from reference compounds were used to calibrate the theoretical references: H_2PtCl_6 for Pt-Cl, and $Rb_2Pt(CN)_4(1.5\ H_2O)$ for both Pt-C and Pt-N since C and N are neighboring atoms in the periodic table. The theoretical references were optimized as described by Koningsberger *et al*[17]. Table 1a gives the FEFF8 input parameters. V_i is estimated to be 3 eV. S_0^2, the Debye-Waller factor and V_r were varied until the generated references produce an optimal fit in *R*-space of the first coordination shell of the Fourier transform of the experimental EXAFS spectra of the above mentioned reference compounds (see Table 1b).

These calibrated references could be used to fit the EXAFS data of the pincer samples down to very low values of k ($k \geq 2.5$ Å^{-1}). During *R*-space fitting of the EXAFS data, the difference file technique was used to judge whether for all applied k-weightings a good analysis for all contributions was obtained.[18]

Table 1a. FEFF8 input parameters used for the calculations of phase shifts and backscattering amplitudes.

Atom Pair	σ^2 [Å^2]	S_0^2	V_r [eV]	V_i [eV]	Potential
Pt-Cl	0.0023	0.67	5.5	3.0	Dirac-Hara
Pt-C/N	0.0020	0.93	10.4	3.0	Hedin-Lundquist

Table 1b. Best fit results for the experimental data using the theoretical references, including fitting parameters. Fits were performed in *R*-space, k^3-weighted.

Shell	N	R [Å]	$\Delta\sigma^2$ [Å^2]	E_0 [eV]	Δk [Å^{-1}]	ΔR [Å]
Pt-Cl	6.1	2.31	0.00001	-0.06	3.6-14.0	1.6-2.3
Pt-C/N	3.9	1.98	0.00001	0.02	2.5-12.9	1.0-2.0

FEFF8 calculations[16]

The FEFF8 code[16] was used to perform ab-initio self-consistent field, real-space, full multiple scattering calculations.[19] FEFF8 implements self-consistent field potentials for the determination of the Fermi-level and the charge transfer. The calculations were performed using the Hedin-Lundquist exchange correlation potential. A core-hole is included on the absorber atom in order to mimic the final state of the photon absorption process. The full crystal structures are used as input for the FEFF8 calculations. The self-consistent field (SCF) radius was chosen slightly longer than the longest Pt - neighbor distance in the complex (i.e. R_{SCF} = 6.7 Å for the [PtCl(NCN-NH$_2$)] pincer complex, R_{SCF} = 5.9 Å for the [PtCl(NCN-H)] pincer complex, R_{SCF} = 7.9 Å for the [PtCl(NCN-COOH)] pincer complex). The experimental broadening V_i was chosen at 3 eV, similar to that used for the calibrated references. S_0^2 was chosen at 1.0 for all complexes.

X-ray absorption near edge spectra (XANES) are simulated using a full multiple scattering (FMS) with R_{FMS} = R_{SCF}. The FMS was not used for the EXAFS/AXAFS calculations since implementation of this card results in large inaccuracies in the calculated EXAFS data at high energy.

Results

XANES

The normalized raw XAFS Pt L_2- and Pt L_3-edge data obtained for the series of [PtCl(NCN-Z)] complexes are shown in Figure 3. Changes in the edge position and features in the XANES region are barely visible. Very small double peaks are present just above the whiteline in both the Pt L_2- and L_3-edge data.

Figure 3. Normalized experimental XAS data of [PtCl(NCN-Z)] pincers (a) Pt L_2-edge, (b) Pt L_3-edge.
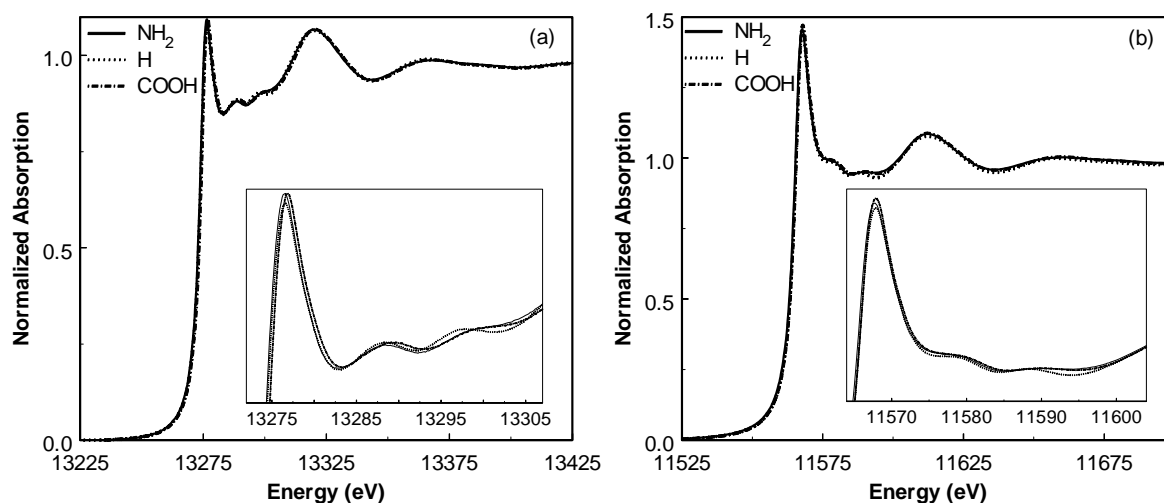
Background subtraction

A careful background subtraction is performed, optimizing the AXAFS and EXAFS contributions in the XAFS data and simultaneously leaving the double electron excitations in the background as described in the literature.[20] However, this background subtraction procedure was described previously for samples in which the first shell contribution is clearly separated from the AXAFS. Moreover, for the [PtCl(NCN-Z)] pincer complexes described here only one Pt(II) atom is present, in contrast to the larger Pt(0) clusters described in the previous studies. The C and N atoms are located close to the Pt, i.e. around 1.8 and 2.1 Å.[3] Consequently, the EXAFS contributions tail to R distances below 1 Å causing interference with the AXAFS peak. This can even result in reduction of the AXAFS peak amplitude in the FT of the raw data.

Figure 4. Fourier Transforms (k^1, Δk = 1.6 - 15 $Å^{-1}$) of the [PtCl(NCN-H)] pincer XAFS data for different smoothing parameters SM (a) k^1-weighted (b) k^3-weighted.
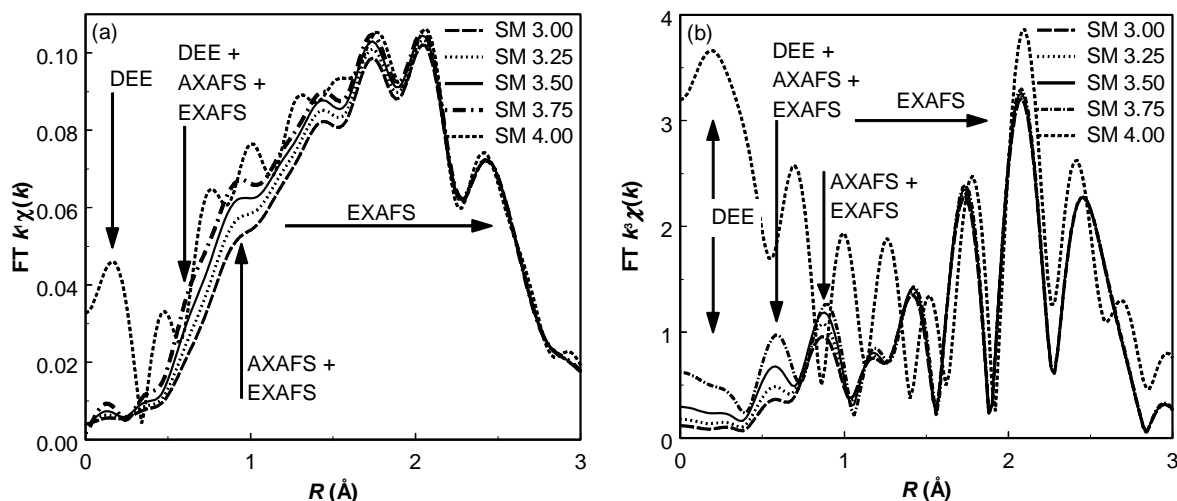
Figures 4a and 4b show respectively the k^1-weigthed and k^3-weighted FT data after background subtraction with different smoothing parameters (SM). The assignment of the different contributions is based upon the results presented in an earlier study.[20] Especially in the k^1-weighted case, it is clear that the EXAFS is tailing to small R distance and is severely overlapping with the DEE and AXAFS contributions (see also Figure 8). Thus the FT's should be very carefully examined in order to determine a reliable background. Figure 4a shows that with increasing SM the intensity of the AXAFS/EXAFS peak at ~0.9 Å and the higher EXAFS peaks are increasing (first shell contribution peaking around 1.4 Å, *vide infra*). For a SM of 3.75 the EXAFS peaks shift to somewhat higher R and a small peak around 0.2 Å is formed. When the SM is even more increased to 4.00, large peaks at low R are now formed, clearly corresponding to DEE. Simultaneously, the EXAFS peaks now significantly shift to longer distances.

The k^3-weighted FT's displayed in Figure 4b, show similar trends. All peaks increase with increasing SM. From SM = 3.75, the increase of peak intensity is accompanied by a significant increase of the contribution at R < 0.5 Å. Moreover, the positions of the peaks between 0.5 and 2.0 Å shift to higher distances. For SM = 4.00, the DEE contribution below 0.5 Å is large and all other contributions (peaks) have significantly shifted position.

Examination of the corresponding backgrounds in Figure 5 with the same SM values as displayed in Figure 4, show that for SM < 3.75 the step-like DEE feature with the usual onset at ~140 eV is visible,[9] whereas for SM parameters of 3.75 and above, the background flattens and the DEE is diminished.

Based on the FT's and corresponding backgrounds, a background with SM = 3.50 is chosen here as optimal. For a correct background subtraction, the DEE are required to be left in the background. This is true for backgrounds with SM < 3.75 (Figure 4). Simultaneously, in the resulting FT, the contribution of DEE/RTR should be diminished as much as possible. In Figures 4a and 4b, this happens for SM < 3.75. Optimization of both the AXAFS and EXAFS contributions in all different k-weightings using the criteria as mentioned above then results in an optimal background with SM = 3.50 (solid line) for the [PtCl(NCN-H)] pincer complex shown here.
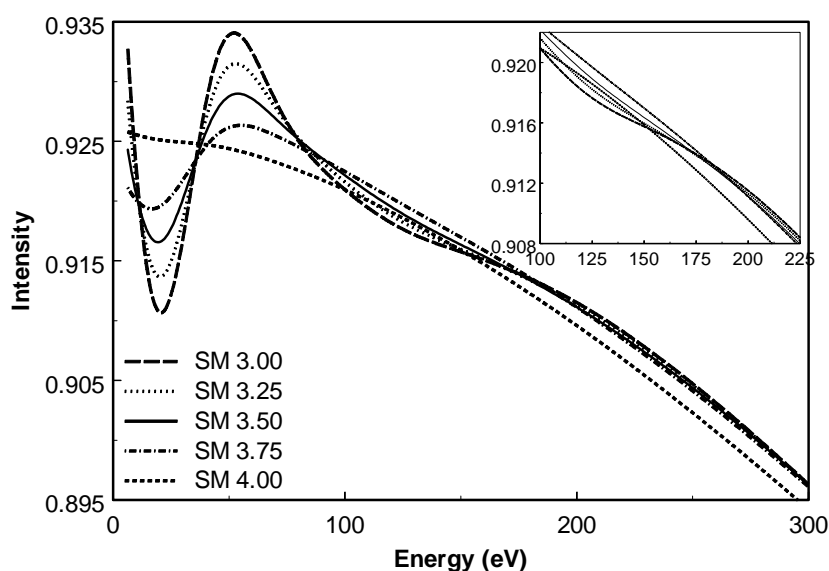

Figure 5. Background of [PtCl-(NCN)-H] pincer XAFS data as a function of the smoothing parameter (SM).

It is always possible that the final choice of the SM parameter does not lead to an optimal separation between the DEE, AXAFS and EXAFS. However, it should be noted that even without an optimal background subtraction, identical trends in the final AXAFS data are still found as long as the background is performed consistently. The final trend in the AXAFS data is the same even though the absolute AXAFS areas may be different. Further, the AXAFS signal obtained is also somewhat dependent on a careful EXAFS analysis since the final choice of the EXAFS parameters of the overlapping shells at low R (overlapping with the AXAFS) easily influences the resulting AXAFS data.

After background subtraction, the absorption data are normalized at 50 eV after the absorption edge and the final $\chi(k)$ is calculated.[13] All pincer complex XAFS data were treated as described above.

EXAFS Analysis

Figure 6. (a) Raw EXAFS data (k^0-weighted) of the [PtCl(NCN-Z)] pincer complexes, for Z=NH$_2$ (solid line), Z=H (striped line), Z=COOH (dotted line). (b) Enlargement of experimental chi data to show the S/N level.
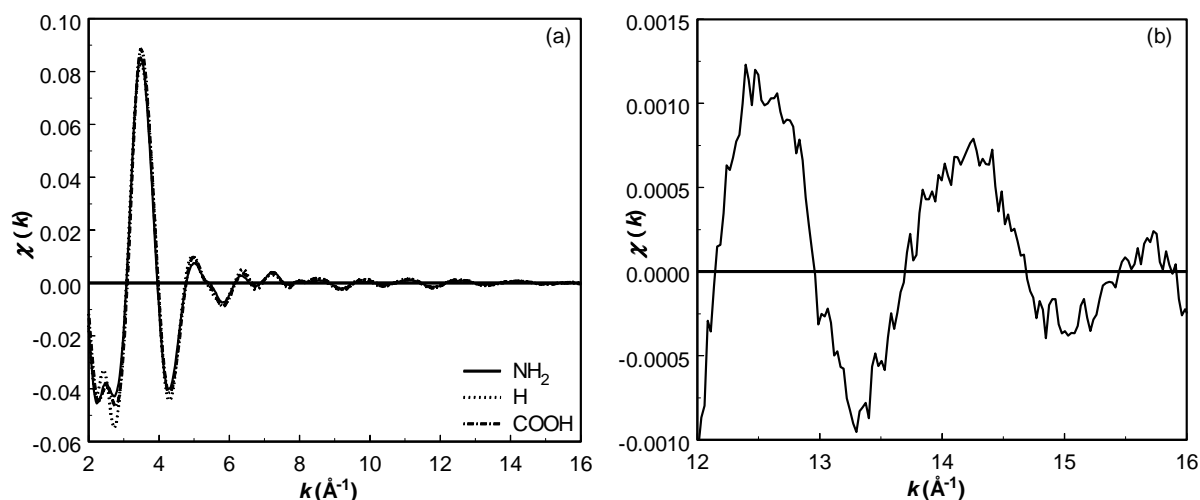
The final EXAFS data of the three [PtCl(NCN-Z)] pincer complexes are shown in Figure 6a. The data are of excellent quality with a very high signal/noise ratio. The noise level can be determined to be ~0.0002 in the high k-range in the enlargement in Figure 6b. Only small changes in the intensity of the final EXAFS data at low values of k can be observed for the different samples. In the corresponding FT's shown in Figure 7, these small changes are visible as small intensity changes over the R-range shown here, whereas the imaginary parts are similar for all complexes.

The difference file technique was used to judge whether a good analysis for all Pt-X contributions in all weightings was achieved.[17,18] A good fit can be concluded from Figure 8 showing the raw data and fit for different k-weightings and from the corresponding low variances in the fit parameters given in Table 2. Moreover, during the fitting procedure the difference files were examined carefully. In Figure 9 the k^1-weighted difference files and fits

for the single shell contributions are shown, which are in good agreement. The same is true for the k^3-weighted difference files (not shown here). Note that these isolated difference files reveal that each peak in the total FT can be attributed to a separate Pt-X neighbor, the first contribution peaking at ~1.4 Å (Figure 8).

Figure 7. Fourier Transforms (k^1-weighted) of EXAFS data of the [PtCl(NCN-Z)] pincer complexes, for Z=NH$_2$ (solid line), Z=H (striped line), Z=COOH (dotted line).
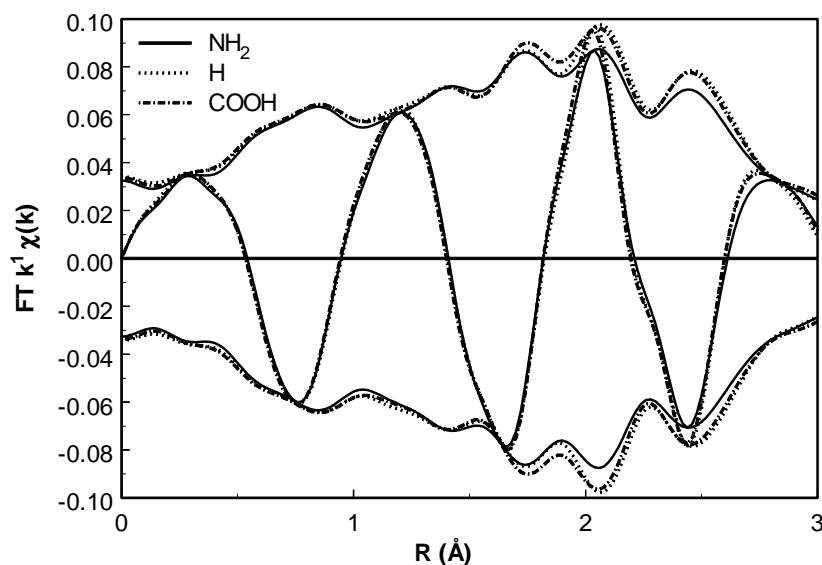

Figure 8. Fourier Transform of the raw EXAFS data and fit (*R*-space fit for 1.0 < *R* < 3.0 Å) of the [PtCl(NCN-H)] pincer complex (a) k^1-weighted, (b) k^3-weighted.
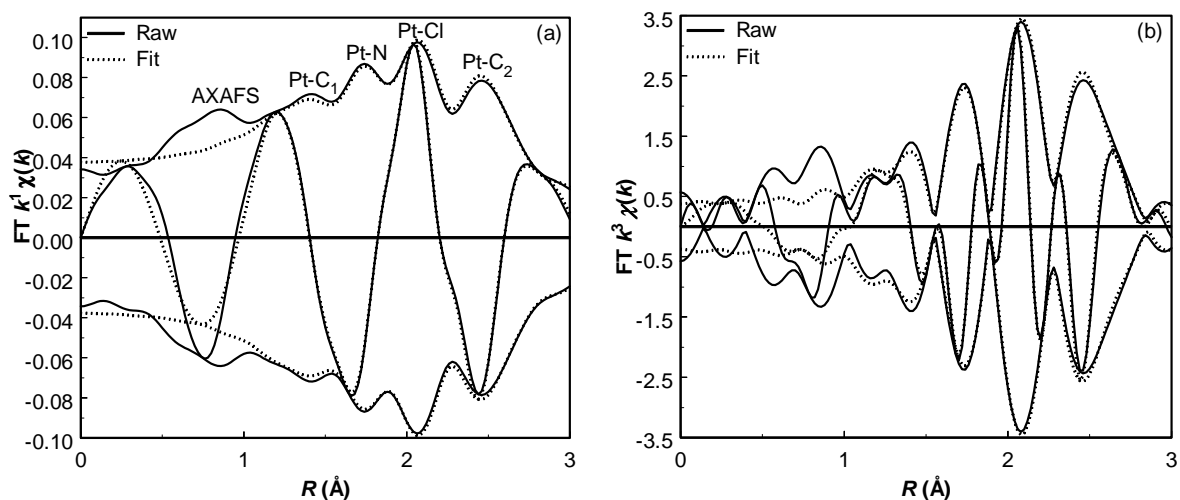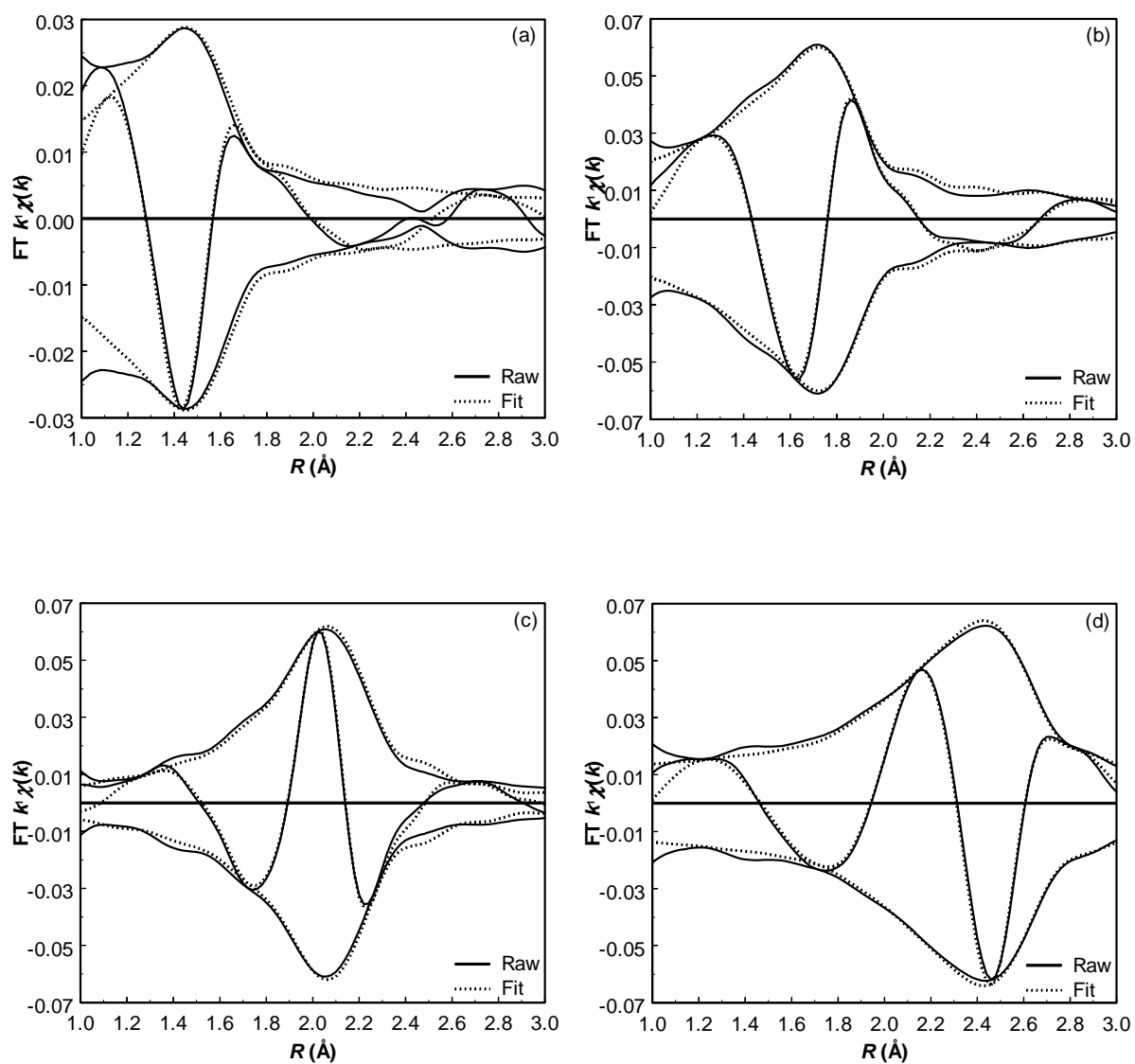
Figure 9. Fitted single shell contributions (dotted line) and difference files (solid line) of *R*-space fit (k^1, 3.0 < k < 15, 1.0 < R < 3.0) for [PtCl(NCN-H)] (a) Pt-C_1, (b) Pt-Cl, (c) Pt-N, (d) Pt-C_2.

Figure 9 shows that a combination of a k^1- and k^3-weighted fit is essential to obtain reliable results since anti-phase behavior is present between the different contributions.[18] Comparing the different single shell contributions, it can be observed that the Pt-C_1 and Pt-Cl contributions are in anti-phase between 1.6 and 2.0 Å, whereas the Pt-N and Pt-C_2 single shell contributions are in anti-phase between 2.1 and 2.8 Å. Plotting the chi data of these single shell contributions in Figure 10, shows that above $k = 3.5$ different contributions are in anti-phase making the total EXAFS amplitude small at high values of k. This means that a fit using only high k weightings could easily result in incorrect results. Examining the same fit with a low k-weighted FT can reveal such an incorrect fit.[18] Only if all difference files reveal a good fit in all k-weightings can a good analysis be assured. The optimal fit parameters are shown in Table 2. These results are show that for all complexes the structure in the vicinity of the Pt is the same, consistent with the structures as established by single crystal X-ray analysis,[3] i.e. one C atom ~1.94 Å, two N atoms ~2.13 Å, 1 Cl atom around 2.53 Å and 8 C atoms at a long distance with an average ~2.9 Å.

Figure 10. Chi differences files to show anti-phase behavior between Pt-X contributions.
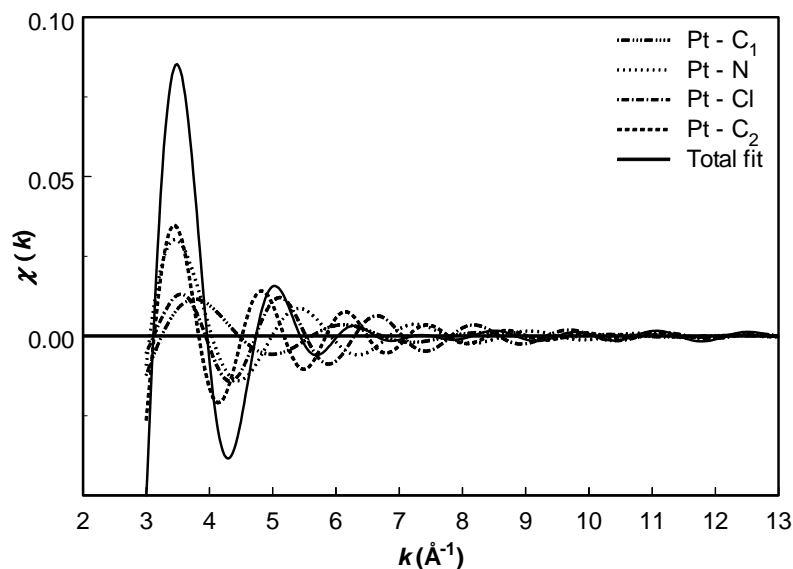
Table 2. EXAFS analyses of [PtCl(NCN)-Z] pincer complexes.

| Ab-Sc*	N	R [Å]	$\Delta\sigma^2$ [Å^2]	ΔE_0 [eV]	Var. Im.*	Var. Abs.*
[PtCl-(NCN-NH₂)] pincer complex						
Pt-C	0.96	1.880	0.00134	-0.26	k^1-weighted:	
Pt-N	2.10	2.131	0.00021	-11.52	0.148	0.0257
Pt-Cl	1.43	2.420	0.00110	2.15	k^3-weighted:	
Pt-C	8.07	2.880	0.00537	1.9	1.04	0.475
[PtCl-(NCN-H)] pincer complex						
Pt-C	0.96	1.878	0.00162	-1.75	k^1-weighted:	
Pt-N	2.06	2.121	0.00021	-9.39	0.224	0.0673
Pt-Cl	1.41	2.432	0.00014	0.58	k^3-weighted:	
Pt-C	8.09	2.885	0.00339	0.60	0.815	0.364
[PtCl-(NCN-COOH)] pincer complex						
Pt-C	0.96	1.878	0.00092	-2.52	k^1-weighted:	
Pt-N	2.01	2.119	0.00011	-9.02	0.297	0.065
Pt-Cl	1.45	2.417	0.00060	1.05	k^3-weighted:	
Pt-C	8.09	2.885	0.00375	0.45	0.936	0.465

<u>Fit:</u> R-space, $3.0 < k < 15.0$, $1.0 < R < 3.0$. *Abbreviations: Ab = Absorber, Sc = Scatterer; Var. Im. and Var. Abs. are the Variances in the fit of the Imaginary and Absolute parts, respectively.

AXAFS Isolation

The AXAFS contribution is isolated from the total XAFS data by subtracting the fitted EXAFS contributions from the experimental XAFS data as shown in Figure 11. Since the geometry around the Pt absorber is similar in all complexes, the obtained EXAFS contributions are similar. The FT of the raw experimental EXAFS and fit for the [PtCl(NCN-H)] pincer complex is shown in Figure 11a, along with the difference [raw EXAFS – fitted EXAFS]. This difference consists of the AXAFS contribution peaking around 0.75 Å. The small contributions at higher R are due to higher shell contributions present above 3 Å. To reveal the AXAFS contribution in comparison to the total XAFS data, the chi data of both are shown in Figure 11b. To be able to plot only the AXAFS contribution here, without possible higher shell contributions present in the difference between raw and fitted data, these higher shells are filtered out (AXAFS shell is isolated (3 $< k <$ 10 Å^{-1}, 0 $< R <$ 1.25 Å) and a backward Fourier transformation is performed). As can be observed in Figure 11b, the amplitude of the AXAFS chi function is almost 50% of the total XAFS function between 4.5 $< k <$ 8 Å^{-1}. Moreover, the AXAFS signal is significantly above the noise level (at $k =$ 3.18 Å^{-1} ~ 40 times and at $k =$ 5.2 Å^{-1} even ~1140 times).

Figure 11. Fourier Transform of the raw EXAFS data, fit (*R*-space fit for 1.0 $< R <$ 3.0 Å) and [Raw-Fit] for the [PtCl(NCN-H)] pincer complex (a) k^1-weighted Fourier Transform, (b) corresponding chi functions with isolated AXAFS.
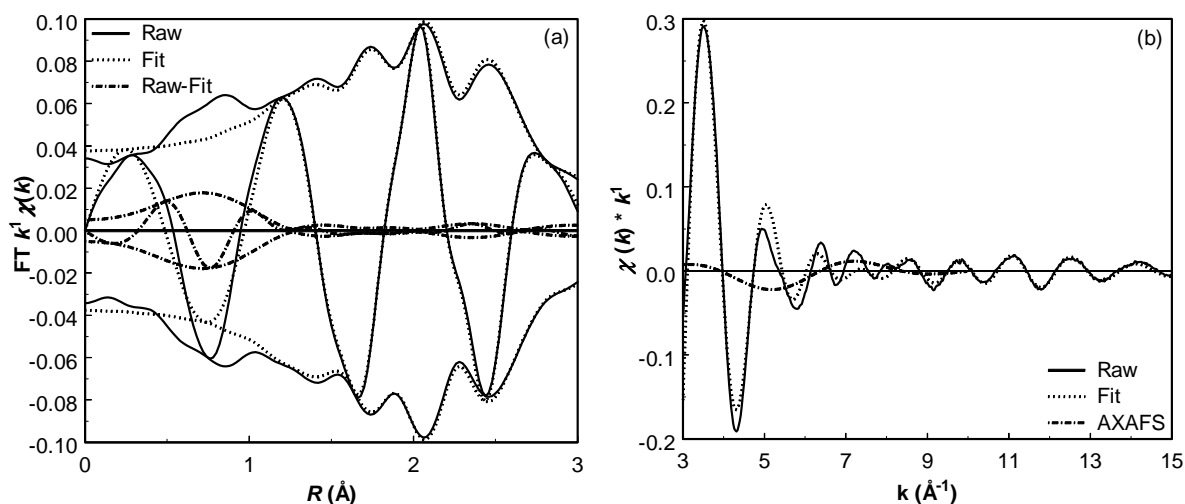
AXAFS Results

The complete background subtraction procedure is performed for all three [PtCl(NCN-Z)] pincer complexes. The absolute parts of the resulting FT's of the AXAFS data are plotted in Figure 12a. For the [PtCl(NCN-Z)] pincer complexes with para-substituents from NH_2 to H to COOH, i.e. with increasing electron withdrawing properties, the AXAFS is decreasing in magnitude and its centroid is slightly shifting to lower R. Moreover, the decrease in magnitude is particularly occurring between 0.75 and 1.5 Å.

The isolated AXAFS chi functions are displayed in Figure 12b, including the noise level obtained. The differences between the AXAFS chi functions are significantly larger than the noise/signal level. A slight decrease in amplitude is observed when a more electron withdrawing substituent is present, consistent with the lower amplitude observed in the FT in Figure 12a. Even more significant is the shift in k of the chi function, especially for $3 < k < 6.5$ Å^{-1}. The increase in wavelength (i.e. Δk between two nodes) correlates with the decrease in distance found in the FT data (Figure 12a).

Figure 12. (a) Fourier Transforms (k^1, $\Delta k = 3.0 - 8$ Å^{-1}) of AXAFS for [PtCl(NCN-NH$_2$)], [PtCl(NCN-H)] and [PtCl(NCN-COOH)] pincer complexes. The solid arrows indicate the change with increasing electronegativity. (b) Isolated AXAFS functions of the same pincer complexes.
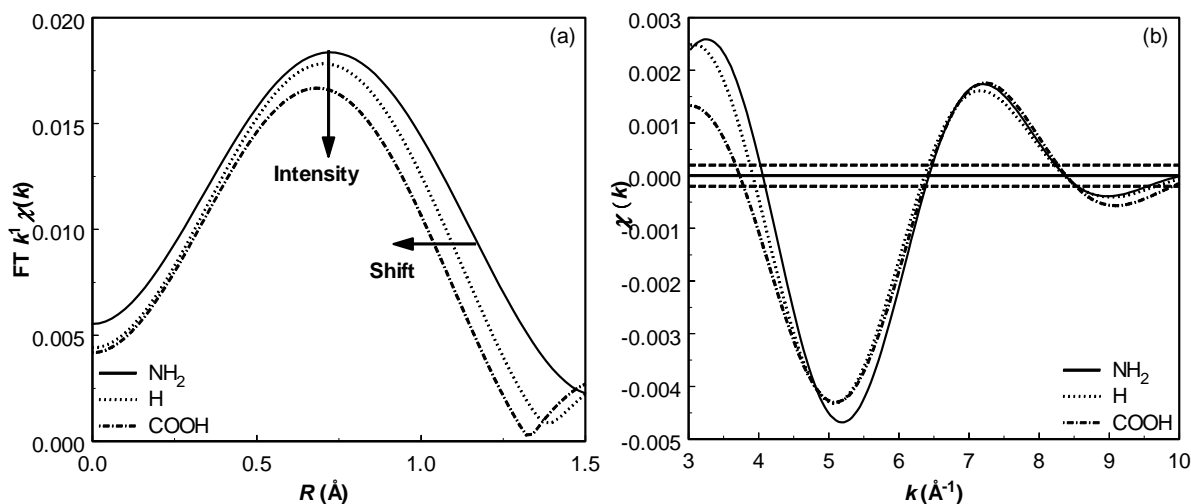
Chapter 5

FEFF8 Results

The XANES of the [PtCl(NCN-Z)] complexes can be simulated using FEFF8 and the results are shown in Figures 13. The simulated XANES spectra clearly do not display the double peak just after the white line as was observed in the experimental spectra, neither for the L_2 edge nor for the L_3 edge, but otherwise the agreement is reasonable. The theoretical XANES spectra are the same for all three samples.

Figure 13. Theoretical Pt XANES data for [PtCl(NCN)-Z] pincer complexes (a) L_2-edge, (b) L_3-edge.
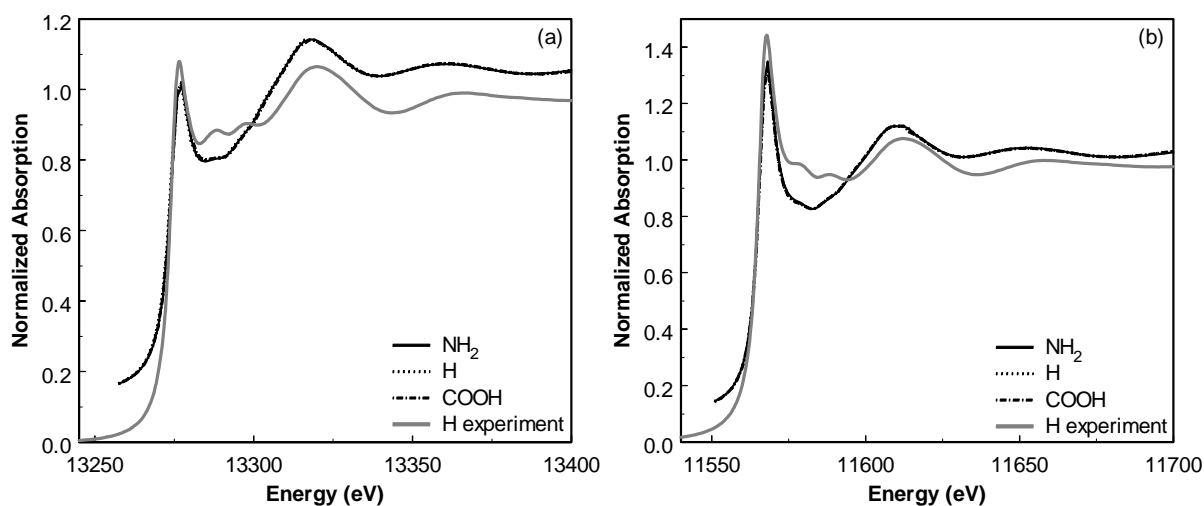
Additional FEFF8 calculations have been performed on the [PtCl(NCN-NH$_2$)] and [PtCl(NCN-COOH)] pincer complexes to simulate the different AXAFS signals as obtained in the experiment (Figure 12). The theoretical AXAFS can be obtained from the theory either by analyzing the μ results from FEFF8 in exactly the same fashion as with the experimental data, or more directly by examining the potentials from FEFF8 used to obtain these μ results. Since the latter technique is more direct, only the potentials are shown in Figure 14. In Figure 14a, the different potentials U_{free}, U_{emb} and V_{int} are shown for the two complexes. The U_{emb} potentials are nearly identical for both complexes (only one line is essentially visible), and U_{free} by definition is the same, whereas the V_{int} shifts down for the [PtCl(NCN-COOH)] pincer complex. The change in V_{int} shown in Figure 14 for the two complexes is slightly larger (about 0.5 compared to 0.2 predicted by FEFF8) to better illustrate the expected changes with Z. To visualize the AXAFS contribution for the

112

calculated complexes, the difference between the calculated potentials (equal to the AXAFS as defined above) is shown in Figure 14b. These results show that the change of Z has no effect on the *U* potentials, and therefore as expected the space-field effect is negligible. Only the bond inductive effect (i.e. change in V_{int}) is playing a role according to FEFF8, and the change is exactly in the direction found in the experimental data (compare Figures 12a with 14), but the change in AXAFS predicted by FEFF8 is much smaller than that found experimentally.

Figure 14. FEFF8 calculated (a) potentials for [PtCl(NCN)-NH$_2$] and [PtCl(NCN)-COOH] pincer complexes and (b) corresponding AXAFS.
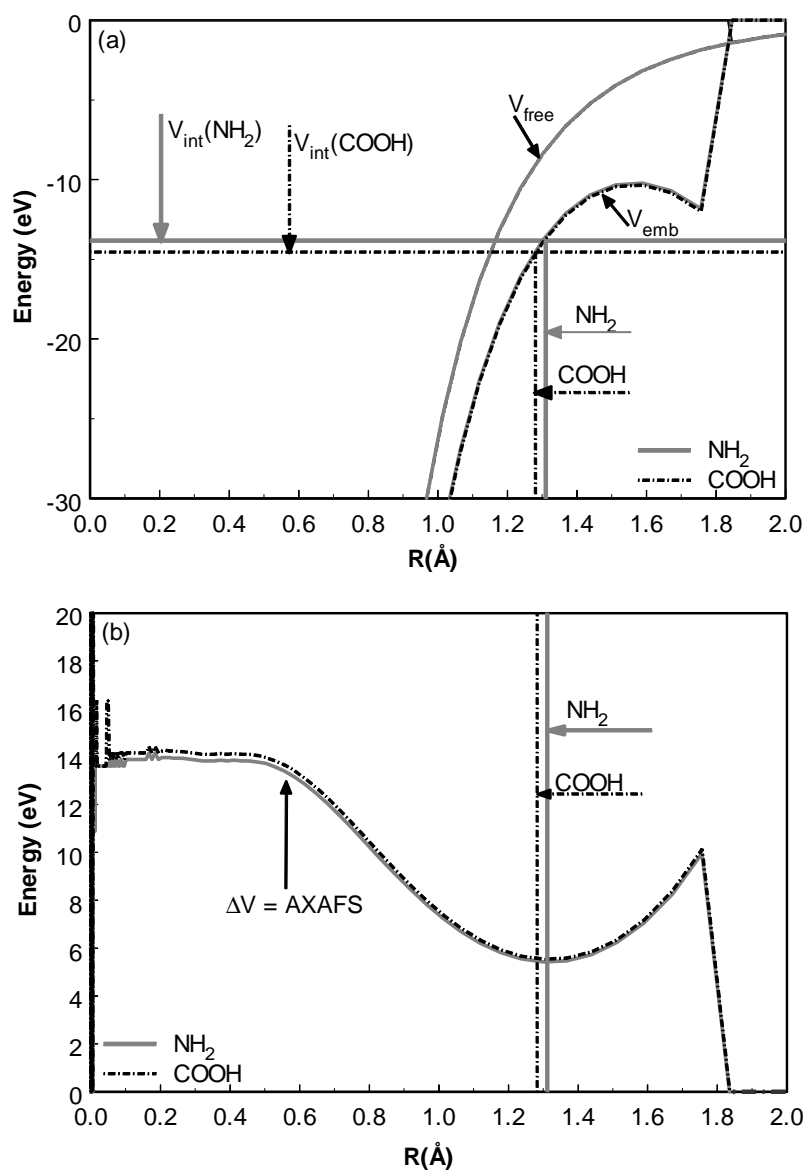
Discussion

The raw Pt L_2 and L_3 XANES data (Figure 3) differ very little upon changing the para-substituent Z in the [PtCl(NCN-Z)] pincer complex. This is in agreement with the XANES data as calculated with FEFF8. Apparently the XANES region is not sensitive to the small electronic changes induced by the *para*-substituent of the pincer complex. The double-peak features observed in the experimental data just above the absorption edge are similar for all complexes and visible in both L-edges. Since this double peak is not simulated with FEFF8 as shown in Figures 13, the origin of these peaks is unclear and may be caused by multiplets or shake up satellites;[21,22,23] interactions not included in the FEFF8 theory.

After a careful background subtraction procedure and EXAFS analysis as described above, the resulting AXAFS signals are shown in Figure 12. The changes in the shape of the FT of the AXAFS signals is strongly suggestive of Figure 2b. A scheme for the potentials applicable specifically for the Pt pincer complexes is drawn Figure 15. It is clear that the changes in the FT of the AXAFS data reflect a downward shift in V_{int} with increasing electron-withdrawing properties of the *para*-substituent, i.e. the bond inductive effect is governing here. This shift in V_{int} is even more obvious in Figure 12b, which shows a systematic shift at low k values. This is exactly what would be expected with a change in V_{int}, since V_{int} determines the effective bottom of the "conduction band" or continuum and hence the effective zero of energy E_o in the continuum. As the zero of energy shifts, the low values of k shift, since $k \propto \sqrt{\left((E - E_0)^2 \right)}$. Chemically, this downward shift in V_{int} means that the electron density near the Fermi level or HOMO on the Pt atom (scheme 1b) is decreasing, i.e. the electron density on the Pt is decreasing.

FEFF8 calculations confirm that the V_{emb} potentials do not change with Z (Figure 14a), i.e. that the Coulomb-field effect is negligible for these complexes. Only changes in V_{int} occur, i.e. the bond inductive effect is significant. Although the changes as predicted by FEFF8 are much smaller than observed in the experimental results, the identical trends in the bond inductive effect is found. The SCF muffin-tin approximation made in FEFF8 is well-known not to be fully adequate for charge-transfer (i.e. ionic) complexes such as those studied here. It is therefore not surprising that FEFF8 underestimates the magnitude of the inductive effect, even though it does predict the proper trends.

Figure 15. Schematic potential model showing the V_{int} changes for the different [PtCl(NCN-Z)] pincer complexes.
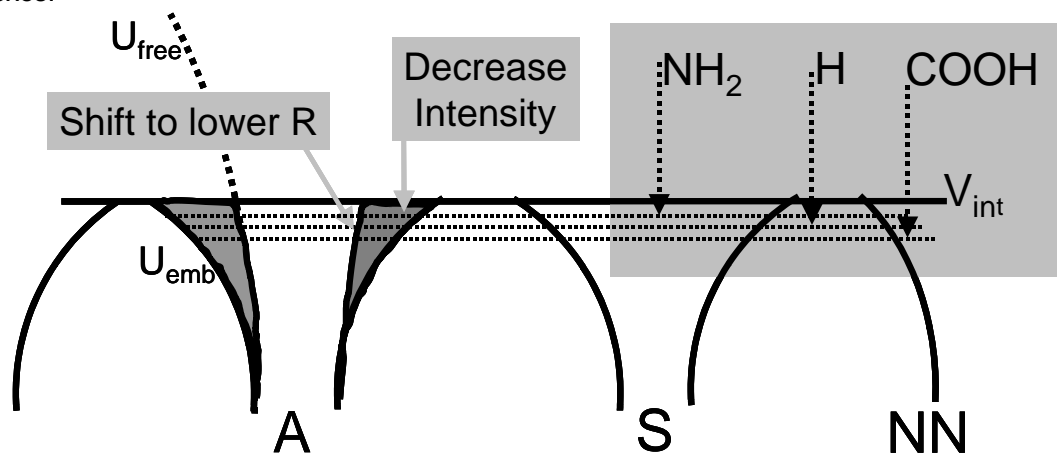
As discussed above, the AXAFS isolation is preceded by a very careful and systematic background procedure. Also the EXAFS analysis has to be carried out reliably. It is still possible that uncertainties occur in the final AXAFS contribution. FEFF8 results in Figure 14 suggest that the AXAFS is significant all the way down to $R = 0$ Å. This is believed to result from the large positive valence of the Pt atom (nominally +1 or more) in these complexes, since in previous work on zero valent Pt clusters, the AXAFS was predicted to go to zero at $R = 0$ Å. Thus our background subtraction criteria, developed from analyses for zero-valent Pt clusters, automatically forced the AXAFS extracted from our experimental data to be near zero at $R = 0$ Å. This suggests that different background subtraction criteria may have to be developed for highly valent absorber atoms.

The applied background subtraction procedure thus can introduce an uncertainty in the AXAFS intensity, which increases when going to lower k and R. As already noted in the results however, the choice of a less perfect SM value (i.e. background) does not influence the trend in AXAFS intensity observed for these complexes, provided that a similar background subtraction procedure is applied for all complexes under investigation. Thus, quantitatively the trend in AXAFS changes is not highly dependent on the exactly correct background subtraction, even though the absolute magnitude may be. The same holds for the EXAFS analysis. Large differences in AXAFS area are observed for different EXAFS analysis results. If however consistent criteria for the EXAFS fitting procedure are applied for all samples, the observed trends are correct. In summery, the AXAFS trends for a series of complexes can be determined quite accurately although the exact quantification is much more difficult. A relative uncertainty of 10% in the FT AXAFS intensity is estimated here.

The AXAFS is defined as $[U_{emb}(R) - U_{free}(R)]$, i.e. the grey area in the Figures 2 and 13 as explained above. The AXAFS integrated areas are therefore obtained from the FT plots in Figure 12a. Figure 16 shows that a linear correlation exists between the AXAFS integrated area and the Hammett constant of the para-substituent (with $R^2 = 0.985$). Although the uncertainty in the AXAFS determination is rather high as described above (and see Figure 12), a good linear correlation is obtained in Figure 16.

A ^{195}Pt NMR study on these [PtCl(NCN-Z)] pincer complexes has been described in detail. NMR is shown to be a sensitive probe for the change in electron density on the metal atom (see reference 3b). In general, an increase in electron density on the metal leads to an increase in shielding of the nucleus. This change in nuclear shielding is reflected in the NMR chemical shift. This shielding can be solely attributed to the *para*-substituent in the pincer systems and Figure 16 shows a linear correlation between the Pt chemical shift and the Hammett constant of the para-substituent (with a correlation of $R^2 = 0.981$).[3b]

Figure 16. ^{195}Pt chemical shift (empty circles) and AXAFS integrated area (filled triangles) of [PtCl(NCN-Z)] versus σ_p Hammett substituent constant.
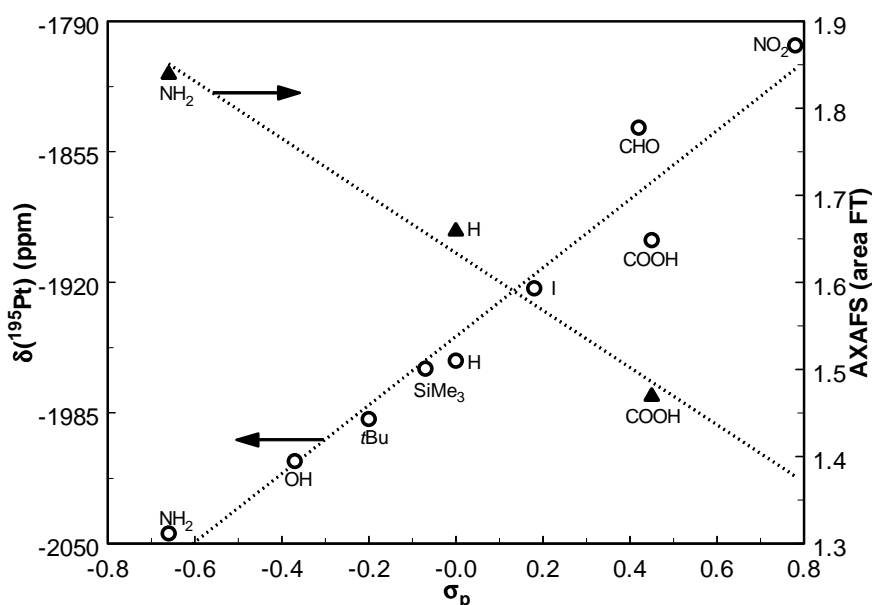
The experimental and data-analysis procedures (and the consequent reliability of the results) required for the AXAFS and NMR techniques described here are completely different. Nevertheless, the correlation between electron donating and withdrawing properties, as reflected in the Hammett constant, and the AXAFS intensity as found for these [PtCl(NCN-Z)] pincer complexes is in very good agreement with that found for the [195]Pt NMR data. The results obtained in this work show that AXAFS is a sufficiently sensitive probe to determine the electron density on a metal atom, similar yet complementary to NMR. The sensitivity of the XANES is observed to be too low to probe the electronic changes induced by the different substituents in this work. This has probably to do with the different energy ranges of respectively AXAFS and XANES spectroscopy. The AXAFS data is carefully extracted from the XAFS data over the range $k = 3 - 8$ Å^{-1}, whereas the XANES data only reflect the energy range up to about $k = 4$ Å^{-1} (E < 50 eV).

In summary, the XAFS data of the [PtCl(NCN-Z)] pincer complexes can be used to demonstrate the validity of the AXAFS technique and its intuitive description in particular. The geometry around the absorber atom remains the same (leading to the same Coulomb field effect) and only the bond inductive effect is playing a role. This facilitates the analysis and interpretation of the data.

Conclusions

We have shown that AXAFS can be used to probe the electronic properties of Pt and, in principal, of every atom, which is especially interesting for systems that, e.g., are not amenable to NMR. Moreover, XAFS measurements can be performed *in situ* so the changes in electronic properties can be monitored under operating or reactive conditions and, most interestingly, even time-resolved measurements can be performed to examine changes in the catalysts with time during reaction.

The results presented in this study show that both the AXAFS and NMR techniques are sensitive to the small electronic changes induced by the para-substituent on [PtCl(NCN-Z)] pincer complexes, whereas the XANES technique is not. Theoretical FEFF8 calculations predict the proper trends. They are inadequate (as expected) to simulate the exact magnitude of the changes in the electronic structure with para substituent. However, they do confirm for the [PtCl(NCN-Z)] pincer complexes the dominance of the bond inductive over the Coulomb-field effect and predict the same trend with the electronegativity of the substituent as observed in experiment.

Chapter 5

Acknowledgements

References

1.   For overview articles on pincer chemistry see: (a) M. Albrecht, G. van Koten, *Angew. Chem., Int. Ed.* **2001**, *40*, 3750; (b) B. Rybtchinski, D. Milstein, *Angew. Chem.* **1999**, *111*, 918; (c) P. Steenwinkel, R. A. Gossage, G. van Koten, *Chem. Eur. J.* **1998**, *4*, 759; (d) R. A. Gossage, L. A. van de Kuil, G. van Koten, *Acc. Chem. Res.* **1998**, *31*, 423; (e) M. H. P. Rietveld, D. M. Grove, G. van Koten, *New J. Chem.* **1997**, *21*, 751; (f) G. van Koten, *Pure & Appl. Chem.* **1998**, *61*, 1681.

2.   L. A. van der Kuil, H. Luitjes, D. M. Grove, J. W. Zwikker, J. G. M. van der Linden, A. M. Roelofsen, L. W. Jenneskens, W. Drenth, G. van Koten, *Organometallics* **1994**, *13*, 468.

3.   (a) M. Q. Slagt, R. J. M. Klein Gebbink, M. Lutz, A. L. Spek, G. van Koten, *J. Chem. Soc., Dalton Trans.* **2002**, 2591; (b) M. Q. Slagt, G. Rodriguez; M. M. P. Grutters, R. J. M. Klein Gebbink, W. Klopper, M. Lutz, A. L. Spek, G. van Koten, *Chem. Eur. J.* **2004**, in press.

4.   D. E. Ramaker, J. de Graaf, J. A. R. van Veen, D. C. Koningsberger, *J. Catal.* **2001**, *203*(1), 7.

5.   H. Wende, Ch. Litwinski, T. Gleitsmann, Z. Li, C. Sorg, K. Baberschke, A. Ankudinov, J.J. Rehr, Ch. Jung, *J. Phys. Condens. Matter* **2003**, *15*, 5197.

6.   F. W. H. Kampers, T. M. J. Maas, J. van Grondelle, P. Brinkgreve, D. C. Koningsberger, *Rev. Sci. Instrum.* **1989**, *60*, 2635.

7.   B. W. Holland, J. B. Pendry, R. F. Pettifer, J. J. Bordas, *Physic. C* **1978**, *11*, 633.

8.   J. J. Rehr, C. H. Booth, F. Bridges, S. I. Zabinsky, *Phys. Rev. B* **1994**, *49*, 12347.

9.   G. E. van Dorssen, D. C. Koningsberger, D. E. Ramaker, *J. Phys.: Condens. Matter* **2002**, *14*, 13529; and references therein.

10. D. E. Ramaker, B. L. Mojet, W. E. O'Grady, D. C. Koningsberger, *J. Phys. Condens. Matter* **1999**, *10*, 1.

11. D. E. Ramaker, X. Qian, W. E. O'Grady, *Chem. Phys. Lett.* **1999**, *299*, 211.

12. B. K. Teo, *EXAFS: Basic Principles and Data-analysis,* Springer, New York, **1986**.

13. D. C. Koningsberger, B. L. Mojet, G. E. van Dorssen, D. E. Ramaker, *Topics in Catal.* **2000**, *10*, 143.

14. J. W. Cook, Jr, D. E. Sayers, *J. Appl. Phys.* **1981**, *52*, 5024.

15. M. Vaarkamp, J. C. Linders, D. C. Koningsberger, *Physica B* **1995**, *208-209*, 159.

16. A. L. Ankudinov, B. Ravel, J. J. Rehr, S. D. Conradson, *Phys. Rev. B* **1998**, 7565.

17. D. C. Koningsberger, B. L. Mojet, G. E. van Dorssen, D. E. Ramaker, *Top. Catal.* **2000**, *10*, 143.

18. M. Tromp, J. A. van Bokhoven, A. M. Arink, J. H. Bitter, G. van Koten, D. C. Koningsberger, *Chem. Eur. J.* **2002**, *8*, 5667.

19. A. L. Ankudinov, B. Ravel, J. J. Rehr, S. D. Conradson, *Phys. Rev. B* **1998**, *58*, 7565.

20. G. E. van Dorssen, D. C. Koningsberger, D. E. Ramaker, *J. Phys. Condens. Matter* **2002**, *14*, 13529.

21. F.M.F. de Groot, *J. Elec. Spec.* **1994**, *67*, 529.

22. J. A. van Bokhoven, T. Nabi, H. Sambe, D. E. Ramaker, D. C. Koningsberger, J. *Phys. Cond. Matter* **2001**, *13*(45), 10247.

23. J. A. van Bokhoven, D. E. Ramaker, D. C. Koningsberger, *J. Phys. Cond. Matter* **2001**, *13*(46), 10383.

Chapter 6a

Structure-Performance Relations in Homogeneous Pd Catalysis by *In Situ* EXAFS Spectroscopy

Abstract

X-ray Absorption Fine Structure (XAFS) spectroscopy is used to unravel the structure of homogeneous catalysts in their catalytically active phase (solution), for which other characterization techniques failed in providing detailed structural information. Application of *in situ* EXAFS shows that the conformation of the allylic fragment of [(P-P)Pd(1,1-dimethylallyl)]$^+$ catalytic intermediate complexes in solution (i.e. reaction medium) differs from that in the solid state, dependent on the bidentate ligand. The change in orientation directly explains differences in regioselectivity in the allylic alkylation reaction, displayed by the distinct complexes.

Introduction

Palladium is one of the most widely used metals in transition-metal-catalyzed organic synthesis, as it is capable of catalyzing a wide variety of commercially important reactions.[1] Ligands are attached to palladium to increase the performance and stability of the catalysts and they are used to fine-tune the steric and electronic properties of the catalyst and thereby the activity and selectivity obtained with these catalysts. The missing link in explaining structure-activity and –selectivity relationships in homogeneous catalysis is the detailed structural information about the catalysts in their active phase, namely in solution.

We have therefore applied Extended X-ray Absorption Fine Structure (EXAFS) spectroscopy to elucidate the origin of the regioselectivity in the Pd-catalyzed allylic substitution reaction. EXAFS spectroscopy provides both structural and electronic information about a specific element in a compound in any state of aggregation.[2] Only a few EXAFS studies on organometallic Pd complexes have been reported in literature so far.[3] This can partly be explained by the complexity of the EXAFS data-analysis, especially as overlapping coordination shells hamper data-analysis severely. Recent developments in EXAFS data-analysis methods,[4] using the so-called difference file technique,[2] allow the reliable separation of the different contributions resulting in a proper analysis.

Scheme 1. Regioselectivity in the Pd-catalyzed Allylic Substitution Reaction.
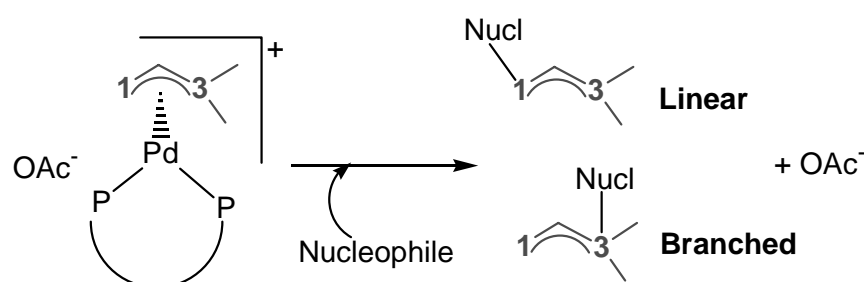
The use of bidentate diphosphine (P-P) ligand Pd catalysts in the allylic substitution reaction of a non-symmetrically substituted dimethylallyl moiety results in either linear or branched products as shown in Scheme 1. For bidentate ligand complexes, it has been suggested that the bonding of the allyl moiety determines the regioselectivity.[5,6] Moreover, the regioselectivity was found to be influenced by the P-Pd-P angle, i.e. bite angle of the bidentate phosphine ligands.[7] Isolated [(ligand)Pd(allyl)]$^+$ complexes are studied in detail by molecular modeling, X-ray crystallography and (solution-) NMR techniques.[6-10] It was proposed that the selectivity in the allylic alkylation reaction is a trade-off between electronic and steric contributions. A larger bite angle of the ligand enhances the electronic preference for nucleophilic attack at the branched position, but also increases the steric hindrance at this position.[6,7] Since these studies are mainly based on characterization of solid samples, they fail in providing a detailed structural analysis of the catalytic complexes in solution, the actual active phase of homogeneous reactions. This study shows that the structure of homogeneous catalytic intermediates in the active phase differs from that in the solid state. This can lead to a direct explanation of the regioselectivity of the different catalysts in the allylic alkylation reaction.

Experimental

EXAFS Pd K-edge data are collected for two cationic (ligand)Pd(allyl) complexes: [(dppe)Pd(C$_5$H$_9$)]$^+$ (dppe 1,2-bis(diphenylphosphino)ethane) and [(DPEphos)Pd(C$_5$H$_9$)]$^+$ (DPEphos 2,2-bis(diphenylphosphino(diphenylether)) with respectively a narrow and wide bite angle and consequently a different product selectivity in the allylic alkylation reaction.[6,7] The complexes were synthesized as described in literature[7,11,12] and characterized with both X-ray crystallography and solution NMR.[6] EXAFS measurements were performed on the solid state complexes (at room temperature) and in THF solution at room temperature. NMR spectra taken before and after EXAFS data collection showed that no changes had occurred in the complexes.

The EXAFS spectra were analyzed by recently developed special methods.[4] Fitting in R-space was used by minimizing the residuals between both the magnitude and imaginary part of the Fourier transforms of the data and the fit. *R*-space fitting has important advantages compared to the usually applied fitting in *k*-space and is extensively discussed in reference 2. Theoretical reference data were generated in the commercially available program XDAP[13] using FEFF8.0.[14]

The difference file technique[2] enables us to separate each single shell contribution. The phase shift and backscattering amplitude of each neighboring atom are element specific and have a unique dependency of the wavefactor k. A combination of a k^0- and k^3-weighting during the EXAFS data-analysis has to be used in order to separate each individual contribution.[2,4] Moreover, in this study the use of both k^0- and k^3-weighting was crucial in order to unravel interference effects of higher coordination shells.[4] Interference effects can lead to invisible higher coordination shells in a k^3 weighted Fourier transform.[4] A good fit is only obtained if the total fit and each individual contributing coordination shell describe correctly the experimental EXAFS and the difference file, respectively, for different applied k-weightings.[2] In this way not only the total EXAFS fit but also the individual fits of all separate contributions can be determined reliably.

Figure 1a (left). The crystal structure of the [(dppe)Pd(C_5H_9)]$^+$ complex as determined with single crystal XRD (omitting the counterion). **Figure 1b (right).** Possible representation of the structure of the [(dppe)Pd(C_5H_9)]$^+$ complex in solution as determined with EXAFS (distances correlate with the found values, the angles between the different atoms are not determined and can be slightly different).
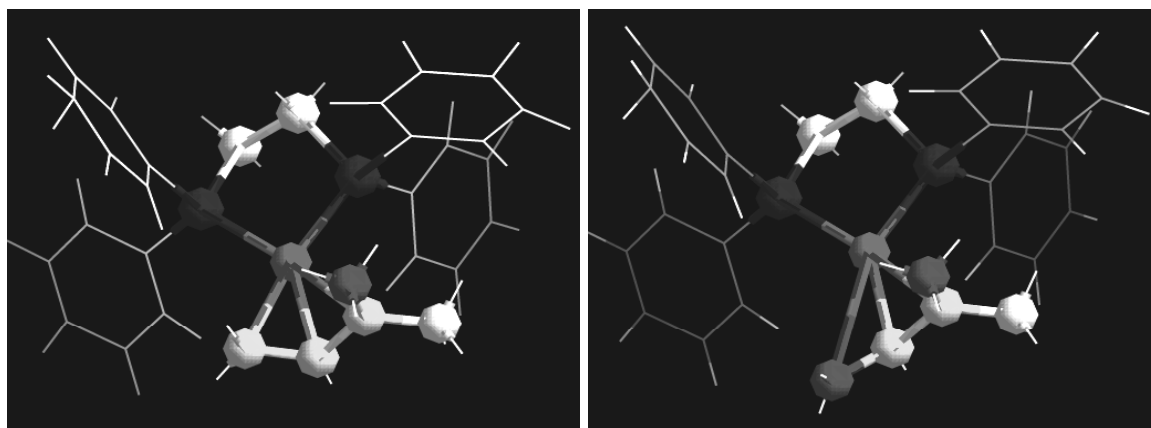
Results and Discussion

The crystal structure of the [(dppe)Pd(C$_5$H$_9$)]$^+$ complex is shown in Figure 1a. The different carbon neighbors of Pd up to a distance of 3.5 Å are denoted as C^{yellow}, C^{red} and C^{white}. The XRD values for the coordination numbers and distances of the Pd-C^{yellow}, Pd-P^{blue}, Pd-C^{red} and Pd-C^{white} coordination shells are given in Table 1a. EXAFS data of excellent quality are obtained. The k^0-weighted Fourier transforms of the EXAFS data collected for the [(DPEphos)Pd(C$_5$H$_9$)]$^+$ and [(dppe)Pd(C$_5$H$_9$)]$^+$ complexes are shown in Figure 2a and 2b, respectively. It can be clearly seen that the Fourier transforms of the EXAFS data of the [(DPEphos)Pd(C$_5$H$_9$)]$^+$ complex are about the same in the solid and the liquid state. However, differences are observed for the [(dppe)Pd(C$_5$H$_9$)]+ complex for 1.5 < R < 3.0 Å pointing to a change in structure in the liquid state compared to the solid state.

Figure 2. (a) Fourier Transform of EXAFS data of [(DPEphos)Pd(C$_5$H$_9$)]$^+$ solid state (solid line) and in solution (dotted line), k^0-weighted, 2.8 < k < 15 Å^{-1}. (b) Fourier Transform of EXAFS data of [(dppe)Pd(C$_5$H$_9$)]$^+$ solid state (solid line) and in solution (dotted line), k^0-weighted, 2.8 < k < 17 Å^{-1}.
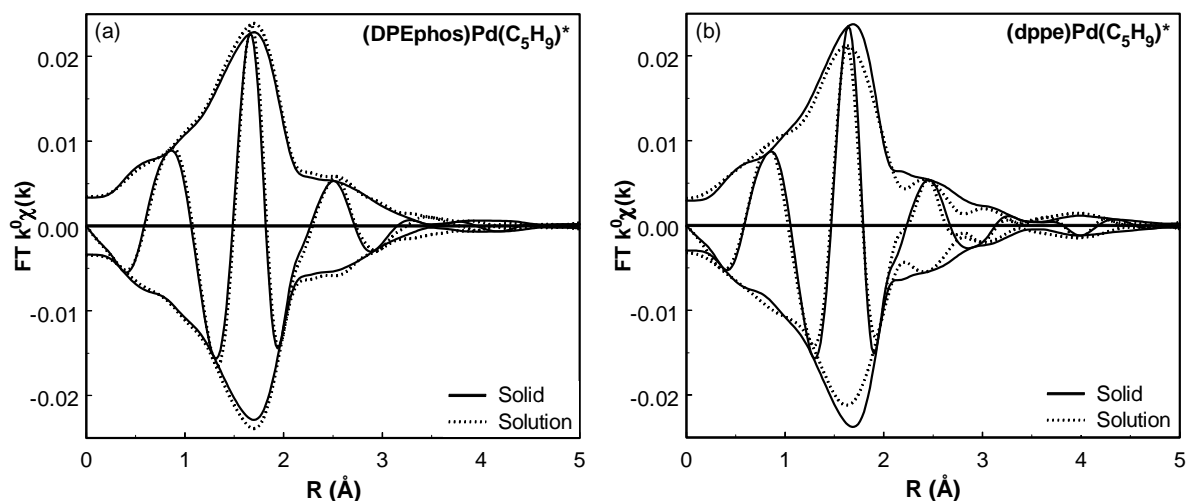
Table 1a: EXAFS analysis of [(dppe)Pd(C$_5$H$_9$)]$^+$.

Shell	Aggregation	N	R (Å)	Δσ² (Å²)	ΔE$_0$ (eV)
Pd-P^{blue}	Solid(XRD)	2	2.30 (±0.02)	-	-
	Solid	1.9	2.28	0.004	11.5
	Solution	1.8	2.28	0.011	4.8
Pd-C^{yellow}	Solid(XRD)	3	2.20 (±0.05)	-	-
	Solid	3.0	2.27	0.015	13.4
	Solution	2.1	2.15	0.001	13.3
Pd-C^{red}	Solid(XRD)	1	2.94	-	-
	Solid	0.9	3.00	0.004	-3.7
	Solution	1.8	2.95	0.007	5.5
Pd-C^{white}	Solid(XRD)	3	3.32 (±0.02)	-	-
	Solid	3.0	3.34	0.017	4.3
	Solution	3.1	3.29	0.023	6.7

<u>Fit:</u> *R*-space, 2.8 < *k* < 17.0, 1.0 < *R* < 3.5, *Nind** = 26; solid *k^0*-weighted V. I.* = 0.03, V. A.* = 0.02 and *k^3*-weighted V. I. = 0.59, V. A. = 0.22; solution *k^0*-weighted V. I. = 0.01, V. A. = 0.01, *k^3*-weighted V.I. = 0.06 V. A. = 0.01. **N$_{ind}$* = number of independent data points, V. I. = Variance in Imaginary Part, V. A. = Variance in Absolute Part.

Table 1b: EXAFS analysis of [(DPEphos)Pd(C$_5$H$_9$)]$^+$.

Shell	Aggregation	N	R (Å)	Δσ² (Å²)	ΔE$_0$ (eV)
Pd-P^{blue}	Solid(XRD)	2	2.36 (±0.02)	-	-
	Solid	1.7	2.33	0.005	5.4
	Solution	1.7	2.33	0.005	6.2
Pd-C^{yellow}	Solid(XRD)	3	2.25 (±0.02)	-	-
	Solid	3.1	2.24	0.009	10.2
	Solution	2.8	2.23	0.009	11.8
Pd-C^{red}	Solid(XRD)	1	3.16	-	-
	Solid	1.2	3.18	0.009	-4.3
	Solution	1.3	3.08	0.012	1.7
Pd-O	Solid(XRD)	1	3.50	-	-
	Solid	1.0	3.50	0.017	2.5
	Solution	1.3	3.50	0.022	5.6

<u>Fit:</u> *R*-space, 2.8 < *k* < 15.0, 1.0 < *R* < 3.5, *N$_{ind}$* = 21; solid *k^0*-weighted V. I. = 0.06, V. A. = 0.03 and *k^3*-weighted V. I. = 0.76, V. A. = 0.35; solution *k^0*-weighted V. I. = 0.05, V. A. = 0.02, *k^3*-weighted V. I. = 1.43 V. A. = 0.73.

In the EXAFS data-analysis it was observed that k^3-weighting of the Fourier transform, as normally used in the literature, leads to the absence of peaks in the Fourier transform at distances above ~2.3 Å. However, as can be seen in Figure 2 the k^0-weighted Fourier transform shows peaks still visible up to distances of ~3.5 Å. The lack of peaks in the k^3-weighted Fourier transforms at distances above 2.3 Å, implies that at high values of k the Pd-C$_{red}$ and the Pd-C$_{whi}$ EXAFS contributions are opposite in phase and cancel each other. The most reliable analysis of the EXAFS data could be obtained by fitting the first two coordination shells (due to a Pd-P and a Pd-C contribution) using a k^3-weighted fit and fitting the additional higher coordination shells using a k^0-weighting, fixing the Pd-P and Pd-C contributions. During the fitting procedure all parameters are optimized. The total fits are of good quality in all weightings applied as can be concluded from the low variances found between both the imaginary and absolute parts of the Fourier transforms of the fits and the spectra (Table 1).[2] The fits of Fourier transform of each difference file with the Fourier transform of the calculated EXAFS of each individual coordination are also of high quality in both k^0- and k^3-weighting.

The results of the EXAFS data-analysis are given in Table 1. The structural parameters for the solid samples obtained with EXAFS are in good agreement with the XRD results. Thus, EXAFS confirms that the orientation of the allyl moiety towards the Pd is similar for both solid state complexes as was found with XRD.[6] However, major structural differences (Table 1a) are found for the [(dppe)Pd(C$_5$H$_9$)]$^+$ complex between solid state and in THF. The differences observed in the Fourier Transform (Figure 2b) are reflected in the fitted data as can be seen in Table 1a. The coordination number of the Pd-C^{red} contribution is increasing from one to two, whereas at the same time the coordination number of the Pd-C^{yel} contribution is changing from three to two. The increase in Debye-Waller factor for the Pd-C^{red} shell is consistent with both the increase in coordination number and the increase in disorder going from solid state to solution. The decrease in Debye-Waller factor for the Pd-C^{yel} contribution agrees with a coordination number of two instead of three. In solid state three carbon atoms contribute to this shell with a rather high deviation in distances, whereas in THF only two carbon atoms remain at a somewhat smaller distance with a smaller deviation. The Pd-P^{blue} and Pd-C^{white} distances are not changing significantly when dissolving the complex, indicating that the Pd-ligand itself is hardly influenced by dissolving the complex. The Debye-Waller factor increases due to a higher disorder in solution.

The differences between solid state and solution can be clearly visualized by showing the difference files of the Pd-C^{red} contribution, given in Figure 3. The increase in intensity in the solution spectrum can be directly correlated to the increase in coordination number from one to two. The observed differences in the imaginary part of the spectrum are indicative for the smaller distance in solution. The Pd-P and Pd-C^{whi} distances are not changing significantly when dissolving the complex, indicating that the Pd-ligand itself is hardly influenced by dissolving the complex. The Debye-Waller factor increases due to a higher disorder in the liquid state.

Figure 3: Pd...C^{red} difference file of both the solid state (solid line) and solution (dotted line) measurement on the [(dppe)Pd(C$_5$H$_9$)]$^+$ complex.
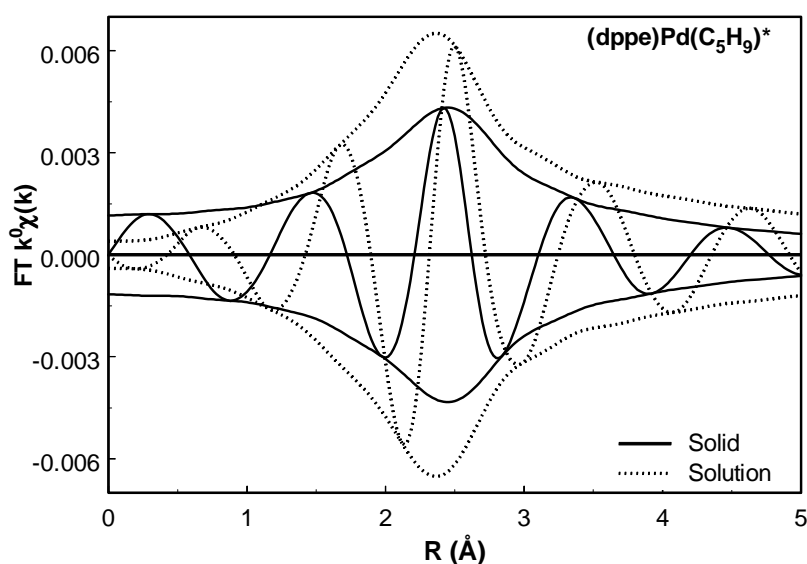
Comparing these structural results in solution with the solid structure of this Pd complex (Figure 1a), a simple but for catalysis very essential explanation for the EXAFS results can be given. The Pd-ligand complex remains unchanged, whereas the Pd-allyl co-ordination and binding in solution is altered.

One C^{yellow} atom bends away from the Pd, possibly as displayed in Figure 1b. This leads to a decrease in the Pd-C^{yellow} co-ordination with a simultaneous increase in the co-ordination number of the Pd-C^{red} shell. As a consequence of this distortion, the two remaining C^{yellow} atoms approach the Pd and the C^{red} atoms are also positioned at a smaller

distance towards the palladium. Since the distances of the methyl groups attached to the allyl (C^{red} and C^{white}) hardly change, most likely the unsubstituted allylic carbon atom changes its conformation. A referee suggested that this change might find its origin in a change in conformation of the dppe ligand relative to the allyl moiety, which cannot be deducted from EXAFS.

The [(DPEphos)Pd(C_5H_9)]$^+$ complex displays almost no structural changes upon dissolution in THF (Table 1b). Dissolving the complex only results in a slight increase in Debye-Waller factors for all contributions, reflecting an increase in static disorder, as expected.

The unsubstituted carbon atom of the allyl moiety changes its conformation in THF and therefore becomes more accessible for a nucleophile to be attacked. In addition, when this carbon atom bends away from the palladium atom, the allyl-Pd binding distorts, decreasing the electron density on this carbon atom so the atom becomes electronically activated. A direct explanation for the favorable formation of linear products using Pd-complexes with a narrow bite angle enforcing ligand[6,10,15] as in dppe is thus proven in this study.

Conclusions

The results of these studies directly establish structure-selectivity relationships in important catalytic reactions. Therefore, we are convinced that the displayed strength of EXAFS techniques of characterizing samples in all aggregation states, and thus in their active phase, will be extremely important in revealing structure-selectivity/activity relationships and reaction mechanisms in homogeneous catalysis.

Acknowledgements

References

1.   L. Hegedus, Transition Metals in the Synthesis of Organic Molecules; University Science Books, **1994**.

2.   D. C. Koningsberger, B. L. Mojet, G. E. van Dorssen, D. E. Ramaker, *Topics Catal.* **2000**, *10*, 143-155.

3.   J. M. Thomas, *Angew. Chem. Int. Ed.* **1999**, *38*, 3588-3628.

4.   M. Tromp, J. A. van Bokhoven, A. M. Arink, J. H. Bitter, G. van Koten, D. C. Koningsberger, *Chem. Eur. J.* **2002**, 8(24), 5667-5678 (**Chapter 3** of this thesis).

5.   (a) B. Åkermark, K. Zetterberg, S. Hansson, B. Krakenberger, A. Vitagliano, *J. Organomet. Chem.* **1987**, *335*(1), 133-142; (b) M. Moreno-Manas, F. Pajuelo, T. Parella, R. Pleixats, *Organometallics* **1997**, *16*(2), 205-209; (c) J. D. Oslob, B. Åkermark, P. Helquist, P.-O. Norrby, *Organometallics* **1997**, *16*(13), 3015-3021; (d) V. Blanchadell, M. Moreno-Manas, F. Pajuelo, R. Pleixats, *Organometallics* **1999**, *18*(24), 4934-4941.

6.   R. J. van Haaren, K. Goubitz, J. Fraanje, G. P. F. van Strijdonck, H. Oevering, B. Coussens, J. N. H. Reek, P. C. J. Kamer, P. W. N. M. van Leeuwen, *Inorg. Chem.* **2001**, *40*, 3363-3372.

7.   R. J. van Haaren, H. Oevering, B. Coussens, G. P. F. van Strijdonck, J. N. H. Reek, P. C. J. Kamer, P. W. N. M. van Leeuwen, *Eur. J. Inorg. Chem.* **1999**, 1237-1241.

8.   M. P. T. Sjorgen, S. Hansson, B. Åkermark, A. Vitagliano, *Organometallics* **1994**, *13*, 1963-1971.

9.   R. J. van Haaren, C. J. M. Druijven, G. P. F. van Strijdonck, H. Oevering, J. N. H. Reek, P. J. C. Kamer, P. W. N. M. van Leeuwen, *J. Chem. Soc. Dalton Trans.* **2000**, *10*, 1549-1554.

10. K. J. Szabo, *J. Am. Chem. Soc.* **1996**, *118*, 7818-7826.

11. (a) R. Pretot, A. Pfaltz, *Angew. Chem., Int. Ed. Engl.* **1998**, *37*(3), 323-325; (b) S. Vyskocil, M. Smrcina, V. Hanus, M. Polasek, P. Kocovsky, *J. Org. Chem.* **1998**, *63*(22), 7738-7748.

12. P. E. Bloch, A. Togni, *Organometallics* **1996**, *15*, 4125-4132.

13. M. Vaarkamp, J. C. Linders, D. C. Koningsberger, *Physica B* **1995**, *208&209*, 159-160.

14. A. L. Ankudinov, B. Ravel, J. J. Rehr, S. D. Conradson, *Phys. Rev. B* **1998**, *58*(12), 7565-7576.

15. M. Kranenburg, P. C. J. Kamer, P. W. N. M. van Leeuwen, *Eur. J. Inorg. Chem.* **1998**, 25-27.

Chapter 6b

Deactivation Processes of Homogeneous Pd Catalysts using *In Situ* Time-Resolved Spectroscopic Techniques

Abstract

UV-Vis, combined with ED-XAFS shows, for the first time, the evolution of inactive Pd-dimers and trimers, that are a possible first stage in the deactivation process of important palladium catalyzed reactions, leading to larger palladium clusters and eventually palladium black.

Introduction

Palladium is the most widely used metal in transition metal catalyzed organic synthesis, as it is capable of catalyzing a wide variety of reactions. While for many applications the desired selectivities and activities can be achieved, the stability of many palladium catalysts is too low for large-scale industrial processes. It is generally assumed that the deactivation of the catalyst occurs via clustering of palladium intermediates in the catalytic cycle.[1] The stability towards the formation of inactive clusters and the performance of the catalyst are influenced by modification of the metal centre with a ligand, most often a phosphine ligand.

Although control of the deactivation is crucial for applications in industry, so far, very few studies to this behavior have been reported.[1] NMR techniques are not suitable to study the aggregation behavior of the catalyst, because the palladium atom itself cannot be observed. The indirect study of the clusters via the phosphorus atoms of the ligand (^{31}P-NMR) is hampered by the high mobility of the complexes.

XAFS spectroscopy[2] is a very powerful technique for the detailed determination of the local structure around an absorbing atom. Measurements can be performed *in situ*. Spectra can be obtained in the millisecond range, using an energy dispersive data acquisition set-up, so-called Energy Dispersive XAFS (ED-XAFS)[3]. Recently, an (ED-)XAFS study on homogenous Pd catalytic systems has been presented in literature.[4] UV-Vis detects the electronic absorption by molecules both *in situ* and time resolved. In our case, absorption bands originating from metal-metal bonds are observed.

Here, we present preliminary results of our UV-Vis[†] and ED-XAFS[††] studies on the deactivation of Pd catalysts in the well-known allylic substitution reaction.[5] The catalytic cycle of these reactions is drawn in the left part of Scheme 1. The size and nature of the inactive homogeneous palladium clusters formed during the reaction as a function of time, depicted on the right hand side, have been studied in detail, as will be described in this paper.

To study the deactivation reactions, the allylic amination is carried out using different (1,1-dimethylallyl)Pd(P-P ligand)OTf complexes as the catalytic intermediate and piperidine as the nucleophile. First, stoichiometric reactions are studied by omitting the allylic substrate, thereby enhancing the rate of deactivation and moreover, decreasing the number of possible reactions. The catalytic reaction is performed using allyl acetate as the substrate. The reactions are monitored *in situ* at ambient conditions. In addition to different (P-P)-ligands, the deactivation behavior in different solvents is investigated.

Results and Discussion

Figure 1. Time resolved UV-Vis spectra of the allylic amination reaction of (dppe)Pd(C$_5$H$_9$)OTf complex in acetone (dotted line, t=0 s) with piperidine. (a) One spectrum every minute (solid lines). (b) One spectrum every ten minutes (solid lines).
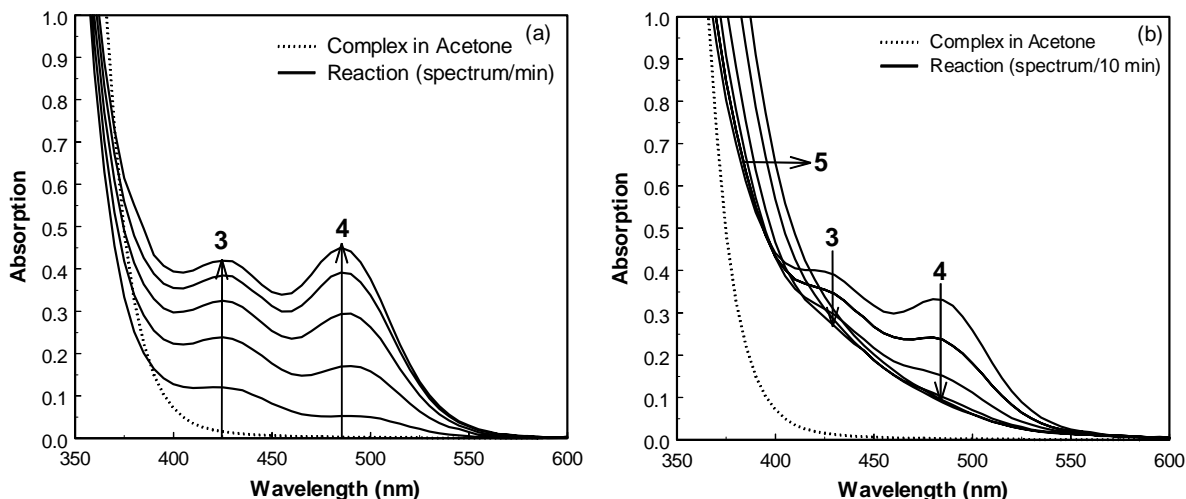
Figures 1a and 1b show typical time resolved UV-Vis spectra for the reaction of 2 mM (dppe)Pd(C$_5$H$_9$)OTf with 10 mM piperidine in acetone (concentrations after mixing). The (dppe)Pd(C$_5$H$_9$)OTf, complex 1, is not UV-Vis active in the energy region > 400 nm (for all solutions applied) as can be observed in Figure 1a (dotted line). Up to ~390 nm the starting complex shows strong absorptions. Immediately after addition of the piperidine, the reaction mixture changes color from light yellow to red which is indicative for the formation of Pd-Pd interactions.[6-9] This color change is reflected in the UV-Vis spectra by the appearance of peaks at ~430 and ~490 nm respectively (peaks 3 and 4 in Figure 1). In time, peaks 3 and 4 first increase, indicated by the arrows in Figure 1a. Deconvolution reveals that two species are formed which are assigned to respectively Pd dimers and Pd trimers, based on peak position.[6-9] Measurements at variable temperatures confirm the assignment of the peaks to metal-metal transitions.[7,10]

In time, the reaction mixture turns dark red while peaks 3 and 4 disappear (Figure 1b). Meanwhile, the band showing strong absorption up to ~390 nm increases and becomes broader (peak 5) in time, suggesting the formation of large palladium clusters (colloidal palladium).[11] The simultaneous disappearance of peaks 3 and 4 suggests that the dimers and

trimers are intermediates in the formation of colloidal palladium. Determination of the colloidal peak is extremely difficult since the peak almost completely overlaps with absorptions of the starting complex. Eventually, Pd metal precipitates in the cuvette.

The rate of formation of dimers, trimers and further deactivation is observed to be a function of both ligand and solvent.[13] For complexes with a small bite angle, both dimers and trimers are observed whereas for large bite angle ligands only dimers are formed. Increasing the polarity of the solvent decreases the deactivation rate.

To gain more insight into the structure of the multi-Pd species, ED-XAFS experiments have been performed. The results of a complex with a large bite angle ligand are shown here, since it forms only dimer complexes and thus facilitates the EXAFS analysis. For a good signal to noise ratio, concentrations of 35 mM (Xantphos)Pd(C_5H_9)OTf complex and 175 mM piperidine in acetone, after mixing, were used. With the ED set-up the reaction was followed with a time resolution of ~1.2 seconds, each spectrum being an average of 15 spectra with an acquisition time of 10 ms each.
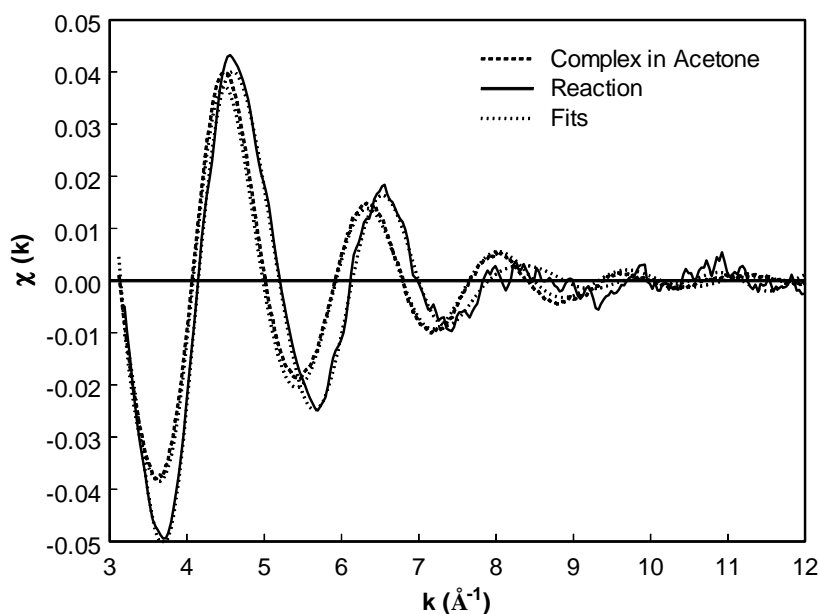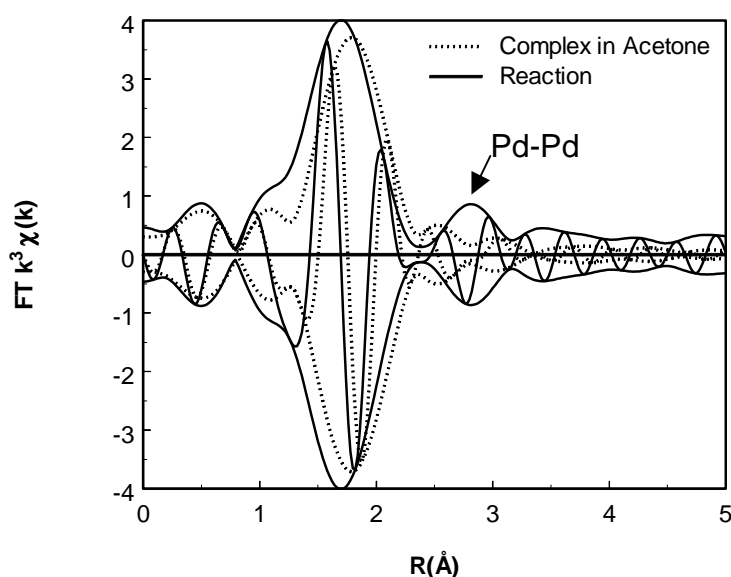

Figure 2. ED-XAFS spectra of (Xantphos)Pd(C_5H_9)OTf in acetone at t = 0 min (striped line) and allylic substitution reaction with piperidine at t = ~5 min (solid line), including fites (dotted lines).

Figure 3: Fourier Transform of EXAFS data of (Xantphos)Pd(C$_5$H$_9$)OTf in acetone (dotted line) and of the reaction of (Xantphos)Pd(C$_5$H$_9$)OTf with piperidine after about 5 minutes (solid line).

Since this deactivation reaction is relatively slow, the EXAFS data of both the (Xantphos)Pd(C$_5$H$_9$)OTf complex in solution (striped line) and the complex after ~5 minutes of reaction (solid line) are given in Figure 2. The corresponding Fourier Transforms are given in Figure 3. The EXAFS data are analyzed using the difference file technique[14] and the EXAFS fitting parameters obtained are given in Table 1. The total fits are of good quality in all weightings applied as can be concluded from the low variances found between both the imaginary and absolute parts of the Fourier transforms of the fits as given in Table 1 and from the raw and fitted EXAFS spectra (dotted lines) shown in Figure 2. The EXAFS data analysis of the (Xantphos)Pd(C$_5$H$_9$)OTf complex in solution shows a structure identical to the solid state. The ED-XAFS measurements of the reaction with piperidine confirm the appearance of a Pd-Pd interaction in time with a Pd-Pd distance of ~2.70 Å, as can also be observed in Figure 3.[15,16] Moreover, EXAFS analysis shows that the Pd-ligand system is still intact and one allylic moiety C$_5$H$_9$ remains present in the formed palladium dimers. Since EXAFS is a bulk technique, the average of all structures is obtained complicating the analysis, especially for Pd complexes forming more different Pd clusters during reaction. Nonetheless, Pd-Pd interaction is always observed in solution. ED-XAFS confirms the rate dependence of formation of multi-Pd clusters on ligand and solvent used.

Both time-resolved techniques indicate the formation of dimers, trimers and possibly larger clusters directly from the start of the catalytic allylic amination reaction. The rate of formation of Pd clusters is lower compared with the stoichiometric reaction.

Table 1: EXAFS analysis results of (Xantphos)Pd(C_5H_9)OTf in acetone (room temperature).[a]

Abs-Sc[b]	N	R (Å)	σ^2 (Å^{-2})	E_0 (eV)
Pd-P	2.2	2.32	0.008	3.7
Pd-C	3.0	2.22	0.015	13.3
Pd-C	2.2	3.03	0.027	-2.1
Pd-C	3.3	3.67	0.036	-7.8

a <u>Fit:</u> R-space, 3.13 < k < 12.3, 1.0 < R < 4.0; k0-weighted V.I.b=0.07, V.A.b=0.04, k3-weighted V.I.=0.25, V.A.=0.14. b Abbreviations: Abs = Absorber, Sc = Scatterer, V.I. = Variance in Imaginary Part, V.A. = Variance in Absolute Part.

Table 2: EXAFS analysis results of (Xantphos)Pd(C_5H_9)OTf in acetone, reaction with piperidine (room temperature).[a]

Abs-Sc[b]	N	R (Å)	σ^2 (Å^{-2})	E_0 (eV)
Pd-P	2.0	2.37	0.018	-9.9
Pd-C	3.1	2.05	0.005	9.6
Pd-C	1.9	3.13	0.002	-3.9
Pd-Pd	1.0	2.70	0.221	-6.9

a <u>Fit:</u> R-space, 3.2 < k < 12, 1.2 < R < 3.5; k0-weighted V.I.b=0.06, V.A.b=0.02, k3-weighted V.I.=0.40, V.A.=0.21. b Abbreviations: Abs = Absorber, Sc = Scatterer, V.I. = Variance in Imaginary Part, V.A. = Variance in Absolute Part.

Based on our EXAFS analysis and on literature of correlated Pd(P-P ligand) dimers[15] and Pd(I) dimers,[16] the dimer and trimer structures, as given in Scheme 1, are proposed. During the allylic amination, the [(P-P ligand)Pd(allyl)]$^+$ complex reacts to a (P-P ligand)Pd^0-complex forming dimers, trimers and bigger clusters, eventually precipitating as palladium black. This deactivation starts immediately at true catalytic conditions, as already observed during kinetic studies,[17] thereby directly lowering the efficiency of the catalyst. Kinetic studies are in progress to model the spectroscopic results obtained and so determine the different reaction rates and equilibriums for the different ligand and solvent systems.[13,18]

Scheme 1. The catalytic cycle of the allylic substitution reaction (left side) and the proposed deactivation mechanism (right side).
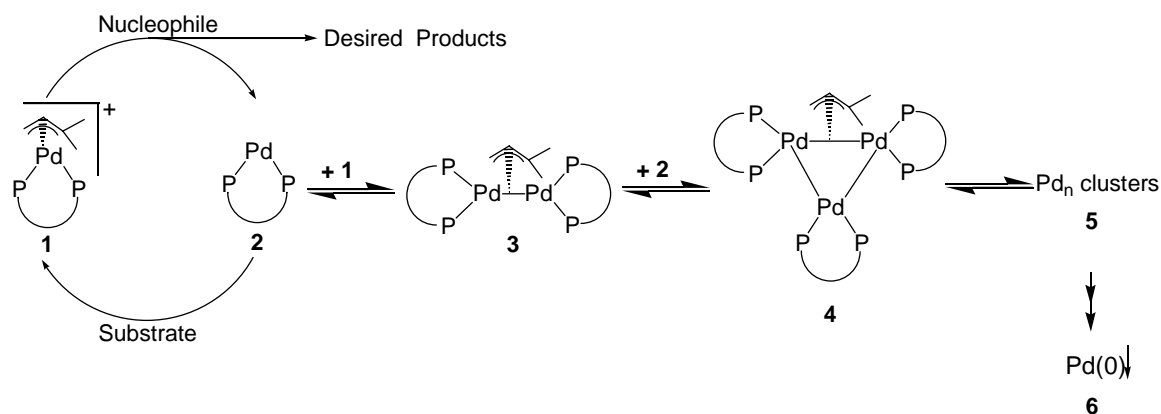
Conclusion

For the first time, time resolved spectroscopic techniques are used for the detailed study of deactivation processes of homogeneous Pd catalysts. Important knowledge about the deactivation mechanism is obtained, directly influencing the efficiency of the catalysts. A set-up for the simultaneous acquisition of both ED-XAFS and UV-Vis spectra is currently tested.

Acknowledgements

Notes and References

†   The UV-Vis spectra were recorded on a Varian Cary 50 UV-VIS spectrophotometer. The time resolved measurements were carried out with an optical fiber probe.

††   ED-XAFS experiments are performed at beamline ID24 of the ESRF, Grenoble, France, using a commercially available BioLogic SFM-4 stopped-flow apparatus in the Energy Dispersive set-up of ID24. Data were acquired using a Laue monochromator.[19] Energy calibration was carried out using a palladium foil. Data are collected using a masked Peltier cooled Princeton CCD camera. (See also **Chapter 2** of this thesis for details on experimental set-up.)

1.   P. W. N. M. van Leeuwen, *Appl. Catal. A* **2001**, *212*, 61.
2.   D. C. Koningsberger and R. Prins, eds. X-ray Absorption, Wiley, New York, **1988**.
3.   e.g. A.J. Dent, *Topics in Catal.* 2002, **18**(1-2), 27; M.A. Newton, A.J. Dent, J. Evans, *Chem. Soc. Rev.* **2002**, *31*, 83.
4.   J. Evans, L. O'Neill, V.L. Kambhampati, G. Rayner, S. Turin, A. Genge, A.J. Dent, T. Neisius, *J. Chem. Soc., Dalton Trans.* **2002**, 2207.
5.   B. M. Trost, D. L. van Vranken, *Chem. Rev.* **1996**, *96*, 395.
6.   O. L. Alves, M.-C. Vitorge, C. Sourisseau, *Nouv. J. Chim.* **1983**, *7*(4), 231.
7.   P. D. Harvey, Z. Murtaza, *Inorg. Chem.* **1993**, *32*, 4721.
8.   L. S. Benner, A. L. Balch, *J. Am. Chem. Soc.* **1978**, *100*(19), 6099.
9.   R. J. H. Clark, C. Sourisseau, *Nouv. J. Chim.* **1980**, *4*(5), 287.
10.   V. M. Miskowski, T. P. Smith, T. M. Loehr, H. B. Gray, *J. Am. Chem. Soc.* **1985**, *107*, 7925.
11.   J. A. Creighton, D. G. Eadon, *J. Chem. Soc. Faraday Trans.* **1991**, *87*(24), 3881.
12.   M. Tromp, J. A. Van Bokhoven, R. J. van Haaren, G. P. F. van Strijdonck, A. M. J. van der Eerden, P. W. N. M. van Leeuwen, D. C. Koningsberger, *J. Am. Chem. Soc.* **2002**, *124*(50), 14814-14815 (**Chapter 3** of this thesis).
13.   G. Rothenberg, M. Tromp, G. P. F. van Strijdonck, in prep.
14.   D. C. Koningsberger, B. L. Mojet, G. E. van Dorssen, D. E. Ramaker, *Topics in Catal.* **2000**, *10*, 143.
15.   P. H. M. Budzelaar, P. W. N. M. van Leeuwen, C. F. Roobeek, *Organometallics* **1992**, *11*, 23.
16.   P. Leoni, M. Pasquali, T. Beringhelli, G. D'Alfonso, A. P. Minoja, *J. Organomet. Chem.* **1995**, *488*, 39.
17.   R. J. van Haaren, Thesis, University of Amsterdam, The Netherlands, **2001**.
18.   G. Rothenberg, S. C. Cruz, G. P. F. van Strijdonck and H. C. J. Hoefsloot, *Adv. Synth. Catal.* **2004**, in press.
19.   M. Hagelstein, C. Ferraro, U. Hatje, T. Ressler, W. Metz, *J. Synchrotron Rad.* **1995**, *2*, 174.

Chapter 7a

Base-free Anaerobic Cu(II) Catalyzed Aryl-Nitrogen Bond Formation

Abstract

The coupling of arylboronic acids with imidazole and benzimidazole in the presence of binuclear bis-μ-hydroxy copper(II) complexes is reported. The reactions can be performed in air as well as under a dinitrogen atmosphere. Reactions are carried out at ambient temperature without the need of base. The presence of water is essential for the reaction to proceed. Ligand effects on the yield and selectivity are reported.

Introduction

The formation of aryl-aryl bonds and aryl-hetero-atom bonds are among the most important tools in organic synthesis. Copper is the most ancient metal used for the coupling of aryl halides to form biaryls,[1] but in the last decade palladium has gained widespread interest.[2-6] In many cases palladium complexes are more active and selective than copper complexes. Reactions such as the *N*-arylation of imidazole, however, generally proceed only when a copper catalyst is used. Because of the low costs of copper in comparison to palladium, the use of copper in industrial processes is preferred.[7] Copper catalyzed aryl-nitrogen bond formations are usually performed under Ullmann-type conditions.[8-11] Several procedures using copper(I) based catalysts have been reported.[12-14] Typically, these reactions require elevated temperatures and have to be performed under a dinitrogen atmosphere. Recent developments by Chan, Lam[15,16] and others[17-19] have shown that the use of stoichiometric quantities of $Cu(OAc)_2$ results in an efficient coupling of amines and arylboronic acids under mild reaction conditions. Collman[20] demonstrated that dimeric copper complexes (10 mol %) give moderate to good yields (40-70%) in C-N coupling reactions. Water can be used as a solvent, but in most methods described, water is excluded from the reaction mixture to avoid the hydrolysis of boronic acid.[21] Procedures described in literature are often performed under a dioxygen atmosphere and in the presence of a base. Base is used to activate the boronic acid for the transmetallation, whereas dioxygen is proposed to play an important role as oxidant for the copper (II) catalyzed arylation of imidazole.[19,20,22]

In this study we report a novel method for the coupling of arylboronic acid and imidazole, using catalytic amounts of a copper catalyst (5 mol %), no base and a NMP/H_2O mixture (1:1 v/v) as the solvent. The reactions were performed at ambient reaction conditions producing moderate to good yields depending on the ligand employed.

Results and Discussion

Our first efforts were directed towards the investigation of solvent effects on the phenylation of imidazole, using 5 mol % $[Cu(OH)TMEDA]_2Cl_2$ as a catalyst, performed under ambient reaction conditions (Scheme 1).

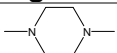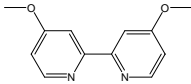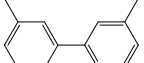**Scheme 1.** Cu(II) catalyzed reaction of imidazole with phenylboronic acid.
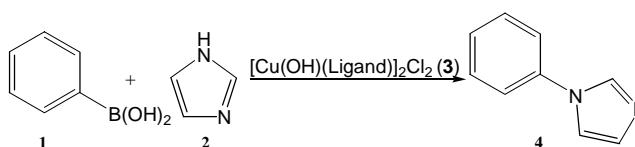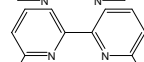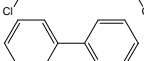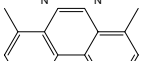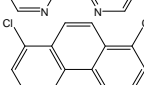

After 20 hours, no conversion is obtained in anhydrous CH_3CN, CH_2Cl_2 or NMP (N-methylpyrrolidone). This can only partly be explained by the poor solubility of the catalyst in these solvents. In water, in which the catalyst is completely dissolved, a 7% yield (GC) was obtained. Also significant amounts of benzene (~7%) and phenol (<2%) were formed. A mixture of NMP and H_2O (1:1 v/v), however, afforded a yield of 56% of the cross coupled product in high selectivity (less than 5% benzene and no phenol was observed). No significant amounts of homo-coupled biphenyl were observed.

To test the effect of ligands on the catalyst performance, dimeric Cu(II) complexes were synthesized bearing several nitrogen-based bidentate ligands. Reaction of CuCl with ligands **a-h** in the presence of dioxygen resulted in a 50-94% yield of the hydroxy bridged dimeric complexes **3a-h**.[21, 23, 24] The results obtained using only 5 mol % of **3a-h** in the arylation of imidazole are summarized in Table 2. Reactions performed with the TMEDA-dimer complex **3a** gave excellent yields (99% after 72 h). Increasing the amount of catalyst **3a** from 5 mol % to 7.5 mol % resulted in a yield of 89% after only 48 hours. Reactions performed with catalyst **3b** bearing an amino alcohol ligand, resulted in a low yield (10% after 20 h). Changing to an aromatic 2,2-bipyridine ligand (**3f**) resulted in a decrease of the yield (68%) after prolonged reaction time (5 days). Using more electron-donating ligands e.g. 4,4-di-MeO-bipyridine (**3c**) and 4,4-di-Me-bipyridine (**3d**) also resulted in a decrease of the yield to respectively 44% (5 days) and 32% (4 days). Reactions performed with dimer complexes possessing the more rigid phenantroline ligands (**3g** and **3h**) showed an increase in yield. The 4,7-di-Cl-phenantroline complex (**3h**) yielded 77% after 4 days. The neocuproine complex (**3g**) even gave full conversion after 4 days.

Table 1. The effect of different ligands on coupling of $PhB(OH)_2$ and imidazole[a]

Entry	Ligand		Time	Yield 4 [%][b]
1		a	20 h	56
			72 h	99
2		b	20 h	10
3		c	5 d	44
4		d	4 d	32
5		e	5 d	24
6		f	5 d	68
7		g	4 d	99
8		h	4 d	77

[a] Reaction conditions: 5 mol % of Cu(II)dimer (**3a-h**), imidazole (68 mg, 1.0 mmol), $PhB(OH)_2$ (121 mg, 1.0 mmol) in NMP/H2O (1:1 v/v, 5 ml), 20 °C in an air atmosphere.
[b] Determined by GC analysis using dihexyl ether as an internal standard.

For further optimization of the reaction conditions, the arylation of imidazole catalyzed by complex **3d** was performed at higher temperatures. Elevation of the reaction temperature to 60 °C raised the yield from 32% to only 39%. At even higher temperatures (60 °C), no significant amount of product is formed, which is probably due to catalyst decomposition. With the increase of temperature there is also an increase of benzene formation.

To investigate the role of dioxygen in our system, we performed reactions with complex **3d** under a pure dioxygen atmosphere, resulting in a similar yield as was obtained at ambient atmosphere. To our surprise, reaction under a dinitrogen atmosphere resulted in the same yield as obtained in the presence of dioxygen. Collman proposed a mechanism for Cu(II) catalyzed C-N bond formations in which the presence of dioxygen is needed for the oxidation of a Cu(II) intermediate to a Cu(III) complex.[21,22] This Cu(III) complex readily undergoes reductive elimination to form the organic product and a Cu(I) complex. This Cu(I) intermediate is then oxidized to the starting dimeric Cu(II) complex by dioxygen. Lam has shown that different oxidizing agents influence the yield of the arylation of imidazole by $Cu(OAc)_2$.[6] Our results suggest that dioxygen is not required as an oxidant under the

conditions employed. This opens the possibility to use oxygen sensitive substrates. Furthermore, this result has important implications for the mechanism (*vide infra*)

Most reported Cu(II) catalyzed arylations of aza-compounds are employed in the presence of a base, limiting the scope of the reaction to substrates which contain base-sensitive functionalities. The method described here does not need the presence of a base. In our search for efficient methods for the arylation of imidazole, however, we studied the effect of pH on the catalyst performance. To this end different buffered solutions were used in the phenylation of imidazole using 5 mol % of catalyst **3a**. At pH 4 and 6 (citrate buffer) no product was observed. At pH 8 (trycine buffer) no product formation was observed either, probably due to the interference of tricine with the copper complex. The use of a $HCO_3^-/CO_3^{2-}/KOH$ buffer (pH 10), yielded only 14 % of coupled product after 20 hours at room temperature. Reactions performed in the presence of 2.5 equivalents (referring to phenyl boronic acid) of NaOH or 1 equivalent of K_2CO_3 yields only traces of product (4% and less than 1% ,respectively). The use of 1 equivalent NaOAc under the same conditions, resulted in a somewhat higher yield of 10 % after 20 hours. Still significantly lower than the results obtained in the absence of a base (56%).

This systematic study towards an efficient Cu(II) catalyzed phenylation of imidazole has resulted in a mild procedure using cheap $[Cu(OH)TMEDA]_2Cl_2$ as a catalyst in NMP/H_2O at ambient reaction conditions. Unfortunately, extension of this method to several aza-compounds such as aniline, diethyl amine, morpholine, piperazine and pyrole was not successful. Benzimidazole, however, could be phenylated using this protocol.

Table 2. Results of C$_{aryl}$-N coupling using different boronic acids [a]

Entry	Boronic Acid	Yield [%][b]
1		75
2		21
3		19
4		7
5		9
6		0
7		21
8		56

[a] Reaction conditions: 5 mol % of Cu(II)dimer **3a**, imidazole (68 mg, 1.0 mmol), ArB(OH)$_2$ (1.0 mmol) in NMP/H2O (1:1 v/v, 5 ml), 20 °C in an air atmosphere.
[b] Determined after 20h. by GC analysis using dihexylether as an internal standard.

Applying the method to several substituted arylboronic acids, resulted in product formation after 20 hours (Table 2). The highest yield (75%) was obtained with an electron withdrawing CF$_3$ substituent at the meta position. The meta nitro analogue, however, only resulted in 21% yield. Introduction of a electron releasing methoxy group at the para position resulted in a similar yield of 19%. The presence of a substituent at the ortho position decreases the yield dramatically. Obviously the steric hindrance caused by these substituents slows down the reaction considerably.

Naphthylboronic acid was coupled to imidazole in 21% yield. Under the conditions employed, hetero aryl boronic acids such as benzofuranboronic acid, resulted in C-C coupling rather than C-N coupling.

The absence of dioxygen as an oxidant for this catalytic reaction, implies the involvement of another oxidant since the reaction is necessarily oxidative. A tentative

mechanism for this reaction is shown in figure 1. The binuclear complex [Cu(OH)(N,N)]$_2$Cl$_2$ (**I)** reacts with imidazole to form a mononuclear Cu(II) species of type **II**. Addition of phenylboronic acid to the starting Cu(II) dimer results in the fast formation of biphenyl. Reaction of this Cu dimer with a stoichiometric amount of phenylboronic acid followed by addition of imidazole does not result in product formation. Addition of stoichiometric amounts of imidazole to the Cu(II) dimer, followed by addition of phenylboronic acid results in the formation of phenylimidazole. From these results we conclude that the first step in the reaction involves imidazole. We propose that imidazole is deprotonated by the hydroxide moiety of the starting complex. The resulting Cu(II)imidazolate complex reacts with the phenylboronic acid reagent to form the product and the starting Cu(II) dimer **I** again. A possible pathway involves the homolytic splitting of the phenyl boronic acid, resulting in the formation of the a transient Cu(iii) species (**III**). After reductive elimination of the product, the known Cu(I) compound **IV** is formed. Next, the boronic species formed (from the phenyl boronic acid) after addition of a phenyl radical to the Cu(ii) intermediate **II**, in combination with water, is involved in the re-oxidation of Cu(I) to the starting Cu(II) dimer. Alternatively, the Cu(II)imidazolate species reacts with the phenylboronic acid to the phenylimidazole product and a Cu(II)-B(OH)$_2$ species. This species decomposes in water to the starting hydroxo-Cu(II) dimer and HB(OH)$_2$. Extensive spectroscopic (EPR, NMR, ED-XAFS, UV-Vis, IR), kinetic and structural (X-ray) studies to further elucidate the reaction mechanism are in progress.

Figure 1. Proposed reaction mechanism for the Cu(II) catalyzed arylation of imidazole under anaerobic conditions.
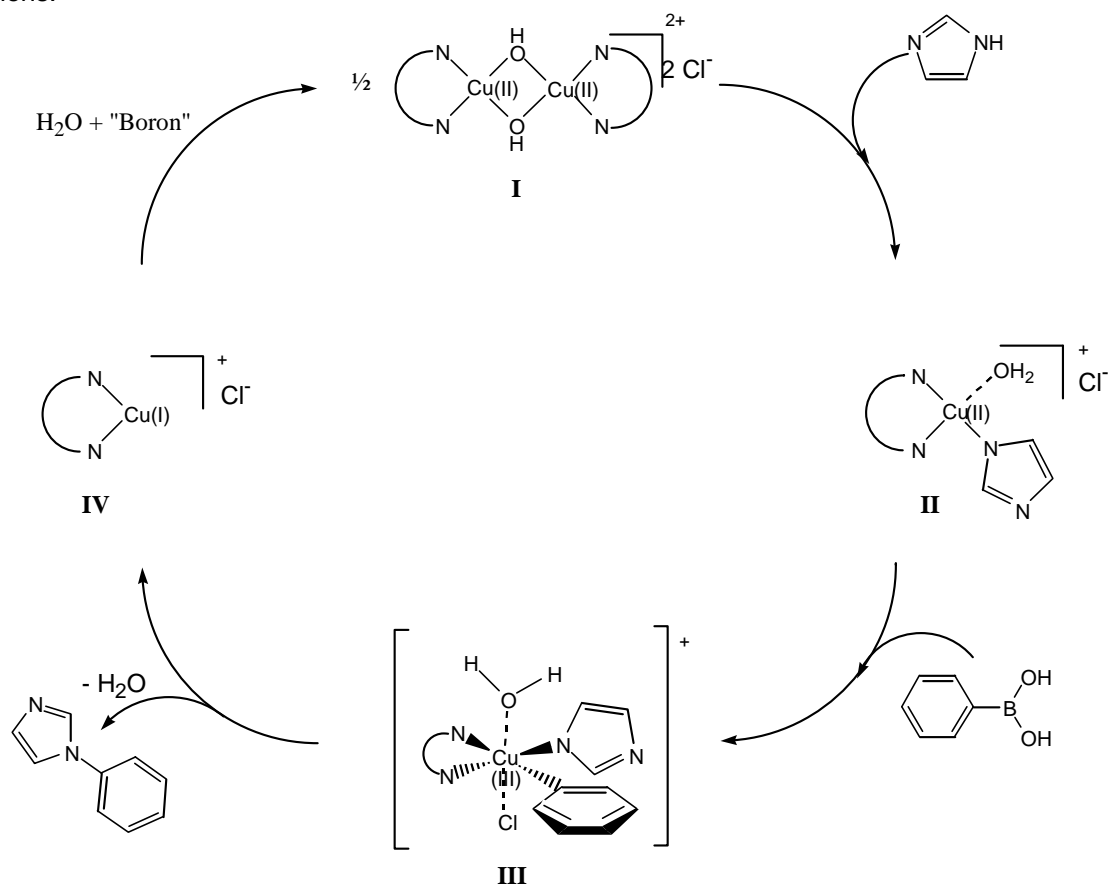
Conclusion

Establishing efficient methods for constructing C_{aryl}-N bonds is currently an active area in organic synthesis. C_{aryl}-N bond containing structures are not only important in biological systems but also common moieties in pharmaceutical research. We have developed a novel, mild method for the N-arylation of imidazole. We have demonstrated that this reaction can be selectively performed in a NMP/H_2O mixture, at ambient temperature and atmosphere, using catalytic amounts of a cheap and commercially available [Cu(OH)TMEDA]$_2$Cl$_2$ dimer as the catalyst. The HSE (Health, Safety and Environmental) acceptable NMP/H_2O mixture makes this an interesting industrial procedure. The product can be separated easily from the reaction mixture by diethyl ether, whereas the catalyst remains in the water layer, making this solvent mixture suitable for recycling. The presence of an NMP/H_2O mixture increases the yield considerably, whereas addition of base and the presence of dioxygen are not needed. Implication of these results for the mechanism, together with spectroscopic studies, will be discussed elsewhere (Chapter 7b).

Experimental Section

General Remarks

Unless stated otherwise, all reactions were carried out in an air atmosphere using 20 cm glass tubes. THF, hexane and diethyl ether were distilled from sodium benzophenone ketyl, CH_2Cl_2, acetonitrile and NMP (*N*-methylpyrrolidone) were distilled from CaH_2 and toluene was distilled from sodium under nitrogen. Reactions in the absence of dioxygen were carried out using standard Schlenk techniques. Reactions under a dioxygen atmosphere were conducted by bubbling dioxygen through the solvent for 15 minutes, followed by presurizing the mixture with 1 bar of dioxygen. Gas chromatographic analyses were run on an Interscience HR GC Mega 2 apparatus (split/splitless injector, J&W Scientific, DB-1 J&W 30 m column, film thickness 3.0 µm, carrier gas 70 kPa He, FID detector) equipped with a Hewlett_packard data system (Chrom-Card). Gas chromatographic mass spectra were run on an Agilent Technologies 6890/5973 GC-MS combined with an Agilent Mass Selective detector. Columtype; HP5MS, length 30 m, film thickness 0.25 µm, crosslinked 5% PhMe-siloxane.

All reagents were purchased from commercial suppliers and used without further purification. Ligand **e**[25] and   bis-*µ*-hydroxy copper(II)complexes (**3a-h**)[21, 23, 24] were prepared according to a literature procedure.

General procedure

To the appropriate amount of Cu-catalyst **3** in 5 ml of solvent was added imidazole **2** (68 mg, 1 mmol) and arylboronic acid **1** (1 mmol). Dihexyl ether (115 *µ*l, 0.5 mmol) was added as an internal standard. When appropriate a base was added. The reaction was stirred under the given conditions. Product formation was determined by GC and GC-MS. Samples (0.05 ml) were taken from the reaction mixture at regular time intervals. CH_2Cl_2 and a saturated solution of NH_4Cl were added to the sample. After separation of the layers, the organic layer was filtered through a plug of $MgSO_4$. The retention time of the products (phenylimidazole, biphenyl, phenol and benzene) were confirmed with authentical samples.

References

1. F. Ullmann, *Ber. Dtsch. Chem. Ges.* **1903**, *36*, 2382.
2. A. R. Muci, S. L. Buchwald, *Topp. Curr. Chem.* **2002**, *219*, 131.
3. J. F. Hartwig, *Angew. Chem. Int. Ed. Engl.* **1998**, *37*, 2046.
4. J. P. Wolfe, S. Wagaw, J.-F. Marcoux, S. L. Buchwald, *Acc. Chem. Res.* **1998**, *31*, 805.
5. G. Mann, J. F. Hartwig, M. S. Driver, C. J. Fernández-Rivas, *J. Am. Chem. Soc.* **1998**, *120*, 827.
6. P. Y. S. Lam, G. Vincent, C. G. Clark, S. Deudon, K. J. Jadhav, *Tetrahedron Lett.* **2001**, *42*, 3415.
7. J. Hassan, M. Sévignon, C. Gozzi, E. Schulz, M. Lemaire, *Chem Rev.* **2002**, *102 (5)*, 1359.
8. J. Lindley, *Tetrahedron* **1984**, *40*, 1433.
9. R. G. R. Bacon, H. A. O. Hill, *J. Chem. Soc.* **1964**, 1097.
10. P. E. Fanta, *Synthesis* **1974**, 9.
11. M. Sainsbury, *Tetrahedron* **1980**, *36*, 3327.
12. R. K. Gujadhur, C. G. Bates, D. Venkataraman, *Org. Lett.* **2001**, *3*, 4315.
13. F. Y. Kwong, S. L. Buchwald, *Org. Lett.* **2003**, *5*, 793.
14. J. C. Antilla, A. Klapars, S. L. Buchwald, *J. Am. Chem. Soc.* **2002**, *124*, 11684.
15. D. M. T. Chan, K. L. Monaca, R. P. Wanag, M. P. Winters, *Tetrahedron Lett.* **1998**, *39*, 2933.
16. P. Y. S. Lam, S. Deudon, K. M. Averill, R. Li, M. Y. He, P. DeShong, C. G. Clark, *J. Am. Chem. Soc.* **2000**, *122*, 7600.
17. J. C. Antilla, S. L. Buchwald, *Org. Lett.* **2001**, *13 (3),* 2077.
18. S. Yu, J. Saenz, J. K. Srirangam, *J. Org. Chem.* **2002**, *67*, 1699.
19. P. Y. S. Lam, D. Bonne, G. Vincent, G. C. Clark, A. P. Combs, *Tetrahedron Lett.* **2003**, *44*, 1691.
20. J. P. Collman, M. Zhong, C. Zhang, S. Costanzo, *J. Org. Chem.* **2001**, *66*, 7892.
21. J. P. Collman, M. Zhong, L. Zeng, S. Costanzo, *J. Org. Chem.* **2001**, *66*, 1528.
22. J. P. Collman, M. Zhong, *Org. Lett.* **2000**, *2*, 1233.
23. W. R. McWhinnie, *J. Chem. Soc.* **1964**, 2959.
24. J. R. Ferraro, W. R. Walker, *Inorg. Chem.* **1965**, *4*, 1382.
25. H. C. Brown, K. LeRor Nelson *J. Chem Soc.* **1953**, *75*, 24.

Multi-technique Approach to Reveal the Mechanism of Cu(II) Catalyzed Arylation Reactions

Abstract

Multiple *in situ* and time-resolved spectroscopic techniques (EDXAFS, UV-Vis, EPR, NMR, XRD) are described to reveal detailed structural and electronic information on reaction intermediates of an important, anaerobic Cu(II) catalyzed N-arylation of imidazole. Based on these results, a novel mechanism for this Cu(II) catalyzed arylation reaction is proposed.

The N-arylation of imidazole was performed in a NMP/H_2O solvent mixture, at ambient temperature and atmosphere, using the commercially available Cu-catalyst [Cu(OH)(TMEDA)]$_2$Cl$_2$ (**I**). The system was shown to be a good and effective catalyst. The reaction does not require the presence of dioxygen or a base. The presence of H_2O is however necessary for the reaction to proceed.

The spectroscopic study resulted in the characterization of several reaction intermediates. The first and selectivity determining step in the reaction is the reaction of the dimeric Cu(II) complex with imidazole, forming a monomeric Cu(II)(Imidazole) intermediate **II**. Upon subsequent addition of phenylboronic acid an Cu(III)(imidazolate)(phenyl) intermediate **III** is formed, which after reductive elimination forms the phenylimidazole product and the Cu(I) monomeric species **IV** as characterized here. Finally, the Cu species is reoxidized forming back Cu(II) monomeric and dimer complexes. Inhibition by imidazole and phenylimidazole is observed. The phenylboronic acid is, in combination with H_2O, involved in the oxidation and reoxidation steps in the described catalytic cycle.

Introduction

The formation of aryl-aryl bonds and aryl-hetero-atom bonds are among the most important reactions in organic synthesis. C_{aryl}-N containing structures are important in biological systems and are common moieties in pharmaceuticals. Copper is the most ancient transition metal used for the synthesis of bi-aryls.[1,2] Since palladium complexes are by far the most used, they are the more studied catalysts for these reactions. In many cases, palladium catalysts are more active and selective under milder conditions compared to copper. Some reactions such as the arylation of imidazole, however, only proceed with copper catalysts. Because of the lower costs of copper compared to palladium, the use of copper is preferred over palladium for industrial processes.[3]

Due to the more general use of palladium catalysts for coupling reactions, much research[2a,4] has been dedicated towards understanding the reaction mechanism of these catalysts and only a few studies concerning the copper catalyzed mechanism have appeared. The mechanisms proposed for Cu catalyzed reactions are as yet reasonable guesses, because none of the intermediates have been isolated or characterized.[5,6,7]

In this paper, Cu(II) catalyzed C_{aryl}-N and C_{aryl}-C_{aryl} couplings reactions are investigated in detail using several spectroscopic techniques. We use a modified[8] Collman protocol[6] for this arylation reaction. As a model reaction we study the coupling of imidazole with phenylboronic acid in the presence of the binuclear tetramethylenediamine bis-μ-hydroxy copper(II) complex [Cu(OH)(TMEDA)]$_2$Cl$_2$ (**I**) in NMP/H$_2$O (1/1 v/v %) at ambient conditions (Scheme 1) (TMEDA = tetramethylenediamine), NMP = *N*-methylpyrrolidone). We have already shown that the presence of water was essential for this reaction, whereas a base was not required. [8] Surprisingly,[5,6,7] the reaction proceeds under anaerobic conditions, i.e. it does not need O$_2$ as an oxidant. Based on these results, we tentatively proposed an alternative reaction mechanism.[8] Here we describe the application of a combination of spectroscopic techniques, time-resolved and *in situ*, in an attempt to identify reaction intermediates.

X-ray Absorption Fine Structure (XAFS) Spectroscopy is a powerful technique to determine the local structure of metal complexes, such as the type and number of neighboring atoms, distances and electronic properties. XAFS can be applied *in situ*, e.g. in solution in which the reaction is taking place. Using an energy dispersive data acquisition set-up (ED-XAFS), spectra can be obtained in the sub-second range during reaction.[9] With the use of UV-Vis spectroscopy, the electronic absorption by molecules can be detected both *in situ* and time-resolved. A newly developed set-up enables the simultaneous

acquisition of time-resolved *in situ* XAFS and UV-Vis data on homogeneous catalytic systems.[10] Extensive Nuclear Magnetic Resonance (NMR) and Electron Paramagnetic Resonance (EPR) studies are performed to gain more insights in the diamagnetic and paramagnetic species present in the reaction mixture. Based on these spectroscopic studies, in combination with catalytic results, a novel reaction mechanism is proposed.

Scheme 1. Copper catalyzed coupling reaction of imidazole with phenylboronic acid.
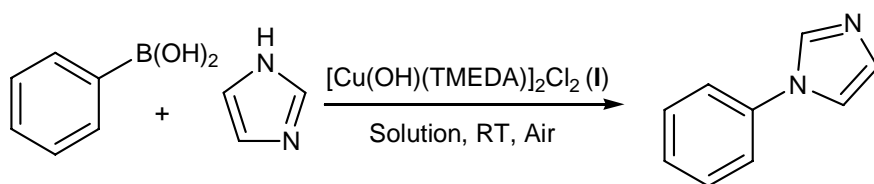
Results and Discussion

Catalysis

Recently, we have established a modified protocol[8] for the N-arylation of imidazole that works under milder conditions than previous ones.[6,7,11,12] It was demonstrated that the reaction can be performed in a NMP/H_2O mixture, at ambient temperature and atmosphere, using catalytic amounts of a cheap and commercially available Cu-catalyst [Cu(OH)(TMEDA)]$_2$Cl$_2$ (**I**). The use of an NMP/H_2O mixture as a solvent, instead of either H_2O or NMP only, increased the yield considerably. Surprisingly, H_2O is necessary for the reaction to proceed whereas the addition of base and dioxygen are not required.

The absence of dioxygen as an oxidant for this catalytic reaction implies the involvement of another oxidant than dioxygen. A reaction mechanism recently proposed in literature[8] suggests the involvement of radicals. To gain more insights in the nature of the oxidizing species in this system, the reaction was performed in the presence of both radical scavengers as well as radical initiators. As can be observed in Table 1, the use of scavengers resulted in a considerable decrease in C-N coupling yield or even complete inhibition of the reaction. This might be indicative for the involvement of radical intermediates; however, it is known that redox reactions or complexation of the scavengers (some scavenger can act as a Cu ligand) with the catalyst can also result in reaction inhibition. Radical initiators on the other hand did also result in a decrease of activity, showing that the reaction does not require a radical initiator and that probably catalytic intermediates are "derailed" by radicals.

The use of only phenylboronic acid as a reactant results in a fast C-C homocoupling, forming biphenyl. A stoichiometric reaction of the Cu(II) dimer and phenylboronic acid, followed by the addition of imidazole does not result in C-N product formation, while the reverse addition sequence (first imidazole and then phenylboronic acid) resulted in a selective formation of the C-N coupled product. We therefore concluded that a Cu complex reacts fast with imidazole in the selectivity-determining step, followed by reaction with the boronic acid.[8] Experiments with increasing amounts of imidazole or phenylimidazole product added to the reaction mixture result in a decrease of the reaction rate. This suggests inhibition of the reaction by excess imidazole and/or phenylimidazole.

Table 1. The influence of radical scavengers and initiators on the reaction of imidazole and phenylboronic acid using the $[Cu(OH)(TMEDA)]_2Cl_2$ catalyst. C-N coupling yield is reported here.

Additive	Time	GC Yield[a]
No	20 h	56
	72 h	99
Scavengers		
2,6-di-t-butyl-phenol	20 h	5
	72 h	23
Hydroquinone	20 h	0
	72 h	0
Tetra-Chloro-Hydroquinone	20 h	0
	72 h	0
Initiators		
H_2O_2 (35% in H_2O)	20 h	2
	72 h	37
Benzoylperoxide	20 h	0
	72 h	0
AIBN	20 h	3
	72 h	19

[a] <u>Reaction conditions</u>: 5 mol% Cu catalyst, 1/1 mmol imidazole/PhB(OH)$_2$ in NMP/H$_2$O (1/1), ambient conditions. The yield was determined by GC.

Spectroscopic studies

The Cu(II) catalyzed reaction of imidazole with phenylboronic acid (Scheme 1) was further investigated using multiple spectroscopic techniques. Stoichiometric reactions were performed to decrease the number of reaction intermediates. Single step reactions were performed to mimic possible subsequent individual steps of the catalytic reaction cycle. An overview of the reactions performed is given in Scheme 2.

Scheme 2. Overview of the reactions studied.
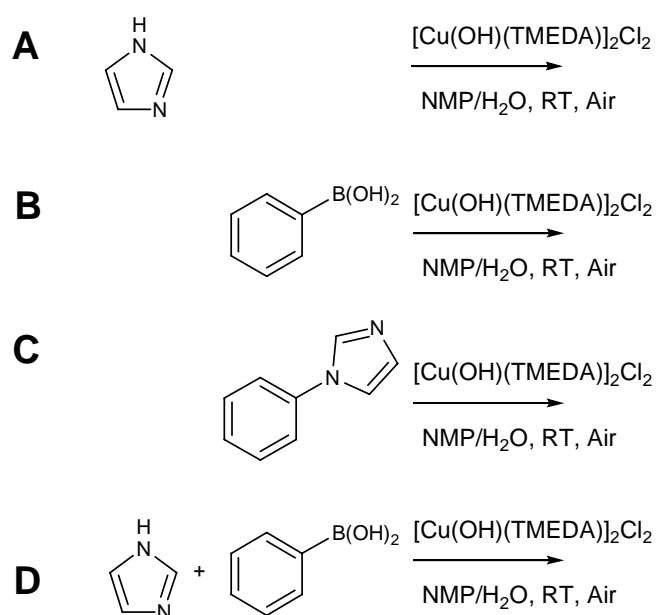
[Cu(OH)(TMEDA)]$_2$Cl$_2$ (I)

First, the dimeric structure of the starting [Cu(OH)(TMEDA)]$_2$Cl$_2$ (**I**) complex in NMP/H$_2$O solution is confirmed. The results obtained with the combined EDXAFS/UV-Vis set up are shown in Figures 1a and 1b. The XANES spectrum (Figure 1a) clearly displays two pre-edge features at 8979 and 8985 eV, assigned to respectively 1s→3d Cu(II) and 1s→4p Cu(II) transitions and characteristic of the presence of a Cu(II) species.[13] The UV-Vis absorption spectrum exhibits a ligand to metal charge transfer (LMCT) band of the bridging O(H) to Cu(II) at ~355 nm.[14] Additional CT bands up to ~300 nm and d-d transitions at ~620 nm are observed.

Figure 1. (a) XANES and (b) UV-Vis spectra of [Cu(OH)(TMEDA)]$_2$Cl$_2$ in NMP/H$_2$O.
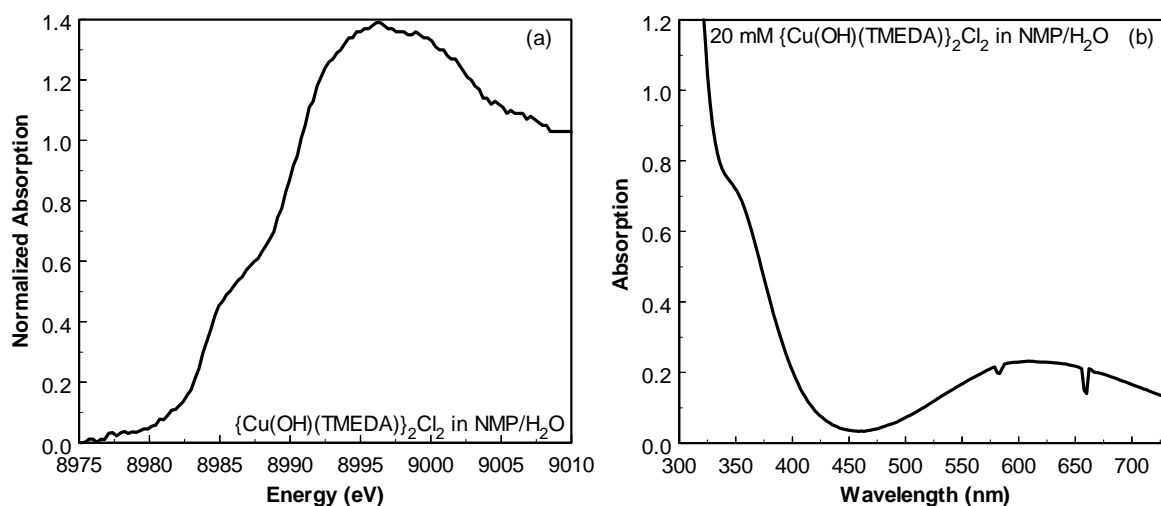
The raw EXAFS data are shown in the Supplementary Materials, Figure S1. EXAFS data analysis of the $[Cu(OH)(TMEDA)]_2Cl_2$ (**I**) complex was performed. The Fourier transforms of the raw EXAFS data and the obtained EXAFS fit for these data are shown in Figure 2. These figures show a good agreement between the raw EXAFS data and fit, which is confirmed by the low variances in fit found for both the imaginary and absolute part (Table 2). The obtained EXAFS fitting parameters show four C/N/O atoms at a short distance of 2.02 Å and one Cu at a longer distance of 2.96 Å. In the EXAFS analysis we cannot distinguish between C, N and O, because they are neighboring atoms in the periodic table and thus have similar backscattering amplitudes.[15] Fitting the first contribution in EXAFS using the three different calibrated Cu-C, Cu-N and Cu-O references only results in slightly different E_0 values. Based on the Cu-Cu contribution detected and the short distance of the four C, N or O atoms to the Cu, we can conclude that the dimeric structure in NMP/H_2O solution is intact. The first shell around Cu thus consists of the two N atoms of the TMEDA ligand and two O atoms of the two bridging OH groups.

Figure 2. Fourier Transform of the EXAFS data of $[Cu(OH)(TMEDA)]_2Cl_2$ in NMP/H_2O (room temperature), raw (solid line) and fit (dotted line); (a) k^0-weighted, (b) k^2-weighted.
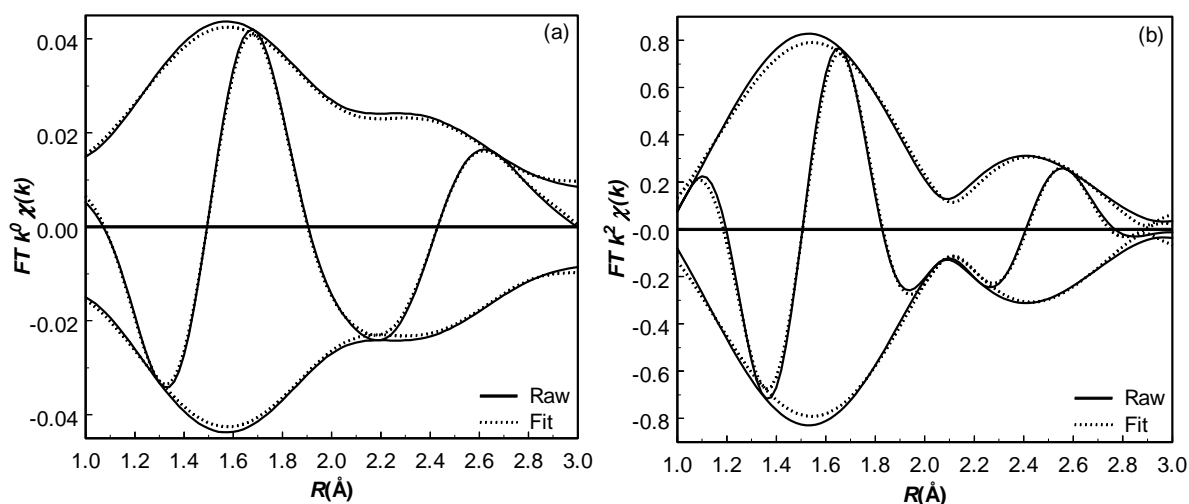
Table 2. EXAFS data analysis results of the [Cu(μ-OH)(TMEDA)]$_2$Cl$_2$ in NMP/H$_2$O (room temperature) and the complexes present after the different reactions.[b]

Abs-Sc[a]	N	R [Å]	σ^2 [Å^{-2}]	E_0 [eV]	V.I.[a]	V.A.[a]
[Cu(OH)(TMEDA)]$_2$Cl$_2$ in NMP/H$_2$O						
[*R*-space fit, 2.4 < *k* < 7.8, 0.8 < *R* < 3.0]						
Cu-N (C/O)	3.8	2.02	0.006	-2.3	k^0-weighted:	
Cu-Cu	0.9	2.96	0.003	6.0	0.10	0.07
					k^2-weighted:	
					0.56	0.27
A. [Cu(OH)(TMEDA)]$_2$Cl$_2$ + Imidazole in NMP/H$_2$O						
[*R*-space fit, 2.35 < *k* < 7.8, 1.0 < *R* < 3.0]						
Cu-N (C/O)	4.2	2.01	0.001	-0.3	k^0-weighted:	
Cu-C (N/O)	3.9	2.94	0.003	-4.6	0.24	0.13
					k^2-weighted:	
					0.07	0.05
B. [Cu(OH)(TMEDA)]$_2$Cl$_2$ + PhB(OH)$_2$ in NMP/H$_2$O						
[*R*-space fit, 2.0 < *k* < 7.7, 1 < *R* < 3.7]						
Cu-N (C/O)	5.7	1.96	0.002	-5.3	k^0-weighted:	
Cu-C (N/O)	1.4	2.77	0.003	-1.1	0.03	0.03
Cu-C (N/O)	3.7	3.92	0.003	-0.3	k^2-weighted:	
					0.007	0.004
C. [Cu(OH)(TMEDA)]$_2$Cl$_2$ + Phenylimidazole in NMP/H$_2$O						
[*R*-space fit, 2.4 < *k* < 8, 0.8 < *R* < 3.8]						
Cu-N (C/O)	4.2	1.97	0.004	-1.0	k^0-weighted:	
Cu-C (N/O)	2.4	2.98	0.001	-8.6	0.80	0.53
Cu-C (N/O)	5.1	3.86	0.001	-0.7	k^2-weighted:	
					0.34	0.19

[a] Abbreviations: Abs = Absorber, Sc = Scatterer, V.I. = Variance in Imaginary Part, V.A. = Variance in Absolute Part.
[b] The raw EXAFS data are shown in the Supplementary Material Figure S1a. The k^0-weighted and k^2-weighted Fourier Transforms of the raw EXAFS and fitted EXAFS data are shown in the Supplementary Material in Figures S2-S4.

The EPR spectrum of a frozen solution (~20 K) of dimer **I** (in NMP/H$_2$O) is shown in Figure 3 (dotted line). A very weak signal with Cu hyperfine structure is observed. This signal possibly originates from a Cu(II) monomeric species formed by dissociation of a small part of the dimer or a small impurity of CuCl$_2$ formed during synthesis of dimer **I**. But as expected for a coupled Cu(II) dimer, this compound is EPR silent. The integrity of the dimeric Cu(II) structure is confirmed by ^{1}H-NMR, showing two broad signals at 70 - 100 ppm. These signals are diagnostic for an anti-ferromagnetic coupling of two copper nuclei.[16]

Thus, the dimeric Cu(II) structure of the [Cu(OH)(TMEDA)]$_2$Cl$_2$ (**I**) complex in NMP/H$_2$O solution is confirmed by all characterization techniques presented here in the wide concentrations range used for the different techniques.

Figure 3. X-band EPR spectra of [Cu(OH)(TMEDA)]$_2$Cl$_2$ in NMP/H$_2$O (dotted black line), after addition of imidazole (solid grey line), and after subsequent addition of phenylboronic acid (solid black line) [T = ~20 K].
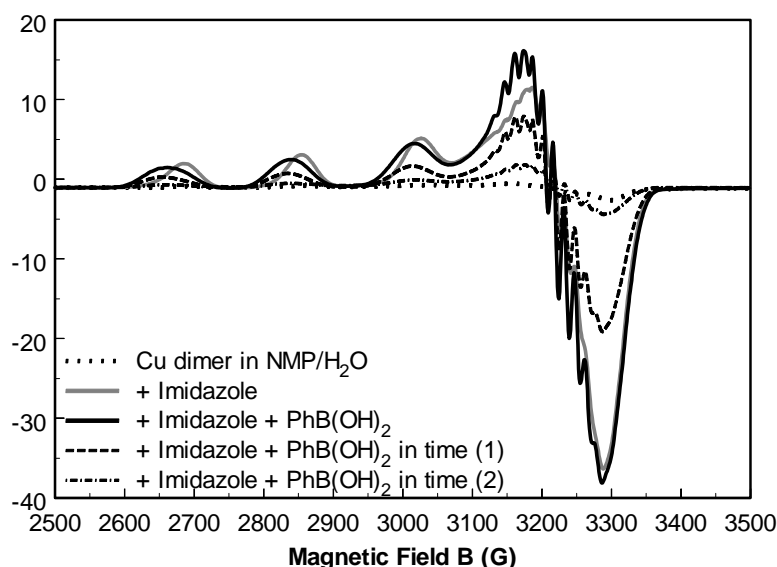
Reaction A: [Cu(OH)(TMEDA)]$_2$Cl$_2$ + Imidazole

From stoichiometric reaction results it was concluded that imidazole reacts with the catalyst prior to reaction with the phenylboronic acid.[8] The addition of one equivalent of imidazole (per mole of Cu) to a solution of [Cu(OH)(TMEDA)]$_2$Cl$_2$ is therefore performed in an attempt to characterize and isolate the resulting reaction intermediate. Based on cryo-magnetic measurements in DMF the formation of a trinuclear Cu(II) compound, bridged by deprotonated ligands has been suggested.[17] The reaction in methanol and subsequent crystallization from methanol diethylether afforded blue crystals suitable for X-ray analysis. Preliminary results of the X-ray diffraction experiment confirms the trinuclear Cu(II) structure as displayed in Figure 4.[18] Each (TMEDA)Cu-unit is bridged by two imidazolate anions to the other two copper centra. This crystal structure suggests that the hydroxy ligand of the copper dimer has deprotonated the imidazole and coordination of the imidazolate to the Cu(II) unit takes places. The deprotonation of the imidazole was confirmed by IR (no N-H stretching mode was observed in the region 3200-3500 cm^{-1}).[17] From a methanol/ether solution, a trinuclear Cu(II) with a coordinating chloro ligand thus crystallizes.

Figure 4. Molecular plot of [Cu(Imidazole)(TMEDA)]$_3$Cl$_3$.[18]
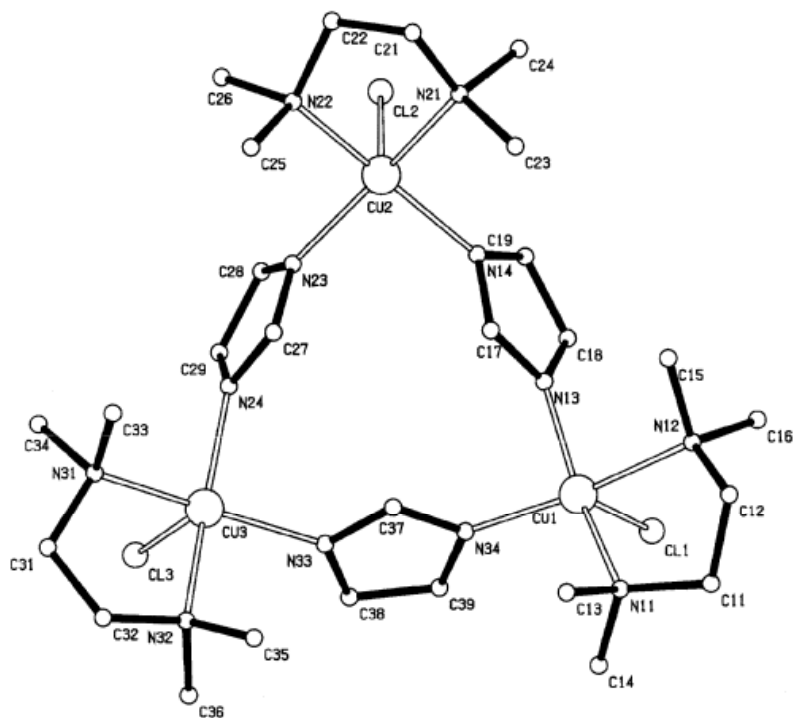
Only one crystal with a similar structure has appeared in literature.[19] The trimeric [L₃Cu₃(Imidazolate)₃]ClO₄ (with L = 1,4,7-trimethyl-1,4,7-triazacylcononane) crystal structure is reported in which the Cu centra are connected via imidazolate anions. In literature, a crystal structure of a monomeric [(TMEDA)Cu(II)(imidazolate)₂] complex obtained from reaction with an excess of imidazole and base was described.[17]

EXAFS analysis of the isolated [Cu(Cl)(Imidazolate)(TMEDA)]₃ complex in NMP/H_2O solution, presented in Table 3, shows the presence of 3 N atoms and 1 chloride, confirming the Cu(Cl)(imidazole)(TMEDA) structure in solution. A Cu-Cu contribution was not observed due to its long distance of ~6Å. The presence of only 3 instead of 4 N atoms in close proximity to the Cu suggests the dissociation of the Cu trimer in monomeric Cu(II) species. In EPR the blue solution of [Cu(Cl)(Imidazolate)(TMEDA)]₃ displays a strong Cu(II) signal, with a small N hyperfine, confirming a monomeric Cu(II) structure. The small N superhyperfine hyperfine structure suggests the presence of three N atoms, i.e. two of the TMEDA ligand and one of an (coordinated) imidazole(at)e. ^{1}H-NMR neither displays distinct characteristics peaks in the range of diamagnetic species, nor the presence of an anti-ferromagnetic species at 70 – 100 ppm. This monomeric structure in NMP/H_2O is in contrast to the proposed trimer described in reference 17 in which the trimeric structure in DMF solution remains intact.

Table 3. EXAFS data analysis results of the isolated Cu complexes.[b]

Abs-Sc[a]	N	R [Å]	σ^2 [Å⁻²]	E_0 [eV]	V.I.[a]	V.A.[a]
[Cu(Cl)(Imidazolate)(TMEDA)]₃ in NMP/H_2O						
[*R*-space fit, 2.7 < *k* < 7.95, 1.0 < *R* < 3.0]						
Cu-N (O/C)	3.2	1.94	0.005	-1.3	k^0-weighted:	
Cu-Cl	1.0	2.62	0.005	-7.4	0.90	0.20
					k^2-weighted:	
					0.60	0.17
[Cu(OH)(PhenylImidazole)(TMEDA)]Cl in NMP/H_2O						
[*R*-space fit, 2.70 < *k* < 7.95 Å⁻¹, 0.8 < *R* < 2.8 Å]						
Cu-N (C/O)	5.0	1.97	0.005	-5.8	k^0-weighted:	
Cu-C (N/O)	5.6	2.97	0.005	-4.4	0.34	0.28
					k^2-weighted:	
					0.54	0.29

[a] Abbreviations: Abs = Absorber, Sc = Scatterer, V.I. = Variance in Imaginary Part, V.A. = Variance in Absolute Part. [b] The raw EXAFS data are shown in the Supplementary Material Figure S1b. The k^0-weighted and k^2-weighted Fourier Transforms of the raw EXAFS and fitted EXAFS data are shown in the Supplementary Material in Figures S5-S6.

Monitoring the stoichiometric reaction of the Cu(II) catalyst (**I**) and imidazole in NMP/H_2O with EDXAFS/UV-Vis, Figure 5, hardly shows any changes in the Cu(II) XANES region in time. The EXAFS data-analysis of the resulting reaction mixture are given in Table 2 and reveal the disappearance of the Cu-Cu contribution. Additionally 4 C/N/O atoms are detected at an average of 2.94 Å. In contrast to the isolated trimer structure in solution, the reaction mixture of dimer **I** with imidazole does not show the presence of chloro atom at a distance less than 3 Å from the Cu absorber atom.

Time-resolved UV-Vis spectra simultaneously taken with the EDXAFS spectra, display the dissociation of the dimeric structure by the disappearance of the LMCT band (Figure 5b, 355nm). The d-d band slightly shifts while retaining its intensity indicating only small changes in Cu(II) surroundings. ^{1}H-NMR confirms the dissociation of the Cu dimers by the disappearance of the lower field peaks at 70 – 100 ppm.

Upon addition of imidazole to the copper dimer (**I**) solution, an intense EPR signal characteristic for a monomeric Cu(II) species appears (Figure 3). Simulation of the axial spectrum yielded the following g-values: $g_{//}$= 2.265, $g_{\perp}$= 2.060. The $g_{//}$ signal reveals strong Cu hyperfine splitting ($A^{Cu}_{//}$ = 514 MHz). The hyperfine coupling pattern for the $g_{\perp}$ signal was satisfactorily simulated by assuming superhyperfine coupling with two pairs of equivalent nitrogen nuclei ($A^{N1}_{\perp}$= 77 MHz and $A^{N2}_{\perp}$= 48 MHz) and an additional small hyperfine contribution from copper ($A^{Cu}_{\perp}$= 11 MHz, unresolved). Contributions from the N-donors are not resolved in the $g_{//}$ direction. EPR thus suggests that addition of excess imidazole to **I** results in mononuclear Cu(II) species **II** with four coordinated N-donors from two distinct pairs of equivalent ligands. These most likely consist of the TMEDA (weaker N-donor; A^{N2}) and two additional imidazole ligands (stronger N-donor; A^{N1}). A typical simulation is shown later, see supplementary information Figure S7. The axial symmetry of the spectrum and the equivalence of the TMEDA and imidazole nitrogen nuclei suggests that **II** is either the square planar [(TMEDA)(imidazole)$_2$Cu^{II}] or the square pyramidal similar to the reported crystal structure[17] (with the N-donors in the basal plane) [(TMEDA)(imidazole)$_2$Cu^{II}(L)] (L=OH$^-$, Cl$^-$, H_2O or imidazole) complex. Due to the Jahn-Teller effect, an octahedral geometry is not considered likely for (TMEDA)Cu^{II} and monodentate ligands.

Figure 5. (a) ED-XAFS and (b) UV-Vis spectra of reaction **A**: [Cu(OH)(TMEDA)]$_2$Cl$_2$ in NMP/H$_2$O + Imidazole.
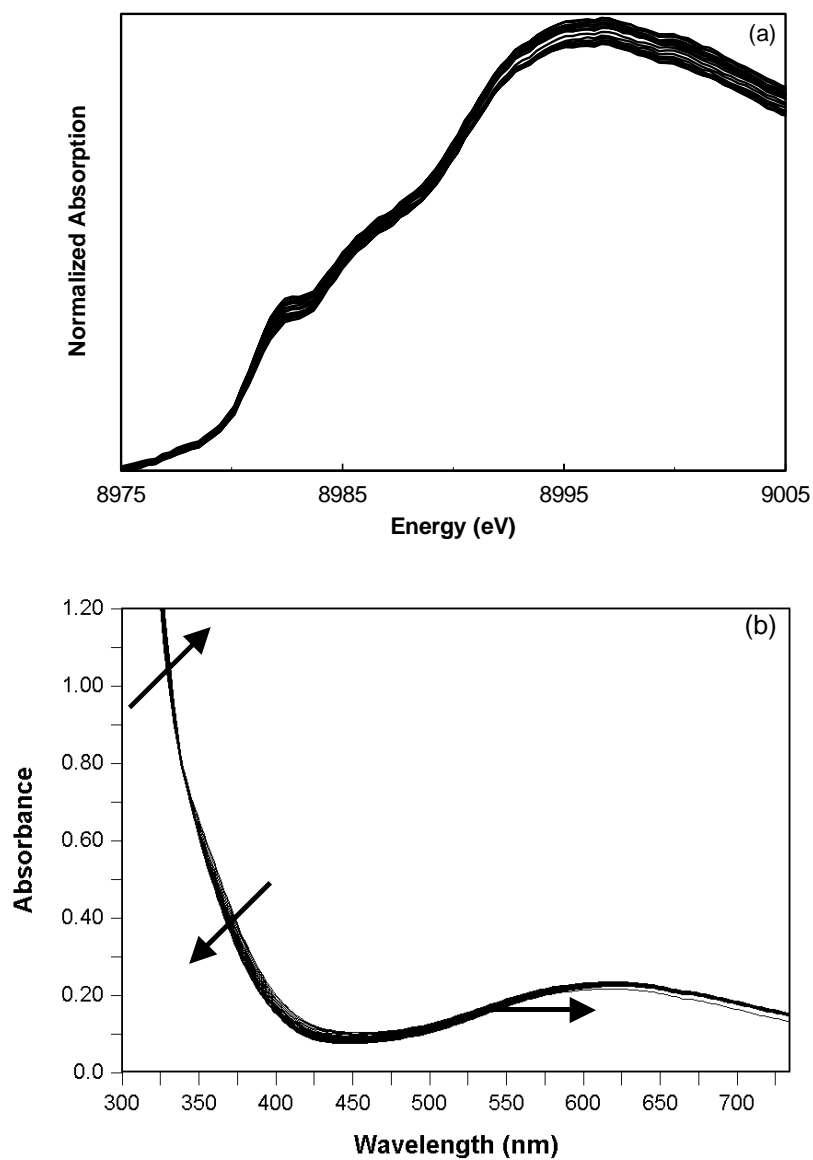
Reaction B: [Cu(OH)(TMEDA)]$_2$Cl$_2$ + Ph(BOH)$_2$

The addition of phenylboronic acid to the dimeric Cu(II) complex resulted in the homo-coupled biphenyl product. The stoichiometric addition of phenylboronic acid (per mole of Cu) to the starting complex was studied with combined EDXAFS and UV-Vis and the results are shown in Figure 6. The signal to noise ratio of these XANES spectra is somewhat lower than for the other experiments due to the shorter time scale used necessary to monitor this fast reaction properly. The XANES spectrum shows the fast appearance of a large pre-edge around 8982 eV, which is assigned to a 1s→4p Cu(I) transition[13] and thus indicates the formation of a large amount of Cu(I) species. No Cu-Cu contribution was detected as can be seen from the obtained EXAFS parameters of the formed Cu(I) complex in Table 2. We now observe three shells around the Cu atom with the first shell at 1.96 Å consisting of more than 5 N/C/O atoms. Besides the two N atoms of the TMEDA ligand, additional neighbors are present which can originate from H$_2$O, coordinated phenyl group(s) or coordinated boronic species. In UV-Vis, the LMCT and d-d band completely disappear, indicating respectively the break-up of the dimeric structure and the consumption of Cu(II) species.

In EPR (Figure 7) this reaction results in small signals indicating marginal rise of concentration of at least two closely related monomeric Cu(II) species of probably axial symmetry (g$_\perp$~ 2.23-2.26 and g$_{//}$~ 2.05). Hyperfine splitting is observed at both the signals along B$_\perp$ and B$_{//}$ (A$_\perp^{Cu}$~ 80-120 MHz, g$_{//}^{Cu}$~ 500-560 MHz). After a short reaction time at room temperature, (the mixture is again frozen for measurement) the Cu signal weakens and probably EPR silent species are formed, i.e. Cu(I) and/or reformation of coupled Cu(II) dimers. ^{1}H-NMR confirms the initial dissociation of the dimeric structure (**I**) by the disappearance of the lower field 70 – 100 ppm peaks, followed by the reformation of dimers.

As was observed in catalysis, the reaction of phenylboronic acid and Cu dimer (**I**) results in the exclusive formation of biphenyl. Spectroscopic results shown here suggest that this reaction proceeds with the formation of a Cu(I) species.

Figure 6. (a) EDXAFS and (b) UV-Vis spectra of reaction **B**: [Cu(OH)(TMEDA)]$_2$Cl$_2$ in NMP/H$_2$O + PhB(OH)$_2$.

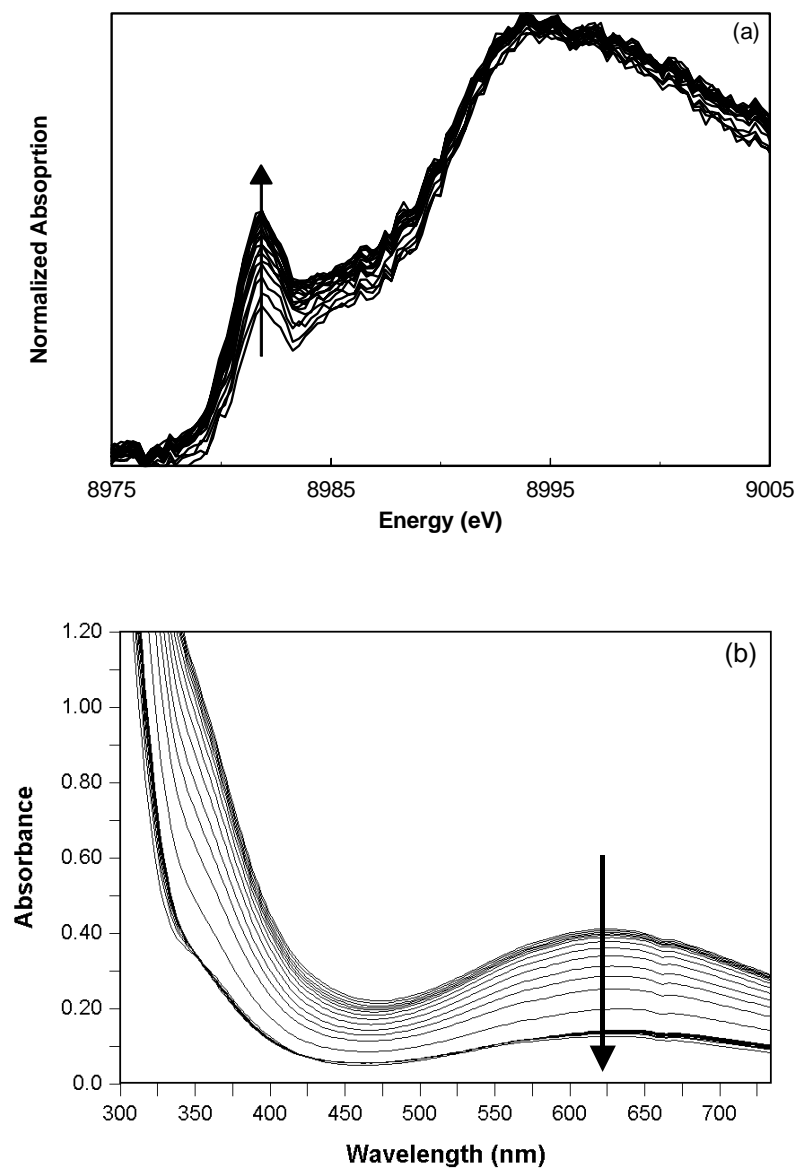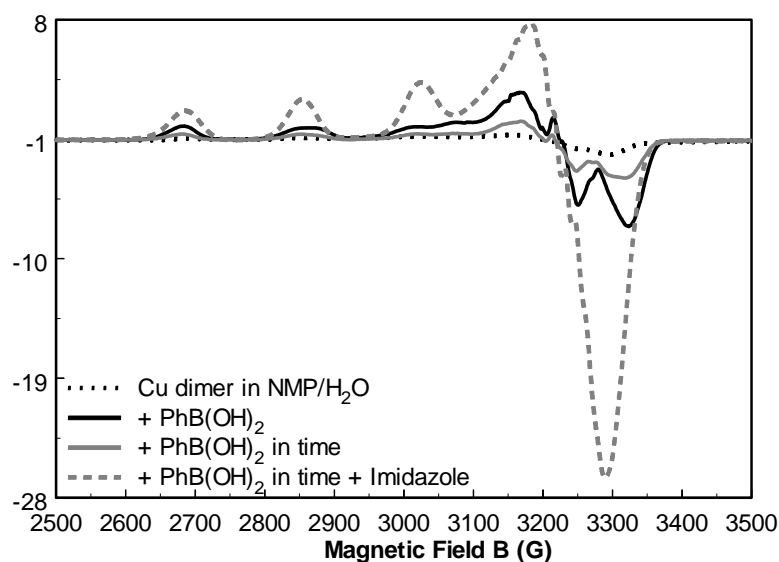**Figure 7.** X-band EPR spectra of [Cu(OH)(TMEDA)]$_2$Cl$_2$ in NMP/H$_2$O solution (dotted black line), after addition of phenylboronic acid (solid black line), in time (solid grey line) and after subsequent addition of imidazole [T = ~20 K].

Reaction C: [Cu(OH)(TMEDA)]$_2$Cl$_2$ + Phenylimidazole

Since catalytic studies showed that product inhibition takes place, the Cu(II) dimer (**I**) in the presence of the phenylimidazole product was studied. EDXAFS/UV-Vis measurements of this mixture, Figures 8a and 8b, shows results similar to reaction **B**. No clear changes can be observed in the Cu(II) XANES region, whereas in UV-Vis the LMCT is disappearing and only small changes in position of the d-d band are observed. The EXAFS results in Table 2 display only three large Cu-C/N/O contributions. The broad peak assigned to phenylimidazole in ¹H-NMR shifts from ~7.3 ppm to 66 ppm after coordination to the Cu complex and the lower field signals (70 and 100 ppm) have disappeared. These results indicate the formation of a monomeric Cu(II) species, similar as observed in reaction **A**. Phenylimidazole is now coordinated to Cu (II) forming a Cu(II) monomeric species.

Dimer **I** and excess phenylimidazole were reacted in methanol and after precipitation with ether, a blue solid was isolated. The EXAFS results of this complex in NMP/H$_2$O solution are presented in Table 3 and show the presence of two large N/C/O contributions at respectively short 1.97 Å and longer 2.97 Å distance to copper. According to XANES and UV-Vis a monomeric Cu(II) species is present. The EPR spectrum of the precipitate in NMP/H$_2$O solution displays a Cu(II) signal nearly identical to that of **II**,

although broader resulting in less resolved hyperfine splitting. In ^{1}H-NMR no characteristic peaks are observed. From these results we conclude that the reaction of phenylimidazole with Cu dimer **I** results in the formation of [(TMEDA((Phenylimidazole)$_2$Cu(II)(X)] **V**, with X probably being OH^{-}.

According to these measurements, the imidazole reagent and the phenylimidazole product have a similar affinity for Cu(II). This is in good agreement with the observed inhibition in catalysis.

Figure 8. (a) EDXAFS and (b) UV-Vis spectra of reaction **E**: [Cu(OH)(TMEDA)]$_2$Cl$_2$ in NMP/H$_2$O + Phenylimidazole.
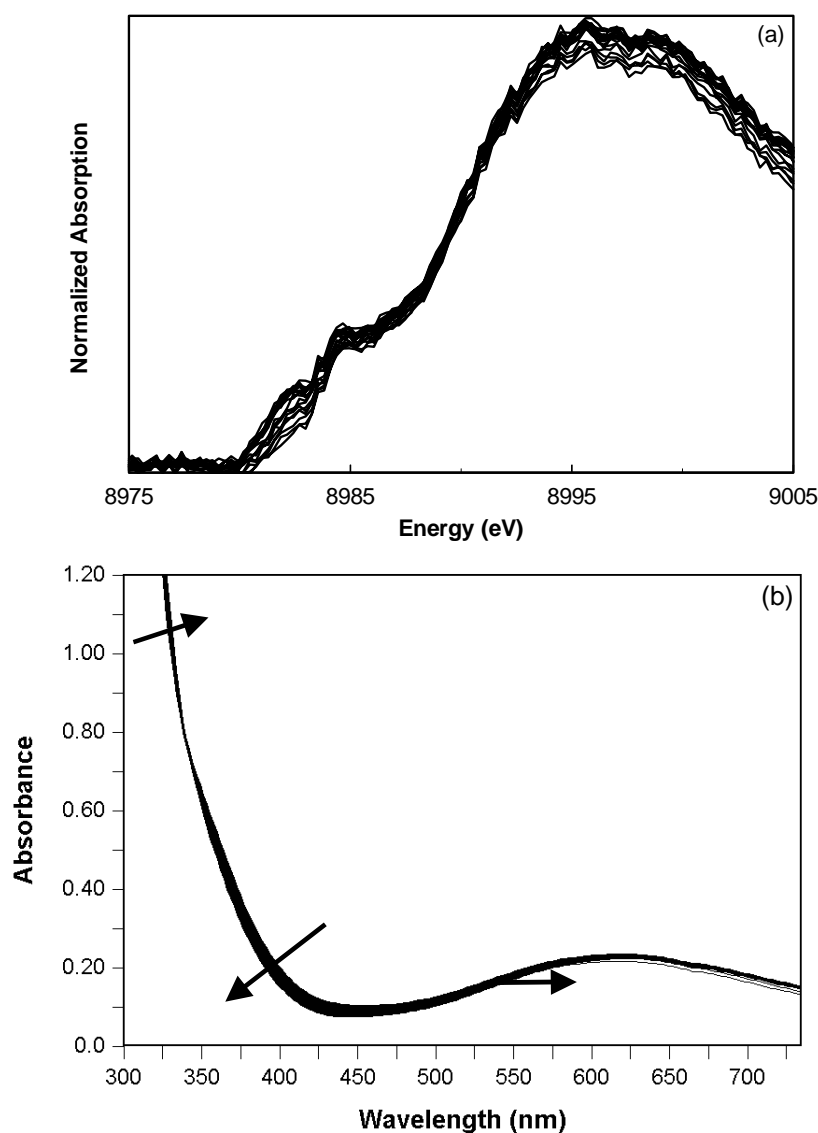
Reaction D: [Cu(OH)(TMEDA)]$_2$Cl$_2$ + Imidazole + PhB(OH)$_2$

a) [Cu(Cl)(Imidazole)(TMEDA)]$_3$ + PhB(OH)$_2$ in NMP/H$_2$O

Addition of phenylboronic acid to [Cu(Cl)(Imidazole)(TMEDA)]$_3$ in NMP/H$_2$O, results in *N*-phenylimidazole product formation. A Cu-coordinated phenylimidazole signal in ^{1}H-NMR at ~66 ppm indicates the coordination of phenylimidazole to Cu.

b) Subsequent Addition of Imidazole and PhB(OH)$_2$

Phenylboronic acid is added to the mixture of Cu dimer (**I**) and imidazole (reaction **A**), i.e. phenylboronic acid is added to the putative [(TMEDA)Cu(imidazole)$_2$X] complex **II**. The EPR Cu hyperfine signal slightly increases in intensity (Figure 3, solid black line), the signal along B$_{//}$ slightly shifts from g$_{//}$= 2.265 to g$_{//}$= 2.275 and slightly broadens and A$_{//}^{Cu}$ has increased from 514 to 522 MHz. The signal parameters along B$_\perp$ are hardly affected, but remarkably the N super hyperfine splitting becomes more pronounced. See Supplementary information Figure S7 for the experimental and simulated EPR spectrum. Probably, a slightly different Cu species is formed, possibly by substitution of X in [(TMEDA)Cu(imidazole)$_2$X] by (a fragment of) phenylboronic acid.

After warming up the sample to ~60ºC and let it react for a ~10 minutes, and cooling down again to ~20 K, the Cu(II) EPR signal has decreased (Figure 3) and the color of the solution changed from blue to colorless, indicating the formation of a Cu(I) species. After subsequent addition of extra phenylboronic acid, both the blue color of the solution and the intensity of the EPR signal are fully regained. This strongly suggest that phenylboronic acid is involved in the reoxidation of Cu(I) to Cu(II) species.

Addition of imidazole to the mixture of Cu dimer (**I**) and phenylboronic acid (reaction **B**, Figure 7) results in a strong signal in the EPR spectrum (grey striped line), similar to the spectrum of [(TMEDA)(imidazole)$_2$Cu(X)] **II**. From EPR measurements we cannot distinguish between the coordination of imidazole or phenylimidazole moieties to the (TMEDA)Cu complex. Stoichiometric experiments with first the addition of phenylboronic acid to the Cu complex **I** and subsequent addition of imidazole, show selective homo-coupling. This suggests that in the EPR solution mixture all the phenylboronic acid has reacted prior to the addition of imidazole (confirming the fast CC coupling), and that imidazole coordinates to the Cu(II) forming intermediate **II** identical to reaction **B**.
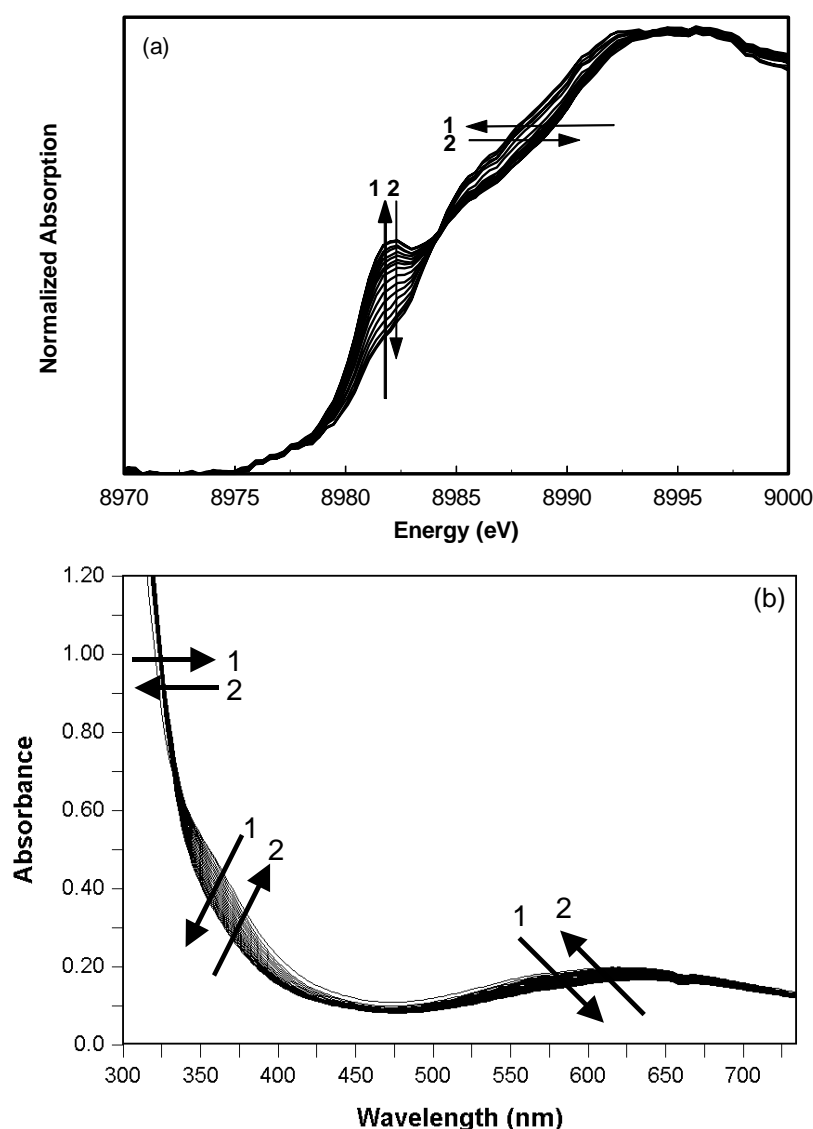
Figure 9. (a) ED-XAFS and (b) UV-Vis spectra of reaction **D**: $[Cu(OH)(TMEDA)]_2Cl_2$ + Imidazole + $PhB(OH)_2$.

c) Simultaneous Addition of Imidazole and PhB(OH)₂

The ED-XAFS and time-resolved UV-Vis spectra of the stoichiometric arylation reaction **D** are shown in Figure 9a and 9b. All reactants are injected simultaneously in the observation cuvette. During the reaction, a pre-edge at ~8982 eV is formed in the XANES (Figure 9a, **1**), indicating the formation of a Cu(I) species. The Cu(II) species disappears, which is concluded from the decrease of the pre-edge peak at 8985 eV (the changes in the peak at 8979 eV are obscured in this experiment). In the UV-Vis spectra, (Figure 9b, **1**) the LMCT band of the starting dimer at ~355 nm disappears, i.e. the copper dimers dissociate. Simultaneously, the d-d band decreases by ~40%, indicating that this amount is most likely converted into Cu(I) species. The small shift in d-d band corresponds to only small changes

in the Cu(II) coordination during reaction. Meaningful EXAFS analysis results could not be obtained due to the fast changing ratios of Cu species present in the reaction mixture. The XANES and UV-Vis results suggest the formation of a monomeric Cu(I) species which is confirmed by the decrease of the Cu(II) signal in EPR.

The stoichiometric reaction **D** is also monitored with ^{11}B-NMR to investigate the role and fate of the boron atom / boronic species during this arylation reaction (Figure 10). Initially, the starting phenylboronic acid is clearly observed by the chemical shift at 30 ppm. Progressing, this signal disappears and the formation of a doublet signal at 26.4 ppm (J = 96.8 Hz) is observed. Since these values are similar to bis-pinacol-borane (chemical shift of 31 ppm), we assign this to a boron hydride intermediate H-BX$_2$, most likely boronic acid H-B(OH)$_2$.[20,21] Finally, this boron hydride reacts to a boric acid B(OH)$_3$ which is observed by the chemical shift at 20 ppm.

With EDXAFS and UV-Vis we observe that, after formation of the Cu(I) species and phenylimidazole product, the intensity of the 8982 eV pre-edge decreases again and the Cu(II) pre-edge at 8985 eV is increasing, forming back Cu(II) species (Figure 9a, **2**). Simultaneously, in UV-Vis the LMCT band is partly regaining intensity, while the intensity of the d-d band is almost fully regained (Figure 9b, **2**). These results indicate the reformation of Cu(II) species, both in monomeric and in dimeric form.

Figure 10. Time-resolved ^{11}B-NMR spectra of reaction **D**: [Cu(OH)TMEDA]$_2$Cl$_2$ in NMP/H$_2$O + Imidazole + Phenylboronic acid. The top spectrum is a reference spectrum of boric acid B(OH)$_3$.
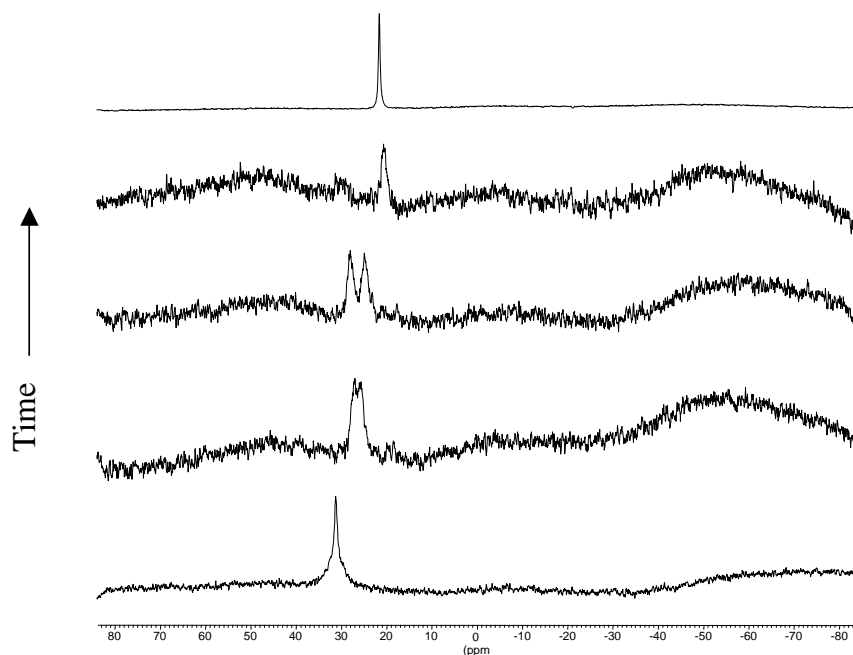
The extensive spectroscopic study as described here has also been performed using exclusively NMP or H_2O as a solvent. For the reactions in NMP, no changes in Cu coordination or oxidation state are observed, in line with the observation that the arylation reaction does not proceed. Reaction in H_2O resulted in the fast and irreversible formation of large amounts of Cu(I) species. Although H_2O is necessary for the reaction to proceed, an excess of H_2O results in a lowering of the catalytic activity.

Spectroscopically monitoring the reaction of Cu(II) catalysts with other bidentate dinitrogen ligands like phenantroline (in NMP/H_2O, NMP or H_2O solvent) only displays a change in reaction rates (i.e. faster in comparison to the TMEDA), all other results (oxidation state, coordination of the Cu) remain the same, suggesting that the same mechanism is followed.

Catalytic Cycle

From the results described above, we propose the formation of a [Cu(imidazole)$_2$(TMEDA)] intermediate **II** from the reaction of imidazole with the starting [Cu(OH)(TMEDA)]$_2$ complex **I** (Scheme 3). Based on the crystal structure of the isolated trimer, and description of a monomeric Cu(imidazolate)$_2$ complex[19] we assume the deprotonation of imidazole forming Cu(II)(imidazolate). Since only one OH group per Cu is present in our starting dimeric complex **I** and the addition of base is not necessary for the reaction to proceed, probably one imidazole per Cu is deprotonated, additional imidazole is only coordinated to the Cu. This implies that reaction intermediate **II** can be described as an [Cu(imidazolate)(imidazole)(TMEDA)] complex. Since imidazole is reversibly coordinated to the Cu center, we believe that the imidazole dissociates from the complex, leaving an empty coordination place. A similar process takes place with phenylimidazole, explaining the observed inhibition of the reaction with addition of these compounds.

In addition to the starting Cu dimer **I** and intermediate **II**, two more reaction intermediates have been characterized. The reaction of **II** with phenylboronic acid forms the phenylimidazole product and Cu(I) intermediate **IV**. Reoxidation of the Cu(I) intermediates is shown to result in Cu(II) monomeric species with either phenylimidazole or imidazole coordinated, respectively **V** or **II** ("resting state"), or the starting dimeric Cu(II) species **I**. Additionally, the oxidative character of phenylboronic acid is shown with EPR. From catalytic studies we established that O$_2$ is not necessary for the reaction to proceed whereas the presence of water in essential.[8] Thus both phenylboronic acid and H$_2$O are likely to be involved in the oxidation steps. The ^{11}B-NMR study has shown the formation of a H-B(OH)$_2$ which, in the presence of water, readily reacts to the boronic acid.

The organic product phenylimidazole could be formed from electrophilic attack of a phenylboron species on the nucleophilic imidazole. Alternatively, it could be produced via reductive elimination from a Cu(III)(aryl)(imidazolate) species **III**. This pathway implies either the addition of a phenyl radical to the Cu(II)(imidazolate) intermediate (**II**), or the disproportionation of the Cu(II) intermediate in Cu(I) and Cu(III) species. Since a Cu(III) intermediate will be rather reactive, it most likely cannot be detected by any of the techniques used. Upon reductive elimination of the product from the Cu(III) transient **III**, the Cu(I) species **IV** is formed.

Addition of a phenyl radical to intermediate **II**, could occur via a homolytic splitting of the phenylboronic acid. Similar boron radicals have been recently described in literature.[22] In the presence of water the boronic radical then reacts to the boronic hydride and a (high

energy) hydroxyl radical, which can oxidize the Cu(I) species and form boric acid. The ^{11}B-NMR study and the use of radical scavengers support this radical mechanism. The formation of the proposed of radicals however, is highly energetic and thus not an easy process. EPR experiments with the addition of radical scavengers would give more details about this proposed homolytic pathway.

Scheme 3. Proposed reaction mechanism for the Cu(II) catalyzed arylation of imidazole and phenylboronic acid.
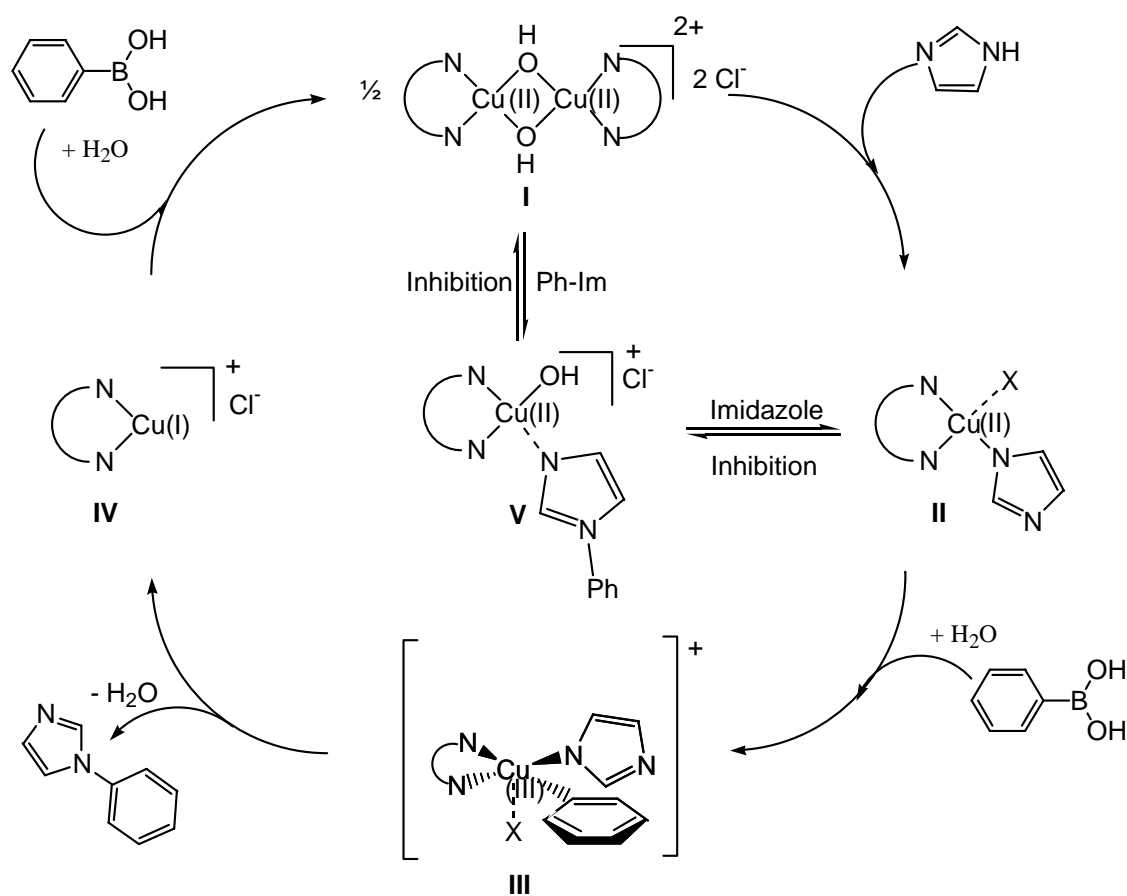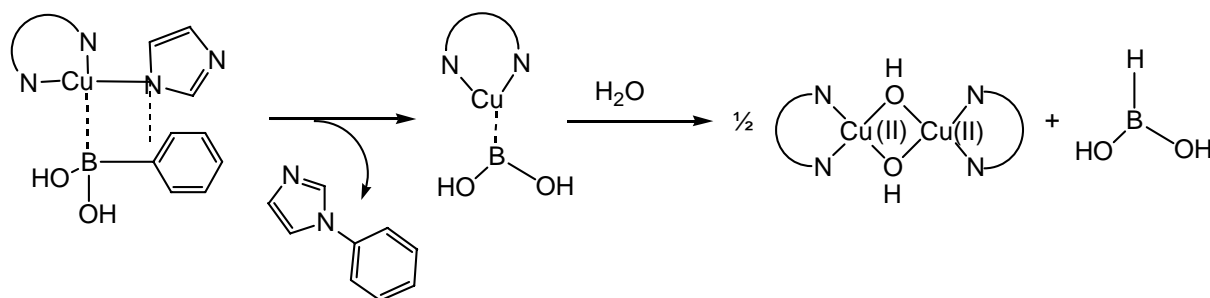
Alternatively, the disproportionation of the Cu(II) intermediate **II** to a Cu(III) species and Cu(I) species is shown in Scheme 4. Phenylboronic acid is converted to a [phenyl-B(OH)$_3$]$^-$ anion, an intermediate often proposed to be involved in transmetalation processes. This 'activated' boric acid reacts with the Cu(II)(imidazolate) species to a Cu(III)(phenyl)(imidazolate) intermediate **III** (similar as in the "homolytic mechanism") and B(OH)$_3$. The disproportionation is likely to be the rate-determining step, whereas the addition of phenyl and reductive elimination are very fast. This allows us to only monitor the increasing amount of Cu(I) species whereas the lifetime of the Cu(III) species is to short to detect. Reoxidation of Cu(I) complex **V** is observed to occur with phenylboronic acid. Moreover, the proton H$^+$ formed during the activation of phenylboronic acid might be involved here. This disproportionation / comproportionation mechanism cannot be ruled out, based on the studies presented here. This mechanism however, does not account for the formation of a HBX$_2$ species as observed in ^{11}B-NMR. Additional ^{11}B-NMR experiments with different concentration and ratios of Cu and phenylboronic acid are required to validate this comproportionation mechanism.

Alternative mechanisms involving a transmetalation type phenyl transfer can be considered, such as a concerted pathway. In this mechanism, both the imidazole and phenylboronic acid coordinate to the Cu(II)(TMEDA) complex, forming a cyclic Cu-N-Ph-B transition state as drawn in Scheme 5. Simultaneously the product and a Cu(II)(TMEDA)-B(OH)$_2$ species are formed, the latter reacting in the presence of H$_2$O to HB(OH)$_2$ and finally boronic acid. In this mechanism the Cu oxidation state remains 2+ throughout the entire cycle. A transmetalation mechanism is, however, not completely ruled out since the proposed Cu(II)-B species can react with water to form a Cu(I) intermediate.

Scheme 5. Transmetalation type pathway.

Scheme 4. Disproportionation / comproportionation mechanism.
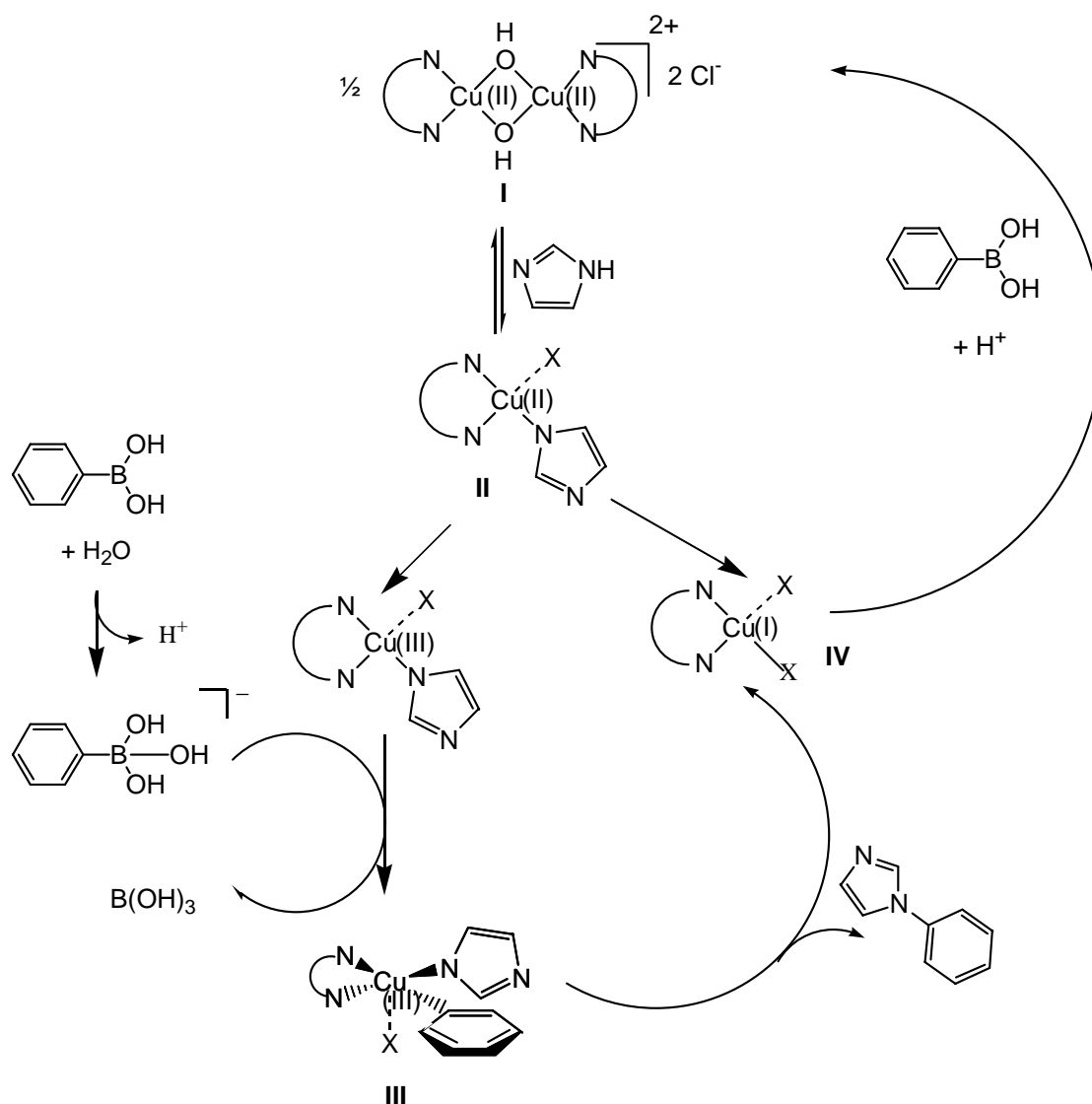
The productive part of this catalytic cycle is established by the characterization of the reaction intermediates as given in Scheme 3 and which are in good correspondence with all spectroscopic results obtained. Further research including quantitative EPR and NMR, electron spray MS, IR and kinetic studies is required to elucidate the mechanism in further detail.

Based on the spectroscopic results described in this paper, the C-C couplings reaction as observed in reaction **B** seems to proceed via a similar reaction mechanism as the C-N coupling. In this case, the first step in the reaction mechanism will be the transmetalation of phenylboronic acid to the Cu dimer (**I**).

Conclusions

In this study we show that the application of a wide range of spectroscopic techniques, including a newly developed combined time-resolved UV-Vis/EDXAFS set-up, gives detailed insights in reaction intermediates involved in the Cu-catalyzed arylation reaction. Several reaction intermediates have been characterized (Scheme 3) and the time-resolved *in situ* techniques allow the monitoring of changing oxidation states and characteristic transitions during reaction. In combination with catalytic results a novel, unexpected reaction mechanism for the important Cu(II) catalyzed arylation reactions has been proposed showing that the presence of dioxygen is not required and only catalytic amounts of base are needed. The productive part of this catalytic cycle is established and in correspondence with all spectroscopic results obtained. More experiments are necessary to give more insight into the oxidation steps involved.

Experimental

Catalytic experiments

Unless stated otherwise, all reactions were carried out in an air atmosphere using 20 cm glass tubes. THF, hexane and diethyl ether were distilled from sodium benzophenone ketyl, CH_2Cl_2, acetonitrile and NMP (*N*-methylpyrrolidone) were distilled from CaH_2 and toluene was distilled from sodium under nitrogen. Reactions in the absence of dioxygen were carried out using standard Schlenk techniques. Reactions under a dioxygen atmosphere were conducted by bubbling dioxygen through the solvent for 15 minutes, followed by presurizing the mixture with 1 bar of dioxygen. Gas chromatographic analyses were run on an Interscience HR GC Mega 2 apparatus (split/splitless injector, J&W Scientific, DB-1 J&W 30 m column, film thickness 3.0 μm, carrier gas 70 kPa He, FID detector) equipped with a Hewlett_packard data system (Chrom-Card). Gas chromatographic mass spectra were run on an Agilent Technologies 6890/5973 GC-MS combined with an Agilent Mass Selective detector. Columtype; HP5MS, length 30 m, film thickness 0.25 μm, crosslinked 5% PhMe-siloxane.

Synthesis of bis-μ-hydroxy copper(II) (TMEDA) complex

This complex has been prepared according to literature. [23]

Elemental analysis results

[Cu(OH)(TMEDA)]$_2$: 30.66 % C, 7.39 % H, 11.70 % N.
[Cu(Cl)(Imidazolate)(TMEDA)]$_3$: 31.89 % C, 8.46 % H, 16.63 % N.
[Cu(OH)(Phenylimidazole)(TMEDA)]Cl : 25.35 % C, 3.78 % H, 6.79 % N.

ED-XAFS and UV-Vis

The novel combined ED-XAFS UV-Vis set-up is described recently[10] and schematically shown in Figure 11. Using the energy dispersive data-acquisition set-up[9], a curved crystal reflects and focuses the total synchrotron white beam on the sample. All energies can be measured at once using a position sensitive detector, thereby enabling the acquisition of EXAFS spectra in the ms-s range. Combining this set-up in a perpendicular manner with an optical fiber UV-Vis apparatus, both techniques can be applied simultaneously. A stopped-flow module with four syringes as shown in Figure 12a is used to perform the homogeneous reactions. The solutions are injected from the syringes (S1-S4) via the delay lines (D1-D2) and mixers (M1-M3) into the observation cuvette. This system has a dead time of ~3 ms (i.e. time before all solutions are mixed and arrived in the cuvette). Special cuvettes have been designed in which the X-rays and UV-Vis light traverse perpendicular to one another (Figure 12b). The different path lengths enable the simultaneous ED-XAFS and optical fiber UV-Vis experiments on the reaction mixture.

The reactions described in this study have been performed stoichiometrically with 10 mM of $[Cu(OH)(TMEDA)]_2Cl_2$ (**1**) (20 mM Cu) in the cuvette after mixing. Higher concentrations would be preferable to increase the quality of the obtained XAFS data, however, we are limited to the solubility of complex **I**. For the Cu system described in this paper, with this set-up it is possible to measure EXAFS spectra with a minimum time resolution of 10 milliseconds and UV-Vis spectra with a minimum time resolution of 0.3 ms.

ED-XAFS measurements at the Cu K-edge and time-resolved UV-Vis measurements were performed simultaneously to study the mechanism of the Cu(II) catalyzed arylation reaction of phenylboronic acid and imidazole to *N*-phenylimidazole at ambient conditions. Unless stated otherwise, ED-XAFS measurements were taken with a time resolution of ~1 s, every ED-XAFS spectrum is an average of 15 spectra with an acquisition time of 50 ms each. UV-Vis spectra were recorded every 30 ms. Static XAFS spectra were measured before and after the reactions, by averaging 50x15 spectra of 100 ms, to enable a reliable EXAFS analysis of the complexes in solution. Simultaneous ED-XAFS at the Cu K-edge and time-resolved UV-Vis experiments were performed at ID24 of the ESRF (European Synchrotron Radiation Facility) Grenoble Cedex, France, project CH-1275. Data were acquired using a Bragg monochromator.[24] The energy calibration was carried out using a copper foil. Data are collected using a masked Peltier cooled Princeton CCD camera. In our combined set-up a commercially available Biologic Stopped Flow Module SFM-400 (Biologic Stopped Flow Module SFM-400; MMS-UV1/500-1 High speed Diode Array Spectrometer with fiber optics) was used to perform the homogeneous reactions.

Figure 11. Schematic representation of the combined ED-XAFS/UV-Vis Set-up.

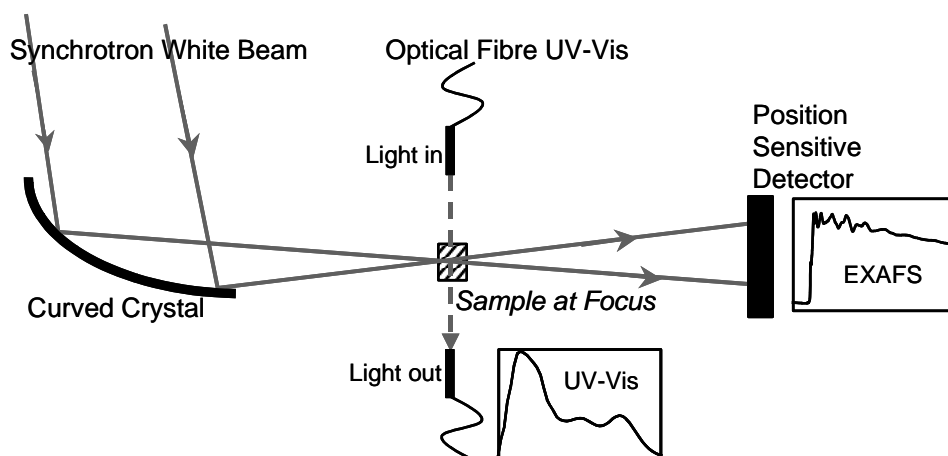**Figure 12.** (a) Schematic drawing of the Stopped-Flow Module, equipped with four syringes (S1, S2, S3 and S4). The solutions (with reagents) are injected via the mixers (M1, M2 and M3) and delay lines (D1 and D2) into the cuvette. (b) Schematic drawing of the specially designed cuvette. In two directions, a cut through the capillary is shown. Two different path lengths allow simultaneous measurements on the same reaction mixture.
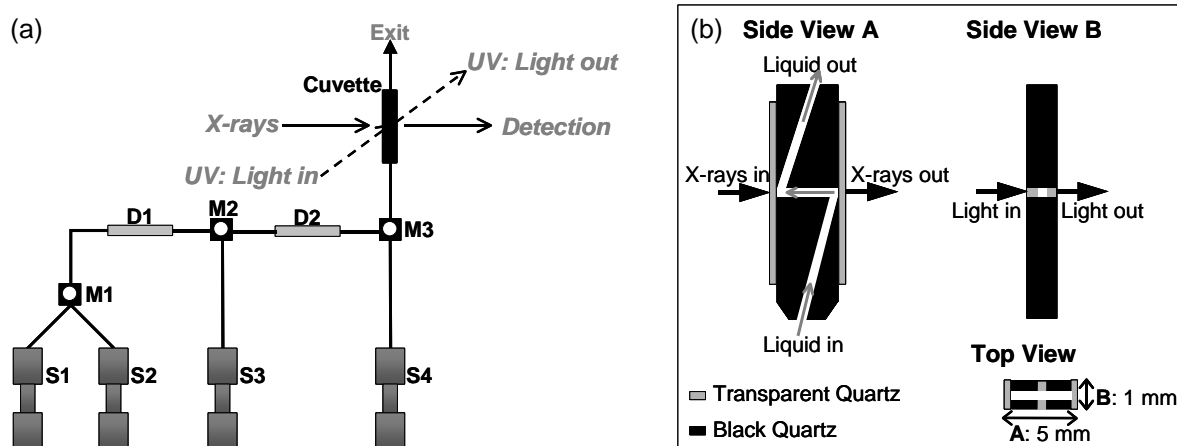
EXAFS Data Analysis

Calibrated references generated as described in reference 25 were used for the analysis for the Cu-N, Cu-Cu and Cu-C coordinations. In a similar way a theoretical reference for Cu-O generated using the code FEFF8, [26] was calibrated and optimized using EXAFS data of a CuO reference compound. The EXAFS data were analyzed using the commercially available program XDAP.[27] During R-space fitting, the difference file technique was used to be able to conclude a good analysis for all contributions in all weightings.[25]

^{1}*H- and* ^{11}*B-NMR measurements*

The ^{1}H and ^{11}B NMR spectra were obtained from a Bruker DRX 300 MHz spectrometer. D_2O was used as solvent if not further specified. Solutions of 0.2 M imidazole and $PhB(OH)_2$ were used. A solution of 0.01 M $[Cu(OH)TMEDA]_2Cl_2$ was used. All reactions were performed at ambient conditions.

EPR Measurements

Experimental X-band EPR spectra were recorded on a ca. 9.30 GHz. Bruker ER-220 spectrometer, equipped with an ESR-9 variable temperature cryostat (Oxford Instruments). Solutions with copper concentrations of ~5 mM were used. Reactions were started at room temperature and subsequently frozen to ~20 K and measured.

The spectra were simulated by iteration of the anisotropic g-values, (hyper)hyperfine coupling constants, and line widths.

Acknowledgements

Supplementary Material

Figure S1. EXAFS data of (a) reaction intermediates and (b) isolated Cu complexes in NMP/H$_2$O.
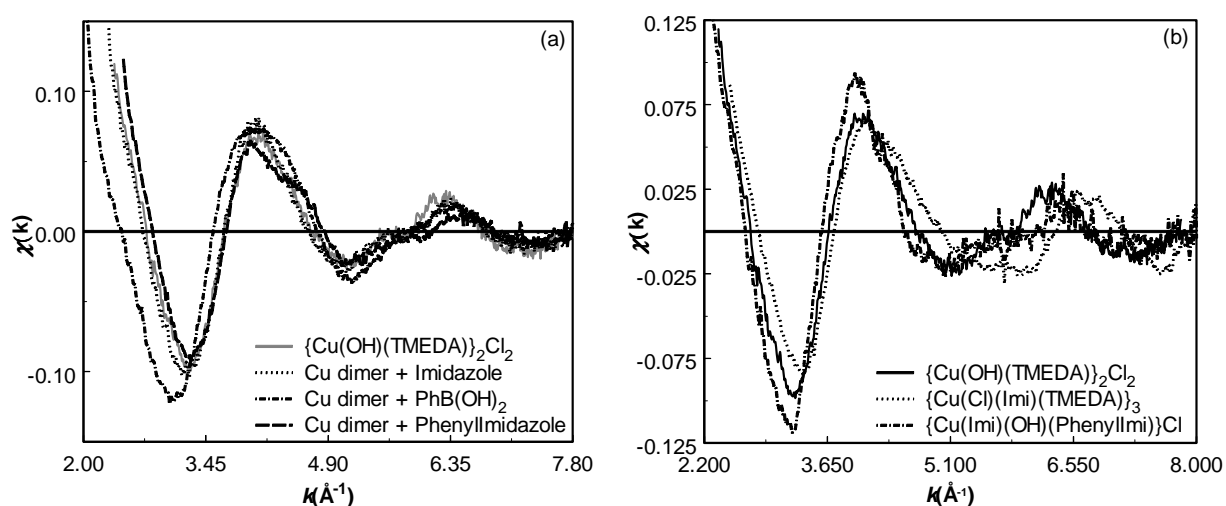
Figure S2. Fourier Transform of the EXAFS data after reaction **A**: [Cu(OH)(TMEDA)]$_2$Cl$_2$ + Imidazole in NMP/H$_2$O (room temperature), raw (solid line) and fit (dotted line); (a) k^0-weighted, (b) k^2-weighted.

181
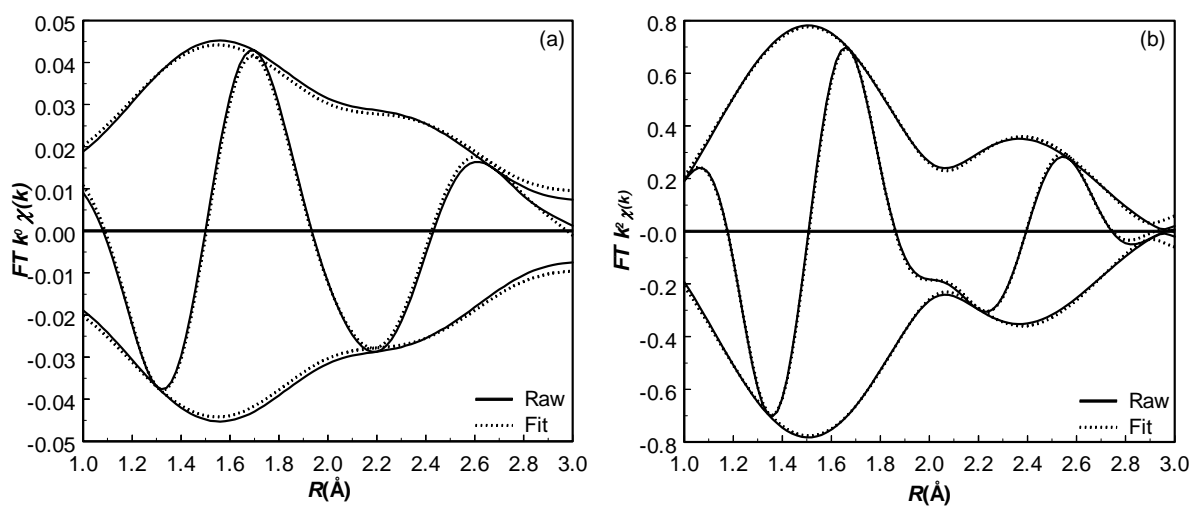
Figure S3. Fourier Transform of the EXAFS data after reaction **B**: [Cu(OH)(TMEDA)]$_2$Cl$_2$ + Phenylboronic acid in NMP/H$_2$O (room temperature), raw (solid line) and fit (dotted line); (a) k^0-weighted, (b) k^2-weighted.
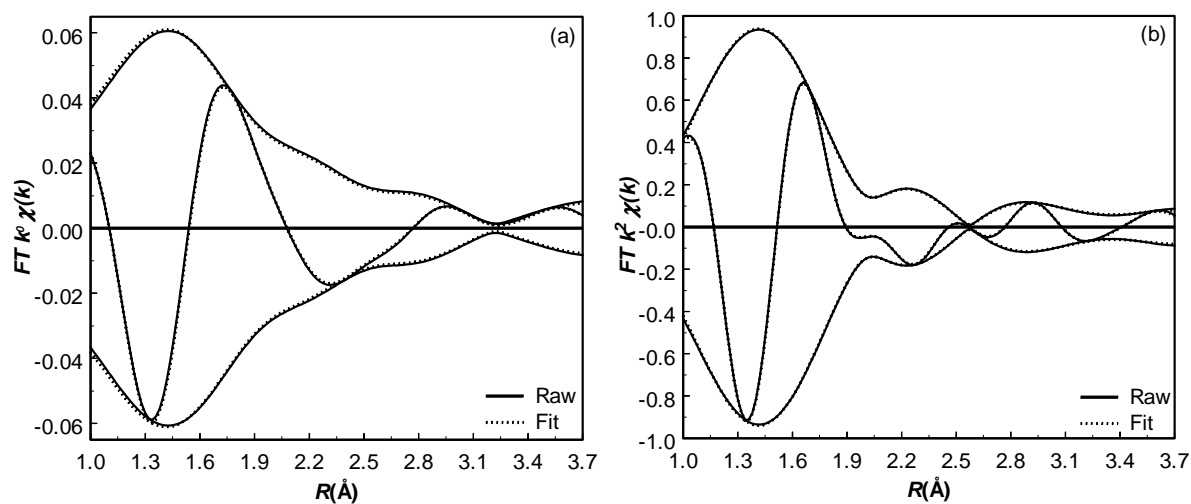
Figure S4. Fourier Transform of the EXAFS data after Reaction **C**: [Cu(OH)(TMEDA)]$_2$Cl$_2$ + Phenylimidazole in NMP/H$_2$O (room temperature), raw (solid line) and fit (dotted line); (a) k^0-weighted, (b) k^2-weighted.
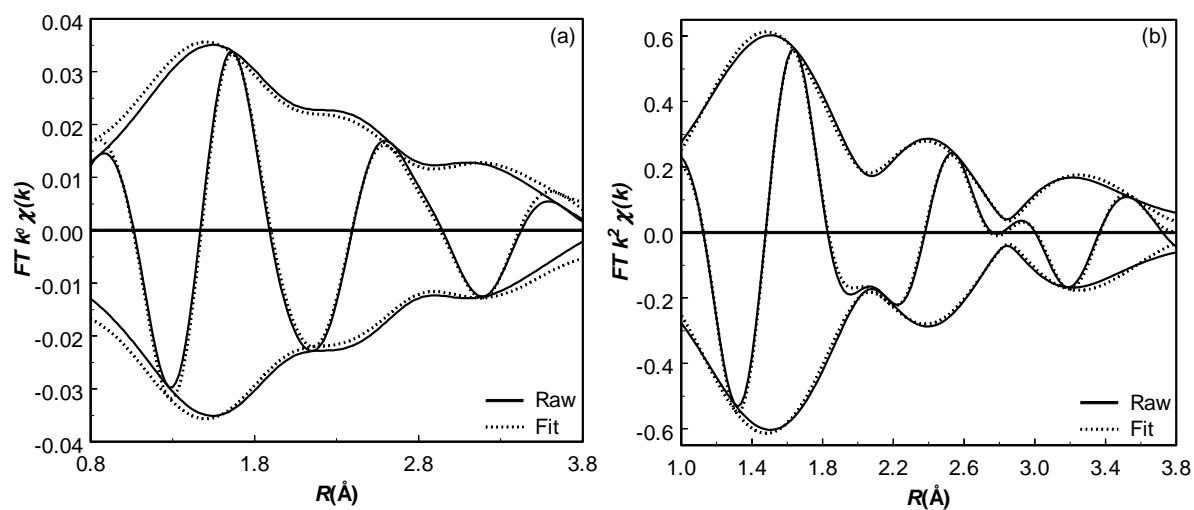
Figure S5. Fourier transform of the EXAFS data raw (solid line) and fit (dotted line) of [Cu(Cl)(Imidazolate)(TMEDA)]$_3$ in NMP/H$_2$O (a) k^0-weighted, (b) k^3-weighted.
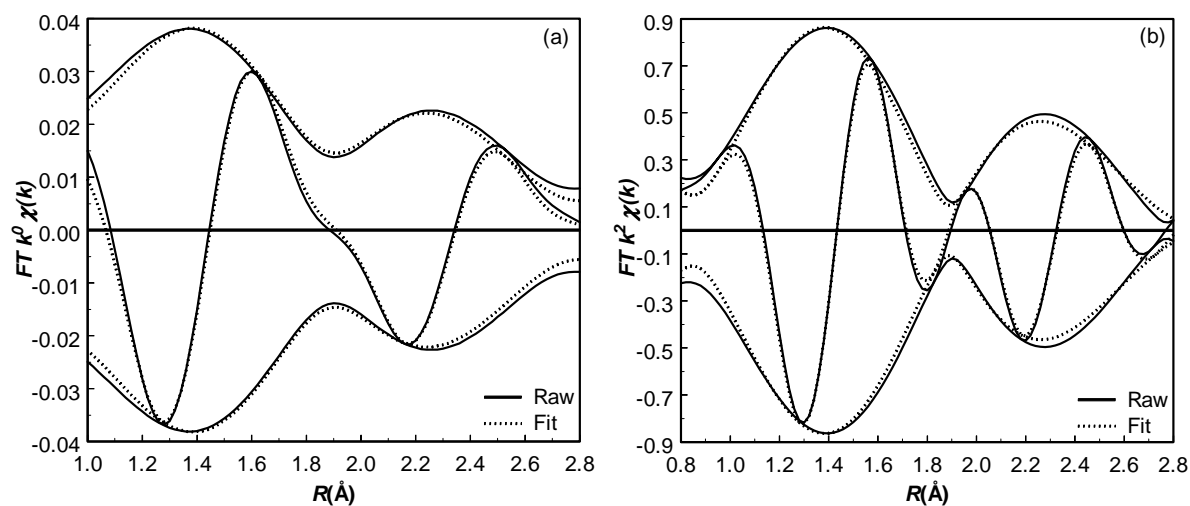
Figure S6. Fourier Transform of the EXAFS data of possibly [Cu(Phenylimidazole)(OH)(TMEDA)]Cl in NMP/H$_2$O (room temperature), raw (solid line) and fit (dotted line); (a) k^0-weighted, (b) k^2-weighted.
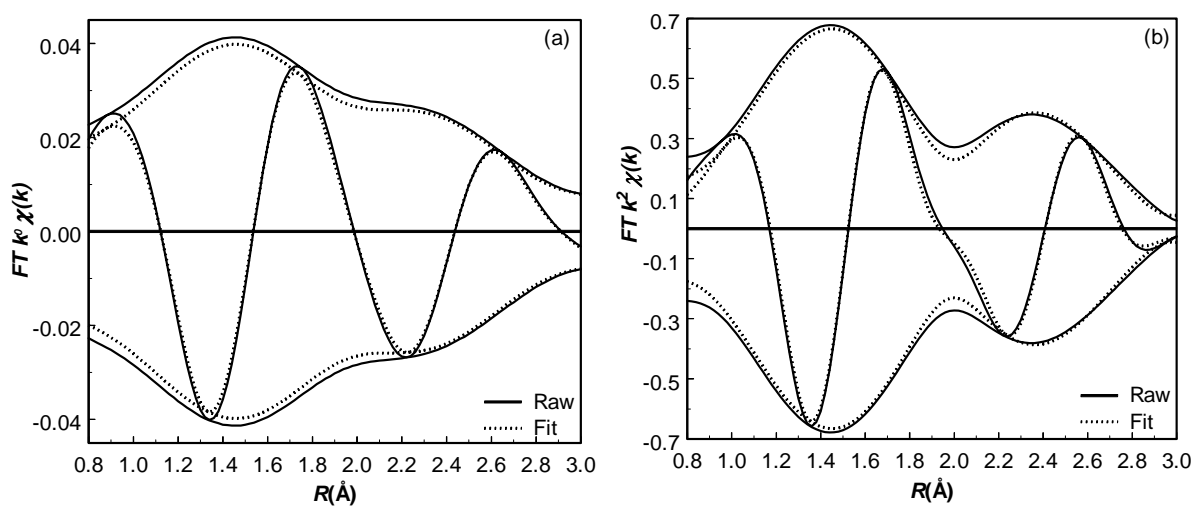
Figure S7. Experimental and simulated EPR spectrum of the $[Cu(OH)(TMEDA)]_2Cl_2$ complex in NMP/H_2O after addition of imidazole and phenylboronic acid (solid black line in Figure 3).

References

1. F. Ullmann, *Ber. Dtsch. Chem. Ges.* **1903**, *36*, 2382.
2. (a) J. F. Hartwig, *Angew. Chem. Int. Ed.* **1998**, *37*, 2046-2067; *Angew. Chem.* 1998, *110*, 2154-2177; (b) J.F. Hartwig, *Synlett* **1997**, 329-340; (c) J. P. Wolfe, S. Wagaw, J. -F. Marcoux, S. L. Buch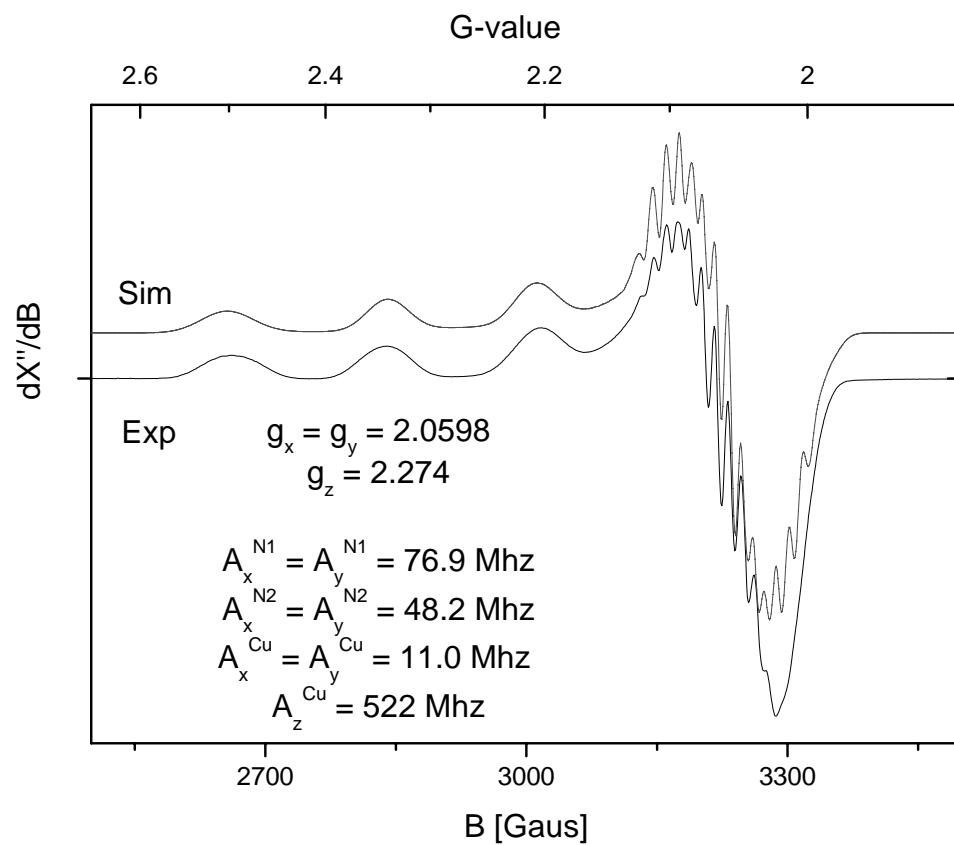wald, *Acc. Chem. Res.* **1998**, *31*, 805-818; (d) B. H. Yang, S.L. Buchwald, *J. Organomet. Chem.* **1999**, *576*, 125-146; (e) A. F. Littke, G. C. Fu, *Angew. Chem. Int. Ed.* **2002**, *41*, 4176.
3. J. Hassan, M. Sevignon, C. Gozzi, E. Schulz, M. Lemaire, *Chem. Rev.* **2002,** *102*, 1359.
4. (a) T. Rosner, J. Le Bars, A. Pfatlz, D. G. Blackmond, *J. Am. Chem. Soc.* **2001**, *123*, 1848; (b) Y. Guari, G. P. F. van Strijdonck, M. D. K. Boele, P. C. J. Kamer, P. W. N. M. van Leeuwen, *Chemistry Eur. J.* , **2001**, *7*, 275
5. D.A. Evans, J. L. Katz, T. R. West, *Tetrahedron Lett.* **1998**, *39*, 2937.
6. J. P. Collman, M. Zhong, *Org. Lett.* **2000**, *2*(9), 1233; b) J. P. Collman, M. Zhong, C. Zhang, S. Constanzo, *J. Org. Chem.* **2001**, *66***,** 7892.
7. P. Y. S. Lam, D. Bonne, G. Vincent, C. G. Clark, A. P. Combs, *Tetrahedron Lett.* **2003**, *44*, 1691.
8. S. S. van Berkel, A. van den Hoogenband, J. W. Terpstra, M. Tromp, P. W. N. M. van Leeuwen, G. P. F. van Strijdonck, under review (**Chapter 7a** of this thesis).
9. e.g. a) M. A. Newton, A. J. Dent, J. Evans, *Chem. Soc. Rev.* **2002**, *31*, 83; e.g. on homogeneous systems; b) J. Evans, L. O'Neill, V. L. Kambhampati, G. Rayner, S. Turin, A. Genge, A. J. Dent, T. Neisius, *J. Chem. Soc., Dalton Trans.* **2002**, 2207; c) M. Tromp, J. R. A. Siestma, J. A. van Bokhoven, G. P. F. van Strijdonck, R. J. van Haaren, A. M. J. van der Eerden, P. W. N. M. van Leeuwen, D. C. Koningsberger, *Chem. Comm.* **2003,** 128 (**Chapter 6b** of this thesis).
10. M. Tromp, S. S. van Berkel, S. G. Fiddy, G. P. F. van Strijdonck, J. A. van Bokhoven, P. W. N. M. van Leeuwen, D. C. Koningsberger, submitted for publication (Described in **Chapter 2** of this thesis).
11. J. C. Antilla, S. L. Buchwald, *Org. Lett.* **2001**, *13 (3),* 2077.
12. J.-B. Lan, L. Chem, X.-Q. Yu, J.-S. You, R.-G. Xie, *Chem. Comm.* **2004**, 188.
13. (a) L.-S. Kau, D. J. Spira-Solomon, J. E. Penner-Hahn, K. O. Hodgson, E. I. Solomon, *J. Am. Chem. Soc.* **1987**, *109*, 6433; (b) J. L. DuBois, P. Mukherjee, T. D. P. Stack, B. Hedman, E. I. Solomon, K. O. Hodgson, *J. Am. Chem. Soc.* **2000**, *122*, 5775.
14. K. D. Karlin, J. C. Hayes, Y. Gultneh, R. W. Cruse, J. W. McKown, J. P. Hutchonson, J. Zubieta, *J. Am. Chem. Soc.* **1984**, *106*, 2121.
15. D. C. Koningsberger, B. L. Mojet, G. E. van Dorssen, D. E. Ramaker, *Top. Catal,* **2000**, *10*, 143.
16. N. N. Marthy, K. D. Karlin, I. Bertini, C. Luchinat, *J. Am. Chem. Soc.* **1997**, *119*, 2156.
17. H. Okawa, M. Mikuriya, S. Kida, *Bull. Chem. Soc. Jpn.* **1983**, *56*(7), 2142.
18. Preliminary results on single-crystal X-ray analysis of [Cu(Cl)(Imidazolate)(TMEDA)]$_3$; M. Lutz, M. Tromp, G. P. F. van Strijdonck, A. L. Spek, in prep.

19. P. Chaudhuri, I. Karpenstein, M. Winter, C. Butzlaff, A. X. Trautwein, U. Florke, H.-J. Haupt, *J. Chem. Soc, Chem. Commun.* **1992**, 321.

20. H. Watanabe, K. Nagasawa, *Inorg. Chem.* **1967**, *6*, 1068-1070.

21. G. La Monica, G. A. Ardizzoia, F. Cariati, S. Cenini, M. Pizzotti, *Inorg. Chem.* **1985**, *24*, 3920-3923.

22. C.-J. Li, *Angew. Chem. Int. Ed.* **2003**, *42*, 4856.

23. (a) McWhinnie, W. R. *J. Chem. Soc.* **1964**, 2959, (b) Ferraro J. R.; Walker, W. R. *Inorg Chem.* **1965**, *4*, 1382, (c) Collman, J. P. ; Zhong, M.; Zeng, L.; Costanzo, S. *J.Org. Chem.* **2001**, *66*, 1528 (d) General procedure: 1 eq. of CuCl and 1 eq. bidentate ligand are added to a solution of EtOH/H20 (95:5 v/v %) and stirred in an air atmosphere for 20 h.

24. M. Hagelstein, C. Ferraro, U. Hatje, T. Ressler and W. Metz, *J. Synchrotron Radiat.* **1995**, *2*, 174.

25. M. Tromp, J. A. van Bokhoven, A. M. Arink, J. H. Bitter, G. van Koten, D. C. Koningberger, *Chem. Eur. J.* **2002**, *8*, 5667.

26. A. L. Ankudinov, B. Ravle, J. J. Rehr, S. D. Conradson, *Phys. Rev. B* **1998**, 7565.

27. M. Vaarkamp, J. C. Linders, D. C. Koningsberger, *Physica B* **1995**, *208&209*, 159.

Chapter 8a

Summary

Catalysis is one of the most important methods to obtain products in a selective and sustainable manner, i.e. in an environmental responsible manner. To be able to modify and optimize these catalytic production pathways, it is important to obtain knowledge on the reaction mechanisms occurring. Many of the commonly applied characterization techniques in this field of catalysis do not enable detailed structural information on the catalytic reaction intermediates formed during reaction. In homogeneous catalysis there is thus a need for an experimental technique that provides detailed structural information of the catalytic system, both *in situ* and time-resolved. X-ray Absorption Fine Structure spectroscopy is a very powerful technique to determine the local structure of compounds: the type and number of neighboring atoms, their distances, and the electronic properties of the absorber atom. Since this technique does not require long-range ordering of the material, amorphous materials and solutions can be studied. Additionally, measurements can be performed *in situ* and time-resolved. Detailed electronic and structural information about the homogeneous catalysts in their chemical active environment can thus be obtained and structure – performance relationships and reaction mechanisms can be derived.

In this thesis the application of XAFS spectroscopy in homogeneous catalytic systems is explored. Theory and data-analysis procedures to reliable analyze and interpret the obtained XAFS data, and instrumentation to monitor homogeneous catalytic reactions *in situ* and in a time-resolved mode were developed. A number of important homogeneous reactions are studied in detail.

In the standard scanning data acquisition mode, EXAFS spectra are obtained in timescales that vary from minutes to hours. An alternative data acquisition method, i.e. the energy dispersive (ED) mode, has been developed which allows short collection times and thus enables structural information on dynamic systems. The ED-XAFS technique is further developed to apply to homogeneous catalytic systems. Moreover, since a combination of spectroscopic techniques gives complementary information about the system under investigation, a new set-up was developed to allow simultaneous time-resolved UV-Vis and ED-XAFS measurements. The set-up and its instrumentation are described in detail in **Chapter 2**.

The limited amount of applications of XAFS spectroscopy to study homogeneous catalytic systems so far is most likely due to the complicated data-analysis of EXAFS data of organometallic compounds. In **Chapter 3** a new refined data-analysis procedure is developed which accurately analyzes EXAFS data of organometallic systems. The obtained EXAFS data have to be analyzed very carefully, especially by looking at the influence of different k-weightings, since using a single k-weighting can lead to false minima in variances. Application of the so-called difference file technique while fitting in R-space, allows one to examine the different individual contributions to the total EXAFS spectrum in detail. This helps to detect and unravel anti-phase behavior of different contributions. When all contributions are statistically relevant (i.e. well above the noise level) and both the total fit and all individual contributions fit the obtained EXAFS data very well in all different k-weightings, a good and reliable analysis is obtained. This analysis procedure is solely based on EXAFS parameters making it applicable to every EXAFS spectrum.

Although crystal structures of many homogeneous catalysts are known, the structures in reaction medium are often not clear. Characterizing the organometallic compounds in reaction medium (solution) reveals essential structural information, which can help to understand their catalytic behavior (activity, selectivity and stability) as shown in **Chapters 3 and 6a**. A Cu K-edge EXAFS study on homogeneous Cu(I) catalysts in solid state and solution (reaction medium) gives insights in their reactivity (**Chapter 3**). The trimeric structure of the $[Cu_3(SAr)_3]$ complex was observed to remain intact after dissolving it in toluene. Only the vibrational behavior of the Cu_3S_3 ring was increased, without preferable vibrations or vibration directions. In **Chapter 6a**, application of *in situ* EXAFS shows that the conformation of the allylic fragment of (PP)Pd(1,1-dimethylallyl) catalytic intermediate complexes in reaction medium differs from that in the solid state, dependent on the bidentate (PP) ligand. For complexes with a large P-Pd-P bite angle, the coordination of the allyl moiety is symmetrical. However, for a small bite angle complex like dppe, the allyl moiety changes its conformation in THF solution. The unsubstituted carbon atom bends

away from the palladium and therefore becomes more accessible for a nucleophile to be attacked. In addition, this distortion of the allyl-Pd binding decreases the electron density on the unsubstituted carbon atom and this atom becomes electronically activated. The change in orientation of the allyl moiety directly explains differences in regioselectivity in the allylic alkylation reaction, displayed by the distinct complexes. The results of these studies thus directly establish structure-selectivity relationships in important catalytic reactions.

In **Chapter 4** we demonstrate that X-ray absorption near edge spectroscopy (XANES) directly probes molecular orbitals. Taking the negative second derivative of these XANES data provides direct information on the energy and charge distribution within the different molecular orbitals probed. The obtained data thus gives essential information about the electronic properties of the sample under investigation. The Pd K-edge of series of organometallic (PP)Pd(XX) complexes is studied in detail. The different charge redistributions possible in these complexes as a function of (PP) ligand bite angle are described. Both the Pd 4d and Pd 5p orbitals facilitate the (PP) ligand to Pd and moiety (XX) to Pd electron density transfer, the magnitude strongly depending on the bite angle. Depending on the nature of the coordinating moiety, which determines the interaction with the Pd(PP) fragment, different amounts of charge redistribution can occur. The corresponding orbital interaction diagrams for the different complexes are determined. Theoretical density functional and FEFF8 calculations help interpret and assign the different molecular orbitals and validate the results obtained. The XANES spectroscopy techniques described can be applied to investigate the molecular orbitals of and charge redistributions within in principle every kind of sample. In this way more insights into the differences in activity and selectivity of the compounds under investigation can be derived.

Transition metal complexes with NCN-pincer ligands have been prepared for numerous applications in the fields of catalysis, catalyst immobilization, supramolecular assembly, and sensor materials. The introduction of substituents at the *para*-position of the pincer ligand benzene ring allows one to tune the metal center electronically and consequently the reactivity of the catalytically active pincers. In **Chapter 5** we have used the Atomic XAFS contributions in the Pt $L_{2,3}$ XAFS spectra of [PtCl(NCN)-Z] pincer complexes to probe the electron density changes on the Pt atom, induced by changes in a *para*-substituent on the neighboring benzene ring. These complexes provide a unique system for examining exclusively inductive effects on the AXAFS data, since the geometry around the Pt atom remains unchanged. The results presented here, including background subtraction and AXAFS isolation, validate the AXAFS technique and the AXAFS theoretical interpretation in particular. The different effects on the AXAFS shape and intensity are shown and discussed in detail. The results show that both the AXAFS and

NMR techniques are sensitive to the small electronic changes induced by the para-substituent on [PtCl(NCN-Z)] pincer complexes, whereas the XANES technique is not. Theoretical FEFF8 calculations predict the proper effects and trends. AXAFS is thus a powerful technique to probe the electronic properties of Pt and, principally, of every atom. This is especially interesting for systems that, e.g., are not amenable to NMR. Moreover, XAFS measurements can be performed *in situ* and time-resolved so the changes in electronic properties can be monitored during reaction.

The novel time-resolved ED-XAFS/UV-Vis set-up was used to elucidate the deactivation pathway of palladium catalysts and to gain insights into the catalytic cycle of a copper catalyzed amination reaction. Homogeneous palladium catalysts are found to be very active and selective in various organic synthesis reactions. However, their stability is often too low for large-scale industrial processes. Information on the deactivation processes is thus required. Bidentate diphosphine ligands are used to influence the properties of the catalyst and thereby it's performance and stability. In **Chapter 6b**, the size and nature of the different inactive Pd-clusters formed during the allylic substitution reaction as a function of ligand and solvent are studied in detail. A combination of UV-Vis and ED-XAFS shows the evolution of inactive Pd-dimers and trimers, that are the first stage in the deactivation process of important palladium catalyzed reactions, leading to larger palladium clusters and eventually palladium black.

In **Chapter 7** it is shown that the application of a wide range of spectroscopic techniques, including the newly developed combined time-resolved UV-Vis/EDXAFS, gives detailed structural and electronic information on the reaction intermediates involved in the Cu(II)-catalyzed arylation reaction. In combination with catalytic results, a novel, unexpected reaction mechanism for the important Cu(II) catalyzed arylation of aza-compounds has been proposed. In contrast to stated in literature, the reaction does not require the presence of dioxygen and only catalytic amounts of base are needed. The presence of H_2O, however, is necessary for the reaction to proceed. Based on our spectroscopic studies we propose that the first and selectivity determining step in the cycle is the reaction of the dinuclear Cu(II) starting complex with imidazole, forming a monomeric Cu(II)(Imidazolate) intermediate. Subsequent reaction with phenylboronic acid leads to a transient Cu(III)(imidazolate)(phenyl) intermediate. Reductive elimination of the phenylimidazole product results in a known Cu(I) species. Finally, the Cu species is reoxidized by a boronic species forming back the Cu(II) dinuclear complexes. The reaction suffers from substrate (imidazole) and product inhibition. The phenylboronic acid is, in combination with H_2O, involved in the oxidation and reoxidation steps in the described catalytic cycle.

Chapter 8b

Samenvatting

Een katalysator is een stof die de snelheid van een chemische reactie verhoogt, zonder daarbij zelf verbruikt te worden. Bovendien kan door middel van een katalysator de selectiviteit van een reactie, het soort producten dat gemaakt wordt, gestuurd worden. Katalytische processen behoren tot de belangrijkste methodes om producten op een voor het milieu verantwoorde manier te produceren. In dit proefschrift wordt onderzoek gedaan op het gebied van homogene katalyse, waarbij zowel de katalysator als de reactanten in vloeistoffase aanwezig zijn. Om katalysatoren te kunnen aanpassen en verbeteren is het belangrijk om te weten hoe ze precies werken. Voor het ophelderen van het reactiemechanisme van homogene katalysatoren, hebben we gedetailleerde structurele en elektronische informatie over het katalytisch actieve deeltje en de gevormde reactie intermediairen nodig. Röntgenabsorptie spectroscopie (Röntgen Absorptie Fijn Structuur spectroscopie, afkorting XAFS) is een techniek die gebruik maakt van hoog energetische straling, geproduceerd door een synchrotron. De techniek geeft informatie over de lokale structuur in verbindingen; het soort en aantal buren, de afstanden van die buren en de elektronische eigenschappen van het bestudeerde atoom. Bovendien kan XAFS spectroscopie worden toegepast onder reactiecondities en als functie van de tijd (tijdsopgelost). De techniek kan dus gebruikt worden voor het bepalen van structuur – activiteit relaties en helpen bij het ophelderen van reactiemechanismen.

In dit onderzoek worden verschillende aspecten van de homogene katalyse nader bestudeerd met behulp van XAFS spectroscopie. Nieuwe theorieën en data-analyse methodes zijn ontwikkeld om de verkregen data goed te kunnen analyseren en interpreteren. Tevens hebben we nieuwe instrumentatie ontwikkeld om homogene reacties tijdens reactie te kunnen volgen en zijn een aantal belangrijke reacties nader bestudeerd.

De standaard manier om XAFS spectra op te nemen is door steeds bij verschillende energieën de absorptie van een sample te meten en zo stap voor stap het XAFS spectrum, de absorptie als functie van de energie, te bepalen. De tijd die nodig is om zo een volledige spectrum op te nemen varieert van enkele minuten tot uren. Om informatie over dynamische systemen, zoals een katalysator in werking, te verkrijgen, is een nieuwe meettechniek ontwikkeld. Met deze zogenaamde energie dispersieve techniek (ED-XAFS) kan de absorptie van alle energieën tegelijkertijd bepaald worden en kunnen spectra gemeten worden in een tijdschaal van milliseconden tot seconden. De ED-XAFS techniek is verder ontwikkeld om homogene katalytische systemen te kunnen bestuderen. Omdat een combinatie van verschillende (spectroscopische) technieken aanvullende informatie over de aanwezige reactie intermediairen geeft, is een nieuwe set-up ontwikkeld waarmee deze reacties met tegelijkertijd met verschillende technieken gevolgd kunnen worden. De verschillende meettechnieken, set-ups en instrumentatie staan beschreven in **Hoofdstuk 2**.

XAFS spectroscopie wordt tot nu toe erg weinig toegepast in homogene katalyse. Dit komt omdat de techniek in dit onderzoeksgebied onbekend is en omdat het analyseren van de EXAFS data voor deze organometaalcomplexen erg ingewikkeld is. EXAFS is het stuk van het totale XAFS spectrum waaruit we de structurele informatie over de bestudeerde systemen verkrijgen. In **Hoofdstuk 3** is een nieuwe data-analyse methode beschreven waarmee de EXAFS data van dit type complexen goed en betrouwbaar geanalyseerd kunnen worden. Het is hierbij van belang dat tijdens de analyse de verschillende delen van het EXAFS spectrum benadrukt of 'uitvergroot', het zogenaamd toepassen van verschillende k-wegingen, en bestudeerd worden. Bovendien moeten alle individuele bijdragen aan het totale XAFS spectrum afzonderlijk gecontroleerd worden door middel van de zogenaamde verschil-file-techniek. Op deze manier kunnen bijvoorbeeld bijdragen die elkaar uitdoven, in tegen-fase zijn, uit elkaar gehaald worden. Door zo de data op veel verschillende manieren te bekijken, kunnen fouten in de analyse voorkomen worden. Alleen als alle individuele bijdragen significant groter zijn dan de ruis van de data, en zowel de gesimuleerde individuele bijdragen als het totale EXAFS spectrum in alle k-wegingen goed overeenkomen met de gemeten EXAFS data, kan een goede en betrouwbare EXAFS analyse verkregen worden. De nieuwe analyse methode is alleen gebaseerd op EXAFS parameters waardoor het in principe voor elk gemeten EXAFS spectrum geschikt is.

Hoewel van veel katalysator complexen een kristalstructuur bepaald is, is de structuur in het reactie medium (oplossing) vaak onbekend. Het bepalen van de structuur van deze katalysatoren in oplossing, kan al belangrijke informatie verschaffen over de activiteit en selectiviteit van de katalysator zoals aangetoond wordt in de **Hoofdstukken 3 and 6a**. In **Hoofdstuk 3** worden koper(I) complexen met behulp van XAFS spectroscopie bestudeerd.

De verkregen gedetailleerde structurele en elektronische structuur van deze homogene koperkatalysatoren in reactiemengsel (oplossing) geeft informatie over hun reactiviteit. De trimeer structuur van het [$Cu_3(Sar)_3$] complex blijkt in oplossing identiek te zijn aan de vaste stof en er wordt alleen een toename in flexibiliteit (beweging) van de gehele structuur waargenomen. In **Hoofdstuk 6a** worden EXAFS metingen beschreven aan (PP ligand)Pd(1,1-dimethylallyl) complexen. De resultaten laten zien dat in THF oplossing de coördinatie van het allyl fragment aan het palladium verschilt van de vaste stof, afhankelijk van het ligand. Voor complexen met een grote P-Pd-P hoek, is de coördinatie van het allyl aan het palladium symmetrisch, identiek aan de vaste stof. Echter de coördinatie van het allyl voor complexen met een kleine P-Pd-P hoek verandert in oplossing aanzienlijk. Het ongesubstitueerde koolstofatoom van het allyl fragment draait weg van het palladium atoom. Hierdoor wordt dit koolstofatoom makkelijker bereikbaar voor een reactant (nucleofiel) en bovendien wordt de elektronendichtheid op dit koolstofatoom verlaagd waardoor deze ook elektronisch voor reactie geactiveerd wordt. Het verschil in oriëntatie van het allyl fragment verklaart direct de verschillen in regioselectiviteit die gevonden worden voor de verschillende complexen. Met behulp van deze EXAFS studies kunnen we dus directe structuur – activiteit relaties in belangrijke homogene katalytische reacties bepalen.

XANES, het eerste deel van een XAFS spectrum, wordt direct bepaald door de (lege) moleculaire orbitalen van het bestudeerde complex (**Hoofdstuk 4**). De negatieve tweede afgeleide van de XANES data geeft directe informatie over de energie van en de ladingsverdeling in deze moleculaire orbitalen. XANES geeft dus essentiële informatie over de elektronische eigenschappen van de bestudeerde samples. In **Hoofdstuk 4** hebben we (PP)Pd(XX) complexen bestudeerd met Pd K-edge XANES spectroscopie. De ladingsverdelingen binnen deze complexen wordt beschreven als functie van de P-Pd-P hoek en het coördinerende fragment (XX). Zowel de Pd 5p als de Pd 4d orbitalen maken verschuivingen van elektronendichtheid van (PP) ligand naar Pd en het coördinerende molecuul (XX) naar Pd mogelijk. De eigenschappen van (XX) bepalen de interactie met het (PP)Pd fragment en dus de mate en aard van de ladingsverschuivingen. De bijbehorende orbitaal interactie diagrammen zijn bepaald. Theoretische berekeningen bevestigen de verkregen resultaten. De XANES techniek, zoals beschreven in dit hoofdstuk, kan worden toegepast om de moleculaire orbitalen van en de ladingsverdelingen binnen ieder soort sample te onderzoeken. Dit kan belangrijke informatie geven over de verschillen in activiteit en selectiviteit van de verschillende samples.

In **Hoofdstuk 5** zijn [PtCl(NCN)-Z] tangcomplexen bestudeerd met behulp van atomaire XAFS (AXAFS). AXAFS blijkt een gevoelige techniek te zijn om de veranderingen

193

in elektronendichtheid op het platina atoom, afhankelijk van de *para*-substituent aan de benzeenring, te bepalen. Deze tangcomplexen zijn bovendien een goed systeem om uitsluitend inductieve effecten of het AXAFS signaal te bestuderen, omdat de structuur rondom het platina atoom voor de verschillende complexen niet verandert. Bovendien wordt de AXAFS techniek, en met name de theoretische interpretatie daarvan, door middel van de resultaten in dit hoofdstuk bewezen. De invloed van verschillende effecten op de vorm en grootte van het AXAFS signaal worden bediscussieerd. Theoretische berekeningen voorspellen dezelfde trends en effecten. De AXAFS techniek is dus een gevoelige techniek om de elektronische eigenschappen van platina, en in principe ieder atoom, te bepalen. Dit is vooral interessant voor complexen waarbij de toepassing van andere meer toegankelijke technieken niet mogelijk is. Bovendien kan XANES spectroscopie worden uitgevoerd in het reactiemedium (oplossing) en tijdsopgelost, dus tijdens reactie.

Enkele homogene katalytische systemen zijn nader bestudeerd met behulp van de nieuw ontwikkelde, tijdsopgeloste, spectroscopische technieken. Homogene palladium katalysatoren zijn erg actief en selectief in verschillende reacties op het gebied van organische synthese. De stabiliteit van deze palladium katalysatoren is echter vaak te laag voor industriële toepassingen. Het is dus belangrijk om deze deactiveringsprocessen beter te begrijpen. Bidentaat liganden worden toegepast om de eigenschappen van de katalysator aan te passen en daarbij de activiteit en stabiliteit van de katalysator te vergtoren. De grootte van en het type inactieve palladiumdeeltjes welke tijdens de allylische substitutiereactie gevormd worden, zijn in **Hoofdstuk 6b** bestudeerd als functie van ligand en oplosmiddel. De combinatie van EDXAFS en UV-Vis technieken laten de vorming van inactieve palladium dimeren en trimeren zien. Deze dimeren en trimeren zijn de eerste stap in het deactiveringsproces van belangrijke palladium gekatalyseerde reacties, waarna grotere palladium deeltjes en uiteindelijk metallisch palladium gevormd wordt.

In **Hoofdstuk 7** laten we zien dat het gebruik van diverse spectroscopische technieken, inclusief de nieuw ontwikkelde combinatie van EDXAFS en UV-Vis, gedetailleerde structurele en elektronische informatie over de reactie intermediairen van een Cu(II) gekatalyseerde aryleringsreactie oplevert. In combinatie met katalytische resultaten wordt een nieuw en onverwacht reactiemechanisme voor deze belangrijke Cu(II) gekatalyseerde arylering van aza-complexen voorgesteld. Het blijkt dat moleculaire zuurstof en extra base niet nodig zijn om de aryleringsreactie te laten plaatsvinden, terwijl de aanwezigheid van water essentieel is. De eerste stap in de katalytische cyclus, en tevens de stap die de productselectiviteit bepaald, is de reactie van de uitgangskatalysator, een Cu(II) dimeer, met imidazool. Er wordt bij deze reactie een Cu(II)(imidazolaat) complex gevormd. Na toevoeging van phenylboorzuur reageert dit Cu(II) complex tot een

Cu(III)(imidazolaat)(phenyl) intermediair. Reductieve eliminatie van het product resulteert in de vorming van een Cu(I) monomeer. Het Cu(I) complex wordt uiteindelijk door middel van een boorcomplex terug geoxideerd tot de Cu(II) dimeren waarmee de reactie begonnen werd. Tijdens de reactie wordt inhibitie door zowel substraat (imidazole) en product waargenomen. Het phenylboorzuur en water blijken betrokken bij de oxidatie en reoxidatie stappen in deze katalytische cyclus.

Er kan geconcludeerd worden dat het onderzoek beschreven in dit proefschrift de XAFS spectroscopie techniek zowel op het gebied van de theorie en data-analyse als op het gebied van instrumentatie verder ontwikkeld heeft. Het is nu mogelijk zowel de structurele als elektronische eigenschappen van homogene katalysatoren in hun reactie medium en tijdens reactie in detail te bestuderen. Met behulp van de zo verkregen resultaten kunnen de eigenschappen van de katalysatoren begrepen worden en reactie mechanismen opgehelderd worden. Dit leidt vervolgens tot het optimaliseren van katalytische processen en/of de nieuwe ontwikkeling van katalysatoren en uiteindelijk tot milieuvriendelijker processen.

Publications

M. Tromp, J. A. van Bokhoven, M. T. Garriga Oostenbrink, J. H. Bitter, K. P. de Jong, D. C. Koningsberger, 'Influence of the Generation of Mesopores on the Hydroisomerization Activity and Selectivity of n-Hexane over Pt/Mordenite', *J. Catal.* **2000**, 190, 209-214.

J. A. van Bokhoven, M. Tromp, D. C. Koningsberger, J. T. Miller, J. A. Z. Pieterse, J. A. Lercher, B. A. Williams, H. H. Kung, 'An Explanation for the Enhanced Activity for Light Alkane Conversion in Mildly Steamed Dealuminated Mordenite: The Dominant Role of Adsorption', *J. Catal.* **2001**, 202, 129-140.

M. Tromp, J. A. van Bokhoven, A. M. Arink, J. H. Bitter, G. van Koten, D. C. Koningsberger, 'Cu K-edge EXAFS Characterisation of Copper(I) Arenethiolate Complexes in both the Solid and Liquid State: Detection of the Cu-Cu Coordination', *Chem. Eur. J.* **2002**, 8(24), 5667-5678 (**Chapter 3** of this thesis).

M. Tromp, J. A. van Bokhoven, R. J. van Haaren, G. P. F. van Strijdonck, A. M. J. van der Eerden, P. W. N. M. van Leeuwen, D. C. Koningsberger, 'Structure-Performance Relations in Homogeneous Pd Catalysis by In Situ EXAFS Spectroscopy', *J. Am. Chem. Soc.* **2002**, 124(50), 14814-14815 (**Chapter 6a** of this thesis).

M. Tromp, J. R. A. Sietsma, J. A. van Bokhoven, G. P. F. van Strijdonck, R. J. van Haaren, A. M. J. van der Eerden, P. W. N. M. van Leeuwen, D. C. Koningsberger, 'Deactivation Processes of Homogeneous Pd Catalysts using *In Situ* Time Resolved Spectroscopic Techniques', *Chem. Comm.* **2003**, 128-129 (**Chapter 6b** of this thesis).

S. S. van Berkel, A. van der Hoogenband, M. Tromp, P. W. N. M. van Leeuwen, G. P. F. van Strijdonck, 'Formation of Aryl-Nitrogen Bonds Using bis-μ-hydroxy Copper(II)-Based Catalysts', *Chem. Comm.*, submitted for publication (**Chapter 7a** of this thesis).

M. Tromp, J. A. van Bokhoven, M. Q. Slagt, G. van Koten, D. E. Ramaker, D. C. Koningsberger, 'Atomic XAFS as a Probe of Charge Redistribution within Organometallic Complexes', *J. Am. Chem. Soc.*, accepted for publication (Communication of **Chapter 5** of this thesis).

M. Tromp, S. S. van Berkel, S. G. Fiddy, G. P. F. van Strijdonck, J. A. van Bokhoven, P. W. N. M. van Leeuwen, D. C. Koningsberger, 'Novel Combined Time-Resolved ED-XAFS / UV-Vis set-up to Study Homogeneous Catalytic Reactions', *Angew. Chem. Int. Ed.*, submitted for publication (combination of parts of **Chapter 2** and **Chapter 7b** of this thesis).

M. Tromp, J. A. van Bokhoven, G. P. F. van Strijdonck, P. W. N. M. van Leeuwen, D. C. Koningsberger, D. E. Ramaker, 'Probing the Molecular Orbitals and Charge Distribution in Organometallic (PP)Pd(XX) Complexes. A Pd K-edge study', *J. Am. Chem. Soc.*, submitted for publication (**Chapter 4** of this thesis).

M. Tromp, M. Q. Slagt, R. J. M. Klein Gebbink, G. van Koten, D. E. Ramaker, D. C. Koningsberger, 'Atomic XAFS as a Probe of Charge Redistribution within Organometallic Complexes', *J. Am. Chem. Soc.*, submitted for publication (Full paper, **Chapter 5** of this thesis).

M. Tromp, S. S. van Berkel, A. van den Hoogenband, M. C. Feiters, B. de Bruin, P. W. N. M. van Leeuwen, G. P. F. van Strijdonck, 'Multi-technique Approach to Reveal the Mechanism of Cu(II) Catalzyed Arylation Reactions', *Chem. Eur. J.*, submitted for publication (**Chapter 7b** of this thesis).

A. M. Arink, M. Tromp, J. T. B. H. Jastrzebski, D. C. Koningsberger, G. van Koten, 'Structural information on copper(I) arenethiolates and organo(thiolato)cuprates using EXAFS and NMR', in preparation.

M. Tromp, D. E. Ramaker, D. C. Koningsberger, 'Demonstration, Explanation and Validation of AXAFS in Homogeneous and Heterogeneous Catalytic Systems', in preparation.

G. Rothenberg, M. Tromp, G. P. F. van Strijdonck, 'Detailed Mechanistic Studies on the Deactivation of Homogeneous Pd Complexes using *In Situ* Spectroscopic Techniques', in preparation (in addition to **Chapter 6b** of this thesis).

M. Lutz, M. Tromp, G. P. F. van Strijdonck, A. L. Spek, 'Crystal Structure of [(TMEDA)Cu(Imidazolate)]$_3$', in preparation (in addition to **Chapter 7b** of this thesis).

Conference proceeding

J.H. Bitter, J.A. van Bokhoven, M. Tromp, A.H. Janssen, K.P. de Jong, D.C. Koningsberger, 'Enhancement of the activity and selectivity of hydro-isomerization of n-hexane over Pt/H-Mordenite by mesopore generation', *Abstracts ZMPC2000*, Sendai (Japan), August 6-9 **2000**, 62

Special Articles

Mitch Jacobi, 'Solution-Phase Catalyst Probe: Homogeneous reactions mechanism yields X-ray absorption method', Chemical & Engineering News, December 23, 2002, *CENEAR* **2002**, 80(51), 8.

Gabby Zegers, 'Momentopnamen van Katalytische Systemen', *Chemisch2Weekblad* **2003,** 99(4), 12-13.

Oral Presentations

M. Tromp, J. A. van Bokhoven, G. van Koten, D. C. Koningsberger, 'Development of Energy Dispersive XAFS – for the Investigation of Homogeneous Reaction Intermediates', National Research School Combination Catalysis – Work Conference, Utrecht, The Netherlands, November 2000.

M. Tromp, J. A. van Bokhoven, R. J. van Haaren, G. P. F. van Strijdonck, P. W. N. M. van Leeuwen, D. C. Koningsberger, 'Characterization of (P-P)Pd(allyl) Catalysts in Solid State and Solution', Kristal- en Structuurchemie Symposium, Lunteren, The Netherlands, April 2001.

M. Tromp, J. A. van Bokhoven, R. J. van Haaren, G. P. F. van Strijdonck, P. W. N. M. van Leeuwen, D. C. Koningsberger, 'Exploration of X-ray Absorption Fine Structure Spectroscopy for the *In Situ* study of Homogeneous Catalysts', 10th Symposium on the relations between Homogeneous and Heterogeneous Catalysis, Lyon, France, July 2001.

M. Tromp, J. A. van Bokhoven, G. P. F. van Strijdonck, A. M. J. van der Eerden, P. W. N. M. van Leeuwen, D. C. Koningsberger, '*In situ* Study of the Formation of Inactive Clusters in the Pd-catalyzed Allylic Alkylation Reaction using Energy Dispersive XAFS', EuropaCat V, Limerick, Ireland, September 2001.

M. Tromp, J. A. van Bokhoven, G. P. F. van Strijdonck, A. M. J. van der Eerden, P. W. N. M. van Leeuwen, D. C. Koningsberger, 'Application of *In Situ* X-ray Absorption Fine Structure Spectroscopy in Homogeneous Catalysis', Colloquium for the Institute of Molecular Chemistry, University of Amsterdam, Amsterdam, The Netherlands, October 2001.

M. Tromp, J. A. van Bokhoven, G. P. F. van Strijdonck, A. M. J. van der Eerden, P. W. N. M. van Leeuwen, D. C. Koningsberger, '*In Situ* Study of the Pd-Catalysed Substitution Reaction and Its Deactivation: An (Energy Dispersive) XAFS Study', 3rd Netherlands' Catalysis and Chemistry Conference, Noordwijkerhout, The Netherlands, March 2002.

M. Tromp, J. A. van Bokhoven, A. M. J. van der Eerden, G. van Koten, D. C. Koningsberger, G. P. F. van Strijdonck, P. W. N. M. van Leeuwen, 'Development of Energy Dispersive XAFS: The *In Situ* Study of Catalytic Reaction Intermediates', Debye Lecture, Utrecht, The Netherlands, May 2002.

M. Tromp, S. van Berkel, S. G. Fiddy, G. P. F. van Strijdonck, J. A. van Bokhoven, P. W. N. M. van Leeuwen, D. C. Koningsberger, 'Development of Time-Resolved Spectroscopic Techniques for the *In Situ* Study of Homogeneous Catalytic Systems', International Congress on Operando Spectroscopy, Lunteren, The Netherlands, March 2003.

M. Tromp, S. van Berkel, S. G. Fiddy, G. P. F. van Strijdonck, J. A. van Bokhoven, P. W. N. M. van Leeuwen, D. C. Koningsberger, 'Development of Time-Resolved Spectroscopic Techniques for the *In Situ* Study of Homogeneous Catalytic Systems', 4th Netherlands' Catalysis and Chemistry Conference, Noordwijkerhout, The Netherlands, March 2003.

M. Tromp, S. van Berkel, S.G. Fiddy, G.P.F. van Strijdonck, J.A. van Bokhoven, P.W.N.M. van Leeuwen, D.C. Koningsberger, 'Development of Time-Resolved Spectroscopic Techniques for the *In Situ* Study of Homogeneous Catalytic Systems', 12th International Conference on X-ray Absorption Fine Structure, Malmö, Sweden, June 2003.

M. Tromp, D.C. Koningsberger, '(Time-Resolved) XAFS Spectroscopy Techniques – Applications in Homogeneous Catalysis', Inorganic Colloquium Cambridge University, Cambridge, United Kingdom, September 2003.

Poster Presentations

M. Tromp, M. T. Garriga Oostenbrink, J. H. Bitter, D. C. Koningsberger, 'On the relation between pore structure and activity/selectivity of hydro-isomerisation catalysts', KNCV Catalysis Congress, Lunteren, The Netherlands, May 1999.

M. Tromp, J. A. van Bokhoven, G. P. F. van Strijdonck, A. M. Arink, P. W. N. M. van Leeuwen, G. van Koten, D. C. Koningsberger, 'Development of Energy Dispersive XAFS for the *In Situ* Study of Homogeneous Catalytic Reaction Intermediates', 2nd Netherlands' Catalysis and Chemistry Conference, Noordwijkerhout, The Netherlands, March 2001.

M. Tromp, J. A. van Bokhoven, G. P. F. van Strijdonck, J. R. A. Sietsma, A. M. J. van der Eerden, P. W. N. M. van Leeuwen, D. C. Koningsberger, 'Deactivation of Homogeneous Pd Catalysts using *In Situ* Time Resolved Spectroscopic Techniques', 13th International Symposium on Homogeneous Catalysis, Tarragona, Spain, September 2002.

M. Tromp, S. van Berkel, S.G. Fiddy, G.P.F. van Strijdonck, J.A. van Bokhoven, P.W.N.M. van Leeuwen, D.C. Koningsberger, 'Development of Time-Resolved Spectroscopic Techniques for the *In Situ* Study of Homogeneous Catalytic Systems', Symposium NRSCC, PEER Review, Eindhoven, The Netherlands, April 2003.

M. Tromp, B. O'Grady, G. van Koten, D.E. Ramaker, D.C. Koningsberger, 'Demonstration of Atomic XAFS', 12th International Conference on X-ray Absorption Fine Structure, Malmö, Sweden, June 2003.

M. Tromp, S. van Berkel, M. Kuil, A. van den Hoogenband, J. W. Terpstra, D. C. Koningsberger, P. W. N. M. van Leeuwen and G. P. F. van Strijdonck, 'C-C and C-N Bond Formations: Pd(0), Cu(I) or Cu(II)?', 12th IUPAC International Symposium on Organometallic Chemistry Directed Towards Organic Synthesis, Toronto, Canada, July 2003.

Awards

NRSC-Catalysis Award for Best Graduate Student Lecture, 4th Netherlands Catalysis and Chemistry Conference, Noordwijkerhout, the Netherlands, March 2003.

Poster Price, NRSCC Symposium, PEER Review, Eindhoven, April 2003.

Dankwoord

Nu is het dan zover: hoe moeilijk het ook is, er moet (voorlopig) een punt achter dit onderzoek gezet worden. Vier jaren gaan ongelooflijk snel voorbij en er zijn nog zoveel ideeën. Maar dat is inherent aan onderzoek, het is nooit af. Ik ben in ieder geval heel trots het resultaat zoals dat nu voor mij en jullie ligt. En ik ben blij dat deze pagina's mij tenslotte de kans geven alle mensen die mij gedurende de afgelopen vier jaar hebben bijgestaan te bedanken. Ik ben ervan overtuigd dat de verschillende samenwerkingsverbanden, zowel qua technieken als personen, de kracht van dit onderzoek zijn geweest.

Allereerst natuurlijk Diek. Mede door jouw onnavolgbare enthousiasme voor de 'science' ben ik vier jaar terug begonnen aan dit onderzoek. Je hebt me de kans gegeven hierin mijn eigen weg te kiezen en mij vervolgens altijd gesteund in al mijn ondernemingen. Je hebt mij geholpen te middelen tussen alle partijen en de beste keuzes te maken, vaak voorafgegaan door de nodige waardevolle discussies en uiteindelijk de toekenning van 'nobelprijzen'. Door alles wat er is gebeurd, maar natuurlijk ook door onze twee maanden in Amerika, ben jij in de afgelopen vier jaar 'meer dan promotor' geworden en heb ik vele waardevolle 'vaderlijke' en 'dochterlijke' adviezen van je mogen krijgen. De periode in Washington DC was zeker een 'high' van mijn promotieperiode, ik voelde me erg thuis bij jou en Pia. Dank jullie wel voor alles.

Gerard, onze plannen aan het begin van mijn promotie bleken helaas soms een beetje te ambitieus. Toch hebben we hele mooie dingen samen kunnen doen, die al veel stof tot discussie in de wetenschappelijke wereld geven, én nog gaan geven. Dank je wel voor je enthousiasme voor en waardevolle bijdrages aan mijn werk, en daarnaast voor je altijd warme belangstelling voor mij persoonlijk.

Naast twee promotoren ben ik ook in het gelukkige bezit van twee copromotoren. Jeroen, jij hebt me vijf jaar geleden als student enthousiast gemaakt voor de wetenschap. Daar blijf ik je altijd dankbaar voor want ik zit er voor mijn gevoel helemaal op mijn plek. Ik heb veel geleerd van je altijd kritische blik en onze vele discussies tijdens de uurtjes op een synchrotron of gewoon onder het genot van een borrel. We zijn een erg goed team en ik ben er van overtuigd dat we nog mooie dingen gaan doen samen. Door de samenwerking met Amsterdam heb ik Gino leren kennen. Het bundelen van onze expertises leidde al snel tot spannende resultaten, steeds meer nieuwe projecten en uiteindelijk tot het grootste deel van dit boekje. Ik hoop dat we op de een of andere manier samen kunnen blijven werken, misschien ooit die gezamenlijke groep? Dank je wel voor alles wat ik van jou geleerd heb over de homogene wereld en voor je bijzondere vriendschap.

In Amsterdam heb ik natuurlijk ook veel hulp gehad van Piet van Leeuwen. Piet, dank je wel voor al je hulp en steun. Je onuitputtelijke kennis van de chemie is ongelooflijk.

Dave, our collaboration was one of the most successful ones. I was lucky to spend time with you and Diek in Washington DC. Since I was for two months in the possession of two 'private professors', we were able to unravel the enormous amount of data, resulting in beautiful papers. Your energy and determination to solve the scientific problems is very inspiring. Moreover, I would like to thank you en Beverly for your hospitality in your home and in your country. And, I cannot omit this; you and Diek have made the making of cappuccino into an art.

Ad, met jou begon het allemaal met een dansje op het kerkplein in Grenoble. Daarna hebben we vier jaar intensief samengewerkt aan het realiseren van de nieuwe opstelling en hebben we vele uurtjes op diverse synchrotrons doorgebracht. Werk en privé probeer je altijd strikt gescheiden te houden, toch is dat in ons geval de afgelopen vier jaar een beetje door elkaar heen gaan lopen. Ik ben blij dat je mij bijzonder genoeg vindt om je principes opzij te schuiven en de 19e als paranimf naast me wilt staan!

Naast deze 'harde kern', heb ik met veel mensen samengewerkt op allerlei verschillende gebieden. Allereerst Anne Arink, de enige vrouw waarmee ik heb samengewerkt. Onze projecten waren via EXAFS en koper aan elkaar verbonden. De experimenten waren vaak moeilijker dan verwacht, toch ben ik blij dat we ze gedaan hebben; we hebben er veel van geleerd en ik heb je daardoor goed leren kennen!

De nieuwe ED-XAFS/UV-Vis set-up, had ik niet kunnen bouwen zonder de hulp van Peter van den Beld en Hans Heesen. We vroegen soms schijnbaar onmogelijke dingen van jullie, maar het is altijd op tijd gelukt en we hebben nooit problemen gehad. Dank jullie wel! Gerbrand en Kaisa, take good care of my 'baby' and I hope your research with it will be as successfull as mine.

Ik heb twee studenten gehad die mij met mijn onderzoek geholpen hebben en die ik daarvoor zelfs mee naar synchrotrons heb genomen. Jelle, jouw meteen al succesvolle werk heeft bovendien geleid tot het bouwen van de nieuwe gecombineerde set-up! Sander, je hebt een enorme hoeveelheid indrukwekkend werk verricht, wat heeft geleid tot hele mooie publicaties. Ik heb veel van jullie geleerd en vond het een eer met jullie te mogen werken. Ik wens jullie allebei heel veel succes met jullie eigen promotie onderzoek.

During the last four years I have spent many hours on different synchrotrons in Europe, but mainly on the Energy Dispersive beamline ID24 in Grenoble. Sakura Pascarelli, thank you for giving us the opportunity to work at your beamline and help us develop our set-up and chemistry. Sofia, thank you for your help in working with the stopped-flow and getting our experiments to work. Sebastien, Trevor and Florian, your help in building the

set-up and getting all the electronics to work was indispensable. And, last but definitely not least, Steven. I have really enjoyed working with you and getting to know you! Thank you for spending so many hours with me on the beamline.

Richard, jij zette me op het pad van de palladium-allyl chemie. We hebben nooit meer daadwerkelijk samen hieraan gewerkt, maar zoals je kunt zien is het een zeer succesvol onderwerp van mijn onderzoek geworden. Dank je wel! Martijn, met jouw pincers kunnen we hopelijk eindelijk de wereld van het bestaan van AXAFS overtuigen! Ook Bert Klein Gebbink, jou wil ik hartelijk danken voor je hulp bij het pincer werk. Adri van de Hoogenband wil ik bij deze bedanken voor zijn hulp bij en enthousiasme en interesse voor ons koper project. Martin Feiters en Bas de Bruin voor de mooie EPR metingen en de alle hulp bij de interpretatie daarvan.

De vakgroep Anorganische Chemie en Katalyse was mijn thuisbasis, waar ik de afgelopen vier jaar met heel veel plezier heb gewerkt. Alle (oud)collega's wil ik bij deze hartelijk danken voor alle interesse, hulp en gezelligheid en dan in het bijzonder: Jeroen, Michiel ('Miekje' heeft me tot het eind geholpen. Tja, dit was het dan!), Tijmen, Ries, Gerbrand, Harry, Marjolein, Jules, Dennis, Krijn (je warme betrokkenheid heb ik altijd erg gewaardeerd), Bert (dank je voor je hulp met de UV-Vis). Natuurlijk een bijzonder plaatsje voor mijn kamergenoten. Sander en Andrea, we hadden vaak flauwe, maar indien nodig ook diepe gesprekken onder het genot van een kop koffie. Dank jullie wel voor de gezelligheid en jullie betrokkenheid. Wanneer gaat ons 'traditionele kamer-etentje' weer plaatsvinden? From the moment Jaap and Daniel accompanied me in room N215, I was hardly there anymore. This had absolutely nothing to do with the both of you; you were great roommates and I wish you all the best with your research projects. Dymph en Monique, dank jullie wel voor alle broodnodige ondersteuning en gezelligheid: we houden zeker contact!

Ik heb zoals gezegd vele weken doorgebracht op de diverse synchrotons in Europa. Tijdens die meetperiodes hebben diverse mensen mij vergezeld en geholpen, waarvoor ik ze heel erkentelijk ben: Ad, Andrea, Anne, Bert, Dennis, Didier, Gerbrand, Gino, Harry, Jan, Jelle, Jeroen, Kaisa, Laurens, Maarten, Marijke, Michiel, Piotr en Sander.

Het enige deel van het boekje wat echt iedereen zal zien is de kaft. Die is dus ook erg belangrijk en het valt nog niet mee iets moois te verzinnen. Hendrik, dank je wel voor je geweldige idee en al het werk; ik vind het supermooi geworden en ben er heel erg blij mee!

Het tot stand komen van dit boekje is natuurlijk werk. Aangezien er dezelfde periode ook daarnaast dusdanig veel gebeurd is, wil ik van deze gelegenheid toch gebruik maken om op deze bijzonder manier mijn vrienden en familie te bedanken. Zonder hen was het onderzoek misschien wel gelukt, maar had ik het zelf heel veel minder leuk gehad. Hoe

makkelijk en vanzelfsprekend het voor mij is om voor mijn werk veel mensen om hulp te vragen en samen met hen de problemen aan te pakken, zo moeilijk is dat vaak voor mij privé. Afgelopen jaren heb ik geleerd dat je niet alles alleen hoeft en soms ook niet kan doen. Ik prijs me gelukkig dat ik heb mogen ervaren dat ik heel veel, hele goede vrienden heb: Jeroen en Katja, ik heb van jullie veel geleerd, over het leven en vooral ook over mezelf. Door jullie durf ik nu de stap te maken en naar het buitenland te gaan, want ik heb ervaren dat als vriendschap echt goed is, de wereld maar heel klein is. Lein, samen is het is ons toch maar mooi gelukt en ik ben heel erg trots op je! Pas goed op jezelf en blijf gelukkig. Sietske, je stond voor me klaar toen het voor anderen ingewikkeld werd en bent nooit meer gegaan. Dit is vriendschap voor het leven! En natuurlijk niet te vergeten Michiel, Tijmen, Ingrid, Anne-Margot, Gabby, Bas, Anne, Marc, Wypke, Fred (je belt altijd op het goede moment), Monique (voor af en toe weekje rust).

Lieve Sander, natuurlijk vergeet ik jou niet. Ik ben heel blij dat je de 19^e naast me zal staan en die dag als mijn paranimf met mij wilt delen. We hebben de afgelopen jaren samen heel veel dingen meegemaakt, zowel hele mooie als minder mooie dingen. Ik ben blij dat we dit altijd samen hebben kunnen delen, elkaar daarin hebben kunnen steunen, en zo 'beste vriendjes' zijn geworden. Dank je voor al je steun, vriendschap en vooral ook je, voor mij soms zeer verhelderende, eerlijkheid. Je bent een schat!

Tenslotte mijn familie. Ik kom altijd graag naar Beekbergen voor een gezellig hapje en drankje! Opa en oma, ik ben blij dat jullie er de 19^e april bij zullen zijn, ik hou van jullie. Arno en Judith, mijn allerliefste broertje (nog altijd) en zusje (sinds kort ook echt!), maar vooral ook lieve en waardevolle vrienden. Ik hoop dat we elkaar veel blijven zien en spreken, waar en hoe druk we ook zijn.

Lieve mam en pap, dankzij jullie heb ik altijd kunnen doen wat me hart me ingaf en kon ik de persoon worden die ik nu ben. Dank jullie wel voor jullie liefde, ik hou ontzettend veel van jullie!

Moniek

Curriculum Vitae

Moniek Tromp werd geboren op 7 september 1977 te Apeldoorn. In 1995 behaalde zij haar VWO diploma aan het Stedelijk Gymnasium te Apeldoorn. In september van datzelfde jaar begon zij aan de studie scheikunde aan de Universiteit Utrecht, waar zij in 1996 haar propedeuse diploma met genoegen behaalde. In 2000 studeerde zij met genoegen af, na universitaire stages bij de secties Gecondenseerde Materie (Prof. Dr. A. Meijerink) en Anorganische Chemie en Katalyse (Prof. Dr. Ir. D. C. Koningsberger). Tijdens haar studie was Moniek onder andere actief als penningmeester van de Utrechtse Scheikundige Studentenvereniging Proton, de β-Bedrijvendagen Utrecht en als voorzitter van de Stichting PAC.

Vanaf 2000 was Moniek werkzaam als Onderzoeker in Opleiding, in dienst van de Toponderzoeksschool Katalyse (National Research School Combination – Catalysis), bij Prof. Dr. Ir. D. C. Koningsberger, Prof. Dr. G. van Koten en Dr. J. A. van Bokhoven binnen de sectie Anorganische Chemie en Katalyse van de Universiteit Utrecht. Het promotieonderzoek werd tevens uitgevoerd in nauwe samenwerking met Dr. G. P. F. van Strijdonck en Prof. Dr. P. W. N. M. van Leeuwen, Universiteit van Amsterdam, en Prof. Dr. D. E. Ramaker, George Washington University, Washington D.C.. De resultaten van dit promotieonderzoek staan beschreven in het proefschrift dat u nu in handen heeft.